Theory and simulation of multi-GeV laser wakefield acceleration at kHz repetition rates



Johannes J. van de Wetering

Wolfson College, University of Oxford

Submitted in partial fulfillment of the requirements for the degree of Doctor of Philosophy at the University of Oxford

April 2024

Abstract

Deploying both analytic methods and particle-in-cell (PIC) simulations, we investigate the operating regime and performance of the Plasma-Modulated Plasma Accelerator (P-MoPA) [1]. This new approach offers the potential for GeV-scale laser wakefield accelerators (LWFA) at kHz repetition rates by taking advantage of pre-existing thin-disk laser technology [2–4], overcoming the < 0.1–1 Hz shot rates of contemporary LWFA systems. We derive a 3D analytic theory of the P-MoPA for the laser pulse and wakefield evolution in long (> 100 mm) pre-formed plasma channels, and benchmark our theory with particle-in-cell (PIC) simulations.

We identify a self-modulational transverse mode instability (TMI) that limits the energy of the drive pulse accepted by the modulator stage of the P-MoPA, and find that our theory agrees well. This shows that the TMI is the limiting factor of the plasma modulator, but still allows multi-joule drive pulses corresponding to multi-GeV electron beams. Extended 3D non-paraxial theory in conjunction with further PIC simulations then demonstrate the viability of multi-GeV LWFA driven by these plasma-modulated pulses. Finally, we evaluate the P-MoPA for a potential application as a kHz driver for a water-window X-ray free electron laser (XFEL).

Acknowledgements

First and foremost, I want to thank my advisors Simon Hooker and Roman Walczak for their invaluable guidance and support throughout my time here. Your vast knowledge of the field, attention to detail and insightful discussions made it an absolute pleasure to do research with you.

I am deeply indebted to my scholarship donors Ken and Veronica Tregidgo for their generous financial support, which allowed me to pursue my research interests without financial constraints.

My heartfelt appreciation goes to my fellow postgraduate students and colleagues in the Oxford group: James Chappell, Linus Feder, Aimee Ross, James Cowley, Oscar Jakobsson, Emily Archer, Warren Wang, David McMahon, Darren Chan and Sebastian Kalos. It has been a pleasure working with you all. I especially want to thank Aimee and James Ch. for the many fruitful conversations and collaborations.

To all the friends I made along the way, you made it the greatest years of my life. The invigorating chats at the Wolfson cafe, the Saturday morning runs in University Parks, the summertime punting along the River Cherwell, and the countless college formals and balls made living here a blast.

To my parents, thank you for your love and fostering my interest in physics since childhood. From measuring Earth's gravitational pull using legos to digging through your old textbooks, you have been my inspiration.

List of Publications

J. J. van de Wetering, S. M. Hooker and R. Walczak. **Stability of the modulator in a plasma-modulated plasma accelerator.** *Physical Review E*, 108, 015204, 2023. https://link.aps.org/doi/10.1103/PhysRevE.108.015204

J. J. van de Wetering, S. M. Hooker and R. Walczak. **Multi-GeV wakefield acceleration in a plasma-modulated plasma accelerator.** *Physical Review E*, 109, 025206, 2024. https://link.aps.org/doi/10.1103/PhysRevE.109.025206

A. J. Ross, J. Chappell, J. J. van de Wetering, J. Cowley, E. Archer, N. Bourgeois, L. Corner, D. R. Emerson, L. Feder, X. J. Gu, O. Jakobsson, H. Jones, A. Picksley, L. Reid, W. Wang, R. Walczak, and S. M. Hooker. **Resonant excitation of plasma waves in a plasma channel.** *Physical Review Research*, 6, L022001, 2024. https://link.aps.org/doi/10.1103/PhysRevResearch.6.L022001

J. J. van de Wetering, S. M. Hooker and R. Walczak. **Self-matching in quasilinear wakefields driven by kilohertz lasers.** *Manuscript in preparation.*

List of Symbols

e	Elementary charge
m_e	Electron mass
ϵ_0	Vacuum permittivity
c	Speed of light in vacuum
$\hbar$	Reduced Planck's constant
r_e	Classical electron radius
n_e	Electron density
T_e	Electron temperature
ω_p	Plasma (angular) frequency
k_p	Plasma wavenumber
λ_p	Plasma wavelength
T_p	Plasma period
E_0	Cold nonrelativistic wavebreaking field
λ_D	Debye length
ω_L	Laser beam (angular) frequency
k_L	Laser beam wavenumber
λ_L	Laser beam wavelength
w	Laser beam spot size
a_0	Laser beam peak normalized vector potential
Ω_w	Laser beam spot size oscillation (angular) frequency in a channel
Ω_c	Laser beam centroid oscillation (angular) frequency in a channel

Contents

1 Introduction **1**
- 1.1 Laser Wakefield Acceleration . . . 1
  - 1.1.1 Motivation . . . 1
  - 1.1.2 State of the Field . . . 4
- 1.2 Thesis Outline . . . 5
  - 1.2.1 Role of the Author . . . 6
- 1.3 Mechanics of LWFA . . . 7
  - 1.3.1 Ponderomotive Force . . . 7
  - 1.3.2 Linear Wakefield Regime . . . 10
  - 1.3.3 Nonlinear Wakefield Regime . . . 13
  - 1.3.4 The Quasistatic Approximation . . . 15
  - 1.3.5 Finite Temperature Effects . . . 19
  - 1.3.6 Summary of LWFA Regimes . . . 23
- 1.4 Fundamental Challenges for LWFA . . . 24
  - 1.4.1 Diffraction . . . 24
  - 1.4.2 Dephasing . . . 26
  - 1.4.3 Energy Efficiency and Repetition Rate . . . 27

2 Pulse Propagation in Plasma Channels **28**
- 2.1 Motivation . . . 28
- 2.2 Paraxial Propagation Theory . . . 29
  - 2.2.1 The Envelope Model . . . 29
  - 2.2.2 The Paraxial Approximation . . . 31
  - 2.2.3 Plasma Channels . . . 32
  - 2.2.4 Time-Dependent Perturbation Theory . . . 37
  - 2.2.5 Envelope Self-Modulation and Relativistic Self-Focusing . . . 40
- 2.3 The Non-Paraxial Description . . . 43
  - 2.3.1 Group Velocity and Channel Mode Dispersion . . . 44
  - 2.3.2 Chromatic Dispersion . . . 46
  - 2.3.3 Time-Dependent Perturbation Theory . . . 48
  - 2.3.4 Stimulated Raman Scattering . . . 49
- 2.4 Ionization Effects . . . 52
  - 2.4.1 Ionization Models . . . 52
  - 2.4.2 Ionization-induced Nonlinearities . . . 58
- 2.5 Wigner Distribution Formalism . . . 62
- 2.6 Wakefield Structure in Plasma Channels . . . 64

2.6.1 Linear Wakefield Theory in Plasma Channels . . . 64
2.6.2 Optimizing Channels for MP-LWFA . . . 68
2.7 Resonant Excitation of Plasma Waves in a Plasma Channel . . . 69
2.7.1 Motivation . . . 69
2.7.2 Fluid Code for Spectral Modulation . . . 70
2.7.3 PIC simulations of conditioning effect . . . 72

3 The P-MoPA Modulator Stage 74
3.1 GeV-Scale LWFA at kHz Repetition Rates . . . 74
3.2 The Plasma Modulator . . . 76
3.2.1 Seeded Spectral Modulation in Plasma Channels . . . 76
3.2.2 Channel Suppression of Spectral Modulation . . . 79
3.2.3 The Shallow Channel Approximation . . . 81
3.2.4 Relativistic Self-Phase Modulation . . . 82
3.2.5 Compression into a Pulse Train . . . 84
3.3 Stability of the Plasma Modulator . . . 85
3.3.1 Group Velocity Dispersion . . . 86
3.3.2 Defocusing of Stokes Sidebands Driving Transverse Mode Transitions . . . 88
3.3.3 Transverse Mode Stability Condition . . . 93
3.3.4 Seed Pulse Donut Mode Effects . . . 102
3.3.5 Wake Suppression of Raman Backscattering . . . 105
3.4 Summary of Design Considerations . . . 107
3.4.1 Channel Profile Effects . . . 108
3.4.2 TMI Energy Limit . . . 109

4 The P-MoPA Accelerator Stage 112
4.1 Multipulse LWFA . . . 112
4.1.1 Scaling Laws . . . 114
4.1.2 Channel Effects on Energy Gain . . . 117
4.1.3 P-MoPA Pulse Shaping . . . 120
4.1.4 The Rosenbluth-Liu Limit . . . 123
4.2 Pulse Propagation Effects . . . 126
4.2.1 Relativistic Self-Phase Modulation and Transverse Mode Excitation . . . 126
4.2.2 Non-Uniform Depletion . . . 132
4.3 Multi-GeV P-MoPA Electron Accelerator . . . 135

5 A P-MoPA-driven Water Window XFEL 138
5.1 Bunch Dynamics . . . 138
5.1.1 6D Phase Space . . . 139
5.1.2 Emittance and Brightness . . . 140
5.1.3 Bunch Self-Fields . . . 142
5.1.4 Transverse Equations of Motion . . . 144
5.1.5 Twiss Parameters . . . 146
5.2 X-ray Free Electron Lasers . . . 147

5.2.1 Motivation . . . 147
5.2.2 Free Electron Lasing . . . 149
5.2.3 Bunch Requirements . . . 151
5.3 Emittance Matching in a P-MoPA . . . 153
5.3.1 Transverse Beam Loading . . . 153
5.3.2 Plasma In- and Out-Matching . . . 158
5.3.3 Laser-Driven Betatron Oscillation . . . 161
5.4 Summary . . . 164

6 Conclusion **165**
6.1 Contributions . . . 165
6.2 Future Work . . . 167
6.2.1 P-MoPA Proof of Concept . . . 167
6.2.2 CHOFI Channel Profile Tuning . . . 167

A A Numerical Method for Evaluating Wakefields in Plasma Channels **169**

B Down-Ramp Injection in Multipulse Quasilinear Wakefields **171**

References **174**

List of Figures

1.1 Wakefields in the 1D linear regime 12

1.2 Wakefields in the 1D nonlinear regime 18

2.1 Laguerre-Gaussian modes 33

2.2 Bessel modes 35

2.3 Spot size and centroid oscillations 37

2.4 Chromatic dispersion 48

2.5 Optical field ionization rate of atomic hydrogen 58

2.6 ADK ionization of a HOFI channel neutral collar 61

2.7 Wakefield in a parabolic channel 67

2.8 Channel optimization by increasing the dephasing length 69

2.9 Mock Michelson pulse train 70

2.10 Example exit mode spectrum 72

2.11 PIC simulation of HOFI channel conditioning 73

3.1 Outline of the P-MoPA scheme 75

3.2 Spectral modulation in 2D vs. 3D 78

3.3 Radially independent spectral modulation 79

3.4 Spectral modulation suppression by plasma channels 1 80

3.5 Spectral modulation suppression by plasma channels 2 81

3.6 Multipulse train formation (theory) 85

3.7 Transmittance of central and (anti-)Stokes sidebands 86

3.8 Group velocity dispersion 88
3.9 Defocusing of Stokes sidebands 90
3.10 Transverse mode instability 100
3.11 Seed wake suppression of Raman backscattering 107

4.1 Resonantly excited wakefields by a P-MoPA pulse train 114
4.2 P-MoPA longitudinal pulse shaping control 122
4.3 Transverse dynamics 127
4.4 Non-uniform depletion effects 134
4.5 Transverse spectral modulation 135
4.6 Multi-GeV electron acceleration with kHz lasers 137

5.1 Transverse beamloaded P-MoPA accelerator stage 155
5.2 Emittance preservation in a P-MoPA accelerator stage 158
5.3 In- and out-matching schematic 159
5.4 Laser-driven betatron oscillations 163

List of Tables

1.1 Typical LWFA laser-plasma parameters 23

1.2 Summary of LWFA regimes 24

3.1 Modulator stage baseline parameters 108

5.1 Example XFEL slice (s) and projected (p) parameters, sourced from [128]. 148

5.2 Proposed P-MoPA water-window XFEL parameters 157

Chapter 1

Introduction

1.1 Laser Wakefield Acceleration

1.1.1 Motivation

Particle accelerators, devices built to accelerate charged particles to high energies using electromagnetic fields, have been a driving force for scientific discovery ever since the early 1930s with the onset of the first Van de Graaff generator [5], cyclotron [6], linac [7] and Cockcroft-Walton generator [8]. In physics alone, particle accelerators have contributed to 28% of Nobel prizes won between 1939 and 2009 [9]. Perhaps the most famous example is the 27 km circumference Large Hadron Collider (LHC) at CERN, where particle beams are driven to collision energies exceeding 10 TeV for fundamental research in particle physics. Just under the particle collider class of accelerators, kilometer-scale accelerators are widely used to access multi-GeV electron energies to drive X-ray light sources, such as the LCLS free electron laser at SLAC, USA and the Diamond synchrotron light source in the UK, serving a plethora of research topics including material science, condensed matter physics and life sciences.

Particle accelerators are not solely limited to applications in fundamental science. On the contrary, according to a recent study [10], out of the estimated $\sim$ 40,000 particle accelerators in civilian use worldwide only 3% are in research labs and ac-

celerator centers. Out of the vast majority of particle accelerators, about two-thirds are used in industry where they are used for applications such as microelectronics, manufacturing, and sterilization to name a few. The remaining third are employed in medicine, where they have found uses in radiotherapy, radioisotope production and imaging.

Currently, the multi-GeV electron energies required for applications such as X-ray free electron lasers (XFELs) are limited to only a handful of large national facilities worldwide [11]. The reason why only national-facility-scale accelerators are able to generate the required electron bunch energies is because the accelerating gradients of contemporary devices are limited to around 10–100 MV/m due to the electrical breakdown limits of the metallic radio-frequency cavities they employ. This size and cost issue severely bottlenecks the availability of these systems to research and industry users.

What if we could fit such accelerators onto an optical table? Bringing such a technology to fruition would enable miniaturization and consequently a mass proliferation of transportable high-energy electron accelerators to university, hospital and industry settings [12–15]. Plasma-based accelerators have become an increasingly attractive avenue to miniaturize these multi-GeV facilities down to the table-top scale. This is because they naturally circumvent the electrical breakdown problem and are capable of producing accelerating gradients three orders of magnitude higher than that of traditional accelerators [16, 17]. The high accelerating gradients achievable by plasma accelerators are characterized by the cold nonrelativistic wavebreaking field [18]

$$E_0 = \frac{m_e \omega_p c}{e}\,, \tag{1.1}$$

which can be on the order of 100 GV/m for relevant parameters for plasma accelerators. The plasma frequency ω_p is the (angular) oscillation frequency of electrostatic

electron density waves, which is given by

$$\omega_p = \sqrt{\frac{e^2 n_e}{m_e \epsilon_0}} \tag{1.2}$$

where n_e is the electron density. It is these electrostatic waves in which an injected electron bunch "surfs" along to get accelerated to high energies.

There are two main ways of driving these waves in a plasma-based accelerator: beam-driven and laser-driven. Beam-driven systems require a high energy particle beam to drive a plasma wave, and are therefore currently still tethered to large national-facility-scale accelerators. In keeping with the fully table-top GeV-scale accelerator goal, we are specifically interested in implementing the Laser Wakefield Accelerator (LWFA). In a LWFA, wakefields are driven by pushing free electrons away from an ultrashort laser pulse propagating in an underdense plasma ($n_e \ll n_\mathrm{c} = m_e \epsilon_0 \omega_L^2 / e^2$, where ω_L is the laser angular frequency) via the ponderomotive force. The heavier ions remain mostly stationary relative to the electrons, thus the electron-ion charge separation collectively forms a strong electric field, with a phase velocity near the speed of light, which can be used to accelerate relativistic charged particles. The ponderomotive force $\boldsymbol{F}_\mathrm{p}$ exerted by a laser pulse described by the vector potential $\boldsymbol{A}$ in the Coulomb gauge on an electron is given by [19]

$$\begin{aligned} \boldsymbol{F}_\mathrm{p} &= -m_e c^2 \nabla \gamma_0 \,, \\ \gamma_0 &= (1 + \boldsymbol{a}^2)^{1/2} \,, \\ \boldsymbol{a} &= \frac{e\boldsymbol{A}}{m_e c} \end{aligned} \tag{1.3}$$

where $\boldsymbol{a}$ is the normalized vector potential and γ_0 is the Lorentz factor associated with the electron's high-frequency "quiver" momentum in the laser field. Because of this scaling with the normalized vector potential $\boldsymbol{a}$, it is useful to characterize laser pulses in LWFA by their peak normalized vector potential [20]

$$a_0 = \frac{eA_0}{m_e c} = \frac{eE_L}{m_e \omega_L c} = 0.85 \sqrt{I_0 [10^{18}\,\mathrm{W cm^{-2}}]}\, \lambda_L [\mu\mathrm{m}] \,, \tag{1.4}$$

where E_L and I_0 are the peak laser electric field and intensity respectively and $\lambda_L = 2\pi c/\omega_L$ is the laser wavelength (note that this relation between the vector potential and electric field only holds for laser pulses with a large duration relative to the laser cycle period). The a_0 of the laser pulse will determine the peak transverse "quiver" momentum of electrons in the laser field, which becomes relativistic ($a_0 \gtrsim 1$) at intensities exceeding $I_0 \gtrsim 10^{18}\,\mathrm{Wcm}^{-2}$ for a laser wavelength of $\lambda_L = 1\,\mu\mathrm{m}$. In most LWFA experiments, the laser pulse must be at least weakly relativistic $a_0 \lesssim 1$ with a duration smaller than the plasma period $T_p = 2\pi/\omega_p$ in order for the ponderomotive force to drive a sufficiently large amplitude wake for acceleration.

1.1.2 State of the Field

The LWFA concept was first introduced in 1979 by Tajima and Dawson [21], who proposed that a wakefield could be driven by either a short single laser pulse or by beatwave interference of two longer laser pulses to drive a wakefield resonantly with the plasma. For a single laser pulse to excite a plasma wave in an efficient manner, its duration must be less than half the plasma period T_p, which is in the 100 fs range for relevant plasma densities. Before these short durations were experimentally accessible, much of the early research on LWFAs was done using the Plasma Beatwave Accelerator (PBWA) concept [21]. In this scheme, two long co-propagating pumps with a carrier frequency mismatch approximately equal to the plasma frequency $\Delta\omega = \omega_1 - \omega_2 \approx \omega_p$ interfere to form a cosine-squared intensity modulation, forming a train of pulses spaced by T_p that resonantly drives a plasma wave.

Ever since the development of chirped pulse amplification (CPA) in 1985 [22], which enabled the generation of joule-scale, sub-picosecond duration pulses, the vast majority of research in LWFAs has utilized high intensity ultrashort laser pulses supplied by Ti:sapphire CPA laser systems. This approach has yielded much progress in LWFA in recent years, regularly achieving GeV-scale LWFA [23–29] of bunches of charge in the 10–500 pC range and $\sim$ 1–10% energy spreads, with the electron energy gain record recently reaching upwards of 10 GeV [30]. However, these laser systems suffer from low ($\sim$ 0.1–10 Hz) repetition rates [31] and poor ($<$ 0.1%)

electrical-to-optical energy efficiencies [32]. Despite the practical advantages gained from being much more compact, the low wall-plug efficiency and repetition rate of the laser drivers used today severely limits the number of applications for which LWFAs offer an advantage over conventional, radio-frequency particle accelerators.

This thesis presents research towards a novel LWFA scheme which we dub the Plasma-Modulated Plasma Accelerator (P-MoPA) [1, 33]. This scheme has been enabled by recent developments in the hydrodynamic optical-field-ionized (HOFI) plasma channel formation technique [34–37], and overcomes the wall-plug efficiency and repetition rate limitations of contemporary LWFA schemes by using a contemporary Yb:YAG thin-disk laser system which can provide the necessary average powers for kHz repetition-rate LWFA.

In this introductory chapter we first provide an overview of the thesis, which describes the subsequent chapters that present research towards the P-MoPA, which aims to achieve GeV-scale LWFA at kHz repetition rates using contemporary thin-disk laser technology. We then review the fundamental mechanics of LWFA. We derive from first principles the ponderomotive force exerted by an ultrashort laser pulse and the fluid equations that govern the plasma wakefield response coupled to the laser pulse evolution, and consider kinetic effects such as anisotropic temperature on wakefield structure. We then address the fundamental challenges which limit the performance of LWFA including energy gain, wall-plug efficiency and repetition rate.

1.2 Thesis Outline

The author's research towards the P-MoPA scheme, which aims to achieve multi-GeV LWFA at kHz repetition rates driven by contemporary laser technology [33, 38, 39], is presented in the following chapters

Chapter 1: Introduction provides an overview of the physics of LWFA and poses its fundamental challenges.

Chapter 2: Pulse Propagation in Plasma Channels outlines and develops the theory of laser-plasma dynamics for pulse propagation in long, pre-formed plasma

channels, which will provide the necessary tools for the subsequent chapters.

Chapter 3: The P-MoPA Modulator Stage introduces the Plasma-Modulated Plasma Accelerator (P-MoPA) scheme, and presents the theory and simulations of the modulator stage, setting laser pulse energy limits and other design constraints [33].

Chapter 4: The P-MoPA Accelerator Stage covers the theory and simulations demonstrating the viability of the P-MoPA accelerator stage accessing multi-GeV energy gains whilst obeying the design constraints of the modulator stage [38].

Chapter 5: A P-MoPA-driven Water Window XFEL presents electron bunch evolution theory and simulations evaluating the P-MoPA as a kHz driver for a water-window X-ray free electron laser.

1.2.1 Role of the Author

All simulations and calculations presented in this thesis were performed by the author using self-developed analytical and numerical techniques, as well as using the open source particle-in-cell code WarpX [40] on the ARCHER2 UK national supercomputing service [41].

The theory of pulse propagation in plasma channels presented in Chapter 2 was developed by the author, building on well-known techniques in the literature, providing a formalism for both the paraxial and non-paraxial descriptions well-suited for describing long-propagation effects in channels. This formalism is then benchmarked by re-deriving previously known laser-plasma dynamics results and instabilities specifically in the channel-dominated guiding regime. The chapter also touches upon the effects of transverse channel profile on wakefield structure known from previous studies. It then concludes with an application of the developed formalism in combination with plasma channel effects in the analysis of the first experimental demonstration of resonant excitation of plasma waves in plasma channels [39].

Applications of this theory and calculations in Chapters 3 and 4 were performed solely by the author. The design constraints and parameters for the P-MoPA as a kHz XFEL driver in Chapter 5 were found by the author, based on previous studies

for beam-driven and single-pulse LWFA [42–46].

The author made a significant contribution to the analysis for the first experimental demonstration of resonant excitation of plasma waves in a plasma channel [39] by applying the theory they had developed outlined in Chapter 2. This experimental campaign was performed with the Astra-Gemini TA3 Ti:sapphire laser system at the Rutherford Appleton Laboratory, the practical portion having been completed just before the author had joined the group. This work is discussed at the end of Chapter 2.

The author contributed to the design requirements of the March–May 2023 down-ramp injection experimental campaign, also at the Astra-Gemini TA3 laser facility. A summary of this work has been included in appendix B for completeness.

1.3 Mechanics of LWFA

1.3.1 Ponderomotive Force

The ponderomotive force exerted by an ultrashort laser pulse emerges from the drift of charged particles as they undergo a high frequency "quiver" motion in an inhomogeneous laser field, and can thus be qualitatively understood as a laser-cycle-averaged drift force. To derive the form of the ponderomotive force, it is convenient to describe the laser field with the vector potential $\boldsymbol{A}$

$$\boldsymbol{E} = -\frac{\partial \boldsymbol{A}}{\partial t}\,, \quad \boldsymbol{B} = \nabla \times \boldsymbol{A}\,, \tag{1.5}$$

where from now on we will be using the Coulomb gauge. Next, we write the momentum equation for a cold collisionless electron fluid in a fixed ion background experiencing the Lorentz force exerted solely by the external laser fields, neglecting bulk plasma effects like charge separation and currents (which we will include later when deriving the plasma wakefield response)

$$\frac{\mathrm{d}\boldsymbol{p}}{\mathrm{d}t} = -e\left(\boldsymbol{E} + \boldsymbol{v} \times \boldsymbol{B}\right) = -e\left(-\frac{\partial \boldsymbol{A}}{\partial t} + \boldsymbol{v} \times (\nabla \times \boldsymbol{A})\right)\,, \tag{1.6}$$

where $\boldsymbol{v}$ is the bulk fluid flow velocity and $\mathrm{d}/\mathrm{d}t = \partial/\partial t + (\boldsymbol{v}\cdot\nabla)$ is the material derivative. Assuming that the laser field inhomogeneity lengthscale is large relative to the laser wavelength, we can split the fluid momentum into the zeroth order high-frequency "quiver" motion and a first order correction $\boldsymbol{p} = \boldsymbol{p}_0 + \boldsymbol{p}_1$, with the quiver momentum being

$$\boldsymbol{p}_0 = e\boldsymbol{A} = m_e c\boldsymbol{a}\,, \tag{1.7}$$

where $\boldsymbol{a} \equiv e\boldsymbol{A}/m_e c$ is the normalized vector potential. We can then substitute this expression into Eq. (1.6) to recover the momentum equation for $\boldsymbol{p}_1$

$$\begin{aligned}\left(\frac{\partial}{\partial t} + (\boldsymbol{v}\cdot\nabla)\right)(\boldsymbol{p}_0+\boldsymbol{p}_1) &= -e\left(-\frac{\partial \boldsymbol{A}}{\partial t} + \boldsymbol{v}\times(\nabla\times\boldsymbol{A})\right)\\ \Rightarrow \frac{\mathrm{d}\boldsymbol{p}_1}{\mathrm{d}t} &= -m_e c(\boldsymbol{v}\cdot\nabla)\boldsymbol{a} - m_e c\boldsymbol{v}\times(\nabla\times\boldsymbol{a})\\ &= -c\left(\frac{\boldsymbol{p}_0+\boldsymbol{p}_1}{\gamma}\cdot\nabla\right)\boldsymbol{a} - c\left(\frac{\boldsymbol{p}_0+\boldsymbol{p}_1}{\gamma}\right)\times(\nabla\times\boldsymbol{a})\end{aligned} \tag{1.8}$$

where $\gamma = (1+\boldsymbol{p}^2/m_e^2c^2)^{1/2}$ is the Lorentz factor associated with the electron fluid motion. Keeping only the first order terms on the RHS of this equation then yields the ponderomotive force [19]

$$\begin{aligned}\boldsymbol{F}_\mathrm{p} &= -m_e c^2(1+\boldsymbol{a}^2)^{-1/2}\left[(\boldsymbol{a}\cdot\nabla)\,\boldsymbol{a} + \boldsymbol{a}\times(\nabla\times\boldsymbol{a})\right]\\ &= -m_e c^2\frac{\nabla(\boldsymbol{a}^2/2)}{(1+\boldsymbol{a}^2)^{1/2}}\\ &= -m_e c^2\nabla\gamma_0\end{aligned} \tag{1.9}$$

where $\gamma_0 = (1+\boldsymbol{p}_0^2/m_e^2c^2)^{1/2} = (1+\boldsymbol{a}^2)^{1/2}$ is the relativistic Lorentz factor associated with their quiver momentum. The form of this expression shows that the ponderomotive force is agnostic to the sign of the charge, and implies that the ponderomotive force can also be understood as a form of radiation pressure as it is proportional to the gradient of laser energy density in the nonrelativistic limit. Note that the $\sim(1+\boldsymbol{a}^2)^{-1/2}$ reduction in the force is associated with the relativistic effect on the electron quiver motion.

We can further simplify this expression by describing the laser field with a complex envelope. For a laser field that isn't focused too tightly such that it is predominantly polarized transverse to its propagation direction $\hat{z}$, its vector potential can be written in the form

$$\boldsymbol{a}(\boldsymbol{x},t) = \begin{cases} \left(ae^{i(kz-\omega t)} + \text{c.c.}\right)\hat{x}/2 & \text{linearly polarized} \\ \left(ae^{i(kz-\omega t)} + \text{c.c.}\right)\hat{x}/2 + \left(ae^{i(kz-\omega t+\pi/2)} + \text{c.c.}\right)\hat{y}/2 & \text{circularly polarized} \end{cases} \tag{1.10}$$

where $a(\boldsymbol{x},t)$ denotes the complex envelope. For the circularly polarized case, the ponderomotive force straightforwardly becomes

$$\boldsymbol{F}_{\text{p}}^{\text{circular}} = -m_e c^2 \frac{\nabla|a|^2/2}{(1+|a|^2)^{1/2}}\,. \tag{1.11}$$

For the linearly polarized case, squaring the vector potential yields a high-frequency component with double the laser frequency. However, if we assume that the envelope a is slowly varying such that it can be assumed to be constant over a laser cycle, we can justify averaging the ponderomotive force over a laser cycle. Performing this average yields

$$\begin{aligned} \boldsymbol{F}_{\text{p}}^{\text{linear}} &= -m_e c^2 \int_0^{2\pi} \frac{d(\omega t)}{2\pi} \frac{\nabla|a|^2/4 + \left[(ika^2\hat{z} + a\nabla a)e^{2i(kz-\omega t)} + \text{c.c.}\right]/4}{\left[1+|a|^2/2 + (a^2e^{2i(kz-\omega t)} + \text{c.c.})/4\right]^{1/2}} \\ &= -m_e c^2 \int_0^{2\pi} \frac{d\phi}{2\pi} \frac{(1+\cos\phi)\nabla|a|^2/4}{\left[1+(1+\cos\phi)|a|^2/2\right]^{1/2}} \\ &= -m_e c^2 \frac{4\left[(1+|a|^2)E\left(\frac{|a|^2}{1+|a|^2}\right) - K\left(\frac{|a|^2}{1+|a|^2}\right)\right]}{\pi|a|^2(1+|a|^2)^{1/2}} \nabla|a|^2/4 \end{aligned} \tag{1.12}$$

where $K(m)$ and $E(m)$ denote the complete elliptic integrals of the first and second kind respectively, and we have made the substitution $\phi = \omega t$ and took advantage of the periodicity of the integrand. This integral was evaluated using Mathematica [47] and then separately verified using known identities for integrals containing $\sqrt{a \pm b\cos(x)}$ for $a > b > 0$ [48]. Note that performing this average did not completely eliminate the contribution from the high frequency terms, as they are still

relevant in the relativistic mass increase of the electrons. In the nonrelativistic $|a|^2 \ll 1$ limit, the ponderomotive force for each polarization reduces to

$$\begin{aligned} \boldsymbol{F}_{\mathrm{p}}^{\mathrm{linear}}(|a|^2 \ll 1) &\approx -m_e c^2 \nabla |a|^2/4\,, \\ \boldsymbol{F}_{\mathrm{p}}^{\mathrm{circular}}(|a|^2 \ll 1) &\approx -m_e c^2 \nabla |a|^2/2\,. \end{aligned} \tag{1.13}$$

Note that the ponderomotive force exerted by circularly polarized light in this limit is double that of linear simply because it contains double the electromagnetic energy density for the same electric field amplitude. To avoid confusion between the two, when writing the ponderomotive force using the complex envelope a, from now on we will always assume linearly polarized light unless stated otherwise.

1.3.2 Linear Wakefield Regime

In the $\boldsymbol{a}^2 \ll 1$ regime, we can model the wakefield response to the laser field $\boldsymbol{a}$ using the non-relativistic cold electron fluid equations with a fixed ion background. For an initially neutral and spatially uniform plasma with electron density n_0, the momentum and continuity equations with Gauss' law are written as

$$\begin{aligned} \left(\frac{\partial}{\partial t} + (\boldsymbol{v}\cdot\nabla)\right)\delta\boldsymbol{v} &= -\frac{e}{m_e}\left(\boldsymbol{E} + \boldsymbol{v}\times\boldsymbol{B}\right) - c^2\nabla(\boldsymbol{a}^2/2)\,, \\ \frac{\partial \delta n}{\partial t} + \nabla\cdot(n_e\boldsymbol{v}) &= 0\,, \\ \nabla\cdot\boldsymbol{E} &= -\frac{e\delta n}{\epsilon_0}\,, \end{aligned} \tag{1.14}$$

where $\boldsymbol{v} = c\boldsymbol{a} + \delta\boldsymbol{v}$ is the fluid velocity, $\boldsymbol{E}, \boldsymbol{B}$ are the fields associated with the plasma wakefield response and $n_e = n_0 + \delta n$ is the total electron density. To recover the wakefield equations in the linear regime, we linearize these equations by treating $\delta n, \delta\boldsymbol{v}, \boldsymbol{E}, \boldsymbol{B}$ as perturbative quantities on the same order as $\boldsymbol{a}^2$. Keeping these

terms only to first order yields

$$\begin{aligned}
\frac{\partial \delta \boldsymbol{v}}{\partial t} &= -\frac{e\boldsymbol{E}}{m_e} - c^2 \nabla (\boldsymbol{a}^2/2)\,, \\
\frac{\partial \delta n}{\partial t} &+ n_0 \nabla \cdot \delta \boldsymbol{v} = 0\,, \\
\nabla \cdot \boldsymbol{E} &= -\frac{e\delta n}{\epsilon_0}\,,
\end{aligned} \tag{1.15}$$

where we also have also implicitly taken the 1D limit by neglecting the $(c\boldsymbol{a}\cdot\nabla)$ part of the material derivative and the $-ec\boldsymbol{a}\times\boldsymbol{B}$ part of the Lorentz force (which is valid for laser pulses with a large spot size relative to the plasma skin depth). Combining these three equations then yields the linear plasma wave equation, which we can write for the density perturbation, electric field and the scalar potential

$$\begin{aligned}
\left(\frac{\partial^2}{\partial t^2} + \omega_p^2\right)\frac{\delta n}{n_0} &= c^2 \Delta (\boldsymbol{a}^2/2)\,, \\
\left(\frac{\partial^2}{\partial t^2} + \omega_p^2\right)\frac{\boldsymbol{E}}{E_0} &= -\omega_p c \nabla (\boldsymbol{a}^2/2)\,, \\
\left(\frac{\partial^2}{\partial t^2} + \omega_p^2\right)\phi &= \omega_p^2 (\boldsymbol{a}^2/2)
\end{aligned} \tag{1.16}$$

where $\omega_p = \sqrt{e^2 n_0/m_e\epsilon_0}$ is the plasma frequency, $E_0 = m_e\omega_p c/e$ is the cold wave-breaking field and $\phi = e\Phi/m_e c^2$, is the normalized wakefield scalar potential. After the laser pulse has passed and perturbed the plasma, these equations describe simple sinusoidal plasma waves with a phase velocity set by the group velocity of the laser pulse:

$$\phi = \phi_0 \cos\left[\omega_p (z/v_g - t)\right]\,. \tag{1.17}$$

Some example wakefield solutions in the 1D linear regime are presented in Fig. 1.1 for both linearly and circularly polarized light, demonstrating how circularly polarized light drives a larger amplitude wake for the same peak normalized vector potential a_0, and how the ponderomotive force exerted by linearly polarized light contains a high-frequency component at double the laser frequency, whose effect is

most apparent of the plasma density perturbation.

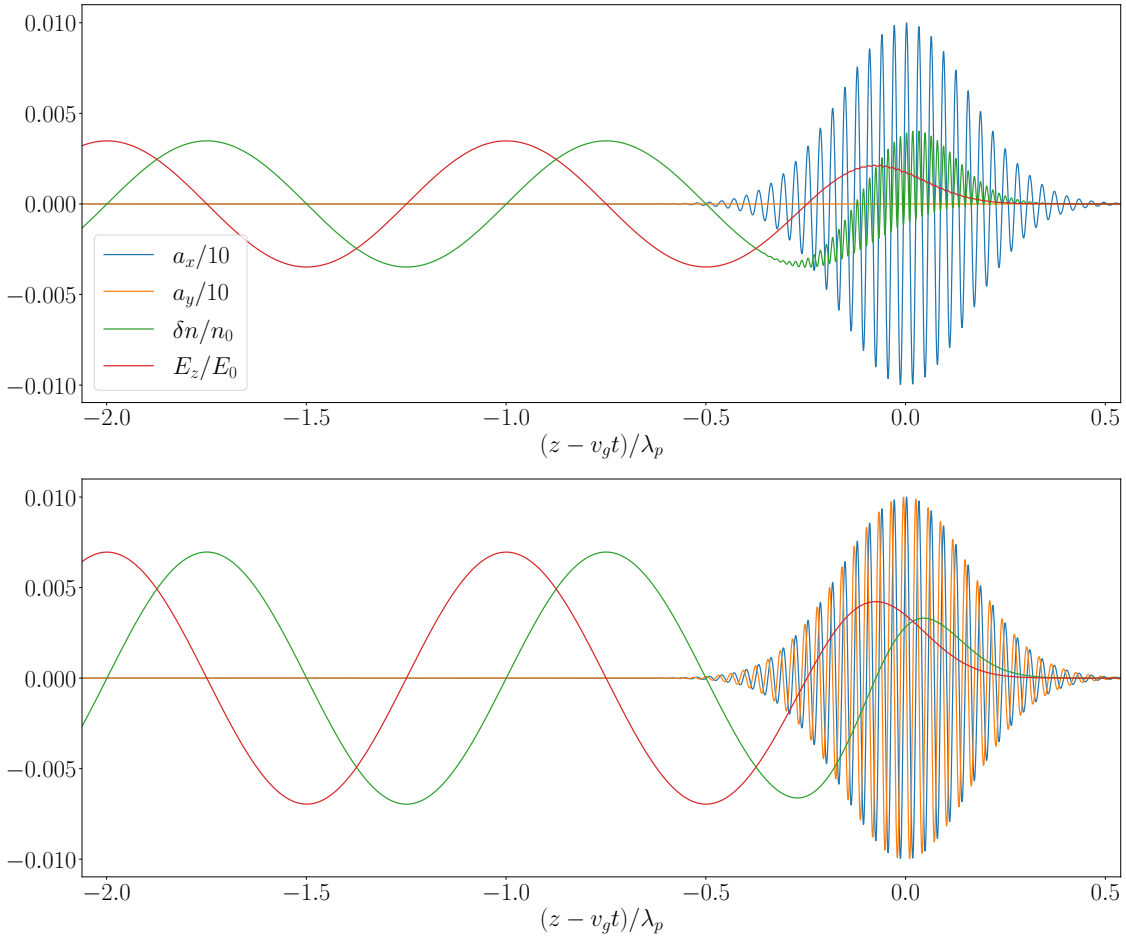


Figure 1.1: Example wakefield solutions in the 1D linear regime for a (top) linearly polarized and (bottom) circularly polarized Gaussian laser pulse with peak normalized vector potential $a_0 = 0.1$, wavelength $\lambda_L = 1030\,\text{nm}$ and FWHM duration $\tau_{\text{FWHM}} = 30\,\text{fs}$ propagating in the z direction at group velocity $v_g = c(1 - \omega_p^2/\omega_L^2)^{1/2}$ in uniform plasma of density $n_0 = 1.0 \times 10^{18}\,\text{cm}^{-3}$ with corresponding plasma wavelength $\lambda_p = 2\pi c/\omega_p = 33.4\,\mu\text{m}$. For the linearly polarized case, the ponderomotive force has a high frequency component at double the laser frequency, whose effect is most pronounced in the density perturbation. The circularly polarized pulse also drives a roughly $2\times$ larger amplitude wake as it contains double the energy density and thus exerts double the ponderomotive force as the linearly polarized pulse for the same a_0, as was derived in Eq. (1.13).

So far we have derived the linear wakefield regime in the 1D limit assuming an initially uniform plasma distribution. However, if the plasma is initially non-uniform $n_0 = n_0(\boldsymbol{x})$, this treatment for the linear regime will fail for large density gradients $|\nabla \ln n_0| \gtrsim \omega_p/c$, even when substituting $\omega_p = \omega_p(\boldsymbol{x})$. The reasons for this will

be addressed in the next subsection for 3D wakefields in the nonlinear regime, and will also come up in subsequent chapters for the linear regime when considering pre-formed axisymmetric plasma channels $n_0 = n_0(r)$. In short, this is due to the conservation of generalized vorticity $\boldsymbol{\Omega} \equiv \nabla \times \delta\boldsymbol{v} - (e/m_e)\boldsymbol{B} = 0$, which introduces a first order correction for the magnetic term in Ampère's law. Strictly speaking, even with a uniform plasma in the linear regime, conservation of generalized vorticity will modify the plasma wave equation for the electric field

$$\begin{aligned}
&\left(\frac{\partial^2}{\partial t^2} + \omega_p^2\right)\frac{\delta n}{n_0} = c^2\Delta(\boldsymbol{a}^2/2)\,,\\
&\left(\frac{\partial^2}{\partial t^2} + \omega_p^2\right)\frac{\boldsymbol{E}}{E_0} + c^2\nabla\times\left(\nabla\times\frac{\boldsymbol{E}}{E_0}\right) = -\omega_p c\nabla(\boldsymbol{a}^2/2)\,,
\end{aligned} \tag{1.18}$$

which can be shown by taking the linear limit with uniform plasma of the full 3D nonlinear wakefield equations in Eq. (1.22) derived in the next section. For this specific case, it is convenient to split the electric field wave equation into electrostatic and S-waves by taking the divergence and curl respectively

$$\begin{aligned}
&\left(\frac{\partial^2}{\partial t^2} + \omega_p^2\right)\left(\nabla\cdot\frac{\boldsymbol{E}}{E_0}\right) = -\omega_p c\Delta(\boldsymbol{a}^2/2)\,,\\
&\left(\frac{\partial^2}{\partial t^2} - c^2\Delta + \omega_p^2\right)\left(\nabla\times\frac{\boldsymbol{E}}{E_0}\right) = 0\,,
\end{aligned} \tag{1.19}$$

which shows that we do not need to worry about the S-wave component of the wakefield in the linear regime as long as the plasma is uniform.

1.3.3 Nonlinear Wakefield Regime

We will now derive the fluid equations governing the cold plasma wakefield response in the 3D nonlinear relativistic regime, again assuming a fixed ion background. To begin, it is convenient to rewrite the cold electron fluid-Maxwell equations using the

canonical fluid momentum $\delta\boldsymbol{u} = \boldsymbol{p}/m_e c - \boldsymbol{a}$, which exactly yields [49]

$$\begin{aligned}
&\gamma = \sqrt{1 + (\boldsymbol{a} + \delta\boldsymbol{u})^2}\,, \\
&\tilde{\omega}_p^2 = \frac{e^2 n_e}{\gamma m_e \epsilon_0}\,, \\
&\frac{\partial \delta\boldsymbol{u}}{\partial t} = c\nabla(\phi - \gamma) + \frac{c(\boldsymbol{a} + \delta\boldsymbol{u})}{\gamma} \times (\nabla \times \delta\boldsymbol{u})\,, \\
&\frac{\partial \delta n}{\partial t} + c\nabla \cdot \left(\frac{n_e(\boldsymbol{a} + \delta\boldsymbol{u})}{\gamma}\right) = 0\,, \\
&\Delta\phi = \frac{e^2 \delta n}{m_e \epsilon_0 c^2}\,, \\
&\left(\frac{\partial^2}{\partial t^2} - c^2\Delta + \tilde{\omega}_p^2\right)\boldsymbol{a} = -c\frac{\partial}{\partial t}\nabla\phi - \tilde{\omega}_p^2 \delta\boldsymbol{u}\,,
\end{aligned} \tag{1.20}$$

where $e\boldsymbol{E}/m_e c = -c\nabla\phi - \partial\boldsymbol{a}/\partial t$ and $e\boldsymbol{B}/m_e c = \nabla \times \boldsymbol{a}$ represent the *total* fields associated with both the laser field and the plasma response, $\tilde{\omega}_p$ is the local effective plasma frequency including the relativistic mass increase of electrons, and $\boldsymbol{F}_{p,\mathrm{NL}}(\boldsymbol{a}; \delta\boldsymbol{u}) = -m_e c^2 \nabla\gamma$ is the generalized nonlinear ponderomotive force. By taking the curl of the momentum equation and applying Faraday's law, we can recover the following relation for the generalized vorticity $\boldsymbol{\Omega} \equiv c\nabla \times \delta\boldsymbol{u} = c\nabla \times \boldsymbol{u} - (e/m_e)\boldsymbol{B}$

$$\frac{\partial \boldsymbol{\Omega}}{\partial t} = \nabla \times \left(\frac{c(\boldsymbol{a} + \delta\boldsymbol{u})}{\gamma} \times \boldsymbol{\Omega}\right)\,. \tag{1.21}$$

This expression is known as the frozen-in law [50], which tells us that the generalized vorticity $\boldsymbol{\Omega}$ is frozen into the flow $\boldsymbol{v} = c(\boldsymbol{a} + \delta\boldsymbol{u})/\gamma$. If the generalized vorticity is initially zero everywhere, it will therefore remain zero. In this case the fluid-Maxwell

equations simplify to

$$\begin{aligned}
&\gamma = \sqrt{1 + (\boldsymbol{a} + \delta\boldsymbol{u})^2}\,, \\
&\tilde{\omega}_p^2 = \frac{e^2 n_e}{\gamma m_e \epsilon_0}\,, \\
&\frac{\partial \delta\boldsymbol{u}}{\partial t} = c\nabla(\phi - \gamma)\,, \\
&\frac{\partial \delta n}{\partial t} + c\nabla \cdot \left(\frac{n_e(\boldsymbol{a} + \delta\boldsymbol{u})}{\gamma}\right) = 0\,, \\
&\Delta\phi = \frac{e^2 \delta n}{m_e \epsilon_0 c^2}\,, \\
&\left(\frac{\partial^2}{\partial t^2} - c^2\Delta + \tilde{\omega}_p^2\right)\boldsymbol{a} = -c\frac{\partial}{\partial t}\nabla\phi - \tilde{\omega}_p^2 \delta\boldsymbol{u}\,.
\end{aligned} \tag{1.22}$$

This system of PDEs describes the 3D relativistic nonlinear wakefield response and the evolution of the normalized vector potential $\boldsymbol{a}$ for any arbitrary initial plasma density distribution $n_0(\boldsymbol{x})$. As a side note, taking the curl of the last equation

$$\left(\frac{\partial^2}{\partial t^2} - c^2\Delta + \tilde{\omega}_p^2\right)(\nabla \times \boldsymbol{a}) = -\nabla\tilde{\omega}_p^2 \times (\boldsymbol{a} + \delta\boldsymbol{u})\,. \tag{1.23}$$

shows that there is a coupling between the electrostatic and magnetic field waves mediated by the gradient in local effective plasma frequency $\nabla\tilde{\omega}_p^2$.

1.3.4 The Quasistatic Approximation

In a LWFA, we usually consider laser pulse propagation in very underdense plasma, i.e. low densities such that the plasma frequency is small relative to the laser carrier frequency $\omega_p \ll \omega_L$. This allows the laser pulse to propagate at a group velocity near the speed of light in vacuum $v_g \approx c$, which is required to keep the highly relativistic accelerating electrons in-phase with the wakefield. It is therefore often convenient when studying LWFA to shift to co-moving coordinates propagating with the laser pulse at some fixed pre-defined group velocity v_g (as the actual group velocity of the

laser pulse may vary as it propagates)

$$\begin{aligned} &\xi = z - v_g t\,, \quad \tau = t\,, \\ &\frac{\partial}{\partial z} = \frac{\partial}{\partial \xi}\,, \quad \frac{\partial}{\partial t} = \frac{\partial}{\partial \tau} - v_g \frac{\partial}{\partial \xi}\,. \end{aligned} \tag{1.24}$$

If we can assume that the laser envelope evolution is slow relative to the wakefield response, which is typically true for laser pulses propagating in very underdense plasma, we can apply the quasistatic approximation:

$$\frac{\partial}{\partial t} = \frac{\partial}{\partial \tau} - v_g \frac{\partial}{\partial \xi} \approx -v_g \frac{\partial}{\partial \xi}\,. \tag{1.25}$$

Another way to understand the quasistatic approximation is that it states that the only variation of the wakefield response is due to the slow evolution of the laser pulse envelope. For example, applying this approximation to the nonlinear wakefield equations in Eq. (1.22) in 1D geometry (which is valid for laser spot sizes large relative to the plasma wavelength $w_0 \gg \lambda_p$), taking the $v_g \to c$ limit and applying the appropriate initial conditions yields

$$\begin{aligned} &\boldsymbol{u}_\perp - \boldsymbol{a}_\perp = 0\,, \\ &\gamma = \sqrt{1 + \boldsymbol{a}_\perp^2 + u_z^2}\,, \\ &\gamma - \phi - u_z = 1\,, \\ &\frac{\delta n}{n_0} - \left(1 + \frac{\delta n}{n_0}\right)\frac{u_z}{\gamma} = 0\,, \\ &\frac{\partial^2 \phi}{\partial \xi^2} = k_{p0}^2 \frac{\delta n}{n_0}\,, \end{aligned} \tag{1.26}$$

where the laser field $\boldsymbol{a}_\perp(\xi;\tau)$ is assumed to be slowly varying in τ for the quasistatic approximation to hold and $k_{p0} = (e^2 n_0/m_e \epsilon_0 c^2)^{1/2}$ is the plasma wavenumber for the unperturbed plasma density n_0. Combining these equations then yields the following

nonlinear ODE for the Poisson equation and respective wakefield quantities

$$\begin{aligned}
\frac{1}{k_{p0}^2}\frac{\partial^2\phi}{\partial\xi^2} &= \frac{1}{2}\left(\frac{1+\boldsymbol{a}_\perp^2}{(1+\phi)^2}-1\right), \\
\frac{E_z}{E_0} &= -\frac{1}{k_{p0}}\frac{\partial\phi}{\partial\xi}, \\
\gamma &= \frac{1+\boldsymbol{a}_\perp^2+(1+\phi)^2}{2(1+\phi)}, \\
\frac{n_e}{n_0} &= \frac{1}{2}\left(\frac{1+\boldsymbol{a}_\perp^2}{(1+\phi)^2}+1\right), \\
u_z &= \frac{1+\boldsymbol{a}_\perp^2-(1+\phi)^2}{2(1+\phi)}, \\
\tilde{\omega}_p^2 &= \frac{e^2 n_e}{\gamma m_e \epsilon_0} = \frac{\omega_{p0}^2}{1+\phi},
\end{aligned} \tag{1.27}$$

where $\omega_{p0} = (e^2 n_0/m_e\epsilon_0)^{1/2}$ is the original unperturbed plasma frequency. As shown in Figure 1.2, as we transition to the nonlinear regime the effective plasma wavelength of the wakefield increases due to a combination of rarefying the plasma and the relativistic mass increase of electrons. The axial electric field E_z also ceases being sinusoidal, and instead forms a sawtooth characteristic of this regime.

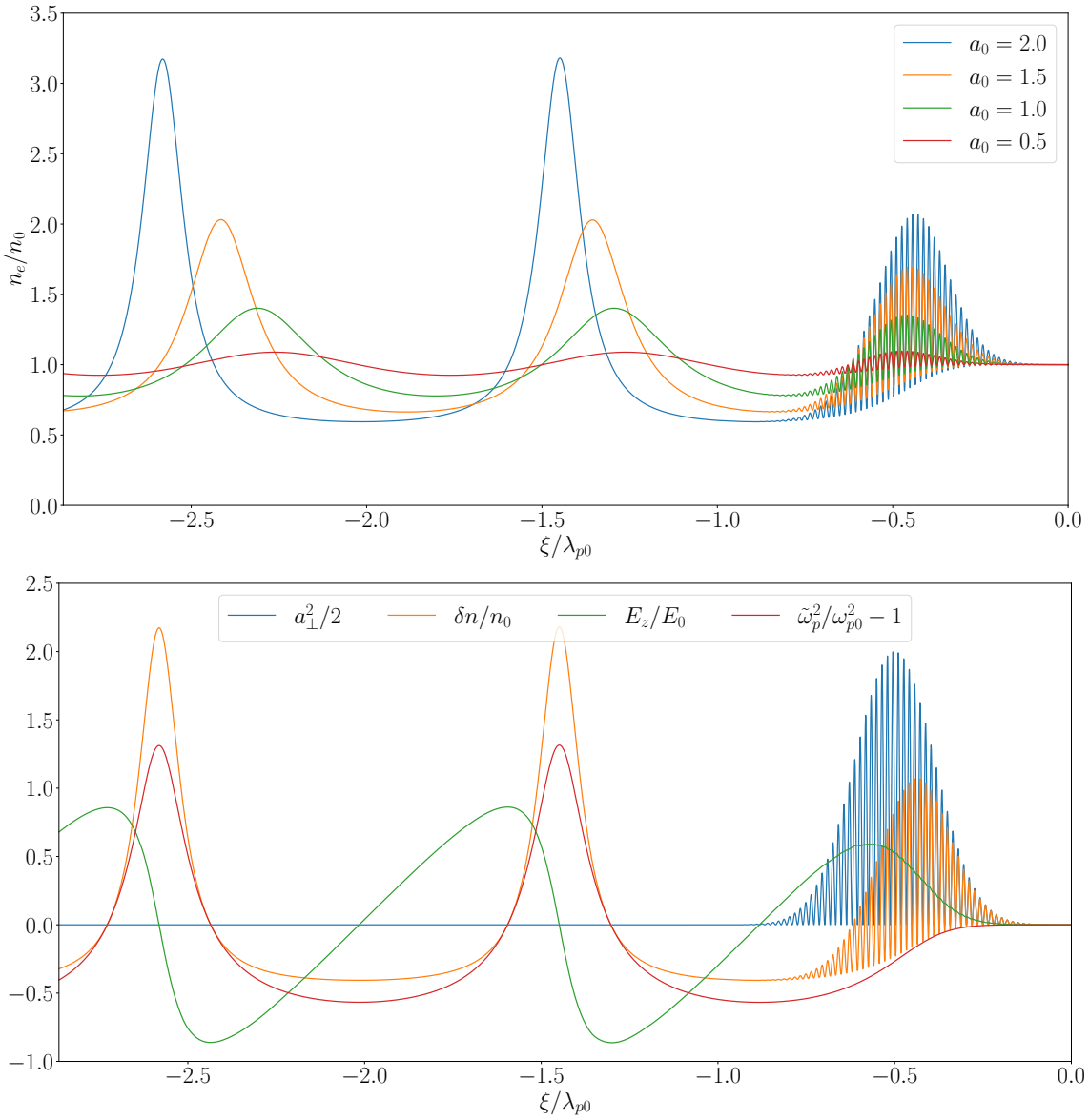


Figure 1.2: Example wakefield solutions in the 1D nonlinear regime of (top) the plasma density n_e/n_0 at various values of peak normalized vector potential a_0 and (bottom) the ponderomotive potential $\boldsymbol{a}_\perp^2$, density perturbation $\delta n/n_0$, axial electric field relative to the cold linear wavebreaking field E_z/E_0 and change in local effective plasma frequency $\tilde{\omega}_p$ for $a_0 = 2.0$. Both cases are evaluated using a linearly polarized Gaussian laser pulse of duration $\omega_{p0}\tau_{\mathrm{rms}} = 1$ and wavelength $\lambda_L = 1030\,\mathrm{nm}$ propagating in uniform plasma of density $n_0 = 1.0 \times 10^{18}\,\mathrm{cm}^{-3}$ with corresponding unperturbed plasma wavelength $\lambda_{p0} = 2\pi c/\omega_{p0} = 33.4\,\mu\mathrm{m}$. In this regime, the effective plasma wavelength increases with the wakefield amplitude and steepens the density gradient. However, we note that within this 1D nonlinear cold fluid picture that the electron density cannot become smaller than half the initial unperturbed plasma density.

Note that in this 1D nonlinear formalism that the minimum plasma density

achievable is half the unperturbed plasma density as it neglects the transverse ponderomotive force. Therefore the full 3D nonlinear theory is required to capture more extreme wakefield regimes like the blowout regime, where a cavity completely lacking in electrons can be formed by a sufficiently intense and focused laser pulse. Following the same procedure, the 3D set of quasistatic cold fluid equations are

$$\begin{aligned}
&\gamma = \sqrt{1 + (\boldsymbol{a}_\perp + \delta\boldsymbol{u}_\perp)^2 + u_z^2}\,, \\
&\gamma - \phi + a_z - u_z = 1\,, \\
&\frac{\partial \delta\boldsymbol{u}_\perp}{\partial \xi} = -\nabla_\perp(\phi - \gamma)\,, \\
&\frac{\partial}{\partial \xi}\left(\delta n - \frac{n_e u_z}{\gamma}\right) = \nabla_\perp \cdot \left(\frac{n_e(\boldsymbol{a}_\perp + \delta\boldsymbol{u}_\perp)}{\gamma}\right)\,, \\
&\left(\frac{\partial^2}{\partial \xi^2} + \Delta_\perp\right)\phi = k_{p0}^2 \frac{\delta n}{n_{00}}\,,
\end{aligned} \tag{1.28}$$

which then allows for a complete evacuation of electrons for the blowout regime. Note that in the 3D regime that we must account for a nonzero axial component a_z of the laser field due to the finite laser spot size and the requirement of zero electric field divergence in vacuum.

1.3.5 Finite Temperature Effects

Up to this point we have been modeling the plasma using the cold electron fluid equations. This approach generally works well for short-pulse LWFA due to its short timescale and low initial plasma temperature $T_e \sim 10\,\mathrm{eV}$ [34, 51], yielding a collisionless plasma regime well outside of a local thermodynamic equilibrium. However, even this small energy spread on top of the relativistic bulk plasma motion introduced by a finite initial electron temperature can still have meaningful effects in LWFA, including improving self-trapping, changing the overall wakefield structure and reducing the maximum nonlinear wavebreaking field [52].

In general, a collisionless two-species plasma can be described using the Vlasov-

Maxwell equations [53]

$$
\begin{aligned}
&\frac{\partial f_e}{\partial t} + \boldsymbol{v}_e \cdot \frac{\partial f_e}{\partial \boldsymbol{x}} - e(\boldsymbol{E} + \boldsymbol{v}_e \times \boldsymbol{B}) \cdot \frac{\partial f_e}{\partial \boldsymbol{p}} = 0\,, \\
&\frac{\partial f_i}{\partial t} + \boldsymbol{v}_i \cdot \frac{\partial f_i}{\partial \boldsymbol{x}} + Z_i e(\boldsymbol{E} + \boldsymbol{v}_i \times \boldsymbol{B}) \cdot \frac{\partial f_i}{\partial \boldsymbol{p}} = 0\,, \\
&\nabla \cdot \boldsymbol{E} = \frac{\rho}{\epsilon_0}\,, \\
&\nabla \cdot \boldsymbol{B} = 0\,, \\
&\nabla \times \boldsymbol{E} = -\frac{\partial \boldsymbol{B}}{\partial t}\,, \\
&\nabla \times \boldsymbol{B} = \mu_0 \boldsymbol{J} + \frac{1}{c^2}\frac{\partial \boldsymbol{E}}{\partial t}\,, \\
&\rho = e \int (Z_i f_i - f_e) d\boldsymbol{p}\,, \\
&\boldsymbol{J} = e \int (Z_i f_i \boldsymbol{v}_i - f_e \boldsymbol{v}_e) d\boldsymbol{p}\,, \\
&\boldsymbol{v}_\alpha = \frac{\boldsymbol{p}}{m_\alpha}\left(1 + \frac{\boldsymbol{p}^2}{m_\alpha^2 c^2}\right)^{-1/2}\,,
\end{aligned}
\tag{1.29}
$$

where $f_e(\boldsymbol{x}, \boldsymbol{p}, t)$ and $f_i(\boldsymbol{x}, \boldsymbol{p}, t)$ are the electron and ion phase space distributions respectively. In theory, the Vlasov-Maxwell equations should near-perfectly describe the laser-plasma interaction for LWFA, aside from missing some negligible collisional effects (and becomes exact when the phase space distribution functions are microscopically described using delta functions in the Klimontovich sense [54]). However, kinetic equations like the Vlasov equation are generally difficult to solve due to the large 6D phase space. It is therefore typical to derive fluid models from kinetic equations by taking moments of the distribution function and applying closure conditions.

By taking advantage of an initially low plasma temperature such that the electron distribution function f_e only occupies the phase-space region where the microscopic momentum spread of particles around the bulk fluid momentum is small relative to the electron rest mass energy, Shadwick, Tarkenton and Esarey [55] derived the following warm electron fluid model of a collisionless relativistic plasma from the

electron Vlasov equation

$$
\begin{aligned}
&\frac{\partial n_e}{\partial t} + \nabla \cdot (n_e \boldsymbol{v}) = 0\,, \\
&\frac{\partial \boldsymbol{p}}{\partial t} + (\boldsymbol{v} \cdot \nabla)\boldsymbol{p} = -e(\boldsymbol{E} + \boldsymbol{v} \times \boldsymbol{B}) - \frac{\nabla \cdot \mathcal{P}}{n_e}\,, \\
&\frac{\partial \Pi_{ij}}{\partial t} + v_k \frac{\partial \Pi_{ij}}{\partial k} = -\Pi_{ik}\frac{\partial v_k}{\partial j} - \Pi_{jk}\frac{\partial v_k}{\partial i} + \frac{\mathcal{P}_{ki}}{n_e}\left(\frac{\partial \tilde{p}_j}{\partial k} - \frac{\partial \tilde{p}_k}{\partial j}\right) + \frac{\mathcal{P}_{kj}}{n_e}\left(\frac{\partial \tilde{p}_i}{\partial k} - \frac{\partial \tilde{p}_k}{\partial i}\right)\,, \\
&v_k = \frac{p_k}{m_e \gamma_0}\left[1 - \frac{\Pi_{ii}}{2\gamma_0^2 m_e^2 c^2} + \frac{3}{2}\frac{p_i \Pi_{ii} p_j}{\gamma_0^4 m_e^4 c^4}\right] - \frac{\Pi_{ki} p_i}{\gamma_0^3 m_e^3 c^2}\,, \\
&\gamma_0 = \sqrt{1 + \frac{\boldsymbol{p}^2}{m_e^2 c^2}}\,, \\
&\mathcal{P}_{ij} = \frac{n_e}{\gamma_0 m_e}\Lambda_{ik}\Pi_{kj}\,, \\
&\Lambda_{ij} = \delta_{ij} - \frac{p_i p_j}{\gamma_0^2 m_e^2 c^2}\,,
\end{aligned}
\tag{1.30}
$$

where $\mathcal{P}$ and Π are the pressure and temperature tensors respectively (which allow for anisotropy) and $\tilde{\boldsymbol{p}} = \boldsymbol{p} - e\boldsymbol{A}/c$ is the canonical fluid momentum. We then also assume that the initial plasma bulk flow is negligible and that its temperature is also initially isotropic, i.e.

$$\Pi_{ij}(t = 0) = m_e T_0 \delta_{ij}\,. \tag{1.31}$$

For $T_0 \sim 10\,\mathrm{eV}$ we initially have $\Pi_{ij}/m_e^2 c^2 \sim 10^{-5}$. This allows us to safely ignore the pressure force in the momentum equation as long as no large density gradients are present, therefore justifying the cold fluid model for evaluating the wakefield structure in most situations. However, note that while this condition may easily be satisfied up to and including the moderately nonlinear regime, the pressure term will no longer be negligible when approaching the blowout regime where sharp density gradients are present. Qualitatively speaking, in the blowout regime the pressure term in the momentum equation will act to minimize plasma density gradients. The minimum characteristic lengthscale in the blowout regime will scale with the Debye

length

$$\lambda_D = \sqrt{\frac{\epsilon_0 T_e}{n_e e^2}}\,. \tag{1.32}$$

The Debye length in LWFA is typically very small. For example, at $n_0 = 1.0 \times 10^{17}\,\mathrm{cm}^{-3}$ and $T_0 = 10\,\mathrm{eV}$, the Debye length is only $\lambda_D = 74\,\mathrm{nm}$, much shorter than the typical laser wavelength of $\lambda_L \sim 1\,\mu\mathrm{m}$ that would be used to drive the LWFA.

Within the 1D quasistatic approximation with a laser pulse linearly polarized in x direction, assuming the pressure term is negligible in the momentum equation, the anisotropic plasma temperature is given by [55]:

$$\begin{aligned}
\Pi_{xx} &= m_e T_0\,, \\
\Pi_{xz} &= m_e T_0 \frac{n_e}{n_0}\frac{p_x}{\gamma_0 m_e c}\,, \\
\Pi_{zz} &= m_e T_0 \left(\frac{n_e}{n_0}\right)^2 \left(1 + \frac{p_x^2}{\gamma_0^2 m_e^2 c^2}\right)
\end{aligned} \tag{1.33}$$

which is consistent with making adiabatic arguments when setting the number of degrees of freedom to 1. This anisotropic temperature becomes important as it can reduce the wavebreaking field in the nonlinear regime [56]. The distinction between the cold and warm regimes becomes more relevant for highly underdense plasmas. For example, the typical photo-ionized electron temperature is 10 eV, corresponding to $T_0/m_e c^2 = 2.0 \times 10^{-5}$. For typical LWFA parameters $n_{00} = 1.0 \times 10^{17}\,\mathrm{cm}^{-3}$ and $\lambda_L = 1030\,\mathrm{nm}$, we have $\omega_{p0}^2/\omega_L^2 = 1.0 \times 10^{-4}$, which is comparable to $T_0/m_e c^2$, yielding $\beta_{\mathrm{th}}^2 \omega_L^2/\omega_{p0}^2 = 0.21$ where $\beta_{\mathrm{th}} = (T_0/m_e c^2)^{1/2}$. This leads to a reduction in the nonlinear wavebreaking field which at low temperatures in 1D geometry is given by [57]

$$\left(\frac{E_{\mathrm{wb}}}{E_0}\right)^2 \approx 2\gamma_\perp(\gamma_p - 1)\left(1 - \frac{\beta_p^2\gamma_p}{2(\gamma_p - 1)}(8\delta_{\mathrm{th}}/3 - 2\delta_{\mathrm{th}}^2)\right)\,, \tag{1.34}$$

where $\gamma_\perp = 1 + \boldsymbol{a}^2$ is the transverse Lorentz factor associated with the quiver motion in the wavebreaking region, $\gamma_p = (1-\beta_p^2)^{-1/2} \approx \omega_L/\omega_{p0}$ is the Lorentz factor associated with the plasma wave phase velocity (which is approximately equal to

the laser pulse group velocity), and $\delta_{\rm th} = (3\beta_{\rm th}^2\gamma_p^2/\gamma_\perp^2\beta_p^2)^{1/4} \approx (3\beta_{\rm th}^2\omega_L^2/\omega_{p0}^2\gamma_\perp^2)^{1/4}$.

1.3.6 Summary of LWFA Regimes

In LWFA we only consider operation in underdense conditions $n_e \ll n_{\rm c} = m_e\epsilon_0\omega_L^2/e^2$, such that the unperturbed plasma frequency is (initially) small relative to the laser frequency $\omega_{p0}^2/\omega_L^2 \ll 1$. To better familiarize with which physical processes are relevant to LWFA, we outline in Table 1.1 the typical range of laser-plasma parameters used in LWFA experiments.

Table 1.1: Typical LWFA laser-plasma parameters

Laser	
Wavelength λ_L	$\sim 1\,\mu$m
Normalized vector potential a_0	$0.3 - 4$
Spot size w_0	$\sim \lambda_p/2 \sim 50 - 5\,\mu$m
FWHM duration $\tau_{\rm FWHM}$	$\sim T_p/2 \sim 200 - 20\,$fs
Group velocity Lorentz factor $\gamma_L = \left(1 - \frac{v_g^2}{c^2}\right)^{-1/2}$	$100 - 10$
Plasma	
Plasma density n_e	$10^{17} - 10^{19}\,{\rm cm}^{-3}$
Temperature T_e	$\sim 10\,$eV (photoionized)
Debye length λ_D	$100 - 10\,$nm
Plasma parameter N_D	$100 - 10$
Cold nonrelativistic wavebreaking E_0	$30 - 300\,{\rm GV/m}$
Dephasing length $L_{\rm d}$	$600 - 0.6\,$mm

Table 1.2 then summarizes the different LWFA regimes for single-pulse driven wakes as a function of laser amplitude, spot size, plasma frequency and plasma temperature. Note that the theory of wavebreaking in both the 3D cold and warm nonlinear regimes is more complicated than those written for 1D due to the possibility for transverse wavebreaking [58] in combination with anisotropic temperature effects and the possibility of a full blowout cavity, and are therefore left blank.

Table 1.2: Summary of LWFA regimes

	a_0^2	$k_{p0}^2 w_0^2/4$	$\beta_{\rm th}^2 \omega_L^2/\omega_{p0}^2$	$E_{\rm wb}/E_0$
1D Cold Linear	$\ll 1$	$\gg 1$	$\ll 1$	1
1D Warm Linear	$\ll 1$	$\gg 1$	$\lesssim 1$	$\lesssim 1$
3D Cold Linear	$\ll 1$	~ 1	$\ll 1 + 4/k_{p0}^2 w_0^2$	1
3D Warm Linear	$\ll 1$	~ 1	$\lesssim 1 + 4/k_{p0}^2 w_0^2$	$\lesssim 1$
1D Cold NL	> 1	$\gg 1$	$\ll 1$	$(2\omega_L/\omega_{p0})^{1/2}$
1D Warm NL	> 1	$\gg 1$	$\lesssim 1$	Eq. (1.34)
3D Cold NL	> 1	~ 1	$\ll 1 + 4/k_{p0}^2 w_0^2$	–
3D Warm NL	> 1	~ 1	$\lesssim 1 + 4/k_{p0}^2 w_0^2$	–

1.4 Fundamental Challenges for LWFA

1.4.1 Diffraction

To achieve the high intensities required to drive a wakefield, we require the driving laser pulse to be focused to spot sizes on the order of tens of microns. However, if not compensated for, such a beam will quickly diffract away from focus. In a vacuum, the spot size of a Gaussian pulse (defined as the radius at which the pulse intensity drops by $1/e^2$) focused down to a minimum spot size w_0 will evolve according to

$$w(z) = w_0 \sqrt{1 + \left(\frac{z}{z_R}\right)^2} \tag{1.35}$$

where $z_R = \frac{\pi w_0^2}{\lambda_L}$ is the Rayleigh range. For example, a $\lambda_L = 1030\,\text{nm}$ laser focused down to a spot size of $w_0 = 30\,\mu\text{m}$ will have a Rayleigh range of just $z_R = 2.75\,\text{mm}$, which poses a problem if we want to accelerate electrons with a wakefield over 100+ mm. To overcome this diffraction to continuously drive a wakefield, the refractive index of the plasma must provide focusing along the acceleration distance. The general refractive index of a plasma is given by [20]

$$\eta = \frac{ck}{\omega_L} = \sqrt{1 - \frac{\omega_p^2}{\gamma \omega_L^2}} \approx 1 - \frac{n_e}{2(1 + \boldsymbol{a}^2) n_{\rm c}} \tag{1.36}$$

where ω_L is the laser angular frequency, γ is the Lorentz factor of electrons due to their high frequency quiver motion in the laser field, $\boldsymbol{a} = e\boldsymbol{E}/m_e\omega_L c$ is the normalized vector potential of the laser pulse and $n_\mathrm{c} = m_e\epsilon_0\omega_L^2/e^2$ is the plasma critical density. For the plasma to provide a focusing effect, the phase velocity $v_\phi = \omega_L/k$ must increase in the transverse coordinate. This can be achieved in two ways. One way is to use intensity-dependent effects such as relativistic self-focusing and ponderomotive self-channeling. Relativistic self-focusing requires a laser pulse above the critical power [20]

$$P_\mathrm{c} = \frac{8\pi\epsilon_0 m_e^2 c^5 \omega_L^2}{e^2\omega_p^2} = [17.4\,\mathrm{GW}]\,\frac{\omega_L^2}{\omega_p^2} \tag{1.37}$$

to generate a sufficient increase in the Lorentz factor towards the axis. Likewise, ponderomotive self-channeling requires a sufficiently intense and long pulse with a sufficiently small spot size to ponderomotively form a plasma channel, increasing the plasma density away from the axis. If we do not have sufficient intensities available to maintain sufficient focusing throughout the accelerator, then we need to rely on a pre-formed plasma channel. The matching condition for a parabolic plasma channel to guide a low-intensity $\boldsymbol{a}^2 \ll 1$ Gaussian pulse of spot size w_0 is [56]

$$\begin{aligned} n_0(r) &= n_{00} + \Delta n(r/w_0)^2, \\ \Delta n &= (\pi r_e w_0^2)^{-1} \end{aligned} \tag{1.38}$$

where $n_{00} \ll n_\mathrm{c}$ is an arbitrary on-axis electron density and r_e is the classical electron radius. Much of our work on the P-MoPA is in a regime where we cannot solely rely on relativistic self-focusing and ponderomotive self-channeling to prevent diffraction, so we will be concentrating on pre-formed plasma channel formation techniques for guiding.

In the majority of previous LWFA research, pre-formed plasma channels were made using either capillary discharges [59, 60] and laser-induced hydrodynamic expansion [61, 62]. Out of these two methods, laser-induced hydrodynamic expansion is the most attractive for kHz repetition rates due to its freestanding nature. How-

ever, prior to 2018, this method was limited to high on-axis plasma densities of at least $1 \times 10^{18}\,\mathrm{cm}^{-3}$ due to its reliance on heating via laser-driven electron-ion collisions [63].

In 2018, on-axis plasma densities as low as $1 \times 10^{17}\,\mathrm{cm}^{-3}$ were demonstrated with the introduction of the Hydrodynamic Optical-Field-Ionized (HOFI) channel forming technique [34]. These HOFI channels, post-conditioning (i.e. CHOFI channels), offer meter-scale attenuation lengths [37] and have been experimentally demonstrated to be stable operating continuously at kHz-scale repetition rates [64]. This makes (C)HOFI channels a well-suited choice for kHz operation of LWFA.

1.4.2 Dephasing

Electrons are only accelerated as long as they remain in phase with the wakefield. The electrons will be highly relativistic, traveling asymptotically close to c, but the group velocity of the laser pulse in a plasma will be slow enough that its wakefield will eventually drift behind the accelerating electrons, causing dephasing. In the 1D limit, this group velocity is given by the plasma refractive index as given in Eq. (1.36)

$$v_g = \frac{\mathrm{d}\omega}{\mathrm{d}k} = \eta c\,. \tag{1.39}$$

In a plasma accelerator, we require that the accelerating electron bunch remain in a region of the wakefield which both provides both a longitudinal accelerating gradient as well as a transverse focusing force to maintain electron bunch quality. In 1D theory, this region corresponds to a length of a quarter of the plasma wavelength $\lambda_p = 2\pi c/\omega_p$. This means that the electron dephasing length L_d corresponds to the propagation distance required for the laser pulse to drift $\lambda_p/4$ behind the electron bunch, and is hence given by [20]

$$(c - v_g)\frac{L_\mathrm{d}}{c} = \frac{\lambda_p}{4} \quad \Rightarrow \quad L_\mathrm{d} = \frac{\lambda_p}{2}\frac{\omega_L^2}{\omega_p^2} \propto n_e^{-3/2}\,. \tag{1.40}$$

For example, for a $\lambda_L = 1030\,\mathrm{nm}$ laser pulse driving a wakefield in a plasma of density $n_e = 2.5 \times 10^{17}\ \mathrm{cm}^{-3}$ in the non-relativistic limit (i.e. the plasma frequency is not modified by quiver motion), assuming that the pulse remains focused and does not appreciably red-shift, we find $L_\mathrm{d} = 140\,\mathrm{mm}$. Beyond this distance, the electron bunch cannot continue to accelerate, unless techniques are employed to circumvent the dephasing problem such as staging multiple accelerators [65].

1.4.3 Energy Efficiency and Repetition Rate

The single pulse drive LWFA scheme only became practical with the onset of chirped pulse amplification (CPA) [22] allowing pulses to be compressed into high-intensity sub-ps duration pulses, and the bulk of LWFA research has since been based on high intensity ultrashort laser pulses from Ti:sapphire laser systems with CPA. However, these systems suffer from low ($\sim$ 0.1–1 Hz) repetition rates and poor ($\lesssim 0.1\%$) energy efficiencies. This poses a problem if we wish LWFA to compete with traditional particle accelerators, which can operate at MHz repetition rates. For many practical applications, we would need at least kHz-scale rates.

Fortunately, contemporary Yb:YAG thin-disk lasers are already able to reliably provide joule-scale laser pulses at kHz repetition rates with high ($\sim 50\%$) electrical-to-optical efficiencies [2–4]. The only caveat is that their joule-scale pulses cannot currently be compressed far enough below picosecond-scale durations with CPA techniques due to their narrower gain bandwidth. This limitation has prevented their implementation in LWFA research. If we want to take advantage of these thin-disk lasers for kHz repetition rate LWFA, we require a method for compressing these pulses down to the 10–100 fs durations.

Enabled by recent developments in the HOFI channel formation technique [34–37], the P-MoPA concept was proposed [1] which uses a plasma-based optic to introduce a sinusoidal spectral chirp to these long pulses, which allows a conventional dispersive optical system to then compress the joule-scale picosecond pulse into a train of femtosecond-class pulses suitable for LWFA.

Chapter 2

Pulse Propagation in Plasma Channels

2.1 Motivation

To prevent the laser pulse diffracting away as it propagates in the plasma, we can introduce a pre-formed plasma channel to keep the pulse focused over many Rayleigh ranges. This allows for wakefield acceleration beyond the diffraction limit without the need for sufficient intensities for relativistic and ponderomotive self-focusing. Our group has developed hydrodynamic optical-field-ionized (HOFI) plasma channels which have been routinely demonstrated to guide laser pulses well over 100 mm of propagation, corresponding to nearly hundreds of Rayleigh ranges [34–36], as well as the more recent conditioned HOFI (CHOFI) channels promising low-loss channels on the meter scale [37]. These plasma channels have also been demonstrated to be stable at kHz operation rates [64], and hence are incredibly desirable for both wakefield acceleration as well as for other plasma-based optics schemes.

The advent of the CHOFI channel-formation technique thus makes it important to understand the long-propagation affects a laser pulse as it evolves under the influence of the pre-formed plasma channel, its own excited wakefield and relativistic effects. In this chapter we derive the theory of pulse propagation and wakefield structure in plasma channels, and apply this theory to a few well known laser-

plasma instabilities. This will serve as a foundational theory for the subsequent chapters.

2.2 Paraxial Propagation Theory

2.2.1 The Envelope Model

From the fluid-Maxwell equations presented in Eq. (1.22), we find that the normalized vector potential $\boldsymbol{a} = e\boldsymbol{A}/m_e c$ evolves in a cold collisionless electron fluid according to the following wave equation

$$\left(\frac{\partial^2}{\partial t^2} - c^2\Delta + \tilde{\omega}_p^2\right)\boldsymbol{a} = -c\frac{\partial}{\partial t}\nabla\phi - \tilde{\omega}_p^2\delta\boldsymbol{u}\,, \tag{2.1}$$

where $\delta\boldsymbol{u} = \boldsymbol{p}/m_e c - \boldsymbol{a}$ and $\tilde{\omega}_p^2 = e^2 n_e/\gamma m_e \epsilon_0$ is the effective local plasma frequency including the Lorentz factor $\gamma = \sqrt{1 + (\boldsymbol{a} + \delta\boldsymbol{u})^2}$. If we also assume that the generalized vorticity $\boldsymbol{\Omega} \equiv c\nabla \times \delta\boldsymbol{u}$ is initially zero everywhere, we can also write the RHS in the following form

$$\left(\frac{\partial^2}{\partial t^2} - c^2\Delta + \tilde{\omega}_p^2\right)\boldsymbol{a} = -\left(\frac{\partial^2}{\partial t^2} + \tilde{\omega}_p^2\right)\delta\boldsymbol{u} - c\frac{\partial}{\partial t}\nabla\gamma\,. \tag{2.2}$$

If we assume that the spectrum of the incident laser pulse is comprised mostly of frequencies much larger than the plasma frequency $\omega \gg \tilde{\omega}_p$ and has an amplitude only up to the weakly relativistic regime, we can usually neglect the RHS as their high-frequency components are small. Therefore, for now we will set the RHS terms to zero

$$\left(\frac{\partial^2}{\partial t^2} - c^2\Delta + \tilde{\omega}_p^2\right)\boldsymbol{a} = 0\,. \tag{2.3}$$

Inspecting this equation we can still see that even after setting the RHS to zero, we still cannot ignore the vector nature of this wave equation due to both the Lorentz factor nonlinearity $\gamma = \sqrt{1 + (\boldsymbol{a} + \delta\boldsymbol{u})^2}$ and the density perturbation nonlinearity $\delta n(\boldsymbol{x}, t; \boldsymbol{a}^2)$ contained within the local effective plasma frequency $\tilde{\omega}_p$. By taking the

weakly relativistic and linear wakefield limit, $\boldsymbol{a}^2 \ll 1$ and $\delta n/n_0 \ll 1$, we can further simplify this equation to

$$\left[\frac{\partial^2}{\partial t^2} - c^2\Delta + \omega_p^2\left(1 + \frac{\delta n}{n_0} - \frac{\boldsymbol{a}^2}{2}\right)\right]\boldsymbol{a} = 0\,, \tag{2.4}$$

where $\omega_p(\boldsymbol{x}) = (e^2 n_0(\boldsymbol{x})/m_e\epsilon_0)^{1/2}$ denotes the unperturbed (but possibly non-uniform) plasma frequency. To construct an envelope model for the laser evolution, consider a laser pulse with a spot size sufficiently large relative to its wavelength such that it is mostly transverse polarized, such that the normalized vector potential can be described using the complex envelope a as written in Eq. (1.10), which we will repeat here with appropriate notation for convenience

$$\boldsymbol{a} = \begin{cases} \left(ae^{i(k_L z - \omega_L t)} + \text{c.c.}\right)\hat{x}/2 & \text{linearly polarized} \\ \left(ae^{i(k_L z - \omega_L t)} + \text{c.c.}\right)\hat{x}/2 + \left(ae^{i(k_L z - \omega_L t + \pi/2)} + \text{c.c.}\right)\hat{y}/2 & \text{circularly polarized} \end{cases} \tag{2.5}$$

where $\omega_L, k_L = \omega_L/c$ are constants. We will now derive the envelope equation for a pulse propagating in an axisymmetric plasma channel $n_0 = n_0(r)$, which also means that the local unperturbed plasma frequency also acquires a radial dependence $\omega_p = \omega_p(r)$. It is convenient to shift from the lab frame to co-moving coordinates $\xi = z - v_{g0}t$, and $\tau = t$, where $v_{g0}/c = (1 - \omega_{p0}^2/\omega_L^2)^{1/2}$ is defined as the group velocity of electromagnetic plane waves in uniform plasma at the on-axis density $n_{00} = n_0(r = 0)$, which may differ from the actual group velocity of a tightly focused laser pulse. Substituting a pulse of this form into Eq. (2.4) in the weakly relativistic and linear wakefield limit yields the following expression for the evolution of the complex envelope

$$\left[-2i\omega_L\frac{\partial}{\partial\tau} - 2v_{g0}\frac{\partial^2}{\partial\xi\partial\tau} - (c^2 - v_{g0}^2)\frac{\partial^2}{\partial\xi^2} - c^2\Delta_\perp + \frac{\partial^2}{\partial\tau^2} + \frac{\omega_p^2}{n_0}(\delta n_0 + \delta n)\right]a = \begin{cases} \omega_p^2|a|^2 a/4 & \text{linearly polarized} \\ \omega_p^2|a|^2 a/2 & \text{circularly polarized} \end{cases} \tag{2.6}$$

where $\Delta_\perp = \partial^2/\partial r^2 + (1/r)\partial/\partial r + (1/r^2)\partial^2/\partial\theta^2$ is the transverse Laplacian operator in cylindrical coordinates, and $\delta n_0(r) = n_0(r) - n_{00}$ is the zeroed axisymmetric plasma channel. This PDE coupled to the wakefield solution to Eq. (2.88) fully describes the evolution of the laser envelope in the axisymmetric, weakly relativistic, quasistatic linear wakefield regime.

2.2.2 The Paraxial Approximation

To further simplify Eq. (2.6) to the paraxial optics approximation, we assume that the discrepancy between the group velocity and speed of light in vacuum is negligible ($v_{g0} \approx c$) and that the pulse envelope has a large enough longitudinal extent to drop the $\partial^2/\partial\xi^2$ term. We also assume that the envelope evolution is slow relative to the carrier frequency to drop the $v_{g0}\partial^2/\partial\xi\partial\tau$ and $\partial^2/\partial\tau^2$ time derivative terms, which also implicitly assumes that no significant red-/blue-shifting has occurred. For simplicity, from now on we will only be considering linearly polarized light unless stated otherwise. This yields a generalized nonlinear paraxial wave equation in an axisymmetric plasma channel

$$\left[\frac{i}{\omega_L}\frac{\partial}{\partial\tau} + \frac{c^2}{2\omega_L^2}\Delta_\perp\right] a = \frac{\omega_p^2}{2\omega_L^2 n_0}\left[\delta n_0(r) + \delta n(r,\xi;|a|^2) - n_0(r)|a|^2/4\right] a \tag{2.7}$$

where the nonlinearities come from relativistic self-focusing and the interaction between the pulse and its own excited wakefield, and we have applied the quasistatic approximation by writing that the wake in the form $\delta n(r,\xi;|a|^2)$ such that its only time-dependence comes from the slow evolution of the laser envelope. If the pulse happens to be too short or too strongly red-/blue-shifted to drop the $v_{g0}\partial^2/\partial\xi\partial\tau$ term, we instead get the modified paraxial equation in a plasma channel with wakefield and relativistic self-focusing nonlinearities

$$\left[\left(\frac{i}{\omega_L} + \frac{v_g}{\omega_L^2}\frac{\partial}{\partial\xi}\right)\frac{\partial}{\partial\tau} + \frac{c^2}{2\omega_L^2}\Delta_\perp\right] a = \frac{\omega_p^2}{2\omega_L^2 n_0}\left[\delta n_0(r) + \delta n(r,\xi;|a|^2) - n_0(r)|a|^2/4\right] a\,. \tag{2.8}$$

2.2.3 Plasma Channels

Parabolic Channels

Using Eq. (2.7) we can derive the well-known form of the matched parabolic plasma channel [66–68], which confines a Gaussian beam whose spot size remains constant as it propagates. By taking the low intensity limit $\boldsymbol{a}^2 \to 0$ we can neglect perturbations to the channel from relativistic self-focusing and wakes. This yields the linear paraxial wave equation in an unperturbed axisymmetric plasma channel

$$\left[\frac{i}{\omega_L}\frac{\partial}{\partial\tau} + \frac{c^2}{2\omega_L^2}\Delta_\perp\right] a = \frac{\omega_p^2 \delta n_0(r)}{2\omega_L^2 n_0} a\,. \tag{2.9}$$

Substituting a Gaussian pulse $a \sim \exp(-r^2/w_0^2)$ with a fixed spot size w_0 yields

$$\left[\frac{i}{\omega_L}\frac{\partial}{\partial\tau} + \frac{2c^2(r^2/w_0^2 - 1)}{\omega_L^2 w_0^2}\right] a = \frac{\omega_p^2 \delta n_0(r)}{2\omega_L^2 n_0} a\,, \tag{2.10}$$

which has the following stable solution

$$\begin{aligned} &a(r,\xi,\tau) = a_0 f(\xi) \exp\left(-\frac{r^2}{w_0^2} - i\frac{2c^2\tau}{\omega_L w_0^2}\right)\,, \\ &n_0(r) = n_{00} + \Delta n (r/w_0)^2\,, \\ &\Delta n \equiv (\pi r_e w_0^2)^{-1} \end{aligned} \tag{2.11}$$

where the pulse's longitudinal profile $0 \le f(\xi) \le 1$ is assumed to be sufficiently slowly varying for the paraxial approximation to hold, n_{00} is an arbitrary on-axis density and r_e is the classical electron radius. This result for the matched channel, in the absence of nonlinear effects, can also confine any linear combination of Laguerre-

Gaussian modes with stable envelope solutions of the form

$$
\begin{aligned}
a_{pm}(r,\theta,\xi,\tau) &= \alpha_{pm}(\xi)\mathrm{LG}_{pm}(r,\theta)e^{-i\Omega_{pm}\tau}\,, \\
\mathrm{LG}_{pm}(r,\theta) &= \sqrt{\frac{p!}{(p+|m|)!}}\left(\frac{\sqrt{2}\,r}{w_0}\right)^{|m|}\exp\left(-\frac{r^2}{w_0^2}+im\theta\right)L_p^{|m|}\left(\frac{2r^2}{w_0^2}\right)\,, \\
\Omega_{pm} &= (2p+|m|+1)\frac{2c^2}{\omega_L w_0^2}
\end{aligned}
\tag{2.12}
$$

where the integers $p \geq 0$, m are the radial and azimuthal indexes respectively, $\alpha_{pm}(\xi)$ is the slowly-varying longitudinal envelope for each mode and the $L_p^{|m|}$ functions are the generalized Laguerre polynomials [69]. The first few Laguerre-Gaussian mode solutions are visualized in Figure 2.1.

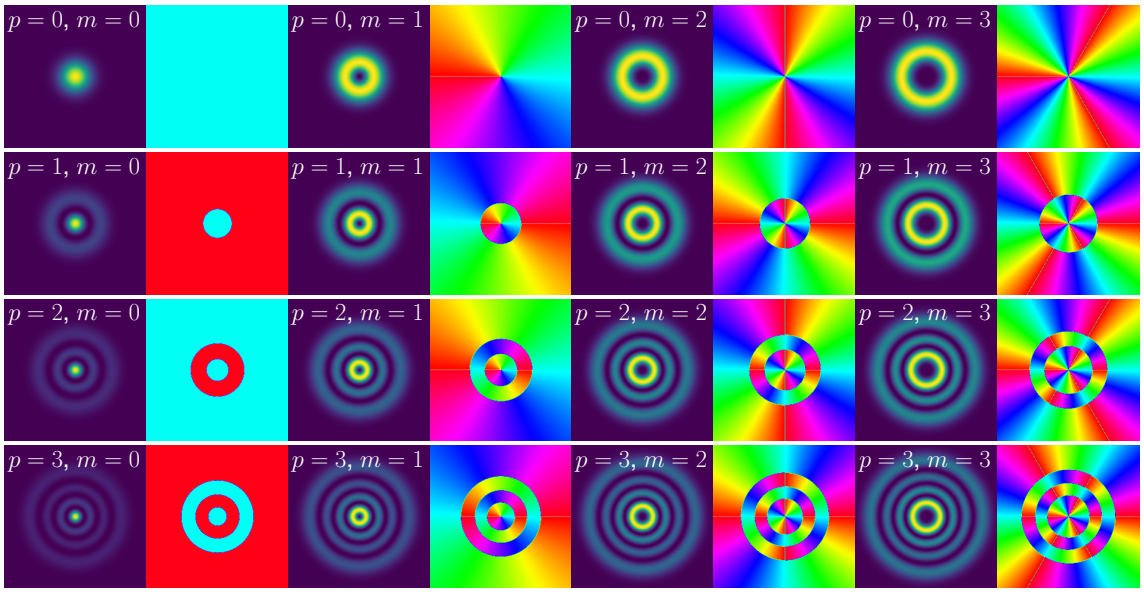


Figure 2.1: Transverse intensity profiles $|\mathrm{LG}_{pm}|^2$ (left) and phasemaps $\mathrm{Arg}\,(\mathrm{LG}_{pm})$ (right) of the Laguerre-Gaussian modes up to $p = 3$, $m = 3$.

Square Channels

In practice, the plasma channel formed may not be well approximated by a parabolic profile of infinite extent. For CHOFI channels [37], whether or not the plasma channel is parabolic or not may be strongly dependent on the plasma and axicon focus parameters due to the variety of channel profiles measured and simulated previously [34, 35, 37, 70].

It is therefore useful to consider other plasma waveguide structures. The next simplest profile that can be solved analytically is that of the infinite square well:

$$n_0(r) = \begin{cases} n_{00} & r \leq R_\infty \\ \infty & r > R_\infty \end{cases}, \tag{2.13}$$

where R_∞ is the channel wall radius. Such a channel will instead guide Bessel modes confined to the $r < R_\infty$ region of the form

$$\begin{aligned} a_{pm}(r,\theta,\xi,\tau) &= \alpha_{pm}(\xi)\mathcal{J}_{pm}(r,\theta)e^{-i\Omega_{pm}\tau}\,, \\ \mathcal{J}_{pm}(r,\theta) &= \frac{J_1(j_{0,1})}{\left|J_{|m|+1}(j_{|m|,p+1})\right|}J_{|m|}\left(\frac{j_{|m|,p+1}r}{R_\infty}\right)e^{im\theta}\,, \\ \Omega_{pm} &= \frac{j_{|m|,p+1}^2 c^2}{2\omega_L R_\infty^2}\,, \end{aligned} \tag{2.14}$$

where $j_{n,k}$ indicates the k^{th} nontrivial root of $J_n(x)$. Examples of these transverse modes up to $p = 3$, $m = 3$ are displayed in Figure 2.2. We can also define the effective spot size $w_{0,\text{eff}}$ of the fundamental mode, which is related to the wall radius R_∞ by

$$w_{0,\text{eff}} = \sqrt{\frac{\int_0^{R_\infty} 2r^2\mathcal{J}_{00}^2(r)rdr}{\int_0^{R_\infty}\mathcal{J}_{00}^2(r)rdr}} \approx 0.66R_\infty\,, \tag{2.15}$$

which is analogous to the result for the standard step-index waveguide in the limit of infinite V-number [71]. These modes behave in similar ways to Laguerre-Gaussian modes, but their key difference is that these modes are strictly contained within the $r < R_\infty$ region. Hence, the effective spot size of each individual mode does not vary strongly with radial mode number p.

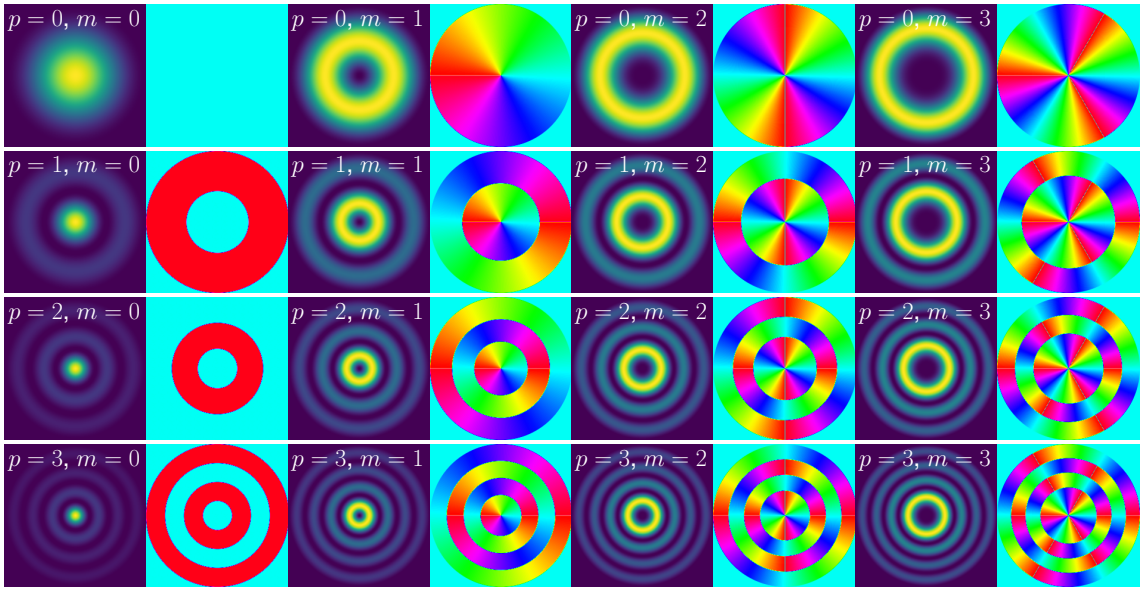


Figure 2.2: Transverse intensity profiles $|\mathcal{J}_{pm}|^2$ (left) and phasemaps $\mathrm{Arg}\,(\mathcal{J}_{pm})$ (right) of the Bessel modes for an infinite square channel up to $p = 3$, $m = 3$.

Spot Size and Centroid Oscillations

Spot size and centroid oscillations occur when the plasma channel is not matched exactly to the input laser pulse. They can thus be understood as interference between the fundamental and higher order channel modes excited by an initial mismatch. By inspecting Eqs. (2.12) and (2.14), assuming a small mismatch, we can recover the spot size and centroid oscillation angular frequencies Ω_w, Ω_c for both a parabolic channel matched to spot size w_0 and an infinite square channel with wall radius R_∞ by comparing the difference in wavenumber between the $p = \{0, 1\}$, $m = 0$ and $p = 0$, $m = \{0, 1\}$ modes respectively

$$\Omega_w = \Omega_{10} - \Omega_{00} = \begin{cases} \frac{4c^2}{\omega_L w_0^2} & \text{parabolic} \\ \frac{(j_{0,2}^2 - j_{0,1}^2)c^2}{2\omega_L R_\infty^2} \approx 1.35\,\frac{4c^2}{\omega_L w_{0,\mathrm{eff}}^2} & \text{square} \end{cases}$$
$$\Omega_c = \Omega_{01} - \Omega_{00} = \begin{cases} \frac{2c^2}{\omega_L w_0^2} & \text{parabolic} \\ \frac{(j_{1,1}^2 - j_{0,1}^2)c^2}{2\omega_L R_\infty^2} \approx 0.97\,\frac{2c^2}{\omega_L w_{0,\mathrm{eff}}^2} & \text{square} \end{cases} \tag{2.16}$$

To calculate the form of small amplitude spot size and centroid oscillations, we start by using the general definition of the laser pulse's spot size and centroid (in the x

direction)

$$w_x^2(\xi,\tau) = \frac{\int_0^{2\pi}\int_0^{\infty} 4(r\cos\theta - x_c)^2 |a(r,\theta,\xi,\tau)|^2 r dr d\theta}{\int_0^{2\pi}\int_0^{\infty} |a(r,\theta,\xi,\tau)|^2 r dr d\theta},$$
$$x_c(\xi,\tau) = \frac{\int_0^{2\pi}\int_0^{\infty} r\cos\theta |a(r,\theta,\xi,\tau)|^2 r dr d\theta}{\int_0^{2\pi}\int_0^{\infty} |a(r,\theta,\xi,\tau)|^2 r dr d\theta}. \tag{2.17}$$

For the axisymmetric case, we can describe small spot size oscillations as interference between the $p = m = 0$ and $p = 1, m = 0$ modes. Assuming a small mismatch such that $|\alpha_{10}| \ll |\alpha_{00}|$, spot size oscillations in a parabolic channel matched to spot size w_0 are described by

$$\begin{aligned}\frac{\delta w(\xi,\tau)}{w_0} &= \frac{\alpha_{00}(\xi)\alpha_{10}^*(\xi)e^{i\Omega_w\tau} + \text{c.c.}}{2|\alpha_{00}(\xi)|^2} \frac{\int_0^{\infty} 2(r/w_0)^2 \text{LG}_{00}\text{LG}_{10} r dr}{\int_0^{\infty} \text{LG}_{00}^2 r dr} \\ &= -\frac{\alpha_{00}(\xi)\alpha_{10}^*(\xi)e^{i\Omega_w\tau} + \text{c.c.}}{2|\alpha_{00}(\xi)|^2},\end{aligned} \tag{2.18}$$

and the equivalent for square channels is given by

$$\begin{aligned}\frac{\delta w(\xi,\tau)}{w_{0,\text{eff}}} &= \frac{\alpha_{00}(\xi)\alpha_{10}^*(\xi)e^{i\Omega_w\tau} + \text{c.c.}}{2|\alpha_{00}(\xi)|^2} \frac{\int_0^{R_\infty} 2r^2 \mathcal{J}_{00}\mathcal{J}_{10} r dr}{w_{0,\text{eff}}^2 \int_0^{R_\infty} \mathcal{J}_{00}^2 r dr} \\ &\approx -0.80\, \frac{\alpha_{00}(\xi)\alpha_{10}^*(\xi)e^{i\Omega_w\tau} + \text{c.c.}}{2|\alpha_{00}(\xi)|^2}.\end{aligned} \tag{2.19}$$

Small centroid oscillations are instead described by the $p = 0, m = \pm 1$ mode interfering with the fundamental mode, which for parabolic channels is described by

$$\begin{aligned}\frac{x_c(\xi,\tau)}{w_0} &= \frac{\alpha_{00}(\xi)\left(\alpha_{01}(\xi) + \alpha_{0-1}(\xi)\right)^* e^{i\Omega_c\tau} + \text{c.c.}}{2\sqrt{2}|\alpha_{00}(\xi)|^2}, \\ \frac{y_c(\xi,\tau)}{w_0} &= \frac{i\alpha_{00}(\xi)\left(\alpha_{01}(\xi) - \alpha_{0-1}(\xi)\right)^* e^{i\Omega_c\tau} + \text{c.c.}}{2\sqrt{2}|\alpha_{00}(\xi)|^2},\end{aligned} \tag{2.20}$$

which means that in order to only have centroid oscillations in the x direction, we require $\alpha_{01}(\xi) = \alpha_{0-1}(\xi)$. Examples of these spot size and centroid oscillations are shown in Figure 2.3.

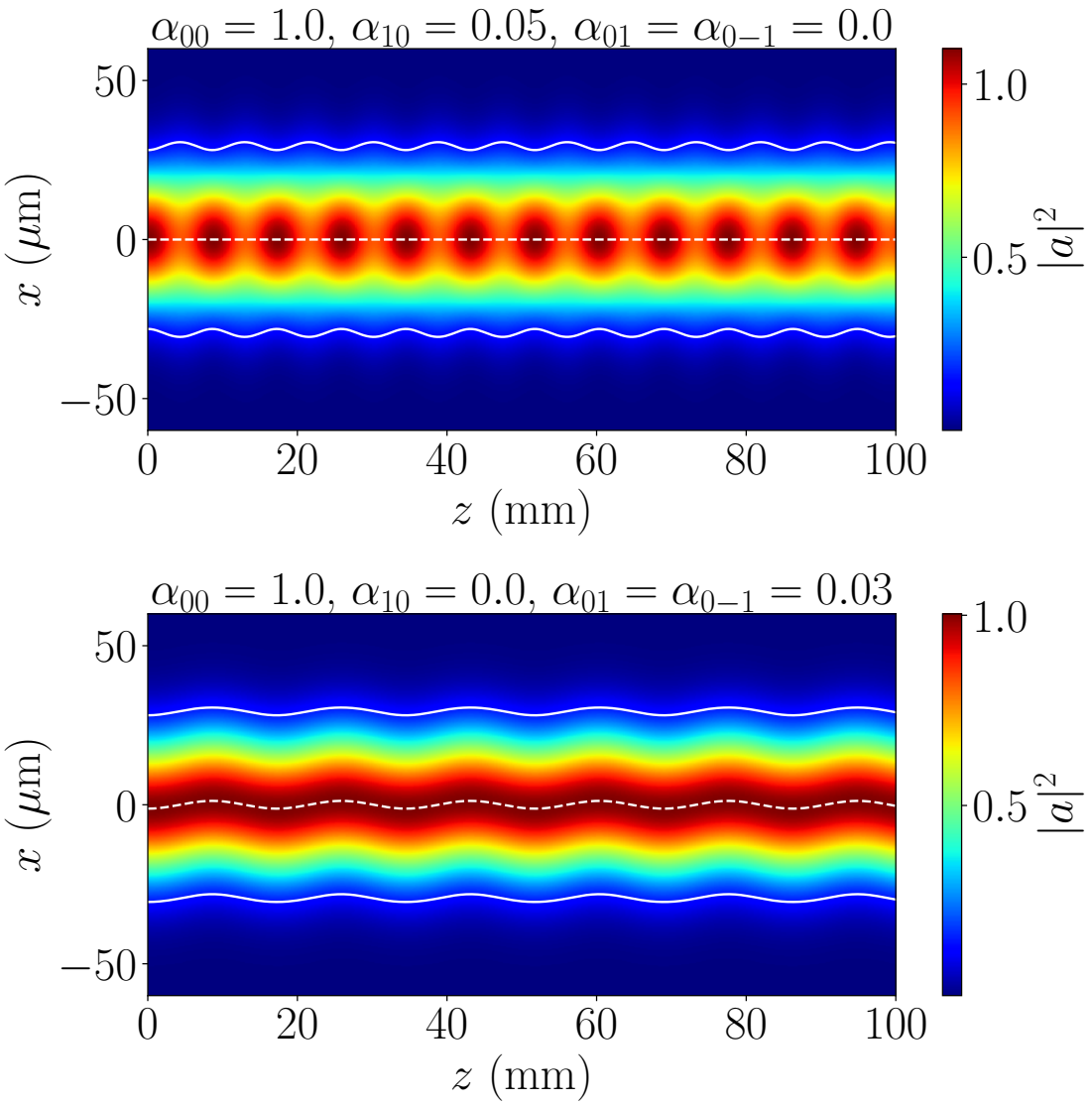


Figure 2.3: Examples of (top) spot size oscillations and (bottom) centroid oscillations for a laser pulse of wavelength $\lambda_L = 1030\,\mathrm{nm}$ propagating in a parabolic plasma channel matched to a spot size of $w_0 = 30\,\mu\mathrm{m}$ assuming that the plasma channel remains unperturbed and that relativistic effects are negligible. The dashed line indicates the laser centroid x_c whilst the solid lines indicate the spot size w relative to the centroid.

2.2.4 Time-Dependent Perturbation Theory

So far in this chapter we have only considered the propagation of pulses in unperturbed plasma channels, which holds in the zero intensity limit $\boldsymbol{a}^2 \to 0$. In general, for highly intense laser pulses $\boldsymbol{a}^2 > 1$, nonlinearities associated with relativistic and

wake effects severely change the guiding properties of the plasma channel, necessitating numerical approaches to capture the full dynamics. However, when operating LWFA in the (quasi-)linear regime $\boldsymbol{a}^2 < 1$, we can often take advantage of perturbations to the plasma channel being small, allowing us to still describe the laser-plasma dynamics in the original basis of unperturbed channel modes.

Inspecting the paraxial wave equation in Eq. (2.7), we can see that it takes the form of a Schrödinger equation with two nonlinear terms due to the plasma wake and relativistic effects, which we will rewrite here in a very suggestive form

$$\begin{aligned}
&\frac{i}{\omega_L}\frac{\partial a}{\partial \tau} = (H_0 + V_1)\, a\,, \\
&H_0 = -\frac{c^2}{2\omega_L^2}\Delta_\perp + V_0\,, \\
&V_0(r) = \frac{\omega_{p0}^2}{2\omega_L^2}\frac{\delta n_0(r)}{n_{00}}\,, \\
&V_1(r,\theta,\xi;|a|^2) = \frac{\omega_{p0}^2}{2\omega_L^2}\left(\frac{\delta n(r,\theta,\xi;|a|^2)}{n_{00}} - \frac{n_0(r)}{n_{00}}|a|^2/4\right)\,,
\end{aligned} \tag{2.21}$$

where we can think of the plasma channel as a confining potential well, and the nonlinear wake and relativistic terms as small perturbations to this potential. In keeping with the Schrödinger equation analogy, we will now introduce bra-ket notation to describe the unperturbed channel modes:

$$|a\rangle = \sum_{pm} \alpha_{pm}(\xi,\tau) e^{-i\Omega_{pm}\tau}\,|pm\rangle\,, \tag{2.22}$$

where $\alpha_{pm}(\xi,\tau)$ is the complex amplitude of the unperturbed channel mode $|pm\rangle$ at every longitudinal slice ξ and propagation time τ, which corresponds to Laguerre-Gaussian modes for a parabolic channel, and Bessel modes for a square channel. Following the method of variation of constants, we can then recover the following

set of coupled nonlinear PDEs governing the evolution of the complex amplitudes

$$\frac{i}{\omega_L}\frac{\partial \alpha_{pm}(\xi,\tau)}{\partial \tau} = \sum_{p'm'} \langle pm|\, V_1(r,\xi;|a|^2)\, |p'm'\rangle\, \alpha_{p'm'}(\xi,\tau) e^{-i\left(\Omega_{p'm'}-\Omega_{pm}\right)\tau}\,,$$
$$|a|^2 = \left|\sum_{pm} \alpha_{pm} e^{-i\Omega_{pm}\tau}\, \langle r,\theta|pm\rangle\right|^2\,, \tag{2.23}$$

where $\langle r,\theta|pm\rangle$ recovers the transverse channel mode (p,m), e.g. $\mathrm{LG}_{pm}(r,\theta)$ for parabolic channels. Note that this description so far is exact within the paraxial approximation. To get a perturbative solution, we assume that the plasma channel is matched sufficiently to the input pulse such that most of the laser light is initially in the fundamental mode, and that the perturbation to the plasma channel is small enough such that most of the light will always remain in the fundamental mode, and predominantly exchanges light with neighboring modes. This imposes the ordering $|\alpha_{00}|^2 \gg \{|\alpha_{10}|^2, |\alpha_{0\pm1}|^2\} \gg |\alpha_{\{p+|m|>1\}}|^2$, which allows us to approximate this as a 4-level system of the modes $p+|m| \leq 1$:

$$\frac{i}{\omega_L}\frac{\partial \alpha_{pm}(\xi,\tau)}{\partial \tau} = \sum_{p'+|m'|\leq 1} \langle pm|\, V_1(r,\xi;|a|^2)\, |p'm'\rangle\, \alpha_{p'm'}(\xi,\tau) e^{-i\left(\Omega_{p'm'}-\Omega_{pm}\right)\tau}\,,$$
$$|a|^2 = \left|\sum_{p'+|m'|\leq 1} \alpha_{pm} e^{-i\Omega_{pm}\tau}\, \langle r,\theta|pm\rangle\right|^2\,. \tag{2.24}$$

If we also impose axisymmetry, we can further reduce this to a 2-level system between the dominant fundamental mode and the first radial mode

$$\frac{i}{\omega_L}\frac{\partial}{\partial \tau}\begin{bmatrix}\alpha_{00}\\ \alpha_{10}\end{bmatrix} = \begin{bmatrix}\langle 00|\, V_1\, |00\rangle & \langle 00|\, V_1\, |10\rangle\, e^{-i\Omega_w\tau}\\ \langle 10|\, V_1\, |00\rangle\, e^{i\Omega_w\tau} & \langle 10|\, V_1\, |10\rangle\end{bmatrix}\begin{bmatrix}\alpha_{00}\\ \alpha_{10}\end{bmatrix}\,,$$
$$|a|^2 = |\alpha_{00}|^2 \langle r,\theta|00\rangle \langle r,\theta|00\rangle + \left(\alpha_{00}\alpha_{10}^* e^{i\Omega_w\tau} + \text{c.c.}\right) \langle r,\theta|00\rangle \langle r,\theta|10\rangle\,. \tag{2.25}$$

This system of equations, coupled with a quasistatic fluid model for the wake response, describes 3D paraxial laser-plasma dynamics including envelope self-modulation (SM) and relativistic self-focusing (SF). However, it does not capture effects like stimulated Raman scattering (SRS), relativistic self-phase modulation (SPM) and

depletion, which require variation in group velocity that the paraxial approximation neglects. For these group-velocity-dependent processes we will require a non-paraxial description, which we will derive later in this chapter.

2.2.5 Envelope Self-Modulation and Relativistic Self-Focusing

Envelope self-modulation (SM) is a laser-plasma instability caused by a feedback loop between a plasma wave driven by the laser pulse and the local transverse focusing/defocusing of the pulse envelope by the excited wave. This forms a plasma-resonant modulation in the pulse envelope, which increases in amplitude towards the tail of the pulse. In the unguided uniform plasma case, envelope SM only grows when relativistic self-focusing (SF) becomes relevant, where relativistic nonlinearities causes a transverse focusing effect on the laser pulse.

To demonstrate the applicability of the time-dependent perturbation theory we previously derived in Eq. (2.23), we will now use it to derive the PDE governing the growth of envelope SM in a plasma channel for a long duration (multiple plasma periods) laser pulse with a slowly varying envelope (such that it does not drive an initial wakefield), which was originally derived using a source-dependent expansion method by Esarey et al. [72]. We begin with the axisymmetric 2-level time-dependent perturbation theory from Eq. (2.25) specifically for parabolic plasma channels. We will also work in the shallow channel limit $k_{p0}^2 w_0^2/4 \gg 1$ such that we can describe the plasma wave using 1D linear quasistatic wakefield theory

$$
\begin{aligned}
&\frac{i}{\omega_L}\frac{\partial}{\partial\tau}\begin{bmatrix}\alpha_{00}\\ \alpha_{10}\end{bmatrix} = \begin{bmatrix}\langle 00|\,V_1\,|00\rangle & \langle 00|\,V_1\,|10\rangle\, e^{-i\Omega_w\tau}\\ \langle 10|\,V_1\,|00\rangle\, e^{i\Omega_w\tau} & \langle 10|\,V_1\,|10\rangle\end{bmatrix}\begin{bmatrix}\alpha_{00}\\ \alpha_{10}\end{bmatrix},\\
&|a|^2 = |\alpha_{00}|^2\,\mathrm{LG}_{00}^2 + \left(\alpha_{00}\alpha_{10}^* e^{i\Omega_w\tau} + \text{c.c.}\right)\mathrm{LG}_{00}\mathrm{LG}_{10}\,,\\
&V_1 = \frac{\omega_{p0}^2}{2\omega_L^2}\left(\frac{\delta n}{n_{00}} - \frac{|a|^2}{4}\right),\\
&\left(\frac{\partial^2}{\partial\xi^2} + k_{p0}^2\right)\frac{\delta n}{n_{00}} = \frac{\partial^2}{\partial\xi^2}\frac{|a|^2}{4}\,.
\end{aligned}
\tag{2.26}
$$

We will now treat the light in the fundamental mode as a fixed pump such that

$\alpha_{00} = a_0$ and assume that the higher order mode is initially zero $\alpha_{10}(\tau = 0) = 0$. To first order, this simplifies the system to the following set of PDEs governing the growth of the higher order mode and wake

$$\begin{aligned}
&\frac{\partial \alpha_{10}}{\partial \tau} = -i a_0 \frac{\omega_{p0}^2}{2\omega_L} \langle 10| \frac{\delta n}{n_{00}} - \frac{|a|^2}{4} |00\rangle e^{i\Omega_w \tau} , \\
&\left(\frac{\partial^2}{\partial \xi^2} + k_{p0}^2 \right) \frac{\delta n}{n_{00}} = \frac{\partial^2}{\partial \xi^2} \frac{|a|^2}{4} , \\
&|a|^2 = a_0^2 \mathrm{LG}_{00}^2 + a_0 \left(\alpha_{10} e^{-i\Omega_w \tau} + \mathrm{c.c.} \right) \mathrm{LG}_{00} \mathrm{LG}_{10} .
\end{aligned} \tag{2.27}$$

We then break up the plasma wave into a fast plasma wave component $\sim \exp(ik_{p0}\xi)$ and a slowly varying carrier envelope $\tilde{n}$ to rewrite the wake response in the quasistatic limit, and similarly do so for the laser envelope

$$\begin{aligned}
&\frac{\delta n}{n_{00}} = \frac{\tilde{n}}{2} e^{ik_{p0}\xi} + \mathrm{c.c.} , \\
&\alpha_{10} e^{-i\Omega_w \tau} = \bar{\alpha}_{10} + \left(\frac{\tilde{\alpha}_{10}}{2} e^{ik_{p0}\xi} + \mathrm{c.c.} \right) ,
\end{aligned} \tag{2.28}$$

where $\bar{\alpha}_{10}$ has been included to capture the spot size oscillations associated with the channel mismatch due to relativistic SF. By assuming that we are not in the strongly coupled regime, i.e. that the pump is sufficiently long such that $k_{p0}\tilde{n} \gg \partial \tilde{n}/\partial \xi$, this allows us to write the wake and envelope modulation equations to first order in the following form

$$\begin{aligned}
&2ik_{p0} \frac{\partial \tilde{n}_0}{\partial \xi} = -\frac{k_{p0}^2 a_0 \tilde{\alpha}_{10}}{2} , \\
&\left(\frac{\partial^2}{\partial \tau^2} + \Omega_w^2 \right) \bar{\alpha}_{10} = \frac{a_0^3 \Omega_w \omega_{p0}^2}{32\omega_L} , \\
&\left(\frac{\partial \tilde{\alpha}_{10}}{\partial \tau} \frac{e^{ik_{p0}\xi}}{2} + \mathrm{c.c.} \right) + i \left(\Omega_w - \frac{a_0^2 \omega_{p0}^2}{16\omega_L} \right) \left(\tilde{\alpha}_{10} \frac{e^{ik_{p0}\xi}}{2} + \mathrm{c.c.} \right) = -i \frac{a_0 \omega_{p0}^2}{8\omega_L} \left(\tilde{n}_0 \frac{e^{ik_{p0}\xi}}{2} + \mathrm{c.c.} \right) , \\
&\tilde{n}(r, \xi, \tau) = \tilde{n}_0(\xi, \tau) \mathrm{LG}_{00} \mathrm{LG}_{10} ,
\end{aligned} \tag{2.29}$$

where we have used the identity $\langle 10| \mathrm{LG}_{00}^2 |00\rangle = \langle 10| \mathrm{LG}_{00} \mathrm{LG}_{10} |00\rangle = 1/4$ in parabolic channels. The PDE for $\bar{\alpha}_{10}$ simply describes spot size oscillations around a new tighter equilibrium spot size $w_{\mathrm{SF}}/w_0 \approx 1 - a_0^2 \omega_{p0}^2 / 32\omega_L \Omega_w$ due to weak rel-

ativistic self-focusing of the pump. For the sake of this derivation, we will assume that the guiding is channel-dominated, that is to say that focusing due to relativistic SF is weak relative to the focusing due to the plasma channel. In this regime, the laser envelope modulation PDE reduces to

$$\left(\frac{\partial^2}{\partial\tau^2}+\Omega_w^2\right)\tilde{\alpha}_{10}=-\frac{a_0\Omega_w\omega_{p0}^2}{8\omega_L}\tilde{n}_0\,, \tag{2.30}$$

in which case the PDE governing the growth of envelope SM is given by

$$c\left(\frac{\partial^2}{\partial\tau^2}+\Omega_w^2\right)\frac{\partial\tilde{n}_0}{\partial\xi}=-\frac{i}{8}\frac{a_0^2\omega_{p0}^3}{k_L^2w_0^2}\tilde{n}_0\,, \tag{2.31}$$

which is consistent with the result in Esarey et al. [72] and Andreev et al. [73] in the channel-dominated guiding regime (accounting for the difference between circular and linear polarization). We then consider the following initial conditions

$$\tilde{n}_0\Big|_{\tau=0}=\tilde{n}_0\Big|_{\xi=\xi_0}=\tilde{n}_{00}\,,\quad \frac{\partial\tilde{n}_0}{\partial\tau}\Big|_{\tau=0}=0\,. \tag{2.32}$$

Using a saddle-point integration procedure, Andreev et al. [73] derived that in the long-propagation limit (specifically $\Omega_w\tau > k_{p0}^3w_0^2a_0^2(\xi_0-\xi)/4$, which they dub the 3D-2 mode), Eq. (2.31) with these initial conditions yields the following characteristic growth rate of envelope SM in the channel-dominated guiding regime

$$\Gamma_{\rm SM}\tau=\frac{a_0k_{p0}w_0}{8}\sqrt{k_{p0}(\xi_0-\xi)\Omega_w\tau}\,. \tag{2.33}$$

Substituting reasonable laser-plasma parameters $a_0=0.1$, $k_{p0}w_0=4$, $k_{p0}(\xi_0-\xi)=6\pi$, $\Omega_w\tau=20\pi$ typical for long-propagation in a plasma channel yields $\Gamma_{\rm SM}\tau=1.7$ e-foldings, making the envelope SM instability important to consider when propagating multi-plasma-period duration pulses.

2.3 The Non-Paraxial Description

Unlike the paraxial equation, this description will include more accurate spectral and group velocity dispersion effects which become important when performing LWFA over long propagation distances in pre-formed plasma channels. Our derivation will initially follow the procedure outlined by [68], but then we will generalize it to fully capture nonlinear effects. We begin by rewriting the full 3D lab frame wave equation as derived in Eq. (2.1)

$$\left(\Delta - \frac{1}{c^2}\frac{\partial^2}{\partial t^2} - \tilde{k}_p^2\right)\boldsymbol{a} = 0 \tag{2.34}$$

where the effective plasma wavenumber $\tilde{k}_p$ contains all of the nonlinearities associated with the Lorentz factor $\gamma \approx (1+\boldsymbol{a}^2)^{1/2}$ and inhomogeneous plasma density due to the pre-formed plasma channel $n_0(r)$ and laser-driven wake $\delta n(r,\theta,z,t;\boldsymbol{a}^2)$. In writing this equation, we have again neglected the higher order source terms associated with the electrostatic response of the plasma. To solve this wave equation without making a paraxial approximation, we instead switch to a new coordinate system $\xi = z - ct$, $\eta = (z+ct)/2$, which yields

$$\left(2\frac{\partial^2}{\partial\xi\partial\eta} + \Delta_\perp - \tilde{k}_p^2\right)\boldsymbol{a} = 0\,. \tag{2.35}$$

Assuming linearly polarized light, we seek envelope solutions in the form $\boldsymbol{a} = [a\exp(ik_L\xi) + \text{c.c.}]\,\hat{x}/2$ where k_L is a constant. This yields the envelope PDE

$$\left[2\left(ik_L + \frac{\partial}{\partial\xi}\right)\frac{\partial}{\partial\eta} + \Delta_\perp - \tilde{k}_p^2\right]a(r,\theta,\xi,\eta) = 0\,. \tag{2.36}$$

We then take the Fourier transform in the variable ξ and apply the convolution theorem

$$\begin{aligned}
&\left[2i\left(k_L+k\right)\frac{\partial}{\partial\eta}+\Delta_\perp\right]a_k=\left(\tilde{k}_p^2\right)_k * a_k\,,\\
&a_k(r,\theta,k,\eta)=\frac{1}{\sqrt{2\pi}}\int_{-\infty}^{\infty}d\xi e^{-ik\xi}a(r,\theta,\xi,\eta)\,,\\
&(f*g)(k):=\frac{1}{\sqrt{2\pi}}\int_{-\infty}^{\infty}f(k')g(k-k')dk'
\end{aligned}\tag{2.37}$$

where we have included a $1/\sqrt{2\pi}$ normalization in the definition of the convolution for notational convenience. In the weakly relativistic limit, we can split $\tilde{k}_p^2(r,\theta,\xi,\eta)$ into separate contributions from the pre-formed axisymmetric plasma channel $n_0(r)$, the wake $\delta n(r,\theta,\xi,\eta)$, and the Lorentz factor $\gamma^{-1}=(1+\boldsymbol{a}^2)^{-1/2}\approx 1-|a|^2/4$

$$\left[i\frac{1+k/k_L}{k_L}\frac{\partial}{\partial\eta}+\frac{1}{2k_L^2}\Delta_\perp-\frac{k_{p0}^2}{2k_L^2}\frac{n_0}{n_{00}}\right]a_k=\frac{k_{p0}^2}{2k_L^2}\left(\frac{\delta n-n_0|a|^2/4}{n_{00}}\right)_k * a_k \tag{2.38}$$

where $k_{p0}^2=e^2n_{00}/m_e\epsilon_0c^2$ is the unperturbed on-axis plasma wavenumber. Inspecting this equation, we can see that we have recovered a k-dependent nonlinear Schrödinger equation in the spectral domain without having to make a paraxial approximation. We can therefore use many of the same techniques on this equation that we used earlier with the paraxial equation, but now also capture dispersive effects.

2.3.1 Group Velocity and Channel Mode Dispersion

Ignoring the wake and relativistic effects for now by setting the RHS of Eq. (2.38) to zero, we can see that substituting a matched parabolic channel of the form $n_0(r)=n_{00}+\Delta n(r/w_0)^2$ guides any linear combination of Laguerre-Gaussian modes of the

form

$$
\begin{aligned}
a_k^{pm}(r,\theta,k,\eta) &= \alpha_k^{pm}(k)\exp[-i\kappa_k^{pm}(k)\eta]\mathrm{LG}_{pm}(r,\theta)\,,\\
\kappa_k^{pm}(k) &= \left(2p+|m|+1+\frac{n_{00}}{\Delta n}\right)\frac{k_c}{1+k/k_L}\,,\\
\mathrm{LG}_{pm}(r,\theta) &= \sqrt{\frac{p!}{(p+|m|)!}}\left(\frac{\sqrt{2}\,r}{w_0}\right)^{|m|}\exp\left(-\frac{r^2}{w_0^2}+im\theta\right)L_p^{|m|}\left(\frac{2r^2}{w_0^2}\right)\,,\\
a_k(r,\theta,k,\eta) &= \sum_{p,m} a_k^{pm}(r,\theta,k,\eta)\,.
\end{aligned}
\tag{2.39}
$$

where $k_c = k_w/2 = 2/k_L w_0^2$ are the centroid and spot size oscillation wavenumbers respectively for the parabolic channel matched to a Gaussian pulse of spot size w_0. Note that we can recover the paraxial solution in Eq. (2.12) by setting $k/k_L = 0$. Assuming that $|k/k_L| \ll 1$ remains valid for the majority of the pulse a_k, (i.e. for pulse durations that are not too short relative to the laser cycle period), we can recover the group velocity of each mode by calculating the Laguerre-Gaussian mode solutions in ξ-space to first order in k/k_L

$$
\begin{aligned}
a_{pm}(r,\theta,\xi,\eta) &= \alpha_{pm}(\xi) * \left(\exp[-i\kappa_k^{pm}(k)\eta]\right)_\xi \mathrm{LG}_{pm}(r,\theta)\\
&\approx \alpha_{pm}(\xi) * \left(\exp[-i\kappa_0^{pm}(1-k/k_L)\eta]\right)_\xi \mathrm{LG}_{pm}(r,\theta)\\
&= \alpha_{pm}(\tilde{\xi}_{pm})\exp(-i\kappa_0^{pm}\eta)\mathrm{LG}_{pm}(r,\theta)\,,\\
\kappa_0^{pm}/k_L &= \frac{\omega_{p0}^2}{2k_L^2c^2} + (2p+|m|+1)\frac{2}{k_L^2 w_0^2}\,,\\
\tilde{\xi}_{pm}(\xi,\eta) &= \xi + \frac{\kappa_0^{pm}\eta}{k_L}
\end{aligned}
\tag{2.40}
$$

where $\alpha^{pm}(\xi)$ is the inverse Fourier transform of $\alpha_k^{pm}(k)$ and the convolution is taken in the variable ξ. This shows that the first order non-paraxial propagation effect amounts to a reduced overall group velocity and dispersion between channel modes due to the on-axis plasma density and finite spot size effects:

$$
\frac{v_g^{pm}}{c} = 1 - \frac{\kappa_0^{pm}}{k_L} = 1 - \frac{\omega_{p0}^2}{2k_L^2c^2} - (2p+|m|+1)\frac{2}{k_L^2 w_0^2}\,,
\tag{2.41}
$$

as well as a correction to the wavenumbers of the Laguerre-Gaussian modes. Likewise we get an increase of the superluminal phase velocity from both plasma and finite spot size effects

$$\frac{v_\phi^{pm}}{c} = 1 + \frac{\kappa_0^{pm}}{k_L} = 1 + \frac{\omega_{p0}^2}{2k_L^2 c^2} + (2p + |m| + 1)\frac{2}{k_L^2 w_0^2}\,. \tag{2.42}$$

We can see that for a pulse primarily in the fundamental mode, after every spot size oscillation the first radial mode ($p = 1$) will fall behind the fundamental mode by a laser wavelength (and similarly for centroid oscillations). Hence we eventually need to take this group velocity dispersion into account if the pulse propagates over many spot size oscillation periods in a long plasma channel.

2.3.2 Chromatic Dispersion

The second order $\sim k^2/k_L^2$ non-paraxial correction introduces chromatic dispersion effects, which can cause both dispersive broadening and chirping of the pulse. Formally, the second order correction modifies the shape and phase of the envelope via the following convolution in ξ

$$\begin{aligned} a_{pm}(r,\theta,\xi,\eta) &\approx \alpha_{pm}(\xi) * \left(\exp[-i\kappa_0^{pm}(1 - k/k_L + k^2/k_L^2)\eta]\right)_\xi \mathrm{LG}_{pm}(r,\theta) \\ &= \left[\alpha_{pm}(\tilde{\xi}_{pm}) * \frac{k_L \exp\left(-\frac{k_L^2\xi^2}{4i\kappa_0^{pm}\eta}\right)}{(2i\kappa_0^{pm}\eta)^{1/2}}\right] \exp(-i\kappa_0^{pm}\eta)\mathrm{LG}_{pm}(r,\theta)\,, \end{aligned} \tag{2.43}$$

which is akin to Gaussian blurring of the original envelope but with a Gaussian filter kernel with a purely imaginary variance that grows linearly with propagation distance $\sigma_{pm}^2(\eta) = 2i\kappa_0^{pm}\eta/k_L^2$. To gain some intuition for what this operation does, consider an originally unchirped pulse with a Gaussian temporal profile of the form

$$a_{pm}(r,\theta,\xi,\eta = 0) = a_{0,pm}e^{-\xi^2/L_0^2}\mathrm{LG}_{pm}(r,\theta)\,, \tag{2.44}$$

where $k_L L_0 \gg 1$ is necessary for $|k/k_L| \ll 1$ to be true for the majority of the pulse. Substituting this into Eq. (2.43) gives us the following expression describing how

this mode's temporal envelope evolves due to chromatic dispersion

$$a_{pm}(r,\theta,\xi,\eta) = a_{0,pm}\mathcal{Z}_{pm}^{-1/2}\exp\left(-\frac{\tilde{\xi}_{pm}^2}{\mathcal{Z}_{pm}L_0^2}\right)\exp(-i\kappa_0^{pm}\eta)\mathrm{LG}_{pm}(r,\theta)\,,$$
$$\mathcal{Z}_{pm}(\eta) = 1 + \frac{4i\kappa_0^{pm}\eta}{k_L^2 L_0^2}\,. \tag{2.45}$$

By taking the modulus of this expression we can see that chromatic dispersion causes the pulse duration of this originally unchirped pulse to grow as it propagates, and does so faster for higher order channel modes via finite spot size effects

$$L_{pm}(\eta) = L_0\left|\mathcal{Z}_{pm}(\eta)\right| = L_0\sqrt{1+\left(\frac{4\kappa_0^{pm}\eta}{k_L^2L_0^2}\right)^2}\,. \tag{2.46}$$

For example, for a laser pulse of wavelength $\lambda_L = 1030\,\mathrm{nm}$ propagating in a parabolic plasma channel with an on-axis plasma density of $n_{00} = 2.5\times10^{17}\,\mathrm{cm}^{-3}$ and a matched spot size of $w_0 = 30\,\mu\mathrm{m}$, considering only chromatic dispersion, the duration of an initially $t_{\mathrm{FWHM}} = 20\,\mathrm{fs}$ pulse in the fundamental Gaussian mode ($p = m = 0$) would increase by 10% after approximately 100 mm of propagation, and double in about 380 mm.

In combination with the temporal broadening, chromatic dispersion also causes a build-up of a negative linear chirp (instantaneous frequency decreasing over time), which we can recover by calculating the complex phase introduced by the convolution

$$\Delta\Phi^{pm} = \mathrm{Im}\left(-\frac{\tilde{\xi}_{pm}^2}{\mathcal{Z}_{pm}L_0^2}\right) + \arg\left(\mathcal{Z}_{pm}^{-1/2}\right) = \frac{4\kappa_0^{pm}\eta\tilde{\xi}_{pm}^2}{k_L^2L_0^4\left|\mathcal{Z}_{pm}(\eta)\right|^2} - \frac{1}{2}\arg\left(\mathcal{Z}_{pm}(\eta)\right)$$
$$\frac{\Delta\omega^{pm}}{k_Lc} = -\frac{1}{k_Lc}\frac{\partial\Delta\Phi^{pm}}{\partial t} = \frac{1}{k_L}\left[\left(1-\frac{\kappa_0^{pm}}{2k_L}\right)\frac{\partial}{\partial\tilde{\xi}_{pm}} - \frac{1}{2}\frac{\partial}{\partial\eta}\right]\Delta\Phi^{pm}$$
$$\approx \frac{8\kappa_0^{pm}\eta\tilde{\xi}_{pm}}{k_L^3L_0^4\left|\mathcal{Z}_{pm}(\eta)\right|^2}\,, \tag{2.47}$$

where we have assumed sufficiently long propagation such that $\eta \gg \tilde{\xi}_{pm}, L_0$. This shows that chromatic dispersion makes the head/tail of the pulse blue-/red-shift proportional to propagation distance. It also shows that the chirp accumulated by

this pulse is bounded by $\Delta\omega^{pm}/k_L c \leq \tilde{\xi}_{pm}/k_L L_0^2$ with equality at $\eta = k_L^2 L_0^2/4\kappa_0^{pm}$, which corresponds to 220 mm of propagation for the aforementioned laser-plasma parameters as shown in Figure 2.4.

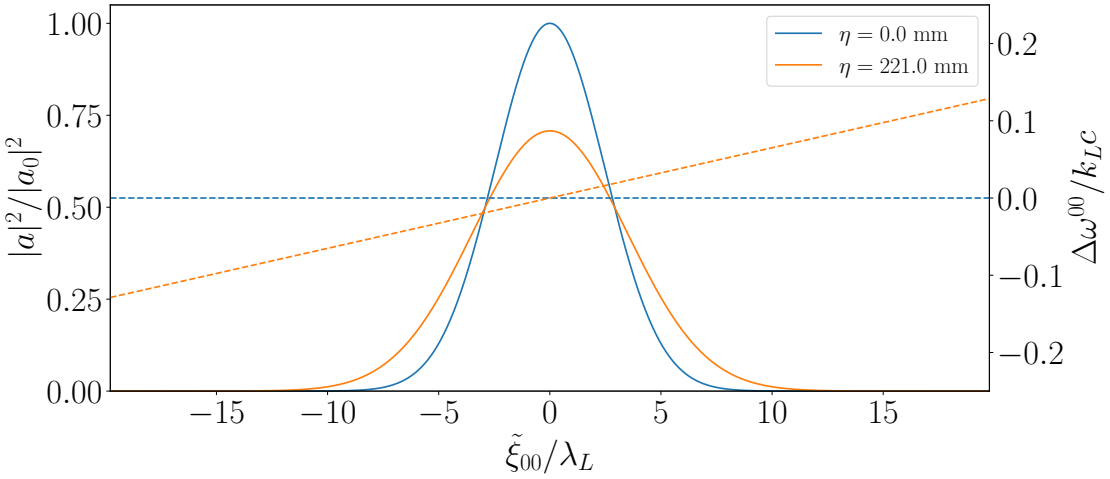


Figure 2.4: Effect of chromatic dispersion on a temporally Gaussian pulse in the fundamental channel mode $p = m = 0$ with initial duration $t_{\mathrm{FWHM}} = 20\,\mathrm{fs}$ and wavelength $\lambda_L = 1030\,\mathrm{nm}$ propagating in a parabolic plasma channel with on-axis density $n_{00} = 2.5 \times 10^{17}\,\mathrm{cm}^{-3}$ and matched spot size $w_0 = 30\,\mu\mathrm{m}$. Chromatic dispersion will broaden the pulse envelope width (solid) of the initially unchirped pulse, and introduce a negative linear chirp, where the instantaneous frequency (dashed) decreases linearly over time.

2.3.3 Time-Dependent Perturbation Theory

As we did before in the paraxial case, we can also apply time-dependent perturbation theory to the non-paraxial description as Eq. (2.38) also takes the form of a nonlinear Schrödinger equation. However, because we are working in the spectral domain, the perturbative term involves a convolution with the complex spectral envelope a_k rather than a simple multiplication. Taking this into account, we again rewrite the

spectral non-paraxial wave equation Eq. (2.38) in nonlinear Schrödinger form

$$\begin{aligned}
&\frac{i(1+k/k_L)}{k_L}\frac{\partial a_k}{\partial \eta} = H_0 a_k + (V_1)_k * a_k \,, \\
&H_0 = -\frac{k_{p0}^2}{2k_L^2}\Delta_\perp + V_0 \,, \\
&V_0(r) = \frac{k_{p0}^2}{2k_L^2}\frac{n_0(r)}{n_{00}} \,, \\
&(V_1)_k(r,\theta,k;|a|^2) = \frac{k_{p0}^2}{2k_L^2}\left(\frac{\delta n(r,\theta,\xi;|a|^2)}{n_{00}} - \frac{n_0(r)}{n_{00}}|a|^2/4\right)_k \,.
\end{aligned} \tag{2.48}$$

We again use bra-ket notation to describe the channel modes and apply the method of variation of constants to retrieve the following set of coupled nonlinear PDEs governing the evolution of the complex spectral amplitudes $\alpha_k^{pm}(k,\eta)$

$$\begin{aligned}
&\frac{i(1+k/k_L)}{k_L}\frac{\partial \alpha_k^{pm}(k,\eta)}{\partial \eta} = \sum_{p'm'} \langle pm| \, (V_1)_k * \left(\alpha_k^{p'm'}(k,\eta) e^{-i\kappa_k^{p'm'}(k)\eta}\right) |p'm'\rangle \, e^{i\kappa_k^{pm}\eta} \,, \\
&|a|^2 = \left| \sum_{p,m} \left(\alpha_k^{pm}(k,\eta) e^{-i\kappa_k^{pm}(k)\eta}\right)_\xi \langle r,\theta|pm\rangle \right|^2 \,.
\end{aligned} \tag{2.49}$$

Note that we cannot take the channel mode phase term $e^{-i\kappa_k^{p'm'}(k)\eta}$ out of the expectation value due to the convolution in the variable k. From here, we can make similar arguments as we did for the paraxial case to reduce this to a 4-level system or 2-level system for the axisymmetric case with the majority of light in the fundamental mode $p = m = 0$.

2.3.4 Stimulated Raman Scattering

We will now demonstrate how the non-paraxial time-dependent perturbation theory derived in Eq. (2.49) can be applied by deriving stimulated Raman scattering (SRS). Raman scattering occurs due to a feedback loop between a pump laser exciting a plasma wave, and that plasma wave causing local variations in the group and phase velocities which stretches and compresses regions of the pump vector potential, forming a longitudinal modulation that drives a larger plasma wave. Considering Raman scattering only in the forward direction (RFS), we only need to consider

light in the fundamental channel mode $\alpha_k^{00}(k,\eta)$. Assuming a parabolic channel and a sufficiently large spot size $k_{p0}^2 w_0^2/4 \gg 1$ such that the plasma response can be described in the 1D limit, this reduces Eq. (2.49) and the plasma response to the following system of PDEs governing only the complex spectral amplitude of the fundamental mode

$$\begin{aligned}
&\frac{i(1+k/k_L)}{k_L}\frac{\partial \alpha_k^{00}(k,\eta)}{\partial \eta} = \langle 00|\,(V_1)_k * \left(\alpha_k^{00}(k,\eta)e^{-i\kappa_k^{00}\eta}\right)|00\rangle\, e^{i\kappa_k^{00}\eta}\,,\\
&|a|^2 = \left|\left(\alpha_k^{00}(k,\eta)e^{-i\kappa_k^{00}(k)\eta}\right)_\xi\right|^2 \mathrm{LG}_{00}^2\,,\\
&(V_1)_k = \frac{k_{p0}^2}{2k_L^2}\frac{\delta n_k}{n_{00}}\,,\\
&\left(-k^2 - ik\frac{\partial}{\partial\eta} + \frac{1}{4}\frac{\partial^2}{\partial\eta^2} + k_{p0}^2\right)\frac{\delta n_k}{n_{00}} = \left(-k^2 + ik\frac{\partial}{\partial\eta} + \frac{1}{4}\frac{\partial^2}{\partial\eta^2}\right)\frac{(|a|^2)_k}{4}\,,
\end{aligned} \tag{2.50}$$

If we treat the laser pulse as an initially infinitely long monochromatic pump of amplitude a_0, then we can write its complex spectral amplitude in the following form

$$\alpha_k^{00}(k,\eta) = a_0\sqrt{2\pi}\delta(k) + \Delta\alpha_k^{00}(k,\eta)\,, \tag{2.51}$$

where the inverse Fourier transform of the propagation-varying part of the complex amplitude is small relative to the pump amplitude $\Delta\alpha_{00}(\xi,\eta) \ll a_0$. This then allows us to write the Fourier transform of the intensity modulation to first order

$$\begin{aligned}
(|a|^2)_k &= \left(\left|\left(\alpha_k^{00}(k,\eta)e^{-i\kappa_k^{00}(k)\eta}\right)_\xi\right|^2\right)_k \mathrm{LG}_{00}^2\,,\\
&= \left(\alpha_k^{00}e^{-i\kappa_k^{00}\eta}\right) * \left(\alpha_k^{00}e^{-i\kappa_k^{00}\eta}\right)^* \mathrm{LG}_{00}^2\,,\\
&= \left((a_0\sqrt{2\pi}\delta(k) + \Delta\alpha_k^{00})e^{-i\kappa_k^{00}\eta}\right) * \left((a_0\sqrt{2\pi}\delta(k) + \Delta\alpha_k^{00})e^{-i\kappa_k^{00}\eta}\right)^* \mathrm{LG}_{00}^2\,,\\
&\approx \left[a_0^2\sqrt{2\pi}\delta(k) + a_0\left(\Delta\alpha_k^{00}e^{-i(\kappa_k^{00}-\kappa_0^{00})\eta} + \text{c.c.}\right)\right]\mathrm{LG}_{00}^2\,.
\end{aligned} \tag{2.52}$$

Likewise, substituting this form of the complex spectral amplitude into Eq. (2.50) to first order yields the following PDE governing the growth of $\Delta\alpha_k^{00}$ due to the

presence of a plasma wave

$$\frac{i(1+k/k_L)}{k_L}\frac{\partial\Delta\alpha_k^{00}}{\partial\eta}e^{-i(\kappa_k^{00}-\kappa_0^{00})\eta}=\frac{k_{p0}^2a_0}{2k_L^2}\left\langle 00\right|\frac{\delta n_k}{n_{00}}\left|00\right\rangle\,. \tag{2.53}$$

We then expand to first order in $k/k_L \ll 1$, which captures modulations in group and phase velocity but neglects higher order effects like chromatic dispersion

$$\begin{aligned}\kappa_k^{00}-\kappa_0^{00}&=-k\left(\frac{k_c}{k_L}+\frac{k_{p0}^2}{2k_L^2}\right),\\ \frac{\partial\Delta\alpha_k^{00}}{\partial\eta}e^{-i(\kappa_k^{00}-\kappa_0^{00})\eta}&=-i(1-k/k_L)\frac{k_{p0}^2a_0}{2k_L}\left\langle 00\right|\frac{\delta n_k}{n_{00}}\left|00\right\rangle\,.\end{aligned} \tag{2.54}$$

For RFS in underdense plasma, we assume that we are in the regime where $\partial/\partial\eta \gg (\kappa_k^{00}-\kappa_0^{00})$, which we can confirm later once we have derived the RFS growth rate. This allows us to write the growth of the Fourier transform of the intensity modulation in the following form

$$\begin{aligned}\frac{\partial}{\partial\eta}(|a|^2)_k&=a_0\left[\left(\frac{\partial\Delta\alpha_k^{00}}{\partial\eta}-i(\kappa_k^{00}-\kappa_0^{00})\Delta\alpha_k^{00}\right)e^{-i(\kappa_k^{00}-\kappa_0^{00})\eta}+\text{c.c.}\right]\mathrm{LG}_{00}^2\\ &\approx a_0\left[\frac{\partial\Delta\alpha_k^{00}}{\partial\eta}e^{-i(\kappa_k^{00}-\kappa_0^{00})\eta}+\text{c.c.}\right]\mathrm{LG}_{00}^2\\ &=\frac{k_{p0}^2a_0^2}{2k_L}\left[-i(1-k/k_L)\left\langle 00\right|\frac{\delta n_k}{n_{00}}\left|00\right\rangle+\text{c.c.}\right]\mathrm{LG}_{00}^2\\ &=\frac{k_{p0}^2a_0^2}{2k_L}(-i+ik/k_L)\left\langle 00\right|\frac{\delta n_k}{n_{00}}-\frac{\delta n_{-k}}{n_{00}}\left|00\right\rangle\mathrm{LG}_{00}^2\,,\end{aligned} \tag{2.55}$$

where we have used the conjugate symmetry property $\delta n_k^* = \delta n_{-k}$ as δn is real. For the fastest growing mode, we are only interested in the growth of the Stokes $k = -k_{p0}$ and anti-Stokes $k = k_{p0}$ sidebands. Applying the quasistatic approximation $k_{p0} \gg \partial/\partial\eta$ then simplifies the plasma response equation in Eq. (2.50) to

$$\pm ik_{p0}\frac{\partial}{\partial\eta}\frac{\delta n_{\pm k_{p0}}}{n_{00}}=k_{p0}^2\frac{(|a|^2)_{\pm k_{p0}}}{4}\,. \tag{2.56}$$

Substituting this into Eq. (2.55) then yields the familiar forward Raman scattering growth rate [74]

$$c^2 \frac{\partial^2}{\partial \eta^2} \left[(|a|^2)_{k_{p0}} + (|a|^2)_{-k_{p0}} \right] = \gamma_{\mathrm{RFS}}^2 \left[(|a|^2)_{k_{p0}} + (|a|^2)_{-k_{p0}} \right] ,$$
$$\gamma_{\mathrm{RFS}} = \frac{c k_{p0}^2 a_0}{2\sqrt{2}\, k_L} = \frac{\omega_{p0}^2 a_0}{2\sqrt{2}\, \omega_L} , \tag{2.57}$$

where we have used the identity $\langle 00| \, \mathrm{LG}_{00}^2 \, |00\rangle = 1/2$ in a parabolic channel.

2.4 Ionization Effects

So far we have only considered laser pulse propagation in fully pre-ionized plasma channels. However, in reality the channel guiding profile may be dominated by the neutral gas collar formed by a HOFI channel which gets ionized by the input laser pulse. This introduces a nonlinearity where the transverse tails of the pulse intensity determine the degree of ionization of the neutral gas collar, which then change the guiding properties of the channel which, in turn, influences the transverse intensity profile of the tails of the pulse. In this section we will provide an overview of ionization models. We then describe how ionization can influence the evolution of laser pulses in plasma channels and provide a few examples.

2.4.1 Ionization Models

The $\lambda_L \sim 1\,\mu\mathrm{m}$ high-power laser systems used for LWFA cannot resonantly ionize the neutral gas to form a plasma due to their low $\sim 1.2\,\mathrm{eV}$ photon energies. Instead, ionization occurs via the optical field ionization (OFI) mechanism. This process can be better understood when separated into two perturbative regimes and one non-perturbative regime. At low intensities and high laser frequencies, ionization is described by the multi-photon regime (MPI), where the atom simultaneously absorbs multiple photons, occurring over many laser cycles. At high intensities and/or low laser frequencies, ionization shifts to the tunneling regime (TI), where the electric field is sufficiently strong such that the electron tunnels out of the atomic potential

faster than a single laser cycle. At very high intensities, regardless of the laser frequency, the electric field is so strong that it completely suppresses the atomic potential barrier, causing barrier suppression ionization (BSI).

Ammosov-Delone-Krainov (ADK) theory [75] describes ionization exclusively in the TI regime, whilst the more general Perelomov-Popov-Terent'ev (PPT) theory [76] describes ionization throughout the TI and MPI regimes. Note that these are both perturbative theories, and do not accurately describe the non-perturbative BSI regime. Sticking to the perturbative regimes for now, to determine whether we require ADK or PPT theory to describe ionization, we introduce the Keldysh adiabaticity parameter γ_{K} [77]

$$\begin{aligned} \gamma_{\mathrm{K}} &= \frac{\omega_L}{\omega_t}\,, \\ \omega_t &= \frac{e|E|}{\sqrt{2m_e U_i}} \end{aligned} \tag{2.58}$$

where ω_t is the tunneling frequency, $|E|$ is the laser electric field amplitude and U_i is the ionization energy of the electron. The Keldysh parameter determines whether ionization occurs either via TI ($\gamma_{\mathrm{K}} \ll 1$) or MPI ($\gamma_{\mathrm{K}} \gg 1$). Rewriting this expression in more convenient units yields

$$\gamma_{\mathrm{K}} = \frac{\alpha\sqrt{2U_i[E_{\mathrm{h}}]}}{|a|} \tag{2.59}$$

where $E_{\mathrm{h}} = \alpha^2 m_e c^2 = 27.2\,\mathrm{eV}$ is the atomic unit for energy and $\alpha \approx 1/137$ is the fine structure constant. Assuming atomic hydrogen $U_i = U_{\mathrm{H}} = 13.6\,\mathrm{eV}$, this expression tells us that regions of a laser pulse with normalized vector potential exceeding $a \gtrsim 0.1$ ionize in the TI regime, whilst regions below $a \lesssim 0.01$ ionize in the MPI regime.

ADK Theory

For simplicity we will only be considering monatomic hydrogen in these discussions. The instantaneous tunneling rate of hydrogen is given by [77]

$$W_i = 4\omega_a \frac{E_a}{|E(t)|} \exp\left(-\frac{2E_a}{3|E(t)|}\right) \tag{2.60}$$

where $E_a = 5.14 \times 10^{11}\,\mathrm{V/m}$ is the atomic unit for electric field, and $\omega_a = 4.13 \times 10^{16}\,\mathrm{s}^{-1}$ is the atomic unit for frequency. Taking the laser-cycle average for linearly polarized light $E(t) = E\cos(\omega_L t)$ then yields

$$W_i = 4\omega_a \left(\frac{3E_a}{\pi E}\right)^{1/2} \exp\left(-\frac{2E_a}{3E}\right), \tag{2.61}$$

which we can rewrite in a more useful form for LWFA

$$\begin{aligned} W_i(a) &= 4\omega_a \left(\frac{3E_a}{\pi E_L}\right)^{1/2} |a|^{-1/2} \exp\left(-\frac{2E_a}{3E_L}|a|^{-1}\right), \\ E_L &= \frac{m_e \omega_L c}{e}. \end{aligned} \tag{2.62}$$

To get a handle for typical ionization rates, consider the example $E_a/E_L = 0.165$ for $\lambda_L = 1030\,\mathrm{nm}$ which yields

$$W_i^{1030\mathrm{nm}}(a) = 1.58\,\omega_a |a|^{-1/2} \exp\left(-0.11\,|a|^{-1}\right). \tag{2.63}$$

Comparing this ionization rate with the plasma period gives

$$W_i^{1030\,\mathrm{nm}}(a) T_p = 2.4 \times 10^4 \left(\frac{n_e}{1 \times 10^{17}\,\mathrm{cm}^{-3}}\right)^{-1/2} |a|^{-1/2} \exp\left(-0.11\,|a|^{-1}\right). \tag{2.64}$$

Substituting $a > 0.1$, which is necessary for ADK to apply, yields $W_i^{1030\,\mathrm{nm}} T_p > 2.5 \times 10^4$ at $n_e = 1 \times 10^{17}\,\mathrm{cm}^{-3}$, meaning that ionization in sufficiently intense regions where ADK applies is effectively instantaneous for LWFA. We therefore should apply corrections from PPT theory to accurately capture ionization in the lower intensity regions where $a < 0.1$.

PPT Theory

To accurately calculate the ionization rate in regions where $a < 0.1$, we require the more general PPT theory, which is valid throughout the TI to MPI regimes. For linearly polarized light, this is given by [76, 78]

$$W_i = 4\omega_a \left(\frac{3E_a}{\pi E}\right)^{1/2} \left(\sqrt{1+\gamma_{\mathrm{K}}^2}\right)^{3/2} A(\omega_L, \gamma_{\mathrm{K}}) \exp\left(-\frac{2E_a}{3E} g(\gamma_{\mathrm{K}})\right) \tag{2.65}$$

where

$$\begin{aligned}
g(\gamma_{\mathrm{K}}) &= \frac{3}{2\gamma_{\mathrm{K}}}\left[\left(1+\frac{1}{2\gamma_{\mathrm{K}}^2}\right)\operatorname{arcsinh}(\gamma_{\mathrm{K}}) - \frac{1}{\beta}\right], \\
A(\omega_L, \gamma_{\mathrm{K}}) &= \frac{4}{\sqrt{3\pi}} \frac{\gamma_{\mathrm{K}}^2}{1+\gamma_{\mathrm{K}}^2} \sum_{n\geq\nu}^{\infty} e^{-\alpha(n-\nu)} f\left(\sqrt{\beta(n-\nu)}\right), \\
f(x) &= \frac{x}{2}\int_0^1 \frac{e^{-x^2 t}}{\sqrt{1-t}} dt = \frac{\sqrt{\pi}}{2} e^{-x^2} \operatorname{erfi}(x), \\
\nu &= \frac{\omega_a}{2\omega_L}\left(1+\frac{1}{2\gamma_{\mathrm{K}}^2}\right), \\
\alpha &= 2\left[\operatorname{arcsinh}(\gamma_{\mathrm{K}}) - \frac{\beta}{2}\right], \\
\beta &= \frac{2\gamma_{\mathrm{K}}}{\sqrt{1+\gamma_{\mathrm{K}}^2}}
\end{aligned} \tag{2.66}$$

where ν is the minimum number of photons required for MPI (in hydrogen) and $\operatorname{erfi}(z) = -i\operatorname{erf}(iz)$ is the imaginary error function. In Figure 2.5, we provide a comparison between the ADK and PPT models for field strengths relevant to LWFA laser pulses. In the $\gamma_{\mathrm{K}} \ll 1$ regime, this reduces to the cycle-averaged ADK model in Eq. (2.61) as expected. In the opposite $\gamma_{\mathrm{K}} \gg 1$ regime, the PPT ionization rate

reduces to

$$g(\gamma_{\mathrm{K}} \gg 1) = \frac{3}{2\gamma_{\mathrm{K}}}\left(\ln 2\gamma_{\mathrm{K}} - \frac{1}{2}\right),$$
$$A(\omega_L, \gamma_{\mathrm{K}} \gg 1) = \frac{4}{\sqrt{3\pi}}\left(\frac{2\gamma_{\mathrm{K}}}{e}\right)^{-2\delta} f\left(\sqrt{2\delta}\right) = \frac{2^{1-2\delta}\mathrm{erfi}\left(\sqrt{2\delta}\right)}{\sqrt{3}}(\gamma_{\mathrm{K}})^{-2\delta},$$
$$W_i(\gamma_{\mathrm{K}} \gg 1) = 4\omega_a\left(\frac{3E_a}{\pi E}\right)^{1/2}\frac{2^{1-2\delta}\mathrm{erfi}\left(\sqrt{2\delta}\right)}{\sqrt{3}}(\gamma_{\mathrm{K}})^{3/2-2\delta}\exp\left(-\frac{E_a}{E\gamma_{\mathrm{K}}}\left(\ln 2\gamma_{\mathrm{K}} - \frac{1}{2}\right)\right) \tag{2.67}$$

where $\delta = \lceil\nu\rceil - \nu$. This produces ionization rates at low intensities but higher than ADK would predict.

Barrier Suppression Ionization

Accurately modeling BSI typically requires a full numerical treatment of the time-dependent Schrödinger equation, as most perturbative methods do not work in this regime. It occurs when the laser pulse electric field exceeds the following threshold amplitude [79, 80]

$$E_{\mathrm{BSI}} = E_a\frac{(U_i/U_{\mathrm{H}})^2}{16Z} = \frac{U_i^2}{4Ze\alpha\hbar c} \tag{2.68}$$

where Ze is the charge of the atomic core and $E_a = 5.14\times10^{11}\,\mathrm{V/m}$ is the atomic unit for electric field. Rewriting this in more convenient units yields the BSI threshold of the laser normalized vector potential

$$a_{\mathrm{BSI}} = \frac{\alpha^3 m_e c^2 U_i [E_{\mathrm{h}}]^2}{4Z\hbar\omega_L}. \tag{2.69}$$

Considering a laser wavelength of $\lambda_L = 1030\,\mathrm{nm}$ ionizing atomic hydrogen yields a BSI threshold normalized vector potential of only $a_{\mathrm{BSI}} = 0.01$. Therefore the vast majority of a laser pulse with a peak a_0 on the order of unity would exceed the BSI threshold. Attempting to apply normal ADK theory would actually overestimate the ionization rate when used with fields exceeding the barrier potential

[81]. However, due to the utility of having reduced models in PIC simulations for evaluating ionization fractions over reasonable timesteps, several over-barrier corrections to ADK theory have been proposed and implemented [80, 82].

For example, by working in the strong-field limit ($E \gg E_{\mathrm{BSI}}$), Kostyukov and Golovanov [80] proposed the following simplified piecewise model for use in PIC codes simulating short highly intense laser pulses

$$W_i(E) = \begin{cases} W_i^{\mathrm{ADK}}(E)\,, & E < E_1\,, \\ 0.8\,\omega_a (E/E_a)\sqrt{(U_{\mathrm{H}}/U_i)}\,, & E > E_1 \end{cases} \tag{2.70}$$

where E_1 is chosen as the lower-amplitude intersection between the ADK curve and the strong-field limit BSI line. This model prevents the ADK theory from over-estimating the ionization rate in the BSI regime.

We present the ADK, PPT and Kostyukov–Golovanov models applied to the ionization of atomic hydrogen in Figure 2.5 for laser field amplitudes relevant to LWFA. Although perturbative OFI theories do not formally work when evaluating ionization rates at the peak field strength for LWFA laser drivers, this does not mean they are not applicable to LWFA. Firstly, the laser pulse does not turn on instantaneously, so the lower amplitude at the head of the pulse will cause ionization in the perturbative regime. Secondly, when considering pulse propagation in HOFI channels, the neutral gas collar resides at least over a spot size away from the axis (if not several), which also reduces the field strength to below the BSI threshold. Therefore perturbative OFI theories can still accurately capture ionization physics in LWFA despite the high peak electric fields involved.

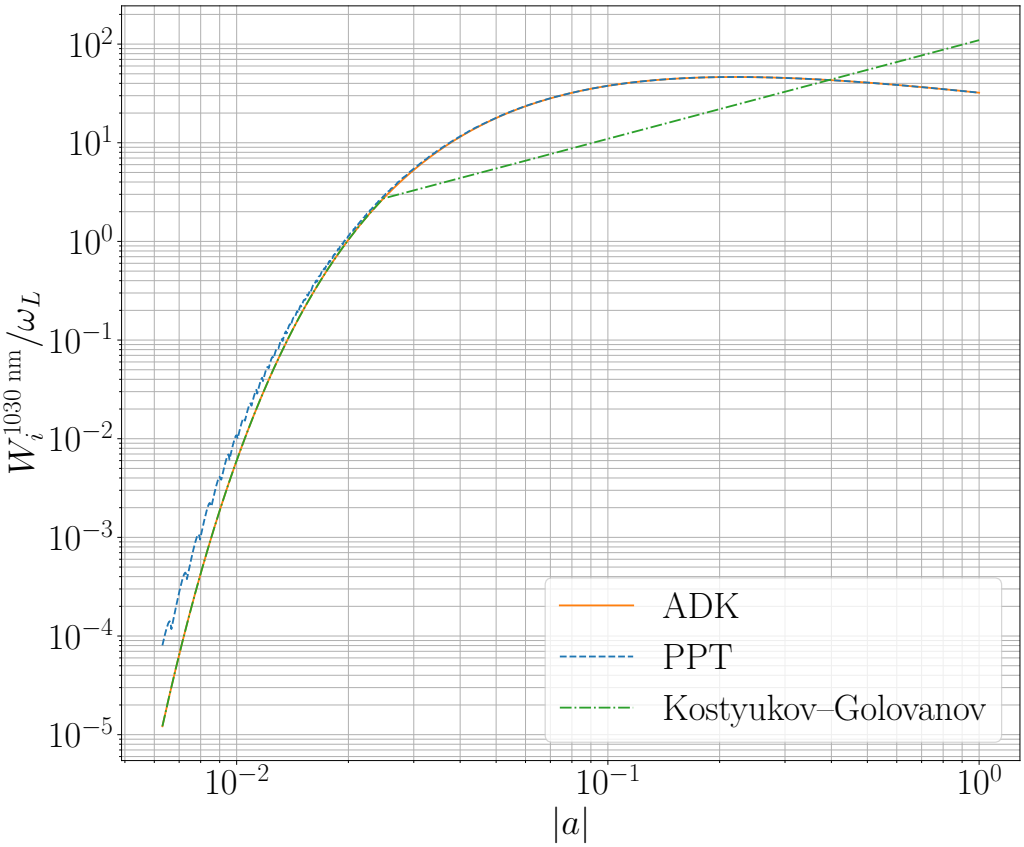


Figure 2.5: Comparison between the ADK, PPT, and the piecewise Kostyukov–Golovanov BSI [80] ionization models for atomic hydrogen for a linearly polarized laser pulse of wavelength $\lambda_L = 1030\,\text{nm}$. The PPT and ADK models agree well with each other for field amplitudes relevant to LWFA, and only start to appreciably diverge at amplitudes below $a \lesssim 0.01$ as it enters the MPI regime. For field amplitudes well exceeding $a \gtrsim 0.02$, the ionization rate becomes much greater than the laser cycle frequency, and can therefore be treated as effectively instantaneous as far physics relevant to LWFA is concerned.

2.4.2 Ionization-induced Nonlinearities

No matter which OFI theory we choose to apply, they will each yield an instantaneous rate of ionization $W_i\left(E(\boldsymbol{x}, t)\right)$, which we substitute into the time-dependent equation for the newly ionized electron density N

$$\frac{\partial N}{\partial t} = W_i(N - N_0) \tag{2.71}$$

where N_0 is the initial density of neutrals. In the timescales involved in LWFA in HOFI channels, we can safely assume that the neutral gas collar $N_0(r)$ is perfectly static and determined only by the pre-formed channel. For a complete pulse propagation theory including ionization of neutrals, we can couple this expression to Eq. (2.1). To see how this affects pulse propagation, we switch to co-moving coordinates and take the quasistatic approximation. We will also assume that the ionization rate is in laser-cycle-averaged form $W_i(|a|)$, which gives

$$\begin{aligned}
&\frac{\partial N}{\partial t} \approx -c\frac{\partial N}{\partial \xi} = W_i(N - N_0) \\
&\Rightarrow \frac{N(r,\xi;|a|)}{N_0(r)} = \frac{-\int_\infty^\xi \exp\left(-\int_\infty^{\xi''} W_i(|a(r,\xi')|)\frac{d\xi'}{c}\right) W_i(|a(r,\xi'')|)\frac{d\xi''}{c}}{\exp\left(-\int_\infty^\xi W_i(|a(r,\xi')|)\frac{d\xi'}{c}\right)} .
\end{aligned} \tag{2.72}$$

In the special case of a constant beam, where $|a|$ has no ξ-dependence, the degree of ionization expression reduces to

$$\frac{N(r,\xi;|a|)}{N_0(r)} = 1 - \exp\left(\frac{W_i\left(|a|(r)\right)\xi}{c}\right) . \tag{2.73}$$

where $\xi = 0$ is set to be at the head of the beam.

Self-conditioning Nonlinearity

Due to the intensity-dependence on ionization rate, there can be a strong radial and longitudinal variation in the degree of conditioning of the neutral gas collar that surrounds a HOFI channel [37], which will change the guiding properties and hence transverse dynamics along the laser envelope. In fact, the degree of ionization rate equation in Eq. (2.71) predicts a very strong, nearly step-wise, radial dependence on the degree of ionization. To see why, consider propagating a continuous wave Gaussian beam with normalized vector potential a_0 and spot size w_0 into some

neutral hydrogen gas. The radial dependence on the ionization rate will be given by

$$W_i(r) = 4\omega_a \left(\frac{E_a}{a_0 E_L}\right)^{1/2} e^{r^2/2w_0^2} \exp\left(-\frac{2E_a}{3a_0 E_L} e^{r^2/w_0^2}\right),$$
$$\frac{N(r,\xi)}{N_0(r)} = 1 - \exp\left(\frac{W_i(r)\xi}{c}\right). \tag{2.74}$$

As we go further behind the head of the beam, making ξ more negative, the degree of ionization increases and eventually saturates to 1. The $1/e$ lengthscale at which this occurs will be defined as the ionization threshold distance ξ_i

$$\xi_i \equiv \frac{c}{W_i} = \frac{c}{4\omega_a}\left(\frac{E_a}{a_0 E_L}\right)^{-1/2} e^{-r^2/2w_0^2} \exp\left(\frac{2E_a}{3a_0 E_L} e^{r^2/w_0^2}\right). \tag{2.75}$$

Due to the double exponential growth of the ionization lengthscale with radius, as long as ionization still occurs at least one spot size away, it is often justifiable to model the degree of ionization as a radial step function

$$\frac{N(r,\xi)}{N_0(r)} \approx \begin{cases} 1 & |\xi|/\xi_i(r) > 1 \\ 0 & |\xi|/\xi_i(r) < 1 \end{cases} \tag{2.76}$$

which is akin to a simple threshold intensity ionization model. According to both the PPT and ADK ionization models, at a plasma density of $n_e \sim 1\times10^{17}\,\mathrm{cm}^{-3}$, the ionization rate of atomic hydrogen by a $\lambda_L = 1030\,\mathrm{nm}$ laser pulse is approximately equal to the plasma frequency when $a \approx 0.01$. Since the rate of ionization is exponentially sensitive to the field amplitude, it is often reasonable to implement such an intensity-threshold ionization model when describing the transverse dynamics of the laser pulse, where ionization occurs immediately when the threshold $a > 0.01$ is met. An example snapshot of radially- and longitudinally-dependent conditioning is presented in Figure 2.6 using ADK theory for the ionization rate.

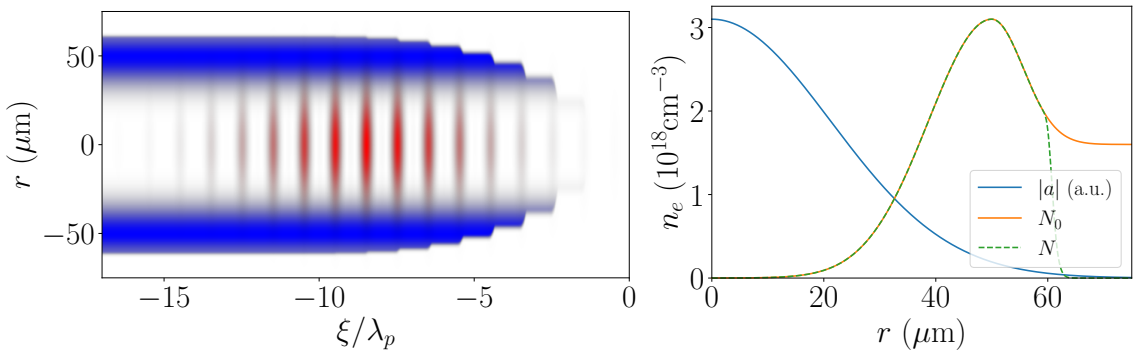


Figure 2.6: Neutral gas collar ionization of a toy HOFI channel model using ADK theory, excluding ponderomotive forces. (Left) a transversally Gaussian pulse train (amplitude in red) of total energy 2 J, $\lambda_L = 1030\,\text{nm}$ wavelength and $w_0 = 30\,\mu\text{m}$ spot size propagating in a HOFI channel with on-axis density $n_{00} = 2.5 \times 10^{17}\,\text{cm}^{-3}$ ionizes a neutral gas collar of atomic hydrogen (density in blue). (Right) Transverse profiles of the normalized laser vector potential $|a|$ (blue), original density of neutral hydrogen N_0 (orange) and ionized electrons N (green, dashed) at the back of the pulse train. We can see that the front low-energy pulses only partially ionize the neutral gas, and would therefore be expected to diffract away as they propagate, whilst the trailing pulses remain guided. For this neutral collar profile, assuming stable laser pulse propagation we expect a depletion rate via photon absorption of $\sim 45\,\text{mJ/m}$.

Photon Absorption

Apart from the intensity-dependent conditioning influencing the transverse dynamics of the laser pulse, we also need to consider the depletion rate associated with photon absorption. The instantaneous depletion rate due to photon absorption is straightforwardly given by

$$P_{\text{dp},i} = \int W_i(N - N_0)U_i dV\,. \tag{2.77}$$

For a ballpark calculation for depletion rates associated with conditioning, ionizing a neutral gas collar of atomic hydrogen of uniform density $n_\text{H} = 5 \times 10^{18}\,\text{cm}^{-3}$, radius $R = 60\,\mu\text{m}$ and thickness $d = 10\,\mu\text{m}$ corresponds with a photon absorption energy depletion rate of $40\,\text{mJ/m}$. Since the laser pulses we usually consider for LWFA are on the joule-scale and propagate over a few 100 mm, this type of depletion is typically not relevant to us.

Ionization-induced Blue-shifting and Defocusing

Due to the short but finite time over which ionization occurs, OFI ionization by an ultrashort laser pulse will produce a co-propagating density down-ramp which will cause local blue-shifting of light [83, 84]. The result from this process seems similar to photon acceleration, but fundamentally differs as photons are initially absorbed in order to ionize the neutrals to form this ramp.

Ionization of neutrals can also lead to increased rates of defocusing in some cases. Consider an ultrashort Gaussian laser pulse propagating in a neutral atomic gas. Because of its intensity drop-off with radius, the degree of ionization at the head of the pulse will always be higher on-axis then away from axis. This forms an inverse plasma channel, which provides defocusing which "etches" away the head of the pulse by increased diffraction [84, 85].

2.5 Wigner Distribution Formalism

It is often convenient to describe the laser pulse dynamics in terms of the Wigner-Ville distribution [86, 87], as it allows us to apply phase-space conservation arguments to the laser envelope. We will be using the non-paraxial description, and will assume that the polarization of the pulse is mostly transverse to the propagation direction. Consider an EM wave propagating in free space of the form

$$\boldsymbol{a}(x,y,\xi,\eta) = \left[a(x,y,\xi,\eta)e^{ik_0\xi} + \text{c.c.}\right]\hat{e}_L/2\,, \tag{2.78}$$

where $\hat{e}_L$ is the laser polarization and we have shifted coordinates to $\xi = z - ct$ and $\eta = (z + ct)/2$. Substituting this into the 3D wave equation exactly yields the following envelope equation

$$\left[2\left(ik_0 + \frac{\partial}{\partial\xi}\right)\frac{\partial}{\partial\eta} + \Delta_\perp\right]a = 0\,. \tag{2.79}$$

We then take the Fourier transform in the variable ξ, yielding a paraxial wave equation in Fourier space:

$$\left[2i\left(k_0+k_\xi\right)\frac{\partial}{\partial\eta}+\Delta_\perp\right]\hat{a}(x,y,k_\xi,\eta)=0\,,$$
$$\hat{a}(x,y,k_\xi,\eta)=\frac{1}{\sqrt{2\pi}}\int_{-\infty}^{\infty}a(x,y,\xi,\eta)e^{-ik_\xi\xi}d\xi\,. \tag{2.80}$$

The Wigner(-Ville) distribution corresponding to the complex spectral envelope $\hat{a}(\boldsymbol{x}_\perp,k_\xi,\eta)$ is defined as

$$W_{\hat{a}}(\boldsymbol{x}_\perp,\boldsymbol{k}_\perp,k_\xi,\eta)=$$
$$\frac{1}{2\pi}\int\hat{a}(\boldsymbol{x}_\perp+\boldsymbol{s}_\perp/2,k_\xi,\eta)\hat{a}^*(\boldsymbol{x}_\perp-\boldsymbol{s}_\perp/2,k_\xi,\eta)\exp(-i\boldsymbol{k}_\perp\cdot\boldsymbol{s}_\perp)d\boldsymbol{s}_\perp\,, \tag{2.81}$$

where $\boldsymbol{x}_\perp=(x,y)$, $\boldsymbol{s}_\perp=(s_x,s_y)$ and $\boldsymbol{k}_\perp=(k_x,k_y)$. Some general properties of the Wigner distribution for some complex analytic signal $\psi(\boldsymbol{x}_\perp,t)$ include:

$$W_\psi(\boldsymbol{x}_\perp,\boldsymbol{k}_\perp,t)\in\mathbb{R}\,,$$
$$\int W_\psi(\boldsymbol{x}_\perp,\boldsymbol{k}_\perp,t)d\boldsymbol{k}_\perp=|\psi(\boldsymbol{x}_\perp,t)|^2\,,$$
$$\int W_\psi(\boldsymbol{x}_\perp,\boldsymbol{k}_\perp,t)d\boldsymbol{x}_\perp=|\varphi(\boldsymbol{k}_\perp,t)|^2\,,$$
$$\int W_\psi(\boldsymbol{x}_\perp,\boldsymbol{k}_\perp,t)d\boldsymbol{x}_\perp d\boldsymbol{k}_\perp=\int|\psi(\boldsymbol{x}_\perp,t)|^2d\boldsymbol{x}_\perp=\int|\varphi(\boldsymbol{k}_\perp,t)|^2d\boldsymbol{k}_\perp\,,$$
$$\int W_\psi(\boldsymbol{x}_\perp/2,\boldsymbol{k}_\perp,t)\exp(i\boldsymbol{k}_\perp\cdot\boldsymbol{x}_\perp)d\boldsymbol{k}_\perp=\psi(\boldsymbol{x}_\perp,t)\psi^*(\boldsymbol{0},t)\,. \tag{2.82}$$

Note that the Wigner distribution can be negative, which is an indicator of the breakdown of ray optics, and is therefore often referred to as a "quasi-probability" distribution in the context of quantum mechanics. It also has a "magnification" property [88], where the Wigner distribution of the signal $\psi_M(\boldsymbol{x}_\perp,t)=(1/|M|)\psi(\boldsymbol{x}_\perp/M,t)$ is given by

$$W_{\psi_M}(\boldsymbol{x}_\perp,\boldsymbol{k}_\perp,t)=W_\psi(\boldsymbol{x}_\perp/M,M\boldsymbol{k}_\perp,t)\,. \tag{2.83}$$

For free space propagation, the equation of motion of the Wigner distribution $W_{\hat{a}}(\boldsymbol{x}_\perp, \boldsymbol{k}_\perp, k_\xi, \eta)$ for each point in phase-space $(\boldsymbol{x}_\perp, \boldsymbol{k}_\perp)$ and each k_ξ-component of the pulse is classical [88]

$$\frac{\partial W_{\hat{a}}}{\partial \eta} + \frac{\boldsymbol{k}_\perp}{k_0 + k_\xi} \cdot \nabla_\perp W_{\hat{a}} = 0\,. \tag{2.84}$$

It also happens to remain classical in the presence of harmonic forces (e.g. propagation in a parabolic waveguide). Therefore, the analogue of Liouville's theorem of phase-space volume conservation applies to the Wigner distribution in $(\boldsymbol{x}_\perp, \boldsymbol{k}_\perp)$ phase-space for each k_ξ-component of the pulse propagating in free space/parabolic waveguides.

However, because the Wigner distribution is not necessarily nonnegative, it cannot be directly interpreted as an energy density function. However, some of its integrals can be. For example, the total spectral power per spectral component k_ξ of our non-paraxial wave is given by

$$\int W_{\hat{a}}(\boldsymbol{x}_\perp, \boldsymbol{k}_\perp, k_\xi, \eta) d\boldsymbol{x}_\perp d\boldsymbol{k}_\perp = \int |\hat{a}(\boldsymbol{x}_\perp, k_\xi, \eta)|^2 d\boldsymbol{x}_\perp = U(k_\xi, \eta)\,. \tag{2.85}$$

Note that the Wigner distribution of the sum of two signals is not, in general, equal to the sum of the corresponding two Wigner distributions. Despite this, due to its useful properties we outlined, it is a helpful tool for understanding and visualizing laser pulse evolution.

2.6 Wakefield Structure in Plasma Channels

2.6.1 Linear Wakefield Theory in Plasma Channels

The introduction of a pre-formed plasma channel will also affect the wakefield structure for the same reason it can guide laser pulses — by producing a radial increase in the plasma frequency. This causes the phase fronts of the wakefield to curve, reducing the on-axis longitudinal field thus negatively impacting acceleration. Since we expect to use plasma channels extensively in our work, it is useful to have a tool

to evaluate the effects of different channels on wakefield structure.

To study the structure of wakefields in plasma channels, we will be following the procedure outlined in [89] for evaluating linear wakefields in axisymmetric coordinates. Due to the short timescales involved and the small electron-ion mass ratio, we can approximate our plasma as an electron fluid with fixed background ions. We assume that the electrons are non-relativistic, but their laser-induced velocities are large compared to their thermal velocities ($c \gg v \gg v_{T_e}$). We also split the electromagnetic fields into their time-averaged high frequency components (ponderomotive force $\sim \nabla|a|^2$) and their low frequency components $\boldsymbol{E}, \boldsymbol{B}$. For the channel, we take the initial electron density profile to be a function of the radial distance $n_0 = n_0(r)$ only, and assume that the ions are configured such that the plasma is initially quasi-neutral. Treating the perturbations to the plasma as small (linearized in $\delta n, \boldsymbol{v}, \boldsymbol{E}, \boldsymbol{B}$), these assumptions give the following set of fluid equations

$$\begin{aligned}
&\frac{\partial \boldsymbol{v}}{\partial t} = -\frac{e\boldsymbol{E}}{m_e} - c^2\nabla|a|^2/4\,,\\
&\frac{\partial \delta n}{\partial t} + \nabla\cdot(n_0\boldsymbol{v}) = 0\,,\\
&\nabla\cdot\boldsymbol{E} = -\frac{e\delta n}{\epsilon_0}\,,\\
&\nabla\cdot\boldsymbol{B} = 0\,,\\
&\frac{\partial \boldsymbol{E}}{\partial t} = c^2\nabla\times\boldsymbol{B} + \frac{en_0\boldsymbol{v}}{\epsilon_0}\,,\\
&\nabla\times\boldsymbol{v} = \frac{e\boldsymbol{B}}{m_e}\,.
\end{aligned} \tag{2.86}$$

The last expression equating the vorticity and the magnetic field can be derived by taking the curl of the (non-linearized) momentum equation to show that the generalized vorticity $\boldsymbol{\Omega} \equiv \nabla\times\boldsymbol{v} - (e/m_e)\boldsymbol{B}$ is always zero as long as it is initially zero everywhere. From these equations we can derive the following expression in $\boldsymbol{v}$

$$\left(\frac{\partial^2}{\partial t^2} + \omega_p^2\right)\boldsymbol{v} + c^2\nabla\times(\nabla\times\boldsymbol{v}) = -c^2\frac{\partial}{\partial t}\nabla|a|^2/4 \tag{2.87}$$

where $\omega_p^2(r) = n_0(r)e^2/m_e\epsilon_0$. For convenience, we change coordinates (assuming

$v_g \approx c$) $\{r, z, t\} \rightarrow \{r,\ \xi = z - ct,\ \tau = t\}$. We also make the quasistatic approximation $\partial/\partial\tau \approx 0$ which states that the pulse does not undergo any significant distortions as it passes its own length. Under these assumptions, we can recover the same wakefield equation derived in [89]:

$$\left[\left(\frac{\partial^2}{\partial\xi^2} + k_p^2\right)\left(\Delta_\perp - k_p^2\right) - \frac{\mathrm{d}\ln n_0}{\mathrm{d}r}\frac{\partial^3}{\partial\xi^2\partial r}\right]\delta\phi = k_p^2\left(\Delta_\perp - k_p^2\right)|a|^2/4 \tag{2.88}$$

where $k_p(r) = \omega_p(r)/c$, $\Delta_\perp = \frac{1}{r}\frac{\partial}{\partial r}(r\frac{\partial}{\partial r})$, and $\delta\phi = |a|^2/4 - v_z/c$. The auxiliary quantity $\delta\phi$ is related to the axial and radial forces on relativistic beam electrons ($\boldsymbol{v}_{\mathrm{beam}} \approx c\hat{z}$) due to the wakefield $\{E_z, E_r, B_\theta\}$ and the density perturbation as follows

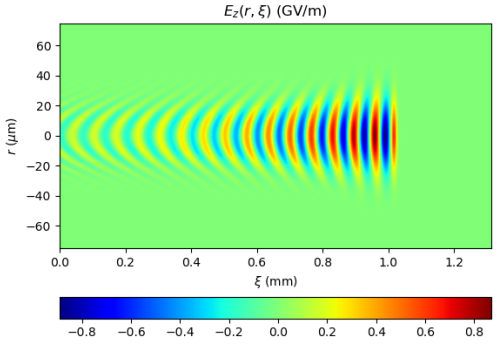
$$\begin{aligned} F_z &= \frac{-eE_z}{m\omega_{p0}c} = k_{p0}^{-1}\frac{\partial\delta\phi}{\partial\xi}\,, \\ F_r &= \frac{-e(E_r - cB_\theta)}{m\omega_{p0}c} = k_{p0}^{-1}\frac{\partial\delta\phi}{\partial r}\,, \\ \frac{\delta n}{n_0} &= k_p^{-2}(\Delta_\perp - k_p^2)\delta\phi + |a|^2/4 \end{aligned} \tag{2.89}$$

where ω_{p0} and k_{p0} indicate the on-axis plasma frequency and wavenumber respectively. Note that the expression for the density perturbation differs from the one given in [89] as this includes the off-axis regions as well as the region with the laser pulse. Eq. (2.88) can then be discretized and solved numerically (method discussed in appendix A), an example of which is shown in Fig. (2.7) for a wake in a parabolic channel. This model provides a quick way to evaluate wakefields in channels useful for performing large parameter scans to optimize our MP-LWFA scheme. For example, it can be used to find the optimal channel profile to maximize the total electron energy gain for a given pulsetrain, as will be discussed below.

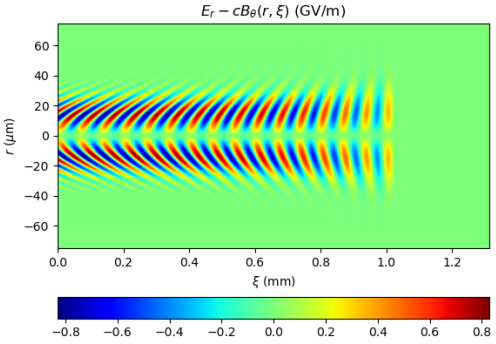
We can also make the following modification to Eq. (2.88) to capture the beam-loading effects of a perturbative relativistic electron bunch $n_{\mathrm{b}}(r,\xi)/n_0 \ll 1$ propagating at $c\hat{z}$, assuming no collisions, and no appreciable electric and magnetic fields

from the bunch

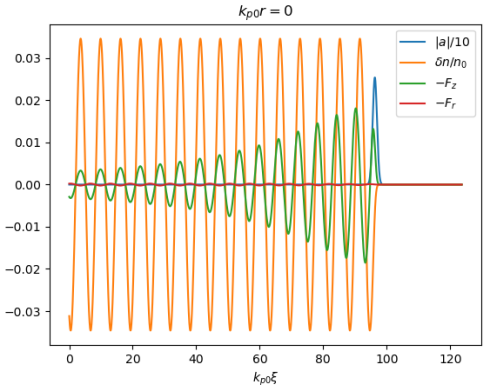
$$\left[\left(\frac{\partial^2}{\partial\xi^2}+k_p^2\right)\left(\Delta_\perp-k_p^2\right)-\frac{\mathrm{d}\ln n_0}{\mathrm{d}r}\frac{\partial^3}{\partial\xi^2\partial r}\right]\delta\phi=k_p^2\left(\Delta_\perp-k_p^2\right)|a|^2/4-k_p^4\frac{n_\mathrm{b}}{n_0} \quad (2.90)$$



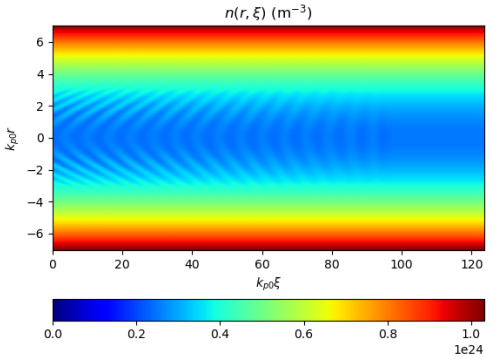
(a) Longitudinal wakefield $E_z(r,\xi)$.



(b) Radial wakefield $E_r(r,\xi) - cB_\theta(r,\xi)$.



(c) On-axis line-outs of the laser pulse $|a|$ (blue), relative density perturbation $\delta n/n_0$ (orange) and longitudinal and radial fields $-F_z, -F_r$ defined in Eq. 2.89 (green, red).



(d) Total plasma density of channel and wakefield perturbation $n(r,\xi)$ (m^{-3}).

Figure 2.7: Example numerical wakefield solution to Eq. (2.88) for a single 50 mJ, 1030 nm, 40 fs full-width-half-maximum (FWHM) Gaussian pulse with a 30 μm spot size in a matched parabolic channel with an on-axis density of 2.5×10^{17} cm^{-3}. Due to presence of the parabolic plasma channel curving the wakefield phase fronts along the axis, the longitudinal wakefield behind the pulse decays further behind the pulse as it is converted into off-axis transverse wakefield.

2.6.2 Optimizing Channels for MP-LWFA

We can generalize the channel matching condition Eq. (1.38) to have higher order channel profiles while still approximately confining a Gaussian mode [90] with

$$\begin{aligned} n_0(r) &= n_{00} + \Delta n (r/w_0)^\alpha, \\ \Delta n &= (\pi r_e w_0^2)^{-1}. \end{aligned} \tag{2.91}$$

Note that depending on the transverse extent of the channel, one may want to increase or decrease the channel depth Δn to make the channel matched to the spot size w_0. This gives us two parameters to study the effect of different matched channels on wakefields for a given spot size: the on-axis density n_{00}, the channel shape α.

For especially curved (small α) and deep (large $\Delta n/n_{00}$) channels, we expect the wakefield structure to be heavily modified. This results in a faster decay of on-axis accelerating wakefield into focusing fields, but conversely increases the dephasing length by increasing the overlap between the accelerating and focusing field regions. This balance between maximum accelerating gradient and dephasing length suggests that there exists an optimal channel profile for a given pulsetrain which maximizes the total work done on an electron bunch. This channel profile optimization is explored as in Fig. (2.8) for pulsetrains comprised of resonantly spaced identical Gaussian pulses for various pulsetrain lengths assumed to be fixed throughout their propagation. This parameter scan shows that wakefields in higher density plasmas or from shorter pulsetrains can yield higher electron energy gain from a smaller channel α due to its associated increase in dephasing length.

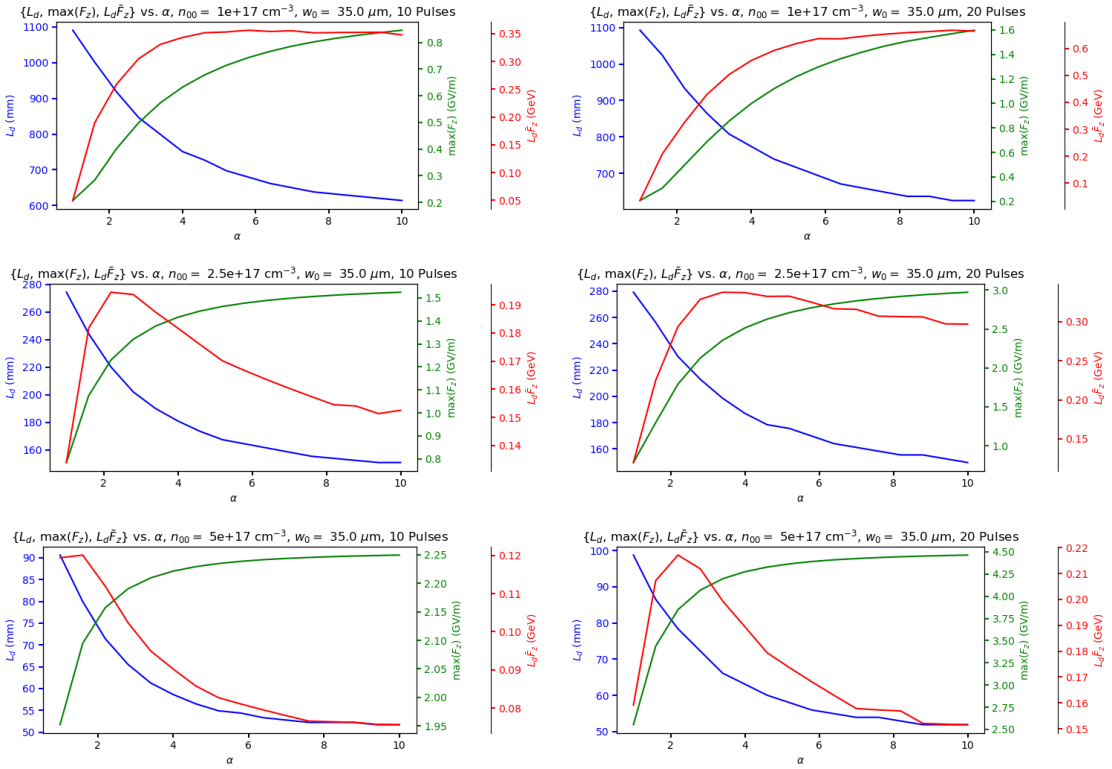


Figure 2.8: The dephasing length L_d (blue) is defined using the overlap between the focusing and accelerating region of the wakefield. The peak longitudinal wakefield $\max(F_z)$ (green) is the maximum accelerating gradient in the accelerating-focusing region. The energy gain $L_\mathrm{d}\bar{F}_z$ (red) is defined as the work done by the wakefield on a relativistic electron travelling along the axis at c injected at the back of the accelerating-focusing region. The columns scan a resonant pulsetrain containing 10 and 20 identical Gaussian pulses respectively. The rows scan on-axis densities of $n_{00} = 1.0 \times 10^{17}$, 2.5×10^{17}, 5.0×10^{17} cm^{-3} respectively.

2.7 Resonant Excitation of Plasma Waves in a Plasma Channel

2.7.1 Motivation

As a stepping stone towards realizing the Plasma-Modulated Plasma Accelerator (P-MoPA) [1, 33, 38] for achieving multi-GeV LWFA at kHz repetition rates with contemporary thin disk lasers, the Oxford group performed the first experimental demonstration of resonant excitation of plasma waves in long ($\sim 100\,\mathrm{mm}$) plasma channels [39]. In this experiment, the group used the 300 TW Astra-Gemini TA3

Ti:sapphire laser at the Rutherford Appleton Laboratory to form a "mock" pulse train in place of the P-MoPA pulse train. This mock pulse train was made by passing a linearly chirped pulse through a Michelson interferometer, as has been previously described in [91, 92], a schematic example of which is shown in Figure 2.9.

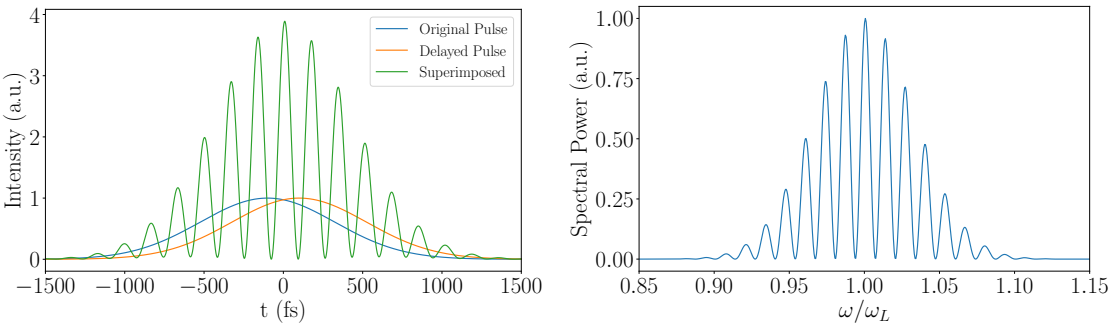


Figure 2.9: Example mock pulse train envelope (left) with a 170 fs spacing and its spectrum (right) formed by passing a linearly chirped 1 ps FWHM pulse centered at $\lambda_L = 800\,\text{nm}$ through a Michelson interferometer with a 200 fs delay. The pulse spacing is influenced by both the delay and the linear chirp.

In this experiment, the plasma density was varied in order to observe a resonance condition (e.g. at 170 fs spacing, there should be resonant wakefield excitation at around $n_{00} = 4.3 \times 10^{17}\,\text{cm}^{-3}$). The wakefield amplitude driven in the plasma channel was inferred from measurements of the output spectra of the pulse trains. This necessitated the application of a 3D spectral modulation theory with an accurate description of wakefield excitation in plasma channels in order to accurately determine the wakefield amplitude from the laser spectra.

2.7.2 Fluid Code for Spectral Modulation

The wakefield excited by the pulse train was solved in cylindrical coordinates following the procedure outlined in [89], which yields the PDE we derived previously in Eq. (2.88). This PDE can be solved numerically (see appendix A) for any arbitrary pulse envelope $|a|^2 \ll 1$ and axisymmetric plasma channel $n_e(r)$. Previous work suggests that the transverse plasma density profiles of HOFI channels under conditions relevant to this experiment are approximately parabolic [93]. Hence for this calculation, we assumed that the plasma channel took the form of the matched

parabolic channel;

$$n_{\mathrm{e}}(r) = n_{\mathrm{e},0} + \Delta n (r/w_0)^2 \tag{2.92}$$

where $n_{\mathrm{e},0}$ is the on-axis plasma density and $\Delta n = (\pi r_e w_0^2)^{-1}$ is the channel depth parameter with r_e being the classical electron radius. This channel guides the fundamental Gaussian mode $|a|^2 \sim \exp(-2r^2/w_0^2)$ of spot size w_0.

To evaluate the spectral modulation, we will assume that the pulse train does not undergo the self-modulational instability. Assuming that the laser coupling quality is high enough such that the envelope $|a|^2$ is initially in the fundamental Gaussian mode LG_{00} and remains fixed throughout the full propagation (i.e. no growth of envelope SM), if the density perturbation is small relative to the channel depth parameter $|\delta n| \ll \Delta n$, the spectral modulation of the pulse train will be given by [33]

$$\frac{\Delta\omega(\xi, z_{\mathrm{end}})}{\omega_L} = -z_{\mathrm{end}} \frac{2c^2}{\omega_L^2 w_0^2} \langle 00| \frac{\partial}{\partial \xi} \frac{\delta n(r, \xi; |a|^2)}{\Delta n} |00\rangle \tag{2.93}$$

where $\Delta\omega = \omega - \omega_L$ is the shift in instantaneous frequency. Eq. (2.93) in combination with the numerical wakefield solution to Eq. (2.88) were used to calculate the spectra of the pulse trains after propagation within the channel over a range of plasma densities, using the pulse envelope extracted from the pulse train retrieval process. The resulting spectra were analyzed and compared with the experimental spectra to estimate the wakefield amplitudes driven within the plasma channel. A correction was also made to this expression to account for the transverse leakage rate of pulse trains which results in less red-shifting. An example calculated spectrum is given in Figure 2.10.

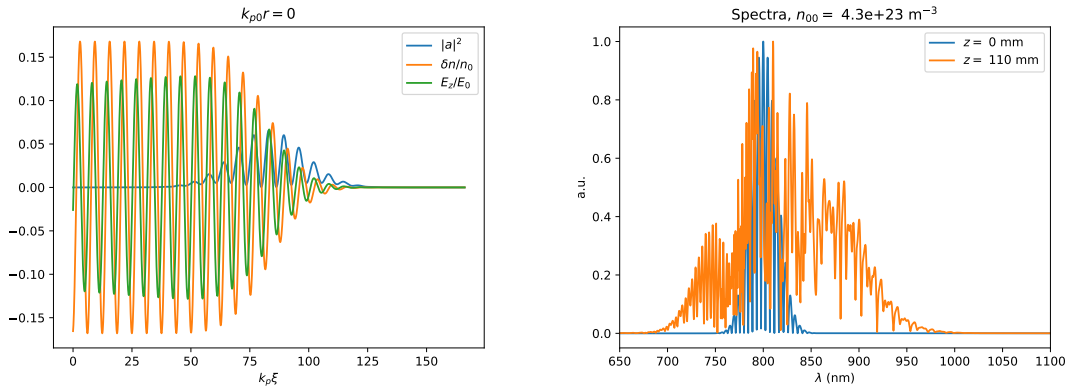


Figure 2.10: On-axis lineouts (left) and calculated spectra (right) of a 2.5 J, 170 fs spaced pulse train of spot size $w_0 = 45\,\mu\text{m}$ propagating in a 110 mm matched parabolic plasma channel with resonant on-axis plasma density $n_{00} = 4.3{\times}10^{17}\,\text{cm}^{-3}$. For this calculation, no transverse leakage was assumed.

2.7.3 PIC simulations of conditioning effect

Conditioning of the neutral gas collar formed by the HOFI channel was studied using the PIC code WarpX [40], which uses ADK theory [75] to model the tunnel ionization of neutral atoms in intense laser fields. For simplicity, a neutral gas of atomic hydrogen was assumed. The HOFI channel profile, which is comprised of the ionized electron $n_{\text{e,OFI}}$ and ion $n_{\text{H}^+,\text{OFI}}$ densities from the OFI process and the density of neutral hydrogen atoms n_{H}, was parameterized in the following form

$$n_{\text{e,OFI}}(r) = n_{\text{H}^+,\text{OFI}}(r) = n_{\text{e},0}\exp\left(-r^2/d_0^2\right)\,, \tag{2.94}$$

$$n_{\text{H}}(r) = \begin{cases} n_{\max} e^{-(r-r_{\max})^2/d_1^2}, & r \le r_{\max} \\ n_\infty + (n_{\max} - n_\infty)\, e^{-(r-r_{\max})^2/d_2^2}, & r > r_{\max} \end{cases} \tag{2.95}$$

where $n_{\text{e},0} = 4.3\times10^{17}\,\text{cm}^{-3}$, $n_{\max} = 6.2\times10^{18}\,\text{cm}^{-3}$, $n_\infty = 3.2\times10^{18}\,\text{cm}^{-3}$, $d_0 = 45\,\mu\text{m}$, $d_1 = 16\,\mu\text{m}$, $d_2 = 8\,\mu\text{m}$, and $r_{\max} = 50\,\mu\text{m}$.

An example of the conditioning effect of the pulse train is shown in Fig. 2.11, which shows that full conditioning of the neutral gas collar is achieved after the first few low-energy pulses have passed.

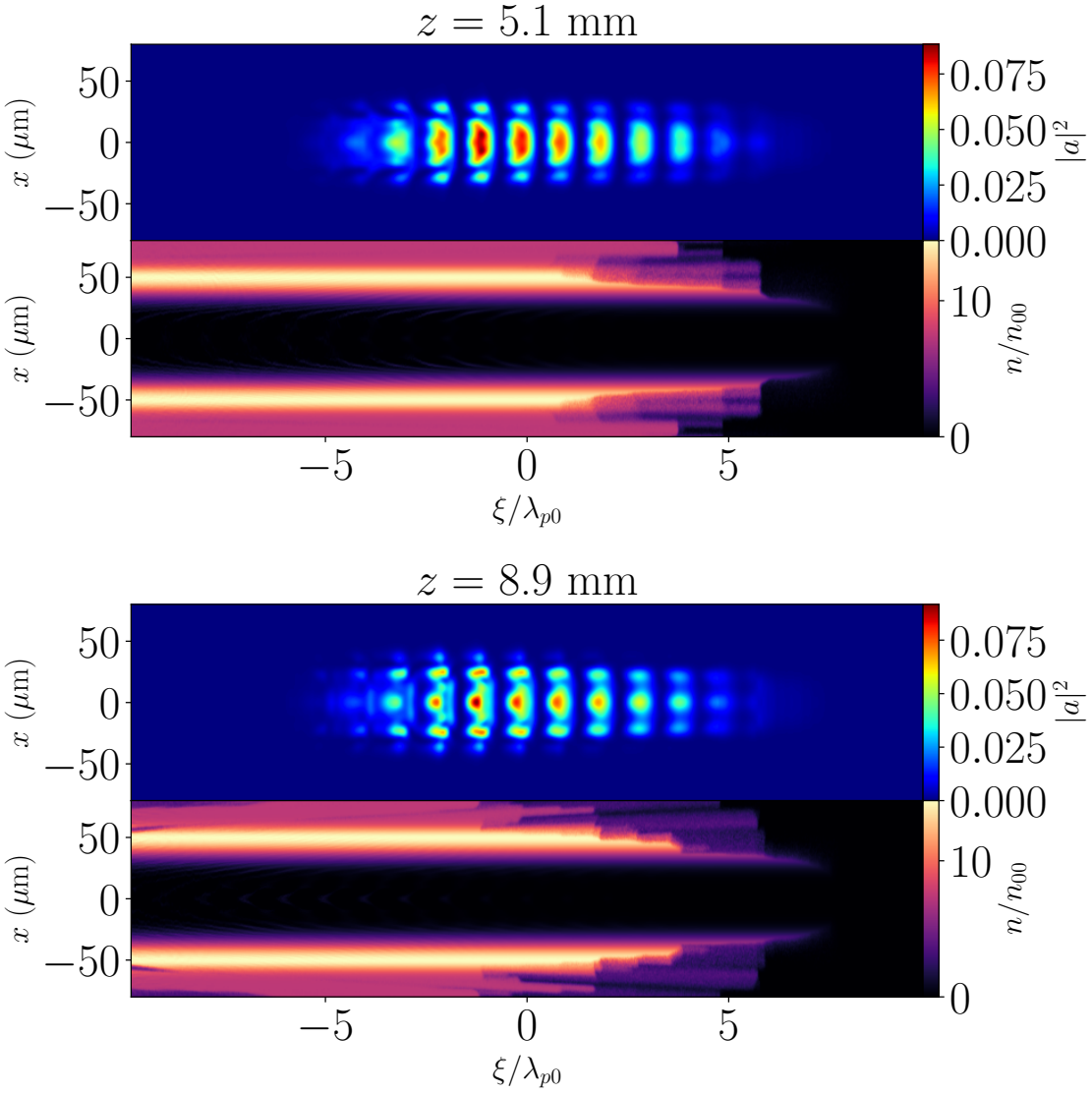


Figure 2.11: Results of a 2D PIC simulation of the propagation of the pulse train and its conditioning of the HOFI channel, whose profile is modeled with the parameterization given in Eq. (2.94). The top panel displays the normalized intensity envelope $|a|^2$, whilst the bottom panel shows the normalized electron density $n_e/n_{e,0}$ including both the electrons initially ionized by the OFI process and the electrons from ionizing the neutral gas collar. The propagation-varying transverse structure of the laser pulses are due to an initial mismatch between this channel profile and the laser spot size.

Chapter 3

The P-MoPA Modulator Stage

3.1 GeV-Scale LWFA at kHz Repetition Rates

Single-pulse LWFA only became practical with the onset of chirped pulse amplification (CPA) [22] allowing joule-scale pulses to be compressed to sub-ps durations. Ever since, the bulk of LWFA research has been based on high intensity ultrashort laser pulses from Ti:sapphire laser systems with CPA. However, these systems suffer from low ($\sim$ 0.1–1 Hz) repetition rates and poor energy efficiencies. This poses a problem if we want LWFA to compete with traditional particle accelerators, which can operate at MHz repetition rates. For many practical applications, we would need at least a kHz-capable LWFA.

Contemporary thin-disk lasers are already able to provide joule-scale pulses at kHz repetition rates [2–4], but have not yet been successfully applied to LWFA. The problem is that their pulses can currently only be compressed to picosecond-scale durations due to the narrow bandwidth of their gain media, which are too long to be useful for driving wakefields for LWFA.

A novel scheme outlined in Figure (3.1) was recently proposed [1] which overcomes this narrow bandwidth problem. By introducing a spectral modulation to the pulse with a plasma modulator. This spectral modulation can then be converted into a temporal modulation using a dispersive optical system, for example by applying group delay dispersion (GDD). This forms a multipulse train which can then

be focused into a plasma accelerator stage to perform multipulse laser wakefield acceleration (MP-LWFA).

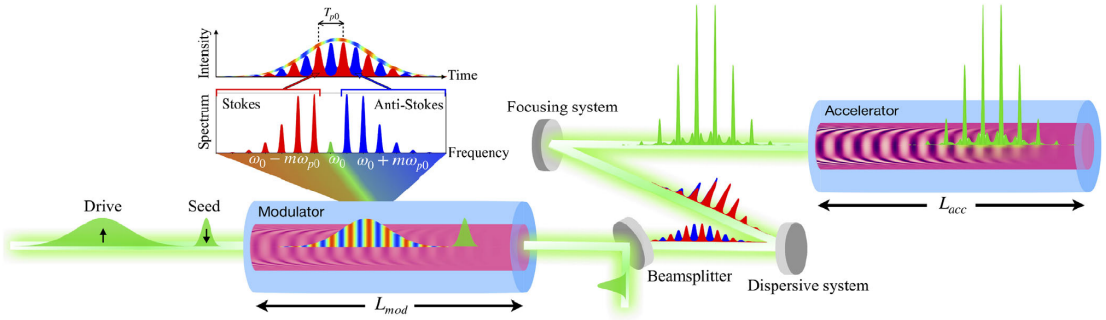


Figure 3.1: Outline of the proposed P-MoPA scheme, taken from [1] with permission. A seed pulse excites a small wakefield in the modulator stage which spectrally modulates a long drive pulse into out-of-phase red-shifted (Stokes) and blue-shifted (anti-Stokes) pulsetrains. Chromatic dispersion (e.g. group delay dispersion) is then applied to the spectrally modulated drive pulse to compress it into a multipulse train, which can then be focused down again to resonantly drive the main wakefield in the accelerator stage.

The plasma modulator works using seeded spectral modulation. This scheme involves using a short (10s fs), low energy (10–100 mJ) seed pulse to drive a low amplitude ($\sim$ 1%) wake in the plasma. A long ($\sim$ 1 ps) joule-scale drive pulse then co-propagates behind the seed pulse. The plasma density perturbations driven by the seed pulse cause local variations in the drive laser's phase velocity, which builds up a spectral modulation as it propagates along the modulator whilst its envelope remains smooth, thus ensuring that minimal energy in the drive pulse is lost in the modulator. A dispersive system then applies chromatic dispersion (e.g. with chirped mirrors) to compress the drive pulse into a pulse train of short pulses exactly separated by the plasma period of the modulator. This pulse train can then resonantly drive a wake in an accelerator stage with the same plasma density.

In this chapter we will first derive the full 3D theory of seeded spectral modulation in plasma channels and what type of chromatic dispersion is required to compress the modulated pulse into a pulse train. Next, we address the constraints on the scheme caused by various self-modulation mechanisms in both the modulator and accelerator stages, and verify these limits in numerical studies with extensive

PIC simulations. After identifying these processes and their scaling laws, we define the parameter space where the P-MoPA scheme can operate without laser-plasma instabilities and provide up to multi-GeV energy gains using pre-existing kHz lasers.

3.2 The Plasma Modulator

3.2.1 Seeded Spectral Modulation in Plasma Channels

To spectrally modulate the long drive pulse for compression into a multipulse train, we introduce a short seed pulse ahead of it to drive a small wakefield. The drive pulse co-propagates with this seed wake whose density gradients provide a linearly growing spectral modulation of the drive pulse with respect to the modulator length L_{mod}.

The seeded spectral modulation scheme requires that relativistic self-focusing and self-wakefield effects of the long modulating drive pulse are negligible. Making these assumptions reduces Eq. (2.7) to a linear paraxial wave equation

$$\left[\frac{i}{\omega_L}\frac{\partial}{\partial\tau}+\frac{c^2}{2\omega_L^2}\Delta_\perp\right]a=\frac{\omega_p^2}{2\omega_L^2 n_0}\left[\delta n_0(r)+\delta n(r,\xi;|a_s|^2)\right]a \tag{3.1}$$

where a_s denotes the seed pulse envelope, which we assume evolves much slower than the modulating drive pulse. We also demand that the channel is matched to the pulse spot size w_0, so that the unperturbed drive pulse envelope takes the form

$$a(r,\tau)=a_0\exp\left(-\frac{r^2}{w_0^2}-i\omega_L\tau\frac{2}{k_L^2 w_0^2}\right), \tag{3.2}$$

which is the stable solution for the fundamental Gaussian mode propagating along a matched parabolic channel as described in Eq. (2.11). Assuming that the seed wake is small relative to the matched channel depth parameter $\delta n(r,\xi;|a_s|^2)\ll\Delta n\equiv(\pi r_e w_0^2)^{-1}$, we can treat it as a perturbation to the plasma channel. Analogous to the quantum harmonic oscillator, first order time-independent perturbation theory

yields the following first order modification to the total phase of the laser pulse

$$\begin{aligned}\Phi(\xi,\tau) &= k_L\xi - \omega_L\tau\left[\frac{2}{k_L^2 w_0^2} + E_1(\xi)\right], \\ E_1(\xi) &= \frac{2}{k_L^2 w_0^2}\left\langle \frac{\delta n(r,\xi;|a_s|^2)}{\Delta n}\right\rangle_\perp\end{aligned} \tag{3.3}$$

where $\langle(...)\rangle_\perp \equiv \langle 00|\,(...)\,|00\rangle = (4/w_0^2)\int_0^\infty(...)\exp(-2r^2/w_0^2)rdr$ denotes the intensity-weighted transverse average for the Gaussian mode case. Note that $E_1 \ll 2/k_L^2w_0^2 \ll 1$ is necessarily true due to our small wake assumption. In other words, the matched spot size needs to be small enough for a given seed wake $w_0^2 \ll \delta n(r,\xi;|a_s|^2)/\pi r_e$ for this result to hold. Using this expression we can also retrieve the shift in instantaneous frequency

$$\begin{aligned}\omega(\xi,\tau) &= -\frac{\partial\Phi}{\partial t} \\ &= -\left(\frac{\partial}{\partial\tau} - v_g\frac{\partial}{\partial\xi}\right)\Phi \\ &= \omega_L + \omega_L\left(\frac{2}{k_L^2w_0^2} + E_1\right) - \omega_L v_g\tau\frac{\partial E_1}{\partial\xi}, \\ \frac{\Delta\omega(\xi;L_{\rm mod})}{\omega_L} &= -L_{\rm mod}\frac{2}{k_L^2w_0^2}\left\langle\frac{\partial}{\partial\xi}\frac{\delta n(r,\xi;|a_s|^2)}{\Delta n}\right\rangle_\perp\end{aligned} \tag{3.4}$$

where $L_{\rm mod} = v_g\tau$. This predicts that the spectral modulation amounts to a radial averaging of the longitudinal gradient of the wake weighted by the pulse intensity profile. Note that this lack of radial dependence is desirable as it allows for easy pulse compression into a multipulse train by applying the same amount of chromatic dispersion across the entire cross-section of the modulated pulse. This expression is compared with a 2D PIC simulation in Figure (3.2) and its beneficial lack of radial dependence despite transverse wakefield structure is also demonstrated in simulations shown in Figure (3.3).

If the drive pulse is not perfectly matched to the channel, we can generalize this theory to capture the spectral modulation of the higher order guided Laguerre-

Gaussian modes present

$$\begin{aligned}
\Phi_{pm}(\xi,\theta,\tau) &= k_L\xi + m\theta - \omega_L\tau\left[(2p+|m|+1)\frac{2}{k_L^2 w_0^2} + E_1^{pm}(\xi)\right], \\
E_1^{pm}(\xi) &= \frac{2}{k_L^2 w_0^2}\langle pm|\,\frac{\delta n(r,\xi;|a_s|^2)}{\Delta n}\,|pm\rangle \\
\frac{\Delta\omega_{pm}(\xi;L_{\mathrm{mod}})}{\omega_L} &= -L_{\mathrm{mod}}\frac{2}{k_L^2 w_0^2}\langle pm|\,\frac{\partial}{\partial\xi}\frac{\delta n(r,\xi;|a_s|^2)}{\Delta n}\,|pm\rangle\ .
\end{aligned} \tag{3.5}$$

This shows that even in the presence of higher order channel modes in the drive pulse, the behavior of spectral modulation should still be similar (though perhaps slower) to that of the fundamental Gaussian mode as long as the modulating drive pulse does not drive its own wake.

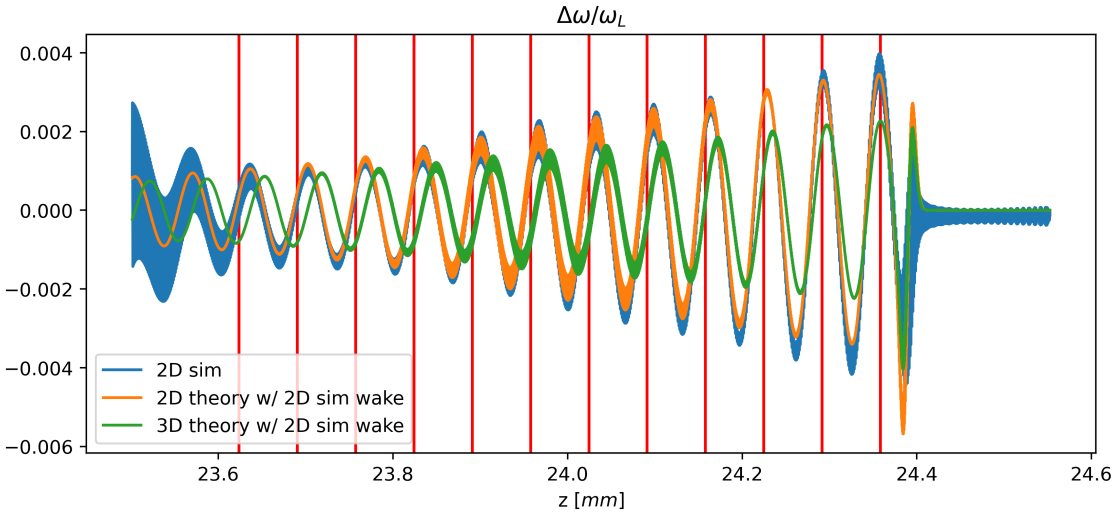


Figure 3.2: Instantaneous frequency on-axis of a long-pulse propagating behind a short seed pulse from a WarpX 2D PIC simulation in a parabolic channel with $n_{00} = 2.5 \times 10^{17}$ cm^{-3}, $w_0 = 30$ μm and laser wavelength $\lambda_L = 1030$ nm. The red lines indicate on-axis plasma wavelength spacings. The orange curve is the predicted spectral modulation from the 2D simulation wakefield and 2D spectral modulation theory (where the intensity-weighted average is in 2D rather than 3D geometry), and is in good agreement with the spectral modulation measured by taking a Hilbert transform (blue). The green curve is the predicted spectral modulation using 3D theory instead along with the 2D simulation wakefield. This shows that spectral modulation is more strongly suppressed by wakefield curvature from channels in 3D than in 2D geometry.

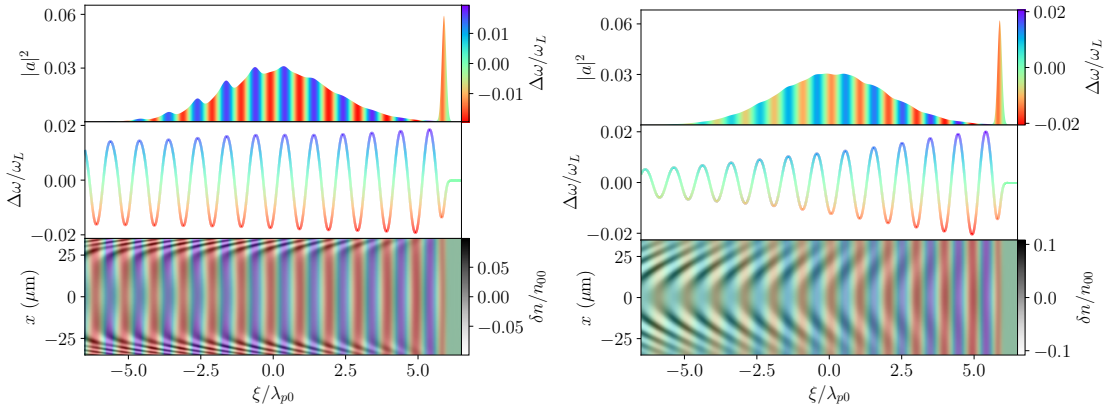


Figure 3.3: WarpX 2D PIC simulations at the end of the modulator stage with both matched square (left) and parabolic (right) plasma channels. The top shows the on-axis seed and drive pulse envelopes. The middle panel plots the on-axis instantaneous frequency calculated with a Hilbert transform. The bottom panel displays the full 2D instantaneous frequency modulation and the wake density perturbation, which demonstrates that the spectral modulation is mostly independent from the transverse coordinate despite the presence of transverse wakefield structure as predicted by Eq. (3.4), which is a desirable feature for the compression stage. We also observe a suppression of spectral modulation towards the tail of the pulse in the parabolic channel due to a buildup of wakefield phase front curvature.

3.2.2 Channel Suppression of Spectral Modulation

The result from Eq. (3.4) implies that the range of effective spectral modulation behind the seed pulse is limited by wakefield phase front curvature due to the preformed plasma channel. For square channels with walls sufficiently far from the bulk of the pulse, this does not pose a problem as the bulk of the wakefield maintains flat phase fronts. But for any channel close to parabolic in shape, the spectral modulation range can be severely suppressed for large channel depths, as demonstrated in Figures (3.4, 3.5). Deep parabolic channels strongly suppress the spectral modulation, similar to how their longitudinal wakefields are also suppressed as shown in Figure (2.7). Because the reduction of spectral modulation asymmetric along the pulse, this effect cannot be completely corrected for by simply propagating over longer distances, as the head of the pulse will start to over-modulate.

On top of the suppression of spectral modulation, the spacings between the spectral modulation peaks also become shorter than the on-axis plasma wavelength,

which is shown in Figure (3.4). This needs to be taken into account when compressing the pulse into a multipulse train.

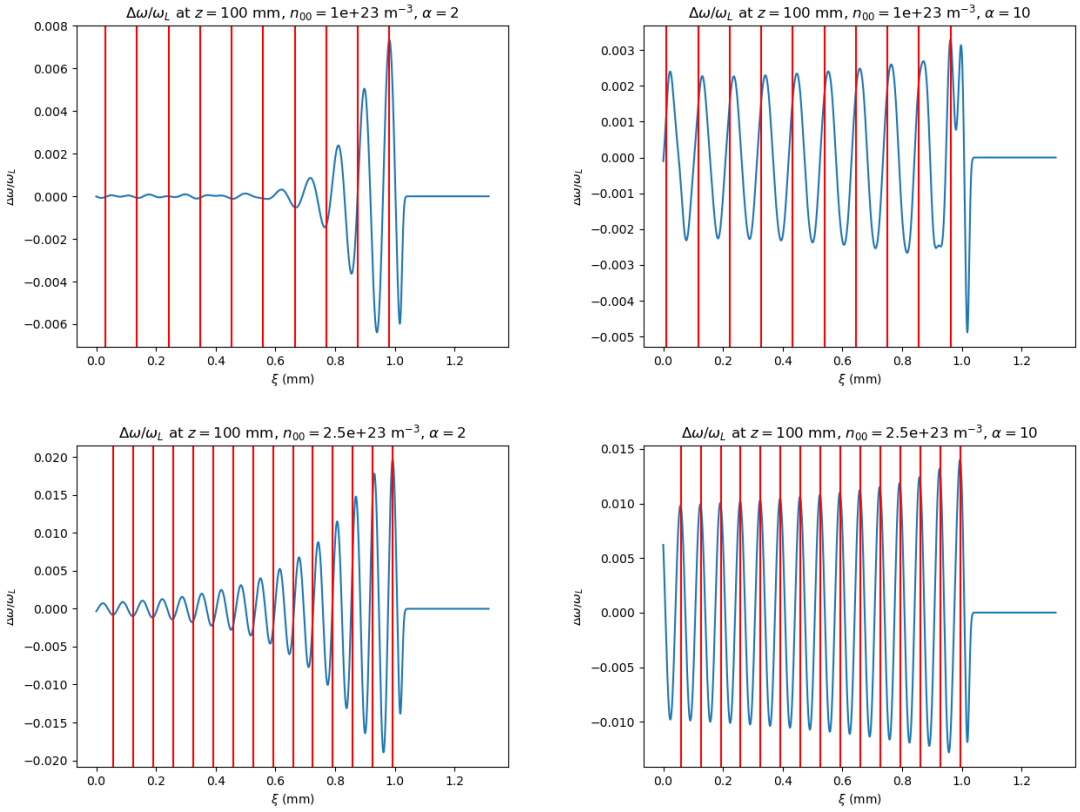


Figure 3.4: Spectral modulation calculated using Eqs. (3.3, 3.4) after 100 mm of propagation traveling behind a short 50 mJ, 40 fs pulse with a 30 μm spot size in a matched channel for varying on-axis densities and for parabolic ($\alpha = 2$) and square ($\alpha = 10$) channels.

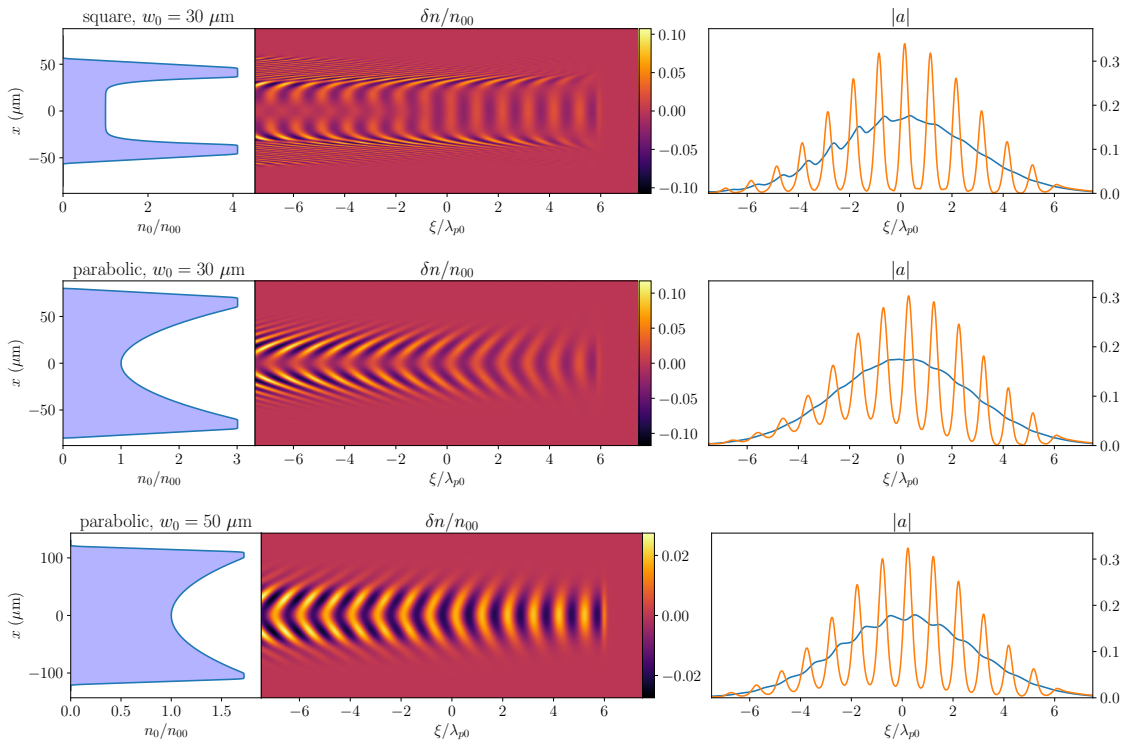


Figure 3.5: WarpX 2D PIC simulations of the plasma modulator for different plasma channel profiles. The left and middle panels display the channel profile and the wake in the channel. The right panel shows the on-axis drive pulse envelope after the modulator both before (blue) and after (orange) compression into a pulse train. The parabolic channel causes curvature of the wake phase fronts, causing suppression of spectral modulation towards the tail of the pulse resulting in a reduction of pulse compression quality. Increasing the matched spot size for a fixed on-axis density mitigates this effect by reducing the wake curvature.

3.2.3 The Shallow Channel Approximation

Working in the shallow channel limit $\Delta n \ll n_{00}$ and assuming that the modulating drive pulse duration is short enough such that $[\omega_p(r \lesssim w_0) - \omega_{p0}]\,\tau_p \ll 1$, the radial dependence of the seed wake becomes separable in the form

$$\delta n(r, \xi; |a_s|^2) = \delta n_s \exp(-2r^2/w_0^2) \cos(k_{p0}\xi + \Delta\phi)\,, \tag{3.6}$$

where δn_s is the on-axis seed wake amplitude and $\Delta\phi$ is a constant phase shift defined by the location of the seed pulse. This allows us to estimate the first order correction to the envelope caused by the focusing/defocusing effects of the seed wake

using the first Laguerre-Gaussian radial mode, resulting in a small variation in peak intensity along the pulse which scales linearly with the seed wake amplitude

$$|a(r,\xi,\tau)|^2 \approx |a_0|^2 \left[1 - \frac{1}{4}\left(1 - \frac{2r^2}{w_0^2}\right)\frac{\delta n_s \cos(k_{p0}\xi + \Delta\phi)}{\Delta n}\right] \exp\left(-2r^2/w_0^2\right) . \quad (3.7)$$

Excluding this correction to the drive pulse envelope, working in the shallow channel limit recovers the 1D spectral modulation theory derived in the original proposal [1] with a factor of 2 correction when integrating the seed wake over cylindrical geometry and a phase correction for the finite spot size

$$a(r,\xi,\tau) = a_0 \exp\left[-\frac{r^2}{w_0^2} - i\omega_L\tau\frac{2}{k_L^2 w_0^2}\left(1 + \frac{\delta n_s \cos(k_{p0}\xi + \Delta\phi)}{2\Delta n}\right)\right] . \quad (3.8)$$

3.2.4 Relativistic Self-Phase Modulation

For modulating drive pulses of finite duration, relativistic self-phase modulation (SPM) can also contribute to the spectral modulation by introducing a chirp. In the weakly relativistic limit, Eq. (2.7) reduces to the following nonlinear paraxial equation

$$\left[\frac{i}{\omega_L}\frac{\partial}{\partial\tau} + \frac{c^2}{2\omega_L^2}\Delta_\perp\right] a = \frac{\omega_p^2}{2\omega_L^2 n_0}\left[\delta n_0(r) + \delta n(r,\xi;|a_s|^2) - n_0(r)|a|^2/4\right] a . \quad (3.9)$$

We again assume that the unperturbed drive pulse envelope takes the same form as in Eq. (3.2), but now allow the envelope vary with ξ

$$a(r,\xi,\tau) = a_0 f(\xi) \exp\left(-\frac{r^2}{w_0^2} - i\omega_L\tau\frac{2}{k_L^2 w_0^2}\right) \quad (3.10)$$

where $0 \leq f(\xi) \leq 1$ is some slowly varying longitudinal profile relative to the plasma wavelength. Treating the self-focusing term as a perturbation $n_0(r)|a|^2/4 \ll \Delta n \equiv (\pi r_e w_0^2)^{-1}$ yields the following correction to the spectral modulation in a matched

parabolic channel

$$\begin{aligned} E_{\mathrm{SPM}}(\xi) &= -\frac{2}{k_L^2 w_0^2}\left\langle \frac{n_0(r) f^2(\xi)|a_0|^2 \exp(-2r^2/w_0^2)/4}{\Delta n}\right\rangle_\perp \\ &= -\frac{2}{k_L^2 w_0^2}\left(\frac{n_{00}}{2\Delta n}+\frac{1}{8}\right) f^2(\xi)|a_0|^2/4\,, \\ \Phi(\xi,\tau) &= k_L\xi - \omega_L\tau\left[\frac{2}{k_L^2 w_0^2}+E_1(\xi)+E_{\mathrm{SPM}}(\xi)\right]\,, \\ \frac{\Delta\omega(\xi;L_{\mathrm{mod}})}{\omega_L} &= -\frac{2L_{\mathrm{mod}}}{k_L^2 w_0^2}\frac{\partial}{\partial\xi}\left[\left\langle\frac{\delta n(r,\xi;|a_s|^2)}{\Delta n}\right\rangle_\perp - \left(\frac{n_{00}}{2\Delta n}+\frac{1}{8}\right) f^2(\xi)|a_0|^2/4\right]\,. \end{aligned} \tag{3.11}$$

Assuming that the longitudinal profile is Gaussian $f(\xi) = \exp\left[-2\ln 2(\xi/v_g\tau_p)^2\right]$ where $\tau_p \gg 2\pi/\omega_{p0}$ is the FWHM duration of the modulating drive pulse, relativistic self-focusing adds the following positive chirp

$$\frac{\Delta\omega(\xi;L_{\mathrm{mod}})}{\omega_L} = -\frac{2L_{\mathrm{mod}}}{k_L^2 w_0^2}\left[\left\langle\frac{\partial}{\partial\xi}\frac{\delta n(r,\xi;|a_s|^2)}{\Delta n}\right\rangle_\perp + 4\ln 2\left(\frac{n_{00}}{\Delta n}+\frac{1}{4}\right)\frac{\xi f^2(\xi)}{v_g^2\tau_p^2}|a_0|^2/4\right]\,. \tag{3.12}$$

This chirp appreciably changes the spectrum of the drive pulse for the laser and plasma parameters we are interested in for P-MoPA, and thus should be considered when designing the optimal dispersive optic for compression into a pulse train. Note that this positive chirp is similar to the chirp applied to pulses propagating in optical fibers undergoing SPM due to the Kerr effect.

Ignoring the contribution from the seed wake, the relativistic term also contributes to a modulation of the intensity via relativistic self-focusing which can be estimated using the first radial Laguerre-Gaussian mode

$$|a(r,\xi,\tau)|^2_{\mathrm{SF}} \approx |a_0|^2 f^2(\xi)\left[1+\frac{1}{4}\left(1-\frac{2r^2}{w_0^2}\right)\left(\frac{n_{00}}{\Delta n}+\frac{1}{4}\right)|a_0|^2 f^2(\xi)\right]\exp\left(-2r^2/w_0^2\right)\,, \tag{3.13}$$

which reduces the effective matched spot size in regions of higher laser intensity.

3.2.5 Compression into a Pulse Train

Once we have a spectrally modulated pulse, we can then apply some form of chromatic dispersion, such as GVD, to compress it into a multipulse train. To evaluate this with the theory developed in this chapter, assume a spectrally modulated long-pulse propagating in vacuum of the form

$$\frac{e\boldsymbol{E}_{\mathrm{mod}}(r,\xi)}{m_e\omega_L c} = \hat{e}_L a_g(r) f(\xi) \exp\left\{ik_L[\xi - L_{\mathrm{mod}}E_1(\xi)]\right\} \tag{3.14}$$

where L_{mod} is the length of the modulator, $f(\xi)$ is some longitudinal envelope function and $E_1(\xi)$ is the dimensionless spectral modulation parameter calculated in Eq. (3.3). Note that from switching from vector potential $\boldsymbol{a}$ to electric field $\boldsymbol{E}$ we used the fact that the $v_g\frac{\partial^2}{\partial\xi\partial\tau}$ term in Eq. (2.6) cancels to first order modulating terms associated with taking the time derivative of the vector potential. For an arbitrary longitudinal envelope, we can calculate the compressed pulse by taking its Fourier transform in the time variable ξ/v_g, applying the desired dispersion $\psi(\omega)$ in Fourier space, then taking its inverse transform

$$\boldsymbol{E}_{\mathrm{acc}}(r,\xi) = \mathcal{F}^{-1}\left\{\mathcal{F}\left[\boldsymbol{E}_{\mathrm{mod}}(r,\xi)\right]\exp[i\psi(\omega)]\right\}. \tag{3.15}$$

As we expect to generate Stokes and anti-Stokes sidebands spaced by the plasma frequency and that these red- and blue-shifted pulsetrains will be out of phase by half a plasma wavelength [1], the ideal dispersion to apply for optimal pulse compression into a multipulse train would push these sidebands together by $\pi/2$ radians each

$$\psi(\omega) = \frac{\pi}{2}\frac{|\omega - \omega_L|}{\omega_{p0}} \tag{3.16}$$

which would ensure that the red and blueshifted pulsetrains will overlap, forming one large pulsetrain for the accelerator stage. An example of a compressed pulse from theory is shown in Figure 3.6.

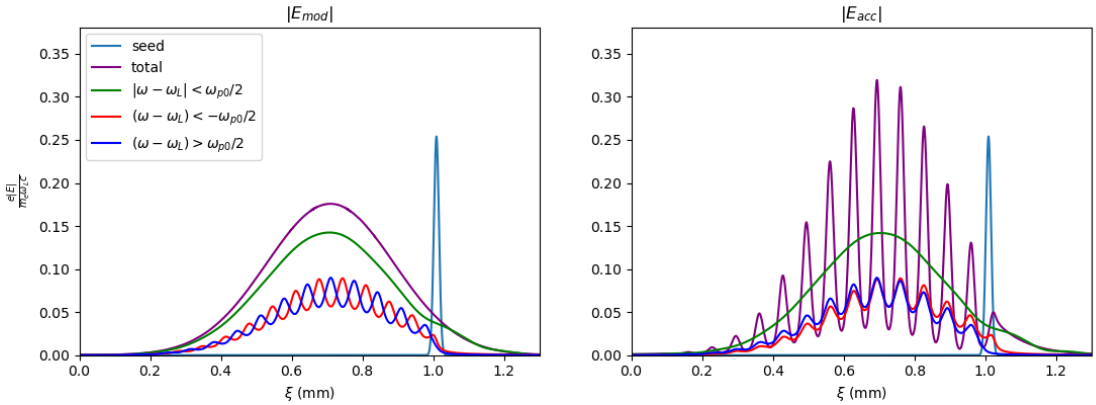
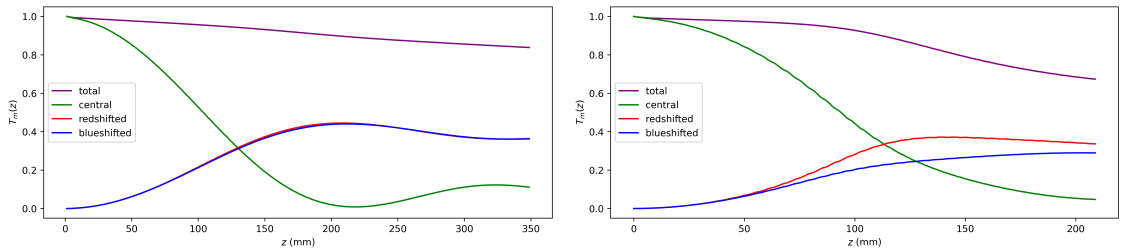


Figure 3.6: Example pulsetrain envelope formation calculated from theory for a $n_{00} = 2.5 \times 10^{17}$ cm^{-3} square channel ($\alpha = 10$) matched to a $w_0 = 30$ μm spot size with a 40 fs, 50 mJ seed and 1 ps, 600 mJ modulating drive pulse with a modulator length of $L_{\text{mod}} = 120$ mm using the ideal form of dispersion given in Eq. (3.16). The modulating pulse is split into its central, redshifted and blueshifted frequency components to demonstrate how applying this dispersion makes the red and blueshifted pulsetrains overlap and form a regularly spaced pulsetrain useful for driving wakefields.

3.3 Stability of the Plasma Modulator

Since we seek to purposely modulate a laser pulse in a plasma over long propagation distances, questions of instabilities breaking up the drive pulse before it has enough spectral modulation for compression will naturally arise. Since we do not want to waste any of the drive pulse energy within the modulator stage, we ideally want its envelope to remain smooth as it propagates. The smoothness of the modulated drive pulse envelope relies on the symmetry and phase between the generated redshifted Stokes and blueshifted anti-Stokes sidebands. If something causes them to deviate, then the drive pulse would start driving its own wake and self-modulate.

A typical signature in PIC simulations of the modulation scheme undergoing unwanted self-modulation is when the Stokes sidebands accumulate more energy than the anti-Stokes, usually indicating that the drive pulse has undergone some form of break-up and is driving its own wake in the modulator causing redshifting via depletion, an example of which is outlined in Figure (3.7).



(a) $W_{\text{drive}} = 600$ mJ (b) $W_{\text{drive}} = 1200$ mJ

Figure 3.7: Relative transmitted energies of the drive pulse in the modulator and its central, redshifted and blueshifted frequency components from WarpX 2D simulations with the same parameters as [1] for a drive pulse energies of 600 mJ and 1200 mJ respectively. Similar to the findings in [1], the energy in the red and blueshifted pulsetrains in the 600 mJ case remain nearly identical even up to 350 mm of propagation, well beyond the $\sim$ 100 mm required for compression into a pulse train. However, doubling the drive pulse energy results in self-modulation starting at a distance of 60 mm, which causes the Stokes to accumulate more energy than the anti-Stokes. This energy is expressed in higher order transverse modes which readily leak out of the channel, causing a significant drop in the total energy in the drive pulse.

Although the specific set of parameters used in the original P-MoPA proposal [1] have been shown to work in simulation, for the scheme to be practical we would instead like to have a large, well-defined parameter space where we know the scheme is stable. These parameters include, but are not limited to, the energies of the seed and drive pulses, their wavelength, spot size and duration, the plasma density and the plasma channel profile (HOFI/CHOFI and their timing), and the length of the modulator. Whilst theory calculations such as evaluating wakefields and spectral shifts in Eqs. (2.88, 3.4) are useful for performing large parameter scans of the scheme, we will combine them with PIC simulations and better physical understanding to set constraints from destructive self-modulation effects.

3.3.1 Group Velocity Dispersion

As the pulse spectrally modulates, we want to avoid group velocity dispersion (GVD) which would prematurely form pulse trains within the plasma modulator. We expect GVD to come from three main sources: density perturbations from the seed wake, color differences between (anti-)Stokes sidebands, and excitation of higher order

guided transverse modes. Combining the contributions from all of these effects in the weakly relativistic limit gives the following expression for the group velocity of Laguerre-Gaussian modes in a matched parabolic channel with a seed wake

$$\frac{v_g^{N,pm}(\xi;|a|^2)}{c} \approx 1 - \frac{\omega_{p0}^2}{2\omega_L^2}\left(1 + \langle pm|\,\frac{\delta n(r,\xi;|a_s|^2)}{n_{00}} - \frac{n_0(r)}{n_{00}}|a|^2/4\,|pm\rangle - (N-\tfrac{1}{4})\frac{\omega_{p0}^2}{\omega_L^2}\right) - (2p+|m|+1)\frac{2}{k_L^2 w_0^2} \tag{3.17}$$

where $N = 0, \pm 1, ...$ corresponds to the $N < 0$ Stokes (redshifted) and $N > 0$ anti-Stokes (blueshifted) sidebands generated by the seeded spectral modulation.

In the plasma modulator, the primary source of GVD comes from the density perturbation δn, followed by the higher order transverse modes if present. Using the relation between the density perturbation and the spectral modulation in Eq. (3.4), we get the following constraint on the modulator to avoid GVD prematurely longitudinally compressing into pulse trains

$$\frac{\Delta\omega(\xi; L_{\rm mod})}{\omega_L} \ll 1 \tag{3.18}$$

which states that the final spectral modulation of the instantaneous frequency must be small. In practice, we only need spectral modulation of the instantaneous frequency on the order of a few percent for good compression into a multipulse train for the accelerator stage, so this source of GVD does not pose an issue to the plasma modulator scheme.

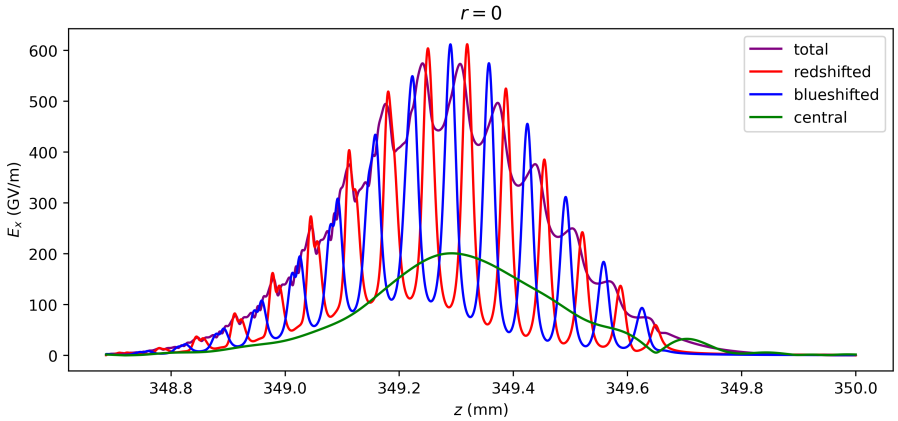


Figure 3.8: On-axis drive pulse envelope in the modulator and its central, redshifted and blueshifted frequency components from a WarpX 2D PIC simulation using the same parameters as the proposed scheme in [1]. After enough spectral modulation has occurred (much more than required for compression into a multipulse train), the red and blueshifted pulsetrains start to overlap due to GVD and prematurely form a small pulsetrain within the modulator stage.

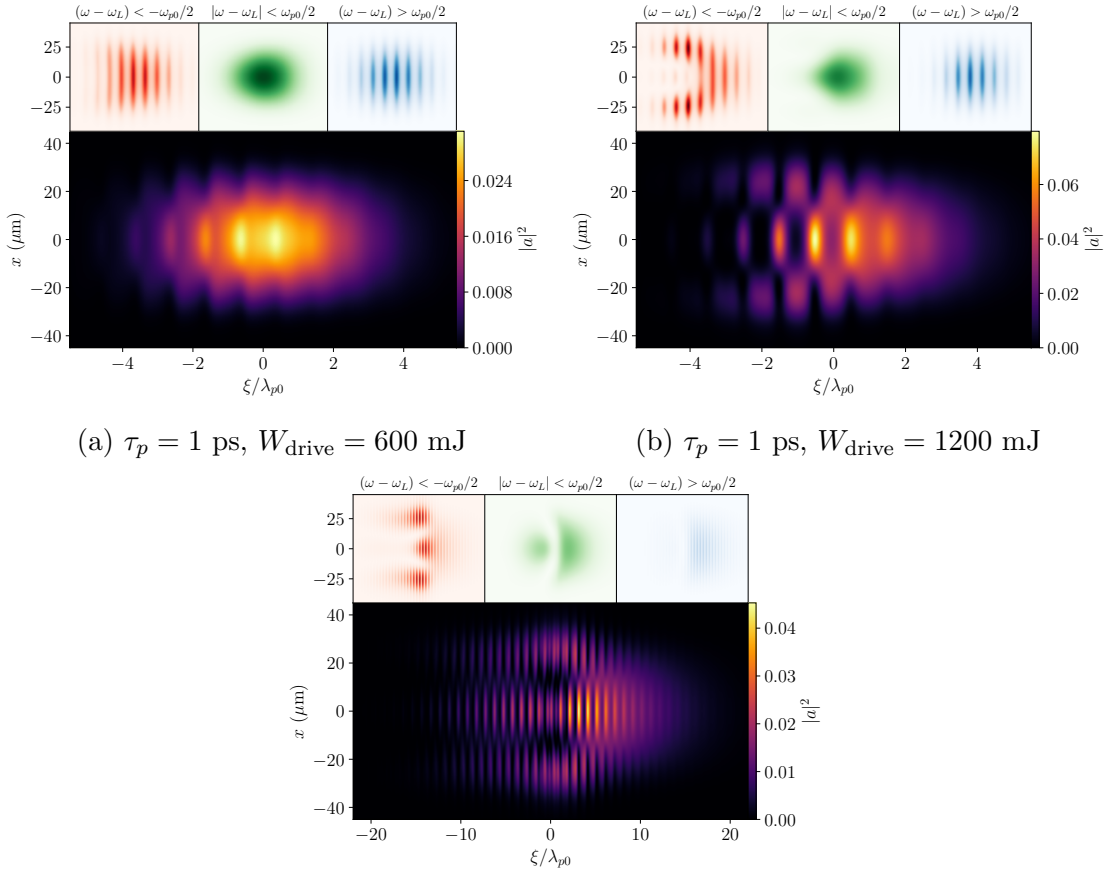
The difference in group velocities between the different sidebands purely due to their different colors is the weakest effect. Instead, the Stokes sidebands tend to be slower than the anti-Stokes as they tend to populate higher order Laguerre-Gaussian modes with sufficient drive energy, the mechanism of which will be discussed in the next section. Ideally, the modulator should be operating in a regime where higher order transverse modes are not excited, as they leak energy more readily from the channel and drive their own wakes. Hence GVD on its own does not constrain the plasma modulator, but is rather a symptom of other self-modulation effects having occurred already.

3.3.2 Defocusing of Stokes Sidebands Driving Transverse Mode Transitions

In PIC simulations of the plasma modulator, we have found that the primary source of destructive self-modulation of the drive pulse is asymmetry of the transverse dynamics of the central, redshifted and blueshifted components of the drive pulse. Previous simulation work [94] found that the Stokes sidebands tend to undergo larger transverse oscillations than the anti-Stokes. In our PIC simulations, we have

found that specifically the trailing half of the redshifted pulsetrain undergoes these transverse oscillations whilst similarly the blueshifted remains relatively stable.

This symmetry-breaking between the red and blueshifted pulse trains causes the total drive envelope to form a time-varying modulation resonant with the plasma. A snapshot of this is shown in Figure (3.9), where drive energies above the original proposal [1] were simulated to produce this effect. This wastes energy and reduces the quality of the compressed pulse for the accelerator stage. Note that despite the presence of severe defocusing of the trailing half of the redshifted pulsetrain for the $W_{\text{drive}} = 1200$ mJ case in Figure (3.9), it is still possible for the pulse to be compressed into a usable pulse train for the accelerator stage as shown in Figure (3.10), meaning that the P-MoPA scheme is still resilient up to a limit against this type of modulation.



(a) $\tau_p = 1$ ps, $W_{\mathrm{drive}} = 600$ mJ

(b) $\tau_p = 1$ ps, $W_{\mathrm{drive}} = 1200$ mJ

(c) $\tau_p = 4$ ps, $W_{\mathrm{drive}} = 2400$ mJ

Figure 3.9: Modulated drive pulses from WarpX 2D PIC simulations in a square channel with $n_{00} = 2.5 \times 10^{17}$ cm^{-3}, $w_0 = 30$ μm, $\lambda_L = 1030$ nm, $W_{\mathrm{seed}} = 50$ mJ, $\tau_{\mathrm{seed}} = 40$ fs and $L_{\mathrm{mod}} = 110$ mm. The top row displays the pulse decomposed into its redshifted, central and blueshifted components, and the bottom displays the full drive pulse envelope at the end of the modulator stage. The Stokes sidebands get progressively more defocused towards the trailing end of the pulse forming higher order transverse modes, whilst the anti-Stokes remains stable. This transverse asymmetry between the Stokes and anti-Stokes prematurely forms small pulse trains in the plasma modulator, with the Stokes forming a train off-axis and the anti-Stokes a train on-axis. This effect gets progressively worse at higher drive pulse energies, and is especially bad for the 2400 mJ pulse which has undergone severe transverse break-up and has strongly redshifted.

However, the spectral modulation we previously derived in Eq. (3.3) does not suggest any transverse asymmetry between the generated Stokes and anti-Stokes sidebands. This is because we did not include any relativistic nor non-paraxial effects. It is known from previous studies in plasma beatwave accelerators [95] that generated Stokes sidebands have a tendency to be defocused and anti-Stokes fo-

cused due to a frequency mismatch between the beatwave frequency and the plasma frequency due to the relativistic mass increase of electrons. The main difference between these studies and the plasma modulator is the presence of the seed wake modulating an initially monochromatic pulse into sidebands. The angular divergence for the first Stokes $\omega = \omega_L - \omega_{p0}$ and anti-Stokes $\omega = \omega_L + \omega_{p0}$ sidebands generated from the central frequency $\omega = \omega_L$ is given by [95]

$$\langle \theta_{\pm 1}^2 \rangle = \langle \theta_0^2 \rangle \mp (2\omega_{p0}/\omega_L)(\Delta - \delta) \tag{3.19}$$

where $\Delta \approx \frac{3}{16}(v_p/c)^2$ is the weakly relativistic correction from the plasma oscillations and δ is the frequency mismatch between the beatwave frequency and the local plasma frequency. Because of this effect, the Stokes and anti-Stokes light will undergo small out-of-phase spot size oscillations along the plasma channel.

Since the plasma modulator works by generating well-defined Stokes and anti-Stokes sidebands separated by the plasma frequency, any asymmetry in the production or transverse dynamics between the Stokes and anti-Stokes sidebands would naturally form resonant beatwave pulse trains, which are apparent in Figure (3.9). These out-of-phase spot size oscillations between the Stokes and anti-Stokes can thus seed a self-modulation instability with the resonant beatwaves they form driving their own wakes. Small spot size oscillations in matched parabolic channels evolve according to [96]

$$w^2(\tau) \approx \frac{w_i^2}{2}\left[1 + \frac{w_0^4}{w_i^4} + \left(1 - \frac{w_0^4}{w_i^4}\right)\cos\left(\Omega_w \tau\right)\right] \tag{3.20}$$

where w_i is the initial spot size and $\Omega_w = 4\omega_L/k_L^2 w_0^2$ is the spot size oscillation frequency. Since the separated Stokes and anti-Stokes form small beatwave pulse trains resonant with the plasma, they will drive a resonantly growing self-wake along the drive pulse which varies in time with the spot size oscillation frequency. To model this effect, we can add a small nonlinear self-wake term δn_{NL} to Eq. (3.1) whose

time dependence is primarily driven by these spot size oscillations

$$\left[\frac{i}{\omega_L}\frac{\partial}{\partial\tau}+\frac{c^2}{2\omega_L^2}\Delta_\perp\right]a=\frac{\omega_p^2}{2\omega_L^2 n_0}\left[\delta n_0(r)+\delta n(r,\xi;|a_s|^2)+\delta n_{\rm NL}(r,\xi;|a|^2)\right]a\,. \quad (3.21)$$

In fact, the spot size oscillation frequency Ω_w happens to be perfectly resonant with the frequency shift between the guided radial Laguerre-Gaussian modes, as evident in Eq. (2.12). This means that if the modulating drive pulse contains enough energy to drive an appreciable Stokes-defocusing-induced self-wake $\delta n_{\rm NL}\sim\delta\tilde{n}_{\rm NL}\cos(\Omega_w\tau)$, then spot-size oscillations of the Stokes will naturally drive $\mathrm{LG}_{p,m}\leftrightarrow\mathrm{LG}_{p+1,m}$ radial mode transitions (or $\mathrm{HG}_{l,m}\leftrightarrow\mathrm{HG}_{l+2,m}$ Hermite-Gaussian mode transitions in 2D geometry). These transitions will have a characteristic "Rabi frequency" of

$$\Omega_{p\to p+1}\sim\frac{\Omega_w}{2}\frac{\langle p+1,m|\,\delta\tilde{n}_{\rm NL}\,|pm\rangle}{\Delta n} \quad (3.22)$$

which grows towards the tail of the drive pulse via resonant beatwave drive and also grows roughly linearly with propagation distance as more red/blueshifted light is generated by the spectral modulation. This picture is consistent with the simulation results in Figs. (3.9, 3.10), where the higher order modes are only populated towards the tail of the pulse and only for pulses with sufficient energy to drive a self-wake as they undergo mismatched spot size oscillations.

A similar argument can be made for small centroid oscillations which have a frequency of $\Omega_c=\Omega_w/2$ [96]. These are instead resonant with the frequency shifts between azimuthal Laguerre-Gaussian modes, thus driving $\mathrm{LG}_{p,m}\leftrightarrow\mathrm{LG}_{p,m+1}$ transitions (or $\mathrm{HG}_{l,m}\leftrightarrow\mathrm{HG}_{l+1,m}$ in 2D). This may pose a problem if the drive pulse is initially offset from the plasma channel axis.

This tendency for asymmetric spot size oscillations between the generated Stokes and anti-Stokes light to drive radial mode transitions sets a fundamental constraint on the plasma modulator. To define the parameter space in which the plasma modulator is stable, we require that sufficient spectral modulation has occurred for pulse compression into a pulse train before this process has a chance to severely break-up the drive pulse. Since this process is highly nonlinear, we conducted numerical

studies with PIC simulations and found a single parameter which captures the constraint set by this instability. We also independently derive this stability parameter analytically.

3.3.3 Transverse Mode Stability Condition

This transverse mode instability can also be understood as a form of the envelope self-modulation instability we derived in Eq. (2.31), but differs both due to the presence of the seed wake and the possibility for an initial channel mismatch. In the following derivation of the modulator stage stability condition, rather than calculating the full instability, we will instead work in the low-intensity limit and calculate the self-consistent oscillatory wake excited by the drive pulse due to modulations caused by the seed wake and channel mismatch. The transverse structure of this wake will oscillate at the spot size oscillation frequency, and could therefore resonantly excite transverse mode transitions if its amplitude is sufficiently large. For stability, we thus require the cumulative effects of this oscillating wake on the drive pulse to be small relative to those of the seed wake at the end of the modulator stage.

To estimate the rate at which the modulating drive pulse undergoes transverse mode transitions, consider coupling the drive pulse into a slightly unmatched channel such that it undergoes some small spot size oscillations, and assume a fixed seed pulse for steady generation of (anti-)Stokes sidebands. For now, we will also assume that no centroid oscillations are present, leaving only radial Laguerre-Gaussian modes LG_{p0}. According to the paraxial time-dependent perturbation theory derived in Eq. (2.23), the coefficients of each radial Laguerre-Gaussian mode composing the drive

pulse envelope as it propagates in the plasma modulator evolve in time according to

$$\begin{aligned} i\frac{\partial \alpha_p(\xi,\tau)}{\partial \tau} &= \sum_n \alpha_n(\xi,\tau)\frac{\Omega_w}{2}\left\langle p0\right| \frac{\delta n + \delta n_{\mathrm{NL}}}{\Delta n}\left|n0\right\rangle e^{i(p-n)\Omega_w\tau} \\ &= \frac{\omega_{p0}^2}{2\omega_L}\sum_n \alpha_n(\xi,\tau)\left\langle p0\right| \frac{\delta n + \delta n_{\mathrm{NL}}}{n_{00}}\left|n0\right\rangle e^{i(p-n)\Omega_w\tau}, \\ a(r,\xi,\tau)e^{i\Omega_c\tau} &= \sum_p \alpha_p(\xi,\tau)\mathrm{LG}_{p0}e^{-ip\Omega_w\tau} \end{aligned} \tag{3.23}$$

where δn is the fixed seed wake, δn_{NL} is the nonlinear self-wake of the drive pulse, $\Omega_c = \Omega_w/2 = 2\omega_L/k_L^2 w_0^2$ are the centroid and spot size oscillation frequencies and $\alpha_p(\xi,\tau)$ indicates the complex amplitude of the radial Laguerre-Gaussian mode p at longitudinal coordinate ξ. Coupling the drive pulse into a slightly unmatched channel gives rise to the following set of initial conditions

$$\alpha_0(\xi,\tau=0) = a_0 f(\xi), \quad \alpha_1(\xi,\tau=0) = \epsilon_w a_0 f(\xi), \quad \alpha_{p\neq 0,1}(\xi,\tau=0) = 0 \tag{3.24}$$

where $\epsilon_w = (1 - w_i^2/w_0^2)/2 \approx -\delta w/w_0 \ll 1$ is the channel mismatch parameter. With these initial conditions along with Eq. (3.23), the only thing we are missing to describe the full time evolution of the drive pulse in the plasma modulator is the self-wake δn_{NL}. In this analysis, we will first assume that the self-wake can be neglected, and calculate only the intensity modulation of the drive pulse caused by the seed wake. We will then use this intensity modulation to calculate the self-wake it would excite. This estimate of the self-wake can then be used to define the plasma modulator stability condition, which sets bounds on the laser/plasma parameters to prevent nonlinear self-modulation from exciting transverse mode transitions.

For convenience, we will be working in the shallow channel limit, which results in a fixed seed wake approximately of the form $\delta n(r,\xi) \approx \delta n_s \cos(k_{p0}\xi)\mathrm{LG}_{00}^2$. Ignoring the nonlinear self-wake, substituting this seed wake into Eq. (3.23) gives

$$i\frac{\partial \alpha_p(\xi,\tau)}{\partial \tau} = \frac{\omega_{p0}^2}{2\omega_L}\frac{\delta n_s \cos(k_{p0}\xi)}{n_{00}}\sum_n \alpha_n(\xi,\tau)\left\langle p0\right|\mathrm{LG}_{00}^2\left|n0\right\rangle e^{i(p-n)\Omega_w\tau} \tag{3.25}$$

As we want the drive pulse in the plasma modulator to remain primarily in the

fundamental mode, we can approximate this as a two-level system of the fundamental and first radial modes

$$\begin{aligned} i\frac{\partial \alpha_0(\xi,\tau)}{\partial \tau} &= 2\Omega_s \cos(k_{p0}\xi)\left(\alpha_0 + \tfrac{1}{2}\alpha_1 e^{-i\Omega_w \tau}\right) , \\ i\frac{\partial \alpha_1(\xi,\tau)}{\partial \tau} &= 2\Omega_s \cos(k_{p0}\xi)\left(\tfrac{1}{2}\alpha_0 e^{i\Omega_w \tau} + \tfrac{1}{2}\alpha_1\right) \end{aligned} \tag{3.26}$$

where $\Omega_s = (\omega_{p0}^2/8\omega_L)(\delta n_s/n_{00})$ is the rate of spectral modulation parameter. We can already see from these expressions that the first radial mode spectrally modulates half as fast as the fundamental mode, as it is more suppressed by the radial drop-off of the seed wake amplitude $\sim \mathrm{LG}_{00}^2$. This will be one of the two main effects contributing to plasma-resonant modulations of the drive pulse intensity which will excite a self-wake. To solve these two coupled PDEs we first write them in matrix form

$$\begin{aligned} &\frac{\partial \boldsymbol{\alpha}}{\partial \tau} = \boldsymbol{D}(\xi,\tau)\boldsymbol{\alpha} , \\ &\boldsymbol{D}(\xi,\tau) = -i\gamma(\xi)\begin{pmatrix} 1 & \frac{1}{2}\exp(-i\Omega_w\tau) \\ \frac{1}{2}\exp(i\Omega_w\tau) & \frac{1}{2} \end{pmatrix} , \end{aligned} \tag{3.27}$$

where $\boldsymbol{\alpha} = (\alpha_0, \alpha_1)^\top$ and $\gamma(\xi) = 2\Omega_s \cos(k_{p0}\xi)$. Since the matrix $\boldsymbol{D}$ commutes with its time integral, the solution to this system of PDEs can be obtained by taking the matrix exponent of the time integral of $\boldsymbol{D}$

$$\begin{aligned} &\boldsymbol{\alpha}(\xi,\tau) = \boldsymbol{A}(\xi,\tau)\boldsymbol{\alpha}(\xi,0) , \\ &\boldsymbol{A}(\xi,\tau) = \exp\left[\int_0^\tau ds \boldsymbol{D}(\xi,s)\right] \\ &= \exp\left[-i\gamma\tau\begin{pmatrix} 1 & \frac{1}{2}\,\mathrm{sinc}(\Omega_w\tau/2)e^{-i\Omega_w\tau/2} \\ \frac{1}{2}\,\mathrm{sinc}(\Omega_w\tau/2)e^{i\Omega_w\tau/2} & \frac{1}{2} \end{pmatrix}\right] . \end{aligned} \tag{3.28}$$

To take the matrix exponential we then diagonalize the matrix

$$\begin{aligned}
\boldsymbol{\alpha}(\xi,\tau) &= \exp\left(\boldsymbol{V}\boldsymbol{D}\boldsymbol{V}^{-1}\right)\boldsymbol{\alpha}(\xi,0) \\
&= \boldsymbol{V}\exp\left(\boldsymbol{D}\right)\boldsymbol{V}^{-1}\boldsymbol{\alpha}(\xi,0) \\
&= e^{-\frac{3}{4}i\gamma\tau}\boldsymbol{V}\begin{pmatrix} e^{-\frac{\sigma}{4}i\gamma\tau} & 0 \\ 0 & e^{\frac{\sigma}{4}i\gamma\tau}\end{pmatrix}\boldsymbol{V}^{-1}\boldsymbol{\alpha}(\xi,0) \\
\boldsymbol{V}(\tau) &= \begin{pmatrix} \frac{1}{2}(1-e^{-i\Omega_w\tau}) & \frac{1}{2}(1-e^{-i\Omega_w\tau}) \\ -\frac{1}{4}i\Omega_w\tau(1-\sigma) & -\frac{1}{4}i\Omega_w\tau(1+\sigma)\end{pmatrix} \\
\sigma(\tau) &= \sqrt{1+4\,\mathrm{sinc}^2(\Omega_w\tau/2)}
\end{aligned} \tag{3.29}$$

Note that $\gamma/\Omega_w \ll 1$ is an equivalent statement to the original $\delta n \ll \Delta n$ condition, which means that the off-diagonal terms of $\boldsymbol{A}(\xi,\tau)$ must be small in regions of high intensity for this TDPT treatment to be self-consistent. Over long propagation distances $\Omega_w\tau \gg 1$, this solution simplifies to

$$\begin{aligned}
&\boldsymbol{A}(\xi,\Omega_w\tau\gg 1) \\
&\approx \begin{pmatrix} \left[1-\left(\frac{\gamma}{2\Omega_w}\right)^2\sin^2(\frac{1}{2}\Omega_w\tau)\right]e^{-i\gamma\tau} & \frac{\gamma}{2\Omega_w}\mathrm{sinc}(\frac{1}{4}\gamma\tau)(e^{-i\Omega_w\tau}-1)e^{-\frac{3}{4}i\gamma\tau} \\ \frac{\gamma}{2\Omega_w}\mathrm{sinc}(\frac{1}{4}\gamma\tau)(1-e^{i\Omega_w\tau})e^{-\frac{3}{4}i\gamma\tau} & \left[1-\left(\frac{\gamma}{2\Omega_w}\right)^2\sin^2(\frac{1}{2}\Omega_w\tau)\right]e^{-\frac{1}{2}i\gamma\tau}\end{pmatrix}
\end{aligned} \tag{3.30}$$

As we only require a spectral modulation on the order of a few percent, i.e. $\Delta\omega/\omega_L \ll 1$, we can also safely take the limit $\mathrm{sinc}(\frac{1}{4}\gamma\tau) \approx 1$. Therefore to first order in γ/Ω_w and channel mismatch ϵ_w, this then yields the following modulation of the pulse envelope

$$\frac{a(r,\xi,\tau)e^{i\Omega_c\tau}}{a_0 f(\xi)} = \mathrm{LG}_{00} + \left(\frac{\gamma}{2\Omega_w}(1-e^{i\Omega_w\tau})e^{-\frac{3}{4}i\gamma\tau} + \epsilon_w e^{-\frac{1}{2}i\gamma\tau}\right)\mathrm{LG}_{10}e^{-i\Omega_w\tau} \tag{3.31}$$

from which we can calculate the intensity modulation to first order

$$\frac{|a(r,\xi,\tau)|^2}{|a_0|^2 f^2(\xi)} = \mathrm{LG}_{00}^2 + \left[\left(\frac{\gamma}{2\Omega_w}(e^{-i\Omega_w\tau}-1)e^{-\frac{3}{4}i\gamma\tau} + \epsilon_w e^{-\frac{1}{2}i\gamma\tau - i\Omega_w\tau}\right) + \text{c.c.}\right]\mathrm{LG}_{00}\mathrm{LG}_{10}\,. \tag{3.32}$$

Substituting $\gamma(\xi) = 2\Omega_s\cos(k_{p0}\xi)$ and assuming that ϵ_w is real then yields

$$\begin{aligned}\frac{|a(r,\xi,\tau)|^2}{|a_0|^2 f^2(\xi)} = \mathrm{LG}_{00}^2 &+ \Big\{\frac{2\Omega_s\cos(k_{p0}\xi)}{\Omega_w}\left(\cos[\tfrac{3}{2}\Omega_s\tau\cos(k_{p0}\xi)+\Omega_w\tau] - \cos[\tfrac{3}{2}\Omega_s\tau\cos(k_{p0}\xi)]\right) \\ &+ 2\epsilon_w\cos[\Omega_s\tau\cos(k_{p0}\xi)+\Omega_w\tau]\Big\}\mathrm{LG}_{00}\mathrm{LG}_{10}\,.\end{aligned} \tag{3.33}$$

This intensity modulation can be physically understood by splitting it into three main effects. The first effect is a longitudinally uniform spot size oscillation of amplitude δw, which can be recovered by simply setting $\Omega_s = 0$ (i.e. by removing the seed wake). The second effect comes from coupling between the δw spot size oscillations and the seed wake spectral modulation due to the fact discussed earlier that higher order radial modes spectrally modulate slower in the $\sim \mathrm{LG}_{00}^2$ seed wake. The third effect depends purely on the seed wake, which can be seen when setting $\epsilon_w = 0$. The seed wake introduces local variations in the matched spot size as it perturbs the channel plasma density, causing longitudinally varying spot size oscillations.

To estimate the self-wake δn_{NL} that would be excited by this intensity modulation, we are only interested in keeping terms resonant with the plasma ($\sim \cos(k_{p0}\xi+\phi)$ with arbitrary phase ϕ) which can resonantly drive a self-wake. We are also only interested in propagation times up to $\Omega_s\tau_{\mathrm{mod}} \sim 1/2$, as this provides sufficient spectral modulation for compression into a well-defined pulse train. With both

of these considerations in mind, we can make use of the following Taylor expansion

$$\begin{aligned}\cos\left[\Omega_s\tau\cos(k_{p0}\xi)+\Omega_w\tau\right] \approx{}& \cos(\Omega_w\tau)-\Omega_s\tau\cos(k_{p0}\xi)\sin(\Omega_w\tau)\\ &-\frac{(\Omega_s\tau)^2(1+\cos(2k_{p0}\xi))}{4}\cos(\Omega_w\tau)\\ &+\frac{(\Omega_s\tau)^3(\cos(k_{p0}\xi)+\cos(3k_{p0}\xi)/3)}{8}\sin(\Omega_w\tau)\end{aligned}\tag{3.34}$$

which shows that we can safely work in only to first order in $\Omega_s\tau \lesssim 1/2$ as long as we only care about the plasma-resonant terms. Substituting this expansion into Eq. (3.33) and keeping only the resonant terms gives us the following plasma-resonant part of the intensity modulation

$$\frac{|a(r,\xi,\tau)|^2_{\text{res}}}{|a_0|^2 f^2(\xi)} = \left(-2\epsilon_w\Omega_s\tau\sin(\Omega_w\tau)+\frac{2\Omega_s\left[\cos(\Omega_w\tau)-1\right]}{\Omega_w}\right)\cos(k_{p0}\xi)\mathrm{LG}_{00}\mathrm{LG}_{10}\,.\tag{3.35}$$

For a drive pulse with a duration of at least a few plasma periods, in the shallow channel limit the wake resonantly driven by this intensity modulation is approximately given by

$$\begin{aligned}&\frac{\delta n_{\text{NL}}(r,\xi,\tau)}{n_{00}\mathrm{LG}_{00}\mathrm{LG}_{10}}\\ &\approx\left(-2\epsilon_w\Omega_s\tau\sin(\Omega_w\tau)+\frac{2\Omega_s\left[\cos(\Omega_w\tau)-1\right]}{\Omega_w}\right)\sin(k_{p0}\xi)k_{p0}\left|\int_\infty^\xi d\xi'|a_0|^2f^2(\xi')/8\right|\\ &=\frac{e^2}{4\pi^2m_e^2\epsilon_0c^5}\frac{\omega_{p0}W_{\text{drive}}(\xi)\lambda_L^2}{\pi w_0^2}\sin(k_{p0}\xi)\left(\epsilon_w\Omega_s\tau\sin(\Omega_w\tau)+\frac{\Omega_s\left[\cos(\Omega_w\tau)-1\right]}{\Omega_w}\right)\end{aligned}\tag{3.36}$$

where $W_{\text{drive}}(\xi)$ indicates the total energy of the drive pulse contained between its head and coordinate ξ, hence the self-wake amplitude and thus nonlinear self-modulation effects grow towards the tail of the drive pulse. To prevent severe nonlinear self-modulation driving transverse mode transitions (and to make this calculation self-consistent), we require that the effects of the self-wake must be negligible compared to that of the seed wake. This means that the following constraint must

be observed throughout the full propagation in the modulator

$$\int_0^{\tau_{\rm mod}} \frac{d\tau}{\tau_{\rm mod}} \langle 10| \left|\delta n_{\rm NL} e^{i\Omega_w \tau} |00\rangle \ll \langle 10| \, \delta n \, |00\rangle \right. . \tag{3.37}$$

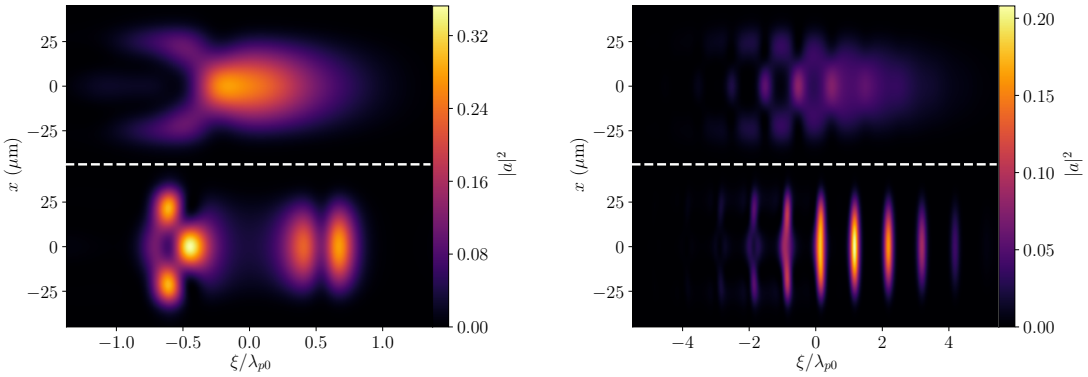
Substituting Eq. (3.36) into this constraint leads to the condition

$$\frac{e^2}{8\pi^2 m_e^2 \epsilon_0 c^5} \frac{\omega_{p0} W_{\rm drive} \lambda_L^2}{\pi w_0^2} \left| \frac{\delta w}{w_0} \frac{\Omega_s \tau_{\rm mod}}{2} + \frac{k_{p0}^2 w_0^2}{16} \frac{\delta n_s}{2 n_{00}} \right| \ll \frac{\delta n_s}{n_{00}} \, . \tag{3.38}$$

As mentioned earlier, for sufficient spectral modulation for compression into a pulse train, we require $\Omega_s \tau_{\rm mod} \sim 1/2$. Substituting this in Eq. (3.38) finally yields the plasma modulator transverse mode stability condition

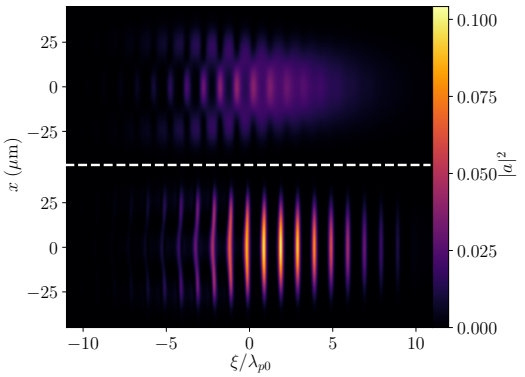
$$\left| \frac{\delta w / w_0}{\delta n_s / n_{00}} + \frac{k_{p0}^2 w_0^2}{8} \right| \frac{\omega_{p0} W_{\rm drive} \lambda_L^2}{\pi w_0^2} \ll 220 \text{ GW} \, . \tag{3.39}$$

This sets a limit on the total energy of the drive pulse $W_{\rm drive}$ for a given plasma density, spot size, laser wavelength, seed wake and spot size oscillation amplitude. Note that for a fixed seed pulse energy, increasing the spot size can only help by reducing the relative channel spot mismatch due to the seed wake amplitude weakening with w_0^2. To emphasize the dependence on total pulse energy rather than intensity, Figure (3.10) presents results from PIC simulations at the end of the modulator stage for drive pulses of fixed energy but varying durations, all undergoing the same transverse mode instability.

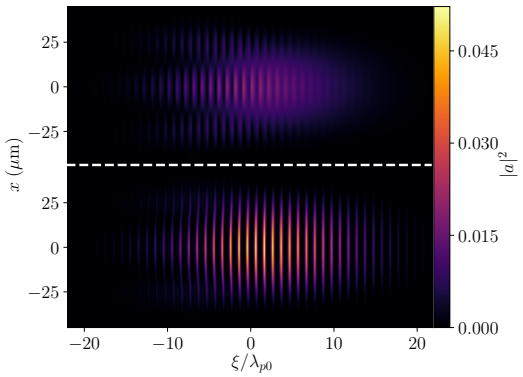


(a) $\tau_p = 250$ fs

(b) $\tau_p = 1$ ps



(c) $\tau_p = 2$ ps



(d) $\tau_p = 4$ ps

Figure 3.10: Drive pulse envelopes after modulation both before (top) and after (bottom) compression into a pulse train for $W_{\text{drive}} = 1200$ mJ with FWHM durations of 250 fs, 1 ps, 2 ps and 4 ps respectively. Despite their different durations, since they all have the same total energy, they each undergo the same amount of defocusing of Stokes sidebands and spot size oscillation driven transitions to higher order transverse modes, resulting in identical transverse structures. Despite this transverse structure, even in this case every pulse except the 250 fs case still compresses into a well-defined pulse train suitable for the accelerator stage. Note that the 250 fs pulse does not compress well only because of its broad bandwidth relative to the plasma frequency.

For example, substituting the laser/plasma parameters used in the original proposal [1] into Eq. (3.39), which has a $\delta n_s/n_{00} \sim 2.5\%$ seed wake and undergoes $|\delta w|/w_0 \sim 12\%$ spot size oscillations, we recover 37 GW. In this regime, we do not expect the self-modulation effects to be debilitating to the plasma modulator, but they should still be somewhat present. In PIC simulations, we have found that even going up to ~ 70 GW remains stable enough for good compression into a pulse train

despite having transitions to the first radial mode.

For most practical applications, the spot size oscillations will be determined primarily by the mismatch between the laser transverse profile at focus and the channel (e.g. coupling a Gaussian pulse into a non-parabolic channel) and can be reasonably expected to be on the order of $\sim 10\%$. However, even in the limit of a perfectly matched channel, we do still expect small spot size oscillations from other sources such as from both ponderomotive and relativistic self-focusing. In addition, the $k_{p0}^2 w_0^2/8$ term in Eq. (3.39), which comes from the plasma-resonant variation in matched spot size, ensures that there will always be an upper limit on the drive pulse energy even in a perfectly matched channel.

There are a couple of ways these transitions to higher order transverse modes can be somewhat mitigated beyond this condition, but they come at a cost. Firstly, this derivation assumed propagation in a shallow channel. If we allow for larger channel depths relative to the on-axis density $\Delta n \sim n_{00}$, then the wake driven by the interfering sidebands will be partially suppressed by the slightly off-resonant plasma and the difference in spectral modulation rate of the higher order mode and the fundamental will be decreased due to the radial component of the seed wake. This allows for more energy to propagate in the modulator without transitions to higher order modes. However, such a channel will also suppress the spectral modulation towards the tail of the pulse, as discussed earlier in this chapter and demonstrated in Figs. (3.4, 3.5), which is detrimental to pulse compression. Another option is to use a sufficiently leaky channel, which leaks out higher order modes faster than the fundamental mode, but comes at the cost of losing a large fraction of the drive pulse energy, as this process continuously pumps energy from the fundamental to higher order modes.

We can follow a similar procedure to derive a plasma modulator stability condition but for centroid oscillations caused by laser jitter rather than spot size mismatch. Assuming a small laser centroid offset $\delta x_c/w_0 \ll 1$, the plasma modulator

stability condition is modified to

$$\left(\left|\frac{\delta w/w_0}{\delta n_s/n_{00}}+\frac{k_{p0}^2 w_0^2}{8}\right|+\frac{1}{2}\sqrt{\frac{\pi}{2}}\frac{|\delta x_c|/w_0}{\delta n_s/n_{00}}\right)\frac{\omega_{p0}W_{\text{drive}}\lambda_L^2}{\pi w_0^2}\ll 220\text{ GW}\,. \tag{3.40}$$

Note that the contribution from centroid oscillations to the stability condition is less stringent than that for spot size oscillations as the centroid oscillation frequency is only half that of the spot size oscillation frequency $\Omega_c = \Omega_w/2 = 2\omega_L/k_L^2 w_0^2$. Nevertheless, this sets a limit on how much laser jitter the plasma modulator can tolerate.

3.3.4 Seed Pulse Donut Mode Effects

The previous analysis assumed that the seed pulse is perfectly matched to the plasma channel, and therefore provides a propagation-invariant wake for spectral modulation. However, in general, the seed pulse may also not be perfectly matched to the plasma channel, which can lower the total drive energy the plasma modulator can accept. It is therefore important to simultaneously match both the seed and drive pulses to the channel.

However, simultaneously matching the seed and drive pulses is not as simple as using the same focusing system for both. This is because the short seed pulse to be generated at the kHz rep-rate must be temporally compressed using a Herriott cell [97]. With current technology, in order to allow energies on the order of $\sim 100\,\text{mJ}$ required for the plasma modulator, the input seed pulse is in the form of a $p = 0, m = 1$ donut mode [98]. After leaving the Herriott cell, a vortex plate is used to remove its orbital angular momentum (OAM). However, if the same focusing system is used for this pulse, then the resultant spot size will be tighter than that of the drive pulse, which we will derive below.

Assuming that the pulse coming out of the Herriott cell is exactly in the $\text{LG}_{01}(r,\theta)$ donut mode, the pulse immediately after the compensating output vortex plate which removes the OAM can be written as the following combination of radial

Laguerre-Gaussian modes

$$\begin{aligned}
\mathrm{LG}_{01}e^{-i\theta} &= \sum_{p,m} \langle 01|\, e^{-i\theta}\, |pm\rangle\, \mathrm{LG}_{pm} \\
&= \sum_{p} \langle 01|\, e^{-i\theta}\, |p0\rangle\, \mathrm{LG}_{p0} \\
&= \sum_{p} \left(\int_0^\infty s^{1/2} e^{-s} L_p^0(s) ds \right) \mathrm{LG}_{p0} \\
&= \frac{\sqrt{\pi}}{2} \sum_{p} \frac{\left(-\frac{1}{2}\right)_p}{(1)_p} \mathrm{LG}_{p0} \\
&= \frac{\sqrt{\pi}}{2} \left(\mathrm{LG}_{00} - \tfrac{1}{2}\mathrm{LG}_{10} - \tfrac{1}{8}\mathrm{LG}_{20} - \tfrac{1}{16}\mathrm{LG}_{30} - \tfrac{5}{128}\mathrm{LG}_{40} - ... \right)
\end{aligned} \tag{3.41}$$

where $(x)_n \equiv \Gamma(x+n)/\Gamma(x)$ is the Pochhammer symbol. This integral was first evaluated using Mathematica [47] and then verified analytically using known integral identities of Laguerre polynomials [48]. Propagating this pulse in free space to a focus, the following phase shifts are introduced

$$\begin{aligned}
&\frac{\sqrt{\pi}}{2} \sum_{p} \frac{\left(-\frac{1}{2}\right)_p}{(1)_p} \mathrm{LG}_{p0} e^{i(2p+1)\pi/2} = i\frac{\sqrt{\pi}}{2} \sum_{p} \frac{(-1)^p \left(-\frac{1}{2}\right)_p}{(1)_p} \mathrm{LG}_{p0} \\
&= i\frac{\sqrt{\pi}}{2} \left(\mathrm{LG}_{00} + \tfrac{1}{2}\mathrm{LG}_{10} - \tfrac{1}{8}\mathrm{LG}_{20} + \tfrac{1}{16}\mathrm{LG}_{30} - \tfrac{5}{128}\mathrm{LG}_{40} + ... \right)
\end{aligned} \tag{3.42}$$

which means that the donut mode appears as approximately Gaussian at focus but with a tighter peak and faster transverse drop-off. This pulse can be treated as approximately Gaussian for any process that occurs within a Rayleigh range from focus, but for anything beyond, such as long propagation in a plasma channel, we need to take the higher order radial modes into account. Dropping the i phase-factor, the time-evolution of this pulse in a parabolic plasma channel matched to a Gaussian drive pulse *sharing the same focusing system* is given by

$$\begin{aligned}
&\frac{\sqrt{\pi}}{2} e^{-i\Omega_c \tau} \sum_{p} \frac{(-1)^p \left(-\frac{1}{2}\right)_p}{(1)_p} \mathrm{LG}_{p0} e^{-ip\Omega_w \tau} \\
&= \frac{\sqrt{\pi}}{2} e^{-i\Omega_c \tau} \left(\mathrm{LG}_{00} + \tfrac{1}{2}\mathrm{LG}_{10} e^{-i\Omega_w \tau} - \tfrac{1}{8}\mathrm{LG}_{20} e^{-2i\Omega_w \tau} + ... \right)
\end{aligned} \tag{3.43}$$

Keeping only the fundamental and first order radial modes, this gives us the following approximate intensity modulation

$$I \approx \mathrm{LG}_{00}^2 + \mathrm{LG}_{00}\mathrm{LG}_{10}\cos(\Omega_w \tau) \tag{3.44}$$

Hence (in the shallow channel limit) the seed wake will now take the form

$$\delta n(r,\xi,\tau) = \delta n_s \cos(k_{p0}\xi)\left[\mathrm{LG}_{00}^2 + \mathrm{LG}_{00}\mathrm{LG}_{10}\cos(\Omega_w\tau)\right] \tag{3.45}$$

where δn_s now indicates the propagation-averaged on-axis seed wake amplitude. This time-varying wake will now drive transverse mode transitions of the modulating drive pulse regardless of how low the drive pulse energy is. Again describing the drive pulse as a two-level system of the fundamental and first radial modes, this time-dependent wake gives us the following modification

$$\begin{aligned} i\frac{\partial \alpha_0(\xi,\tau)}{\partial \tau} &= 2\Omega_s \cos(k_{p0}\xi)\left[\left(1+\tfrac{1}{8}\cos(\Omega_w\tau)\right)\alpha_0 + \left(\tfrac{1}{2}+\tfrac{1}{2}\cos(\Omega_w\tau)\right)\alpha_1 e^{-i\Omega_w\tau}\right] , \\ i\frac{\partial \alpha_1(\xi,\tau)}{\partial \tau} &= 2\Omega_s \cos(k_{p0}\xi)\left[\left(\tfrac{1}{2}+\tfrac{1}{2}\cos(\Omega_w\tau)\right)\alpha_0 e^{i\Omega_w\tau} + \left(\tfrac{1}{2}+\tfrac{1}{4}\cos(\Omega_w\tau)\right)\alpha_1\right] . \end{aligned} \tag{3.46}$$

Applying the rotating wave approximation (RWA), which we can apply since we are not currently interested in self-wake effects, then yields

$$\begin{aligned} i\frac{\partial \alpha_0(\xi,\tau)}{\partial \tau} &= 2\Omega_s \cos(k_{p0}\xi)\left(\alpha_0 + \tfrac{1}{4}\alpha_1\right) , \\ i\frac{\partial \alpha_1(\xi,\tau)}{\partial \tau} &= 2\Omega_s \cos(k_{p0}\xi)\left(\tfrac{1}{4}\alpha_0 + \tfrac{1}{2}\alpha_1\right) . \end{aligned} \tag{3.47}$$

which has the following solution assuming the pulse was initially in the fundamental

mode and that no higher order modes beyond the first get populated

$$\begin{aligned}\alpha_0(\xi,\tau) &= a_0 f(\xi) e^{-3i\Omega_s\tau\cos(k_{p0}\xi)/2}\Big[\cos\Big(\Omega_s\tau\cos(k_{p0}\xi)/\sqrt{2}\Big) \\ &\quad - \frac{1}{\sqrt{2}}\sin\Big(\Omega_s\tau\cos(k_{p0}\xi)/\sqrt{2}\Big)\Big] \\ \alpha_1(\xi,\tau) &= a_0 f(\xi) e^{-3i\Omega_s\tau\cos(k_{p0}\xi)/2}\frac{1}{\sqrt{2}}\sin\Big(\Omega_s\tau\cos(k_{p0}\xi)/\sqrt{2}\Big)\end{aligned} \tag{3.48}$$

From this we can see that a compensated donut mode seed will spectrally modulate the drive pulse $\sim 3/4$ times as fast as a fundamental mode seed pulse of the same energy. This means that $\Omega_s\tau_{\rm mod} \sim 2/3$ instead of $\sim 1/2$ is now required for compression into a pulse train. Taking this into account, we can Taylor expand Eq. (3.48) to first order in $\Omega_s\tau$ and recover

$$\begin{aligned}\alpha_0(\xi,\tau) &\approx a_0 f(\xi) e^{-3i\Omega_s\tau\cos(k_{p0}\xi)/2}\left[1-\Omega_s\tau\cos(k_{p0}\xi)/2\right] \\ \alpha_1(\xi,\tau) &\approx a_0 f(\xi) e^{-3i\Omega_s\tau\cos(k_{p0}\xi)/2}\Omega_s\tau\cos(k_{p0}\xi)/2\end{aligned} \tag{3.49}$$

which describes large amplitude longitudinally-varying transitions to the higher order LG mode regardless of the drive pulse energy. This effect would severely limit the energy the plasma modulator could accept. Therefore experimentally the seed pulse must pass through a separate overall weaker focusing system so that the Gaussian drive and compensated seed can be simultaneously matched to the plasma channel.

3.3.5 Wake Suppression of Raman Backscattering

Of all the stimulated Raman scattering (SRS) instabilities, Raman backscattering (RBS) has the fastest growth rate. In underdense plasma, this process causes laser photons (k_L, ω_L) to each decay into a backscattered Stokes photon $(-k_L, \omega_L - \omega_p)$ and a plasma wave $(2k_L, \omega_p)$ with a very slow phase velocity. This process is known to limit the propagation of laser energy in various applications [99], so it is worth verifying if it could also potentially pose a problem for the plasma modulator. The

growth rate of RBS in the strongly coupled $a_0^2 > 2\omega_p/\omega_L$ regime is given by [100–103]

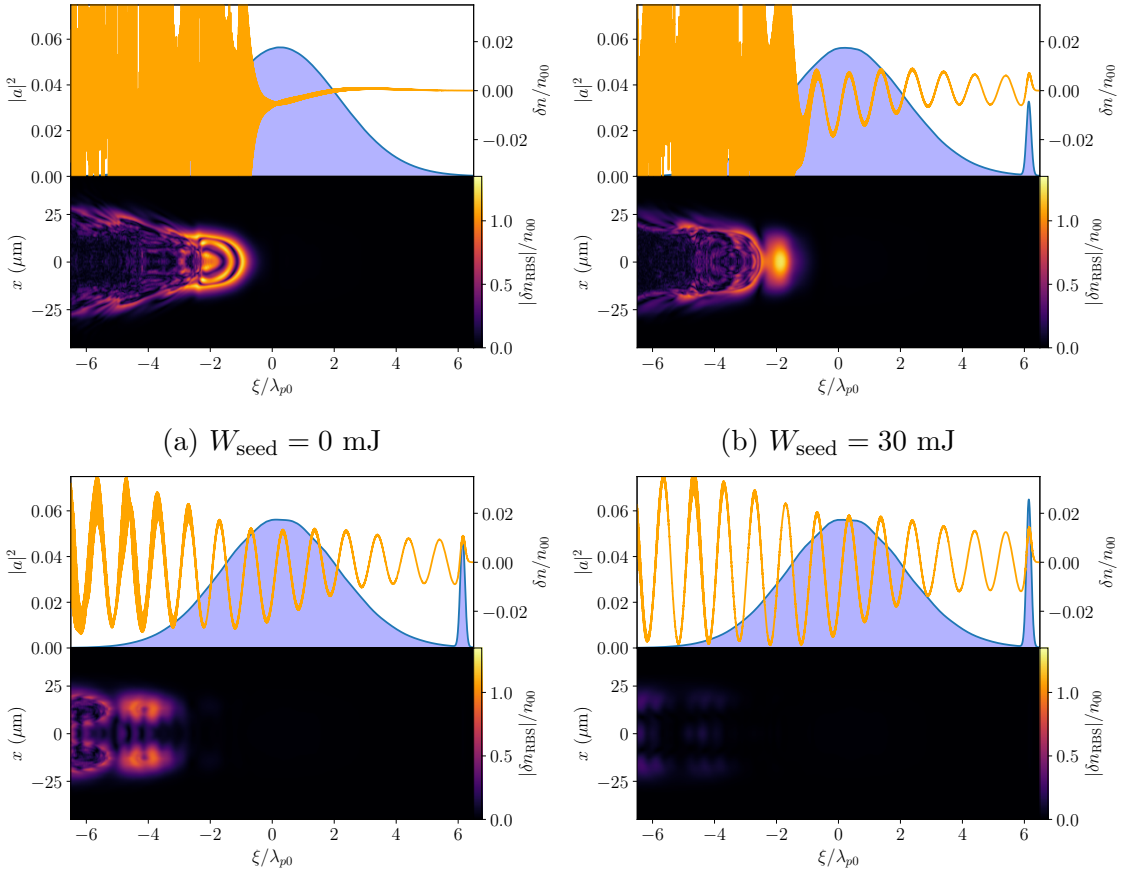
$$\Gamma_{\mathrm{RBS}} = \frac{\sqrt{3}\,\omega_p}{2}\left(\frac{\omega_L}{2\omega_p}\right)^{1/3}\frac{a_0^{2/3}}{(1+a_0^2/2)^{1/2}}\,. \tag{3.50}$$

For a 600 mJ modulating drive pulse with laser/plasma parameters in the original P-MoPA proposal [1], this expression predicts a growth rate of $\Gamma_{\mathrm{RBS}} = 24$ ps^{-1}, which is more than enough for a 1 ps duration drive pulse to suffer from RBS well into saturation in the plasma modulator. This problem only gets worse if we wish to include more energy in the drive pulse, with an RBS growth rate of $\Gamma_{\mathrm{RBS}} = 30$ ps^{-1} when doubling the drive energy to 1200 mJ.

Fortunately, it is known that the growth of RBS can be suppressed in the presence of plasma waves with high phase velocities ($v_\phi \sim c$) such as wakes driven by Raman forward scattering (RFS) or beatwave excitation [104]. The presence of the high phase velocity plasma wave catalyzes the decay of the RBS plasma wave $(2k_L, \omega_p)$ into non-resonant daughter waves primarily of the form $(2k_L + k_p, 2\omega_p)$ and $(2k_L - k_p, \omega \ll \omega_p)$, thus preventing further growth of the instability. In the plasma modulator, the presence of a sufficiently strong seed wake is enough to fully mitigate RBS effects. The seed wake amplitude required to suppress RBS is given by [104]

$$\frac{\delta n_s}{n_{00}} \gtrsim \left(\frac{n_{00}}{n_{\mathrm{c}}}\right)^{1/2} \tag{3.51}$$

where n_{c} is the critical plasma density. Since the plasma modulator operates with significantly underdense plasma, this criterion can be met with reasonable seed pulse energies. For example, for the original P-MoPA proposal parameters [1] a minimum seed wake of $\delta n_s/n_{00} \sim 1.5\%$ is required to suppress RBS (a seed wake of $\delta n_s/n_{00} \sim 2\%$ driven by a 50 mJ, FWHM 40 fs seed pulse happened to be used in the proposal).



(a) $W_{\mathrm{seed}} = 0$ mJ

(b) $W_{\mathrm{seed}} = 30$ mJ

(c) $W_{\mathrm{seed}} = 45$ mJ

(d) $W_{\mathrm{seed}} = 60$ mJ

Figure 3.11: WarpX 2D PIC simulations of a 1200 mJ, FWHM 1 ps drive pulse after 1.5 mm of propagation in the plasma modulator for FWHM 40 fs seed pulses with various energies assuming a cold plasma channel. The top panels show the on-axis seed and drive pulse envelopes and the density perturbation (smoothed over two laser wavelengths), whilst the bottom panels show the amplitude of RBS plasma waves (calculated by selecting for plasma waves with wavenumbers within the range $|k - 2k_L|/k_L < 0.1$). We can see that if the seed pulse is energetic enough to drive a wake amplitude satisfying the criterion in Eq. (3.51), the RBS instability is strongly suppressed.

3.4 Summary of Design Considerations

We will now condense all of the physics discussed in this chapter into a set of well-defined design constraints for the plasma modulator stage, with an overview given in Table 3.1. Though the physics can be generalized for a range of laser systems, we will be centering our discussions around parameters specifically configured for the

PFS-Pro Yb:YAG thin-disk laser at CALA [98].

Table 3.1: Modulator stage baseline parameters

Laser	
Wavelength λ_L	$1030\,\mathrm{nm}$
Seed Duration $\tau_{\mathrm{FWHM}}^{\mathrm{seed}}$	$40\,\mathrm{fs}$
Drive duration τ_{FWHM}	$1.0\,\mathrm{ps}$
Drive Energy W_{drive}	$\leq$ Eq. (3.57)
Plasma	
On-axis plasma density n_{00}	$1\times10^{17}\,\mathrm{cm}^{-3} - 1\times10^{18}\,\mathrm{cm}^{-3}$
Modulator length L_{mod}	$\lesssim 100\,\mathrm{mm}$
Matched spot size w_{mod}	$> (2\tau_{\mathrm{FWHM}}/T_{p0}k_{p0}^2)^{1/2}$
Longitudinal inhomogeneity $\sigma_{n_{00}}/n_{00}$	$< T_{p0}/4\tau_{\mathrm{FWHM}}$
Modulator parameter β	$1.0 < \beta < 1.43$

3.4.1 Channel Profile Effects

As demonstrated in Fig. 3.4, the channel profile in certain situations can suppress the spectral modulation towards the tail of the drive pulse. For channel profiles close to square in shape, this is never an issue. However, for parabolic or parabolic-like channels, this sets the following constraint on the plasma density and matched spot size for a given drive pulse duration

$$k_{p0}^2 w_{\mathrm{mod}}^2 \gtrsim \frac{2\tau_{\mathrm{FWHM}}}{T_{p0}}\,. \tag{3.52}$$

For example, for a parabolic channel with on-axis density $n_{00} = 1.0\times10^{17}\,\mathrm{cm}^{-3}$, to modulate a drive pulse of duration $\tau_{\mathrm{FWHM}} = 1.0\,\mathrm{ps}$ the matched spot size must be at least $w_{\mathrm{mod}} \gtrsim 40\,\mu\mathrm{m}$. Note that this expression assumes that the seed pulse is ahead of the drive pulse by one drive pulse duration. If the seed pulse is further ahead, then the channel suppression effect becomes more pronounced.

Also depending on the exact form of the channel profile, we may also expect attenuation of both the seed and drive pulses via transverse leakage, which sets an

upper bound on the length of the modulator stage L_{mod}.

The longitudinal homogeneity of the plasma channel is also relevant, as this too can suppress the overall spectral modulation. However, this is not a very strong constraint at low plasma densities where the drive pulse duration only spans a few plasma periods. This constraint can be summarized with

$$\frac{\sigma_{n_{00}}}{n_{00}} < \frac{T_{p0}}{4\tau_{\mathrm{FWHM}}}\,. \tag{3.53}$$

For example, a modulator with an on-axis density of $n_{00} = 1.0 \times 10^{17}\,\mathrm{cm}^{-3}$ with a 1 ps drive pulse can tolerate longitudinal inhomogeneity of up to $\sim 9\%$ before suffering from suppression of spectral modulation. Again, similar to the channel profile suppression, if the seed pulse is further ahead of the drive pulse then this suppression effect becomes more pronounced.

3.4.2 TMI Energy Limit

Assuming stable operation of the modulator, the P-MoPA pulse train envelope after both modulation and compression is given by [38]

$$a = a_0 e^{-r^2/w_{\mathrm{acc}}^2} f(\xi) \left(J_0(\beta) + 2\sum_{n=1}^{\infty} J_n(\beta) \cos\left[n k_{p0}(\xi + \Delta\varphi)\right] \right)\,, \tag{3.54}$$

where w_{acc} is the accelerator spot size (which can differ from the modulator) and $0 \leq \Delta\varphi < 2\pi$ is the phase factor set by the phase of the seed wake relative to the drive pulse peak . For optimal operation in the accelerator stage (which we discuss later in Chapter 4), the modulator parameter β should be in the range

$$1.0 < \beta < 1.43\,, \tag{3.55}$$

where the modulator parameter is given by the following expression for a parabolic channel

$$\beta = \frac{\omega_{p0}^2}{4\omega_L}\frac{\delta n_s}{n_{00}}\frac{L_{\mathrm{mod}}}{c} \tag{3.56}$$

where δn_s is the propagation-averaged on-axis seed wake amplitude (as the amplitude may decay due to transverse leakage of the seed pulse from a finite channel). The plasma modulator has a total laser energy limit as it must introduce a spectral modulation while simultaneously avoiding the seeded self-modulational instability. This total drive pulse energy limit is given by

$$W_{\mathrm{drive}}^{\mathrm{max}} \sim 0.3 \times \frac{8\pi m_e^2 \epsilon_0 c^4}{e^2}\frac{k_L^2 (k_{p0} w_{\mathrm{mod}})^2}{k_{p0}^3}\left(\frac{\delta w / w_{\mathrm{mod}}}{\delta n_s / n_{00}}\beta + \frac{(k_{p0} w_{\mathrm{mod}})^2}{8}\right)^{-1}, \tag{3.57}$$

where typical values for laser spot size mismatch with the pre-formed plasma channel, and the on-axis seed wake amplitude for the laser energy limit (corresponding to a 1030 nm, 100 mJ, 40 fs seed pulse) are

$$\delta w \sim 3\,\mu\mathrm{m}\,, \quad \frac{\delta n_s}{n_{00}} \sim 5\% \times \frac{(30\,\mu\mathrm{m})^2}{w_{\mathrm{mod}}^2}\,. \tag{3.58}$$

For example, substituting in modulator parameters $n_{00} = 2.5 \times 10^{17}\,\mathrm{cm}^{-3}$, $w_{\mathrm{mod}} = 30\,\mu\mathrm{m}$ and $\beta = 1.0$, the maximum drive pulse energy is $W_{\mathrm{drive}}^{\mathrm{max}} \sim 2.0\,\mathrm{J}$, and increases to $W_{\mathrm{drive}}^{\mathrm{max}} \sim 2.5\,\mathrm{J}$ when the modulator spot size is increased to $w_{\mathrm{mod}} = 40\,\mu\mathrm{m}$. Note that we can choose to have a larger spot size in the modulator than the accelerator $w_{\mathrm{mod}} > w_{\mathrm{acc}}$ to allow for higher pulse energies.

We also note that this TMI limit is effectively a cap on the total energy of the drive pulse (and not the fluence) due to the $1/w_{\mathrm{mod}}^2$ scaling of the seed wake amplitude for fixed seed pulse energy. Arbitrarily increasing the matched spot size w_{mod} to allow for more energy also does not work due to the diminishing seed wake amplitude which necessitates a larger modulator length L_{mod}, which in practice will increase the total attenuation via transverse leakage. Therefore we should choose parameters such that $\beta \sim 1.0$ can be achieved with a modulator stage within roughly

$L_{\mathrm{mod}} \lesssim 100\,\mathrm{mm}$.

On top of the spot size matching quality of the drive pulse, the seed pulse spot size must simultaneously be matched to the plasma channel, which requires a separate focusing system due to the donut mode technique used to achieve the compression to $\sim 40\,\mathrm{fs}$, $100\,\mathrm{mJ}$ seed pulse [98].

Chapter 4

The P-MoPA Accelerator Stage

In the previous chapter, we identified the parameter space in which the modulator stage of the P-MoPA can be operated in a stable manner, and found that it can handle multi-joule pulses with experimentally plausible laser-plasma parameters and tolerances [33], which is summarized in the last section of Chapter 3. The following chapter presents the author's research on the accelerator stage of the P-MoPA in van de Wetering et al. [38] with added figures and discussions and written in notation consistent with Chapter 2 to better contextualize it within this thesis.

We derive a full 3D analytic theory of the pulse train wakefield evolution in long plasma channels and examine the dynamics and performance of P-MoPA pulse trains as LWFA drivers with PIC simulations, finding that they are suitable for multi-GeV LWFA. We also find that a beneficial feature of the P-MoPA scheme is the ability to control the longitudinal profile of the pulses in the train independent of their pulse spacing; this allows for more resilient pulse trains and more efficient wake excitation and offers a degree of control over the onset of depletion effects.

4.1 Multipulse LWFA

For a laser pulse to efficiently excite a plasma wave, its duration must be "resonant" with the plasma, meaning that its duration must be less than half the plasma period $T_p = 2\pi/\omega_p$, which is in the 100 fs range for plasma densities of interest. In

the early development of LWFA, sufficiently short joule-scale pulses were not yet feasible. Therefore Tajima and Dawson also proposed the plasma beatwave accelerator (PBWA) in their original LWFA proposal [21]. In this configuration, two long co-propagating pumps with a carrier frequency mismatch approximately equal to the plasma frequency $\Delta\omega = \omega_1 - \omega_2 \approx \omega_p$ interfere to form a train of short pulses via beatwave modulation. The resulting cosine-squared modulation corresponds to a train of evenly spaced pulses that can be used to resonantly excite a plasma wave. More generally, we will refer to resonant wakefield excitation with trains of uniformly or non-uniformly spaced pulses as multipulse-LWFA (MP-LWFA) [105].

The P-MoPA scheme is related to the PBWA since in both schemes the wakefield is resonantly excited by a train of laser pulses, and are therefore both forms of MP-LWFA. However, the P-MoPA differs from the PBWA in two important ways. First, in a P-MoPA only a single input driver frequency is required to generate the pulse train. This avoids the requirement for two driving systems that differ in output frequency by precisely the plasma frequency. Second, the temporal profile of the pulse trains generated in a P-MoPA can be controlled and can excite the wakefield more efficiently than the cosine-squared profile pulse trains generated in a PBWA.

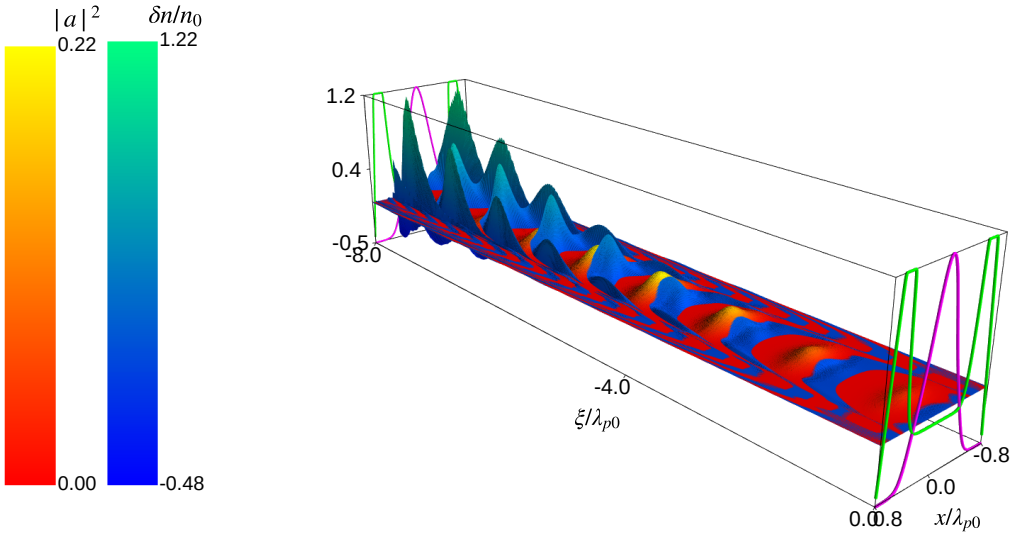


Figure 4.1: Snapshot at $z = 2.1\,\text{mm}$ of the relative plasma density perturbation $\delta n/n_0$ (blue-green) resonantly excited by a P-MoPA pulse train with normalized intensity $|a|^2$ (red-yellow) and its average transverse profile (violet) propagating in a quasi-square channel (green) of the form given in Eq. (4.7). Results are from a 2D simulation using the PIC code WarpX [40] with $W_{\text{drive}} = 1.2\,\text{J}$, $\tau_{\text{drive}} = 1\,\text{ps}$, $\lambda_L = 1030\,\text{nm}$, $R = 30\,\mu\text{m}$, $w_0 = 30\,\mu\text{m}$, $n_{00} = 2.5 \times 10^{17}\,\text{cm}^{-3}$ and modulator parameter $\beta = 1.2$ as defined in Eq. 4.9.

4.1.1 Scaling Laws

We envision that the P-MoPA accelerator stage will be operated in the quasilinear wakefield regime, where the wakefield amplitude is approximately half of the cold nonrelativistic wavebreaking limit $E_z \sim 0.5\,E_0$. We would therefore expect the energy gain scaling laws to behave similarly to those of the single pulse linear regime [56]. The primary limit to acceleration in this regime is the dephasing length, previously derived in the 1D limit in Eq. (1.40), which scales with $L_{\text{d,1D}} \propto n_e^{-3/2}$. Since the cold wavebreaking field scales with $E_0 \propto n_e^{1/2}$, the total energy gain possible in a quasilinear LWFA will scale with n_e^{-1}, preferring acceleration in lower density plasmas over longer dephasing lengths. For the P-MoPA, we are considering pulse train propagation in low density plasmas $n_e \sim 1 \times 10^{17}\,\text{cm}^{-3}$ in order to boost energy gains to the multi-GeV range by increasing the dephasing length to $\sim 300\,\text{mm}$. However, at these low densities the 1D dephasing length is typically insufficient, as

finite spot size effects will also reduce the laser group velocity.

To extend the acceleration length beyond the Rayleigh range, the pulse train is guided in a pre-formed plasma channel. For example, we previously derived the known form of the parabolic plasma channel matched to a Gaussian pulse of spot size w_0 [66–68] in Eq. (2.11), which we will repeat here for convenience

$$n_0(r) = n_{00} + \Delta n (r/w_0)^2 \tag{4.1}$$

where n_{00} is the on-axis plasma density and $\Delta n = (\pi r_e w_0^2)^{-1}$ is the channel depth parameter with r_e as the classical electron radius. We previously derived the known corresponding group velocity of a Gaussian pulse propagating in such a matched channel [68] due to first-order non-paraxial effects in Eq. (2.41), which is given by

$$\frac{v_g}{c} = 1 - \frac{\omega_{p0}^2}{2\omega_L^2} - \frac{2c^2}{\omega_L^2 w_0^2}\,, \tag{4.2}$$

where $\omega_{p0} = \omega_p(r = 0)$ indicates the on-axis plasma frequency. For example, at an on-axis plasma density of $n_{00} = 1.0 \times 10^{17}\,\mathrm{cm}^{-3}$, a spot size of $w_0 = 34\,\mu\mathrm{m}$ would contribute equally to the reduction of laser group velocity as the plasma density. Its corresponding dephasing length, defined as the propagation distance over which an electron propagating at c slips relative to the wakefield by a the quarter plasma wavelength $\sim \lambda_{p0}/4$ (assuming no channel effects on wake structure), is thus given by

$$L_\mathrm{d} = \frac{\lambda_{p0}}{2}\frac{\omega_L^2}{\omega_{p0}^2}\left(1 + \frac{4}{k_{p0}^2 w_0^2}\right)^{-1} \tag{4.3}$$

which sets a limit on the total length of the accelerator stage, taking finite spot size effects into account. Note that a method has been proposed [106] which allows MP-LWFA to accelerate beyond the dephasing length by introducing a short region of higher plasma density, which lets the accelerated electron bunch rephase into the next accelerating bucket back at the resonant density without deceleration.

Integrating the equations of motion for a relativistic particle moving in a sinu-

soidal wakefield gives the energy gain ΔW_e before the onset of dephasing as

$$\frac{\Delta W_e}{m_e c^2} \approx \frac{2}{\pi}\frac{eE_{\max}L_{\mathrm{d}}}{m_e c^2} = 2\,\frac{E_{\max}}{E_0}\frac{\omega_L^2}{\omega_{p0}^2 + 4c^2/w_0^2} \tag{4.4}$$

where $E_{\max}$ is the peak accelerating field and $E_0 = m_e\omega_{p0}c/e$ is the wavebreaking field. This shows that for a given spot size, the maximum energy gain cannot be increased indefinitely by reducing the plasma density as the dephasing length becomes dominated by finite spot size effects when $\omega_{p0}^2 \ll 4c^2/w_0^2$. This is a well known effect in LWFA [107], where the prescription is to scale the spot size with the plasma density such that

$$k_{p0}w_0 \gtrsim 2\,. \tag{4.5}$$

On top of preventing an excessive reduction in group velocity, scaling the spot size this way also prevents the wakefield from becoming largely radial [107, 108], examples of which we previously presented in Figure 2.7. As the required spot size increases with the plasma wavelength, the total laser energy must necessarily increase. The total energy of the pulse train W_{drive} required to excite a given accelerating field relative to the wavebreaking field $E_{\max}/E_0$ scales with the volume enclosed by the spot size and the plasma wavelength, i.e. $W_{\mathrm{drive}} \sim w_0^2\lambda_{p0} \sim \lambda_{p0}^3$. This grows faster with the plasma wavelength than the electron energy gain $\Delta W_e \sim \lambda_{p0}^2$ and the maximum bunch charge $Q_e \sim n_{00}w_0^2\lambda_{p0} \sim \lambda_{p0}$, but the overall laser-to-bunch energy efficiency $Q_e\Delta W_e/eW_{\mathrm{drive}}$ has no plasma density scaling. These scaling laws, which we have derived for pulse trains in the linear regime, are identical to that of a linear single pulse LWFA [56].

Another limit to acceleration is the pump depletion length. Similar to the dephasing length, the depletion length will also be reduced by finite spot size effects. This is due to the extra pulse energy spent exciting the aforementioned transverse wakefield for pulses with spot sizes comparable to the plasma wavelength. The depletion length can be estimated by comparing the laser energy with the energy contained within the linear wakefield of the form $E_z \sim \exp(-2r^2/w_0^2)\cos[k_p(z-ct)]$

and its transverse counterpart spanning the depletion length L_{pd}. Assuming that the pulse train is resonantly spaced and is comprised of individual Gaussian pulses of index m of the form $a_m^2 = a_{0,m}^2 \exp(-(\xi - \xi_{0,m})^2/L^2)$ with sufficiently short lengths L relative to the plasma wavelength such that each (linearly polarized) pulse increases the normalized wake amplitude by $\sqrt{\pi/2}\, a_{0,m}^2 k_{p0} L/4$ [109], the pump depletion length is given by

$$L_{\mathrm{pd}} = \left(\frac{\pi}{8}\frac{E_{\max}}{E_0}\right)^{-1} L_{\mathrm{d}}\,. \tag{4.6}$$

This expression shows that the depletion length is always larger than the dephasing length in the linear wakefield regime, which is also true for single pulse LWFA [56]. To make efficient use of the available laser energy, we would ideally want the pump depletion length to be larger but similar to the dephasing length. As this is not feasible, the P-MoPA accelerator stage should at least be operated in the quasilinear regime, whilst avoiding nonlinear detuning effects associated with the large amplitude wake which will be discussed later.

One caveat to the analysis above is that pulse trains do not deplete uniformly. Instead, trailing pulses, which co-propagate with steeper density gradients, will deplete faster than those near the beginning of the pulse train. We thus expect the pulses towards the rear of the train to have individual depletion lengths up to half as short as in Eq. (4.6), whilst the pulses near the beginning of the train will experience minimal depletion. This effect can be intuitively understood by considering the contribution of a small pulse at the end of the train increasing the wakefield amplitude of original maximum potential ϕ by a small quantity $\delta\phi$, which scales with the pulse's intensity $a_{0,m}^2$. The total energy added to the wake will then increases by $2\phi\delta\phi$.

4.1.2 Channel Effects on Energy Gain

Driving the accelerator within a pre-formed plasma channel causes the laser to remain focused well beyond the Rayleigh range. However, the transverse variation of

plasma density within the channel leads to a concomitant variation of the plasma frequency that can also influence the structure of the excited wakefield and hence the energy gain of an injected electron bunch.

It is well known for single-pulse LWFA that plasma channels can strongly influence wakefield structure via the curvature of wake phase-fronts [110]. For example, shallow parabolic channels matched to the spot size w_0, i.e. $\frac{1}{2}k_{p0}^2 w_0^2 \gg 1$, result in an increase in overlap between the accelerating and focusing regions of the wakefield, up to a factor of two at sufficient distances behind the laser pulse. This can be beneficial for acceleration as it can increase the dephasing length by a factor of up to two without sacrificing much accelerating gradient. However, deep matched parabolic channels, i.e. those for which $\frac{1}{2}k_{p0}^2 w_0^2 < 1$, yield a rapid conversion of axial field into radial field with distance behind the drive pulse, meaning that LWFA is only possible in the first few buckets behind the drive pulse. This quick conversion of axial field into radial field readily outpaces other known wakefield decay mechanisms such as the ion motion modulational instability [111, 112] which only becomes relevant on the ion plasma frequency timescale, corresponding to about forty plasma wavelengths for hydrogen. Therefore the transverse profile of the plasma channel is the limiting effect on axial wakefield losses.

The depth of a parabolic channel will determine the maximum useful number N of pulses used in a MP-LWFA, as the axial wakefield contribution of the first pulse in a train will disappear by the time the N^{th} pulse passes. There are two ways to allow for longer trains. The first way is to operate well in the shallow channel limit $\omega_{p0}^2 w_0^2/2c^2 \gg N$. However, this forces the required matched spot size to become large at low plasma densities and large pulse train lengths (e.g. $w_0 \gg 75\,\mu\text{m}$ at $n_{00} = 1.0 \times 10^{17}\,\text{cm}^{-3}, N = 10$), bringing the required laser energy to the 10-joule scale. The other solution is to use square-profile channels, analogous to step-index optical fibers. Their effect on wake structure is much weaker than parabolic channels for guiding modes with comparable spot sizes due to a lack of plasma frequency gradient in the regions of high intensity. Fortunately, the transverse density profiles of CHOFI plasma waveguides are closer to square than parabolic in shape [37, 93,

113], makes them well suited to driving P-MoPAs.

An example PIC simulation of the wake structure driven by a P-MoPA pulse train is presented in Figure 4.1, where the pulse train is guided along a quasi-square channel of the form

$$\frac{n_0(r) - n_{00}}{\Delta n} = \begin{cases} (r/R)^{10} & r < 1.2R \\ (1.2)^{10} & 1.2R \leq r < 1.2R + d \\ (1.2)^{10}\left(1 - \frac{r-1.2R-d}{d}\right) & 1.2R + d \leq r < 1.2R + 2d \\ 0 & \text{otherwise} \end{cases} \tag{4.7}$$

where R, $\Delta n = (\pi r_e R^2)^{-1}$ and $d = 10\,\mu\text{m}$ are the channel wall radius, depth and thickness parameters respectively. The flat plasma density profile in the axial region ensures that the axial wake is not lost due to wake phase-front curvature effects that a parabolic channel would incur.

In addition to the resonantly driven on-axis wake, a large amplitude wake is also observed in Figure 4.1 at the inner channel wall boundary. This is due to the steep plasma density gradient

$$\frac{\mathrm{d} \ln n_0}{\mathrm{d}r} > k_p \,, \tag{4.8}$$

which is characteristic of plasma channels at these spot sizes and low $\sim 10^{17}$ cm^{-3} on-axis densities. The wake amplitude in this region continues to grow even after the laser driver has already passed due to the aforementioned conversion of the wakefield from the longitudinal to transverse component [110]. This accumulated wall-boundary wake can eventually exceed the on-axis wake amplitude, suggesting that large-amplitude wakefields driven by pulse trains in plasma channels would undergo transverse wavebreaking effects before longitudinal wavebreaking.

4.1.3 P-MoPA Pulse Shaping

The plasma modulator offers a degree of control of the longitudinal shape of the pulses comprising the pulse train, allowing for further optimization of the accelerator stage. The pulse train formed after compression will be comprised of pulses evenly spaced by the modulator plasma period with pulse heights and lengths determined by the amount of spectral modulation introduced by the modulator stage. This lets a P-MoPA form pulse trains with lengths shorter than those possible using the beatwave method, allowing for larger wake amplitudes to be driven with the same laser energy.

According to 3D spectral modulation theory [33], assuming that the spectral modulation remains primarily in the fundamental channel mode, the pulse trains formed using the "ideal compressor" described by Jakobsson et al. [1], with a seed wake of the form $\delta n(r,\xi) = \delta n_s \cos(k_{p0}\xi)\exp(-2r^2/w_0^2)$, will have the following temporal amplitude envelope

$$f_{\mathrm{acc}}(\xi;\beta) = f_{\mathrm{mod}}(\xi)\left(J_0(\beta) + 2\sum_{n=1}^{\infty} J_n(\beta)\cos(nk_{p0}\xi)\right),$$
$$\beta = \frac{2\Omega_s L_{\mathrm{mod}}}{v_{g,\mathrm{mod}}} \tag{4.9}$$

where $\xi = z - ct$ is the longitudinal co-moving coordinate, $0 \leq f_{\mathrm{mod}}(\xi) \leq 1$ is the original slowly-varying unmodulated temporal amplitude envelope, L_{mod} and $v_{g,\mathrm{mod}}$ are the plasma modulator length and laser group velocity respectively and $\Omega_s = (\omega_{p0}^2/8\omega_L)(\delta n_s/n_{00})$ is the rate of spectral modulation of a Gaussian pulse co-propagating with a seed wake of on-axis amplitude δn_s in a parabolic channel [33]. This expression gives us the modulator parameter β, which determines the effective number of sidebands generated in the drive pulse spectrum. This parameter can control the temporal profile of the pulse train produced by the plasma modulator (whilst obeying the modulator stability condition outlined in [33]). Figure 4.2 shows how the temporal intensity profiles of the pulses within the train, their full-length at half maximum duration, and their contrast, varies with β. It can be seen that adjusting the parameter β allows the duration and contrast of the pulses within the

train to be controlled.

For a given laser energy, the peak intensity occurs at $\beta = j_{0,1} \approx 2.405$, where $j_{m,n}$ indicates the n^{th} nonzero root of the Bessel function $J_m(x)$. This can be shown by evaluating the temporal envelope at the pulse center using well-known identities for Neumann series of Bessel functions [48, 114]

$$\begin{aligned}\frac{f_{\text{acc}}(0;\beta)}{f_{\text{mod}}(0)} &= J_0(\beta) + 2\sum_{n=1}^{\infty} J_n(\beta) \\ &= 1 + \int_0^{\beta} J_0(s)ds \end{aligned} \tag{4.10}$$

which shows that its global maximum is at $\beta = j_{0,1}$, where it takes the value $f_{\text{acc}} \approx 2.470\, f_{\text{mod}}$. As evident in Figure 4.2, increasing β above this value leads to the formation of shorter pulses, but also an increasing intensity in the wings of each pulse, which wastes energy since it does not contribute to wake excitation. Thus when optimizing the P-MoPA scheme we only need to consider $\beta \leq j_{0,1}$.

The additional control that the parameter β enables more efficient wake excitation than is possible with PBWA. This is shown in Figure 4.2(b), which shows that β in the range of 1.1–1.6 optimizes the wake amplitude according to linear wakefield theory [56]. We can also show in the linear regime that the ratio between the amplitude of the wake potential driven by a P-MoPA pulse train and an ideal beatwave pulse train with a temporal intensity modulation of the form $1+\cos(k_{p0}\xi)$ containing the same laser energy is given by

$$\begin{aligned}\frac{\phi_{\text{P-MoPA}}}{\phi_{\text{PBWA}}} &= \frac{\int_{-\pi}^{\pi} \left[J_0(\beta) + 2\sum_{n=1}^{\infty} J_n(\beta)\cos(ns)\right]^2 \cos(s)ds}{\int_{-\pi}^{\pi} [1+\cos(s)]\cos(s)ds} \\ &= 4\sum_{n=0}^{\infty} J_n(\beta)J_{n+1}(\beta) \\ &= 2\beta\left[J_0^2(\beta) + J_1^2(\beta)\right]\,. \end{aligned} \tag{4.11}$$

This ratio is maximized for $\beta \approx 1.43$, at which value the wake amplitude in a P-MoPA is 72% larger than that driven by an ideal PBWA with the same total drive energy.

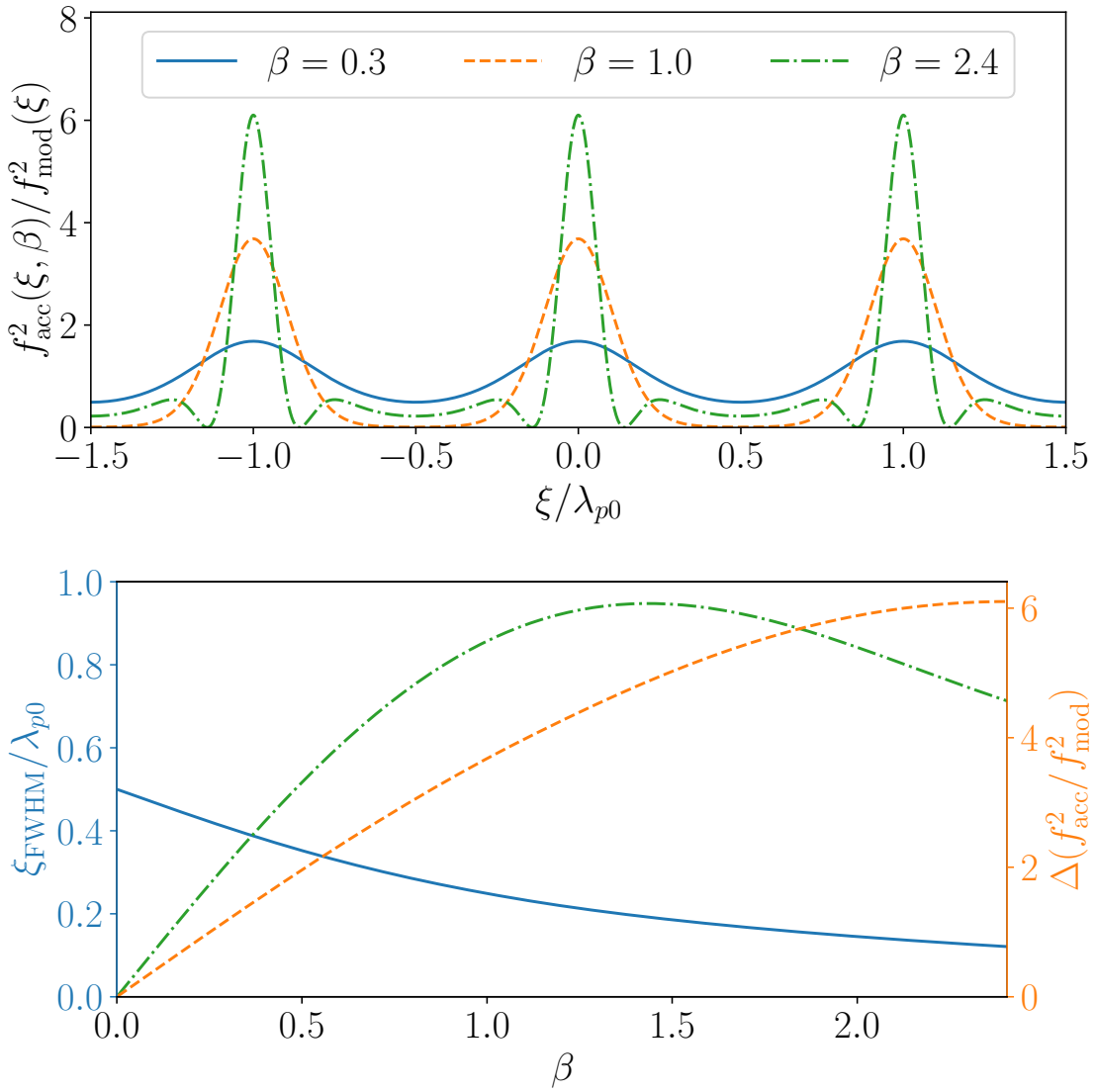


Figure 4.2: (Top) pulse train temporal profiles for various values of the modulator parameter β and their respective FWHM durations (dashed). (Bottom) FWHM duration (blue, solid), peak prominence (orange, dashed) and the wakefield amplitude according to 1D linear theory as derived in Eq. (1.16) (green, dot-dashed, arb. units) as a function of β.

If we are instead constrained by the plasma modulator energy limit (as discussed in Chapter 3) rather than the total energy available from the laser system, then we expect the optimal modulator parameter to be lower than the previously discussed 1.1–1.6 range. In this case, we can estimate the optimal modulator parameter β_{opt} by taking the ratio between Eq. (4.11) with the plasma modulator maximum energy

scaling $W_{\text{drive}}(\beta)$ in Eq. (3.57), which yields

$$\beta_{\text{opt}} = \arg\max_{\beta} \beta \left[J_0^2(\beta) + J_1^2(\beta)\right] \left(\frac{\delta w/w_{\text{mod}}}{\delta n_s/n_{00}}\beta + \frac{(k_{p0}w_{\text{mod}})^2}{8}\right)^{-1}. \tag{4.12}$$

For example, at on-axis density $n_{00} = 2.5 \times 10^{17}\,\text{cm}^{-3}$, matched modulator spot size $w_{\text{mod}} = 30\,\mu\text{m}$, initial spot size mismatch $\delta w = 3\,\mu\text{m}$ and on-axis seed wake amplitude $\delta n_s/n_{00} = 5\%$, the optimal modulator parameter is $\beta_{\text{opt}} \approx 0.86$, at which the P-MoPA would still drive a 43% larger amplitude wakefield than a PBWA of the same laser energy, and would correspond with a maximum laser pulse energy of $W_{\text{drive}}^{\text{max}} \sim 2.3\,\text{J}$ according to Eq. (3.57) for these parameters.

4.1.4 The Rosenbluth-Liu Limit

Resonant wakefield acceleration requires the driving pulses to be spaced by the plasma period. However, as the plasma wave amplitude increases beyond the linear regime, its wavelength increases due to relativistic effects. The consequent build-up of plasma wave phase difference relative to the laser pulse centroids sets a limit on the maximum wake amplitude achievable.

The saturation effect arising from this detuning was first derived by Rosenbluth and Liu [115] in the context of PBWA. In their derivation, two infinite-duration pumps interfere to form a cosine beatwave pulse train resonant with the plasma, which results in the saturated wakefield amplitude scaling with the third root of the intensity of the beatwave modulation. P-MoPA pulse trains, which are also spaced uniformly by design, are thus expected to exhibit a similar limit. However, for a P-MoPA, the key difference is that finite duration of the pulse train must be taken into account, especially when operating at lower plasma densities where the pulse train envelope may only be a few plasma wavelengths long.

According to 1D nonlinear plasma wave theory [56], the nonlinear correction to the plasma wavelength for a plasma wave of amplitude $\phi_a = E_a/E_0$ at non-

relativistic laser intensities in the $\phi_a^2 \ll 1$ limit is given by

$$\lambda_p^{\mathrm{NL}} \approx \lambda_p(1 + 3\phi_a^2/16)\,,$$
$$k_p^{\mathrm{NL}} \approx k_p(1 - 3\phi_a^2/16)\,. \tag{4.13}$$

Resonant excitation of the wakefield eventually saturates due to detuning caused by the progressive growth of the plasma wavelength. The co-moving coordinate ξ_{sat} at which this detuning occurs is approximately given by

$$\int_{\xi_{\mathrm{sat}}}^{\infty} (k_p - k_p^{\mathrm{NL}}) d\xi \approx \frac{\pi}{2}\,. \tag{4.14}$$

Since the pulse train in a P-MoPA pulse train corresponds to a sequence of short pulses spaced by T_p, within an envelope determined by the duration of the ps-duration drive pulse, most of its energy will be contained within only a few pulses close to its center. Modelling the original pulse envelope as a temporally Gaussian pulse of the form

$$f_{\mathrm{mod}}^2(\xi) = \exp\left(-\frac{\xi^2}{2\sigma^2}\right)\,, \tag{4.15}$$

where $\sigma = c\tau_{\mathrm{drive}}/2\sqrt{2\ln 2}$ with τ_{drive} being the FWHM duration of the drive pulse. According to linear wakefield theory ignoring detuning, the wakefield potential amplitude $\phi_a(\xi)$ excited by the pulse train will be given by

$$\frac{\phi_a(\xi)}{\phi_{\max}} = \frac{\int_{\xi}^{\infty} d\xi' f_{\mathrm{acc}}^2(\xi')}{\int_{-\infty}^{\infty} d\xi' f_{\mathrm{acc}}^2(\xi')} \approx \frac{1}{2}\,\mathrm{erfc}\left(\frac{\xi}{\sqrt{2}\,\sigma}\right)\,, \tag{4.16}$$

where $\mathrm{erfc}(z) = 1 - \mathrm{erf}(z)$ is the complementary error function and $\phi_{\max} = E_{\max}/E_0$ is the maximum wakefield amplitude resonantly excited by the pulse train. For the pulse train to efficiently drive a wakefield, resonant detuning must not occur before the majority of the pulses have already passed. For example, to allow at least $\sim 90\%$ of the pulse train energy to pass before the full $\pi/2$ detuning, combining Eqs. 4.13,

4.14 and 4.16 results in the following condition

$$-\frac{\xi_{\rm sat}^{90\%}}{\lambda_p} > 0.27\, N_{\rm eff}\,, \tag{4.17}$$

where $N_{\rm eff} = 2\tau_{\rm FWHM}/T_p$ is defined as the number of pulses in the pulse train within two FWHM durations of the original unmodulated envelope. Substituting this expression along with Eq. (4.16) into Eq. (4.14) yields the resonant detuning limit for wakefields driven by P-MoPA pulse trains

$$\phi_{\rm max}^{90\%} = \frac{E_{\rm max}^{90\%}}{E_0} < \frac{2.8}{\sqrt{N_{\rm eff}}}\,. \tag{4.18}$$

For example, for $\tau_{\rm FWHM} = 2\,{\rm ps}$ at $n_{00} = 2.5\times10^{17}\,{\rm cm}^{-3}$, a P-MoPA would form a pulse train comprised of $N_{\rm eff} = 18$ pulses. Substituting this into Eq. 4.18 then limits the maximum accelerating gradient before detuning to $E_{\rm max} < 32\,{\rm GV/m}$, or $< 66\%$ of the wavebreaking field. As we seek to operate the P-MoPA up to the quasilinear regime where $\phi_{\rm max}^{90\%} \lesssim 0.5$, Eq. (4.18) means that as long as the number of pulses comprising the pulse train satisfies $N_{\rm eff} < 30$, wakefield saturation caused by this detuning mechanism does not pose an issue.

Beyond the Rosenbluth-Liu detuning mechanism, another consideration for P-MoPA pulse trains is that the individual pulses can be much shorter than in PBWA, such that $a \ll 1$ can no longer be assumed. Thus, to maximize the wake amplitude, the relativistic effects associated with the quiver motion in regions of high intensity, rather than the relativistic effects associated with the fluid motion, should also be corrected for by using a slightly higher plasma density in the accelerator than the modulator stage to counteract this detuning mechanism.

Aside from limiting the wakefield amplitude, resonant detuning can also lead to focusing/defocusing effects associated with pulses co-propagating with larger amplitude regions of the wake, which will be discussed in the subsequent section.

4.2 Pulse Propagation Effects

4.2.1 Relativistic Self-Phase Modulation and Transverse Mode Excitation

Up until now we have been treating the pulse train envelope as unchanging as it propagates along the accelerator. While this assumption is useful for deriving scaling laws and isolating certain physics, in reality it is a dynamic 3D structure which will evolve under the influence of both relativistic nonlinearities and its own excited wake. Neglecting depletion for now, the two main effects to consider for MP-LWFA in long channels are relativistic self-phase modulation (SPM) and transverse mode dynamics caused by the excitation of higher order transverse channel modes by the focusing/defocusing effects of the large amplitude wake.

Relativistic SPM causes further red-/blue-shifting near the head/tail of each pulse, especially for the shortest duration, highest a_0 pulses. Transverse mode excitation results in spot size oscillations and hence oscillations in the wakefield structure, which become more pronounced towards the back of the pulse train where the wake amplitude is the greatest. Such oscillations can impact beam quality, as a propagation-varying focusing field could increase the energy spread and emittance of the accelerated bunch.

Before significant pump depletion has occurred, i.e. when $|\omega - \omega_L|/\omega_L \ll 1$ can be assumed of the laser spectrum, the evolution of the pulse train propagating in an axisymmetric channel of the form $n_0(r) = n_{00} + \delta n_0(r)$ can be described using the paraxial wave equation in the weakly relativistic limit [116–119] as we derived in Eq. (2.7)

$$\left[\frac{i}{\omega_L}\frac{\partial}{\partial\tau} + \frac{c^2}{2\omega_L^2}\Delta_\perp\right] a = \frac{\omega_p^2}{2\omega_L^2 n_0}\left[\delta n_0(r) + \delta n(r,\xi;|a|^2) - n_0(r)|a|^2/4\right] a \qquad (4.19)$$

where $a(r,\theta,\xi,\tau)$ is the envelope of the normalized vector potential of the pulse, ω_L is the laser frequency and the propagation is described in co-moving coordinates $\xi = z - v_{g0}t$, $\tau = t$, with $v_{g0}/c = (1 - \omega_{p0}^2/\omega_L^2)^{1/2}$ defined as the group velocity of

electromagnetic plane waves in uniform plasma of density n_{00}, corresponding to the on-axis plasma channel frequency ω_{p0}, and $\Delta_\perp = \partial^2/\partial r^2 + (1/r)\partial/\partial r + (1/r^2)\partial^2/\partial\theta^2$ is the transverse Laplacian.

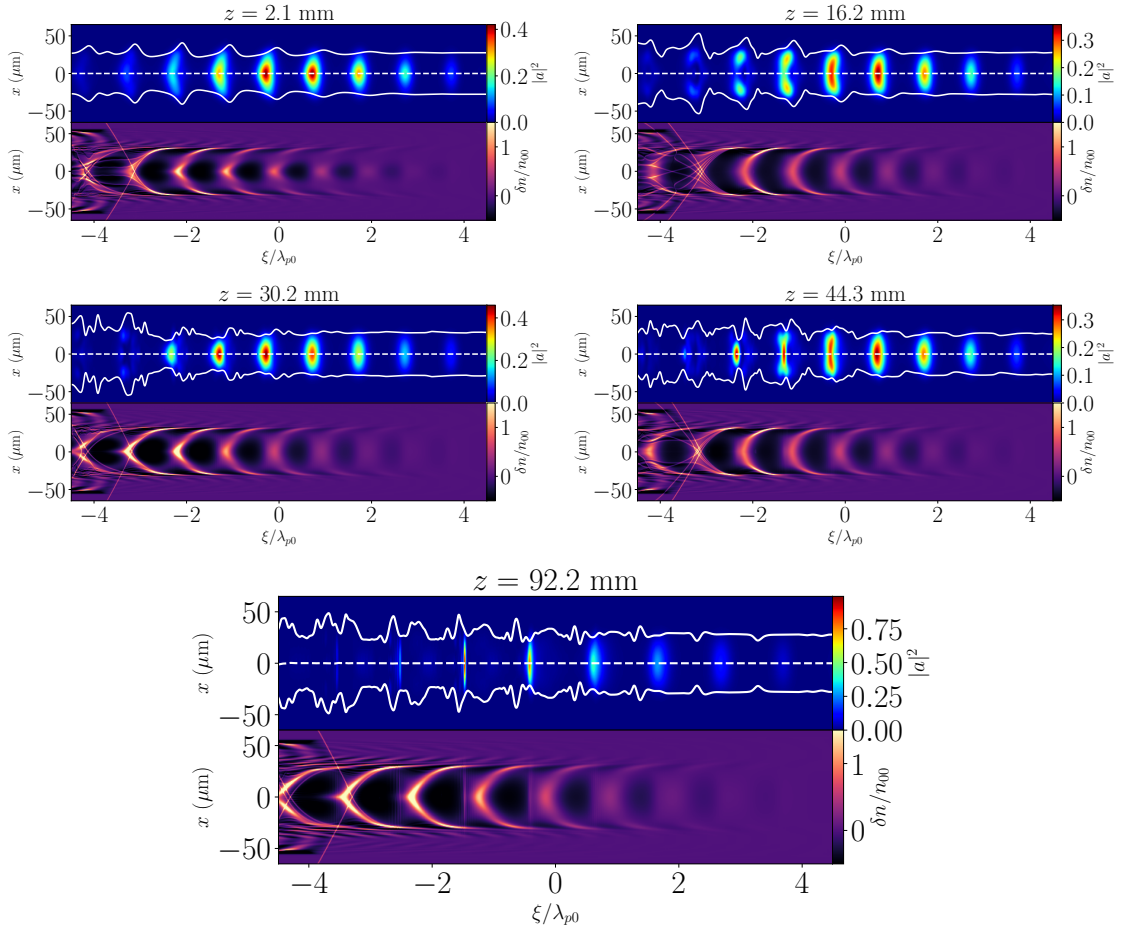


Figure 4.3: Results of a 2D PIC simulation of the propagation of a pulse train in a quasi-square plasma channel. For this simulation, ξ as defined after Eq. (2.7) at varying propagation distances z in a quasi-square channel of the form given in Eq. (4.7) with $n_{00} = 2.5 \times 10^{17}\,\mathrm{cm}^{-3}$, $\Delta n = 1.26 \times 10^{17}\,\mathrm{cm}^{-3}$, $R = 30\,\mu\mathrm{m}$, $W_{\mathrm{drive}} = 2.4\,\mathrm{J}$, $\tau_{\mathrm{drive}} = 1\,\mathrm{ps}$ and modulator parameter $\beta = 1.2$. The pulse train at the entrance of the channel initially has a Gaussian transverse profile with spot size $w_0 = 30\,\mu\mathrm{m}$. For each plot, the top panel displays the laser intensity profile $|a|^2$ along with the local longitudinal variation of the laser centroid $x_c(\xi)$ (dashed) and local effective spot size $w_{\mathrm{eff}}(\xi)$ (solid). The bottom panel displays the wake density perturbation $\delta n/n_{00}$.

Pre-formed plasma channels have often been modelled using parabolic transverse profiles, as these guide Laguerre-Gaussian modes. The long ($\gtrsim 100\,\mathrm{mm}$), low-attenuation and kHz production rate plasma channels required for this scheme

have been experimentally demonstrated using the CHOFI technique [37, 93, 113], which forms deep, low-loss channels with on-axis densities as low as $1 \times 10^{17}\,\mathrm{cm}^{-3}$. These CHOFI channels are often better modelled with transverse profiles closer to square rather than parabolic [93], meaning that wake phase-front curvature effects can be neglected. In the following analysis we will use a simplified profile and treat the plasma channel as an infinite square well of the form

$$n_0(r) = \begin{cases} n_{00} & r \leq R_\infty \\ \\ \infty & r > R_\infty \end{cases}, \tag{4.20}$$

where R_∞ indicates the wall radius parameter specifically for this infinite square well. Note that this analysis can be generalized to any axisymmetric, monotonically increasing channel profile. Assuming that the channel is unperturbed and that relativistic effects are negligible, substituting Eq. (2.13) into Eq. (2.7) yields the same orthogonal set of Bessel mode solutions for $r \leq R_\infty$ as we previously derived in Eq. (2.14)

$$\begin{aligned} a_{pm}(r,\theta,\xi,\tau) &= \alpha_{pm}(\xi)\mathcal{J}_{pm}(r,\theta)e^{-i\Omega_{pm}\tau}\,, \\ \mathcal{J}_{pm}(r,\theta) &= \frac{J_1(j_{0,1})}{\left|J_{|m|+1}(j_{|m|,p+1})\right|} J_{|m|}\left(j_{|m|,p+1}\frac{r}{R_\infty}\right)e^{im\theta}\,, \\ \Omega_{pm} &= \frac{j_{|m|,p+1}^2 c^2}{2\omega_L R_\infty^2}\,, \end{aligned} \tag{4.21}$$

where the integers $p \geq 0$ and m are the radial and azimuthal indexes respectively. Similar to a previous analysis of the P-MoPA modulator stage [33], long-propagation of pulse trains in plasma channels are expected to excite higher order transverse channel modes, with an amplitude that scales with the wake amplitude. To model this effect, we first assume a fixed multipulse-driven wake of the form

$$\delta n(r,\xi) = \delta n_a(\xi)\mathcal{J}_{00}^2(r)\,, \tag{4.22}$$

which is consistent with a pulse train primarily in the fundamental mode exciting

a wake in the (quasi-)linear regime. Applying the time-dependent perturbation theory (TDPT), which we derived previously in Eq. (2.25), to pulses propagating in a square channel with only the $m = 0$ radial transverse modes present, we find the following set of PDEs for the coefficients $\alpha_p(\xi, \tau)$ of each of the square channel's radial modes $\mathcal{J}_{p0}(r)$

$$
\begin{aligned}
i\frac{\partial \alpha_p(\xi,\tau)}{\partial \tau} &= \frac{\omega_{p0}^2}{2\omega_L}\sum_n \alpha_n(\xi,\tau)\,\langle p0|\,\frac{\delta n}{n_{00}} - \frac{|a|^2}{4}\,|n0\rangle\, e^{i(\Omega_{p0}-\Omega_{n0})\tau}\,, \\
a(r,\xi,\tau) &= \sum_p \alpha_p(\xi,\tau)\mathcal{J}_{p0}(r)e^{-i\Omega_{p0}\tau}\,, \\
\langle p'm'|\,(...)\,|pm\rangle &\equiv \frac{\int_0^{2\pi} d\theta \int_0^R r dr \mathcal{J}^*_{p'm'}(...)\mathcal{J}_{pm}}{J_1^2(j_{0,1})\pi R_\infty^2}\,.
\end{aligned}
\tag{4.23}
$$

We note that TDPT requires that $\pi r_e(2R_\infty/j_{0,1})^2\delta n \ll 1$, which is *not* true everywhere in the accelerator stage due to the large amplitude wake. However, specifically for wakes resonantly excited by pulse trains, the zeros of $\delta n_a(\xi)$ are located near the laser centroids, so TDPT *is* still valid for resonantly spaced pulse trains with pulse durations sufficiently short such that δn is sufficiently small in regions of high intensity. Hence we can still use TDPT to describe the evolution of the pulse train despite the large amplitude wake. Assuming that most of the light is initially in the fundamental mode, transverse mode transitions will be dominated by excitations of only the first radial mode, with higher order mode excitations being much weaker. Hence substituting our expression for the wake and approximating Eq. (4.23) as a two-level system description of the fundamental and first radial transverse modes

yields

$$\begin{aligned}
&\frac{\partial}{\partial\tau}\begin{pmatrix}\alpha_0\\ \alpha_1\end{pmatrix} = \boldsymbol{D}(\xi,\tau)\begin{pmatrix}\alpha_0\\ \alpha_1\end{pmatrix}\,,\\
&\boldsymbol{D}(\xi,\tau) = -i\gamma(\xi)\begin{pmatrix}d_{00} & d_{01}e^{-i\omega_w\tau}\\ c.c. & d_{11}\end{pmatrix}\,,\\
&\gamma(\xi) = \frac{\omega_{p0}^2}{2\omega_L}\left(\frac{\delta n_a(\xi)}{n_{00}} - \frac{|a_0|^2 f_{\mathrm{acc}}^2(\xi)}{4}\right)\,,\\
&\omega_w = \Omega_{10} - \Omega_{00} \approx \frac{12.3\,c^2}{\omega_L R_\infty^2}\\
&d_{00} = \langle 00|\,\mathcal{J}_{00}^2\,|00\rangle \approx 0.57\,,\;\; d_{01} = \langle 00|\,\mathcal{J}_{00}^2\,|10\rangle \approx 0.27\,,\\
&d_{11} = \langle 10|\,\mathcal{J}_{00}^2\,|10\rangle \approx 0.48
\end{aligned} \tag{4.24}$$

where ω_w is the spot size oscillation frequency, *c.c.* indicates the complex conjugate of the upper anti-diagonal entry, and we have assumed the fundamental intensity profile $|a|^2 \approx |a_0|^2 f_{\mathrm{acc}}^2(\xi)\mathcal{J}_{00}^2(r)$ for the weakly relativistic term. This linear system of PDEs can then be solved analytically

$$\begin{aligned}
&\begin{pmatrix}\alpha_0(\xi,\tau)\\ \alpha_1(\xi,\tau)\end{pmatrix} = \boldsymbol{A}(\xi,\tau)\begin{pmatrix}\alpha_0(\xi,0)\\ \alpha_1(\xi,0)\end{pmatrix}\,,\\
&\boldsymbol{A}(\xi,\tau) = \exp\left[-i\gamma(\xi)\tau\begin{pmatrix}d_{00} & d_{01}\mathrm{sinc}\left(\frac{\omega_w\tau}{2}\right)e^{-i\omega_w\tau/2}\\ c.c. & d_{11}\end{pmatrix}\right]\,,\\
&w_{\mathrm{eff}}(\xi,\tau) \approx w_{0,\mathrm{eff}}\left(1 - 0.40\,\frac{\alpha_0^*\alpha_1 e^{-i\omega_w\tau} + c.c.}{|\alpha_0|^2}\right)\,.
\end{aligned} \tag{4.25}$$

This solution describes the excitation of the first radial transverse mode due to transverse (de-)focusing and self-modulation, both of which can arise through the effects of the wake and self-focusing. The interference between the fundamental and first radial mode then leads to a modulation of the local effective spot size $w_{\mathrm{eff}}(\xi,\tau)$. Evaluating this matrix exponential yields a unitary matrix with diagonal entries of $\mathcal{O}(1)$ and anti-diagonal entries of $\mathcal{O}(\gamma/\omega_w) \ll 1$. This ensures that, as long as the original TDPT condition is satisfied in regions of high intensity, laser light

initially in the fundamental transverse channel mode will also remain primarily in the fundamental mode, with small $\mathcal{O}(\gamma^2/\omega_w^2)$ and $\mathcal{O}(|\delta w|^2/w_0^2)$ oscillating exchanges in energy between the fundamental and first radial modes, where $\delta w/w_0 \ll 1$ is some small initial spot size mismatch.

Since the bulk of the wake is already excited by the zeroth order intensity $\sim \mathcal{J}_{00}^2(r)$, we can neglect the wake contribution of the $\mathcal{O}(\gamma/\omega_w) \ll 1$, $\sim \mathcal{J}_{00}(r)\mathcal{J}_{10}(r)$ first order correction to the laser transverse mode dynamics. However, the near-axis wakefield itself can be significantly affected as laser energy continuously oscillates towards and away from the axis, resulting in propagation-dependent accelerating and focusing fields which could, in principle, impact both the emittance and energy spread of an injected electron bunch.

An example of this phenomenon in 2D PIC simulations is evident in Figure 4.3, which shows snapshots of the laser intensity envelope and density perturbation as it propagates in a quasi-square channel. We can see that transverse mode excitation is the strongest for the trailing pulses which co-propagate with the largest amplitude wake, as described by Eq. 4.25. This results in an oscillation of the wake structure and hence the maximum on-axis accelerating field $E_{\max}$. This oscillation of on-axis field can also be observed directly in Figure 4.6. Despite the transverse mode excitation causing a break-up of the trailing pulses, Figures 4.3 and 4.4 show that the pulse train is still able to resonantly excite a wakefield even in the quasilinear regime with $E_{\max}/E_0 \sim 0.5$.

To compare the spot size oscillation frequency ω_w for a square channel given in Eq. (4.24) with the PIC simulations presented in Figure 4.6, a correction has to be made for the fact that the plasma channel used in all of the presented PIC simulations is quasi-square with walls of finite height and width of the form given in Eq. (4.7). For this quasi-square channel we define an effective channel radius, R_∞^{eff}, as that radius for which the fundamental mode, $\mathcal{J}_{00}(r)$, of an infinite square channel best matches the lowest-order mode of the quasi-square channel. For the $R = 30\,\mu\text{m}$ case, this results in an effective channel radius of approximately $R_\infty^{\text{eff}} \approx 46\,\mu\text{m}$. Substituting this into Eq. (4.24) then gives a spot size oscillation wavelength of

$2\pi c/\omega_w \approx 6.6\,\mathrm{mm}$, which is in good agreement with the observed oscillation period of the on-axis accelerating field in Figures 4.6 (a) and (b).

Various strategies can be employed to minimize this effect. The first step is to optimize the coupling quality of the pulse train into the channel, which would minimize oscillations associated with $|\delta w|/w_0$. After this is achieved, the next step involves minimizing the quantity $\left|\left(\int_{-\infty}^{\infty} d\xi(\gamma(\xi)/\omega_w) f_{\mathrm{acc}}^2(\xi)\right) / \left(\int_{-\infty}^{\infty} d\xi f_{\mathrm{acc}}^2(\xi)\right)\right|$, which is a measure of the oscillation of the wakefield structure behind the pulse train. For a given wake amplitude $\delta n_a(\xi)/n_{00}$, the two ways to minimize this quantity are: (i) to reduce detuning effects to ensure that the plasma wave zeros are as close to the pulse centroids as possible; and (ii) to increase the modulator parameter β, which shortens the pulse duration of each pulse in the train, so that they only sample the plasma wave as close to its zeros as possible; although we note that this strategy also increases SPM, which hastens the onset of depletion effects towards the heads of the pulses.

We also note that propagation over long distances in a finite plasma channel damps spot size oscillations by preferentially leaking out higher-order modes [120]. This, in combination with the spot size oscillation frequency locally varying across each single pulse due to $\gamma(\xi)$, causes the on-axis accelerating field to stabilize after some distance, as observed in Figure 4.6.

4.2.2 Non-Uniform Depletion

We also have to consider that the paraxial description which led to the result in Eq. (4.25) breaks down when depletion becomes non-negligible, which becomes important when driving quasilinear wakes where the dephasing length is a large fraction of the depletion length.

One caveat to the earlier analysis of the depletion length in Eq. (4.6) is that pulse trains do not deplete uniformly. Instead, trailing pulses, which co-propagate with steeper density gradients, will deplete faster than those near the beginning of the pulse train. We thus expect the pulses towards the rear of the train to have individual depletion lengths up to half as short as in Eq. (4.6), whilst the pulses

near the beginning of the train will experience minimal depletion.

The non-uniform depletion effects include group velocity dispersion (GVD) between the pulses, caused by the trailing depleted pulses slowing down more, and detuning spot size oscillations as depleted pulses have shorter spot size oscillation periods due to their shorter Rayleigh lengths.

As demonstrated in Figure 4.4, the pulse train is initially uniformly spaced and can therefore suffer from Rosenbluth-Liu detuning, though it remains a small effect due to the low number of pulses. However, as the pulse train depletes, the strongly red-shifting trailing pulses fall behind and become resonant with the wake. We also observe a small portion of the heads of each of the trailing pulses strongly blue-shifting and catching up with the train.

The onset of depletion effects is also expedited by relativistic SPM, as this increases the rate at which the heads of each pulse in the pulse train red-shifts and causes pulse steepening [121], which is observed in Figure 4.4(a). On one hand, depletion causes bunch dephasing to occur sooner than predicted by Eq. (4.3) by a reduction in group velocity. On the other hand, the resulting reduction in instantaneous laser frequency increases the ponderomotive force (which scales with $\boldsymbol{F}_\mathrm{p} \propto \omega^{-1}$ when holding photon number density constant), causing the wakefield amplitude to gradually increase with propagation distance, similar to the effect observed experimentally by M. J. V. Streeter et al. [122].

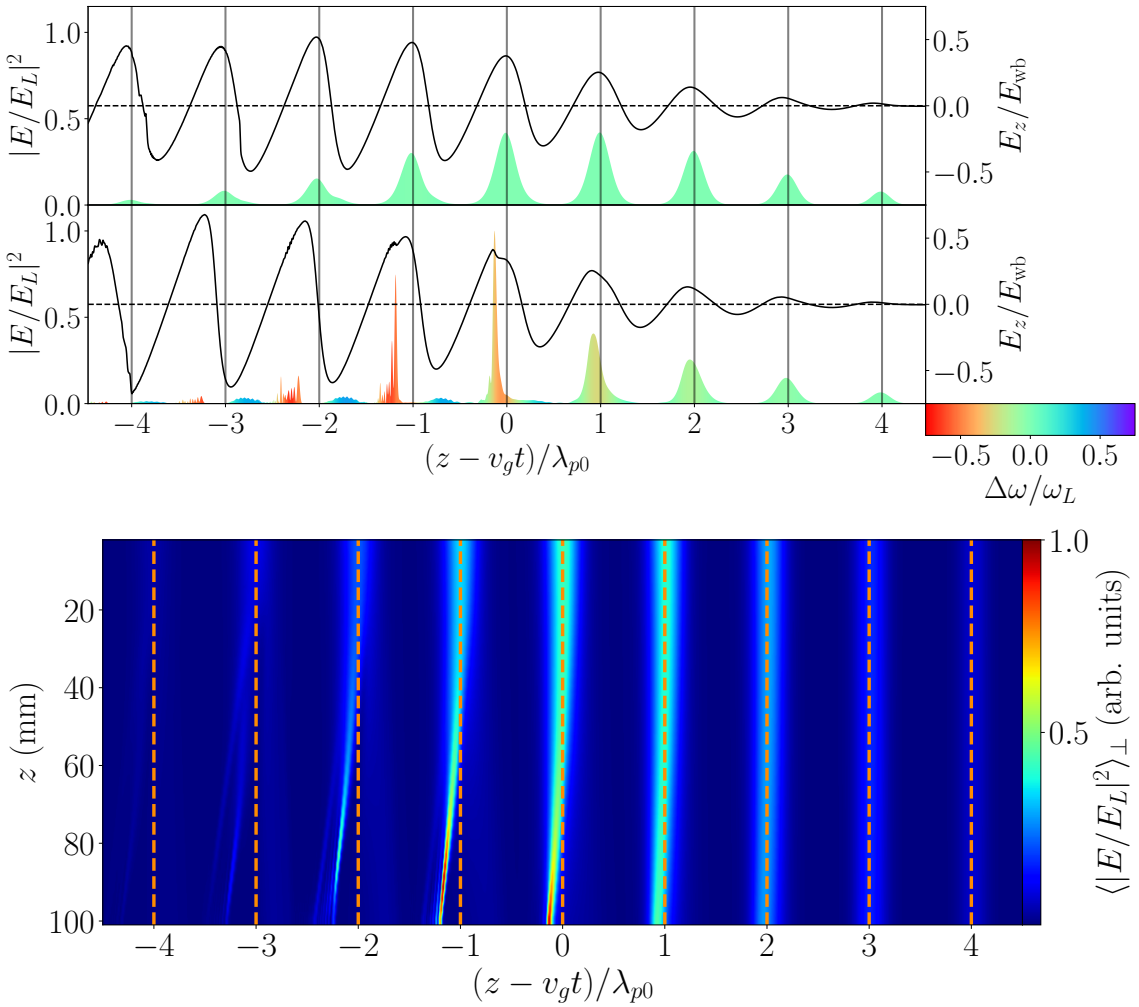


Figure 4.4: Results from the same PIC simulation presented in Figure 4.3 of (a) the on-axis normalized axial electric field E_z/E_0 and the normalized laser intensity envelope $|E/E_L|^2$ with $E_L = m_e\omega_L c/e$ and its shift in instantaneous frequency $\Delta\omega/\omega_L$ after 2 mm (top) and 100 mm (bottom) of propagation, and (b) the evolution of the transverse-averaged intensity envelope $\langle |E/E_L|^2 \rangle_\perp$. The pulse train is initially uniformly spaced and can therefore suffer from Rosenbluth-Liu detuning, though it remains a small effect due to the low number of pulses. However, as the pulse train depletes, the strongly red-shifting trailing pulses fall behind and become resonant with the wake. Conversely, we also observe a small portion of the heads of each of the trailing pulses strongly blue-shifting and catching up with the train. Note that $|E/E_L| \neq |a|$ at large propagation distances due to the significant red-shifting of the trailing pulses.

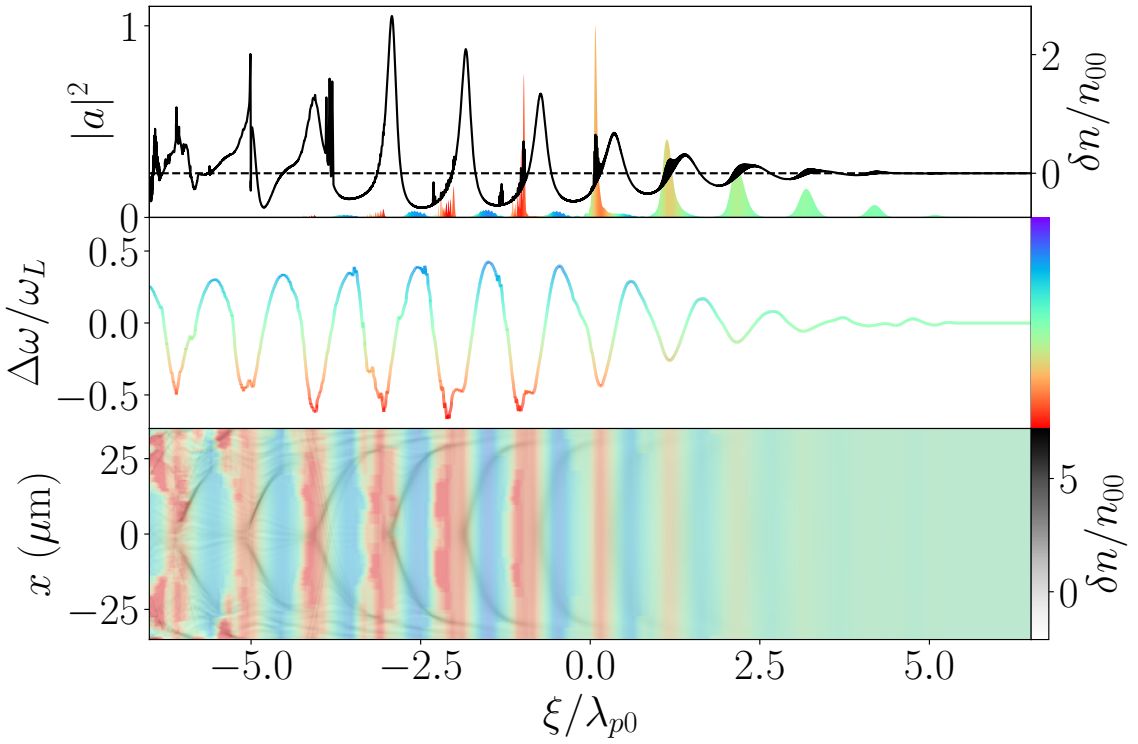


Figure 4.5: Results from the same PIC simulation as in Figure 4.3 after 100 mm propagation. Despite driving a quasilinear wakefield with transverse structure, the spectral modulation/depletion of the pulse train still remains approximately independent of transverse coordinate.

4.3 Multi-GeV P-MoPA Electron Accelerator

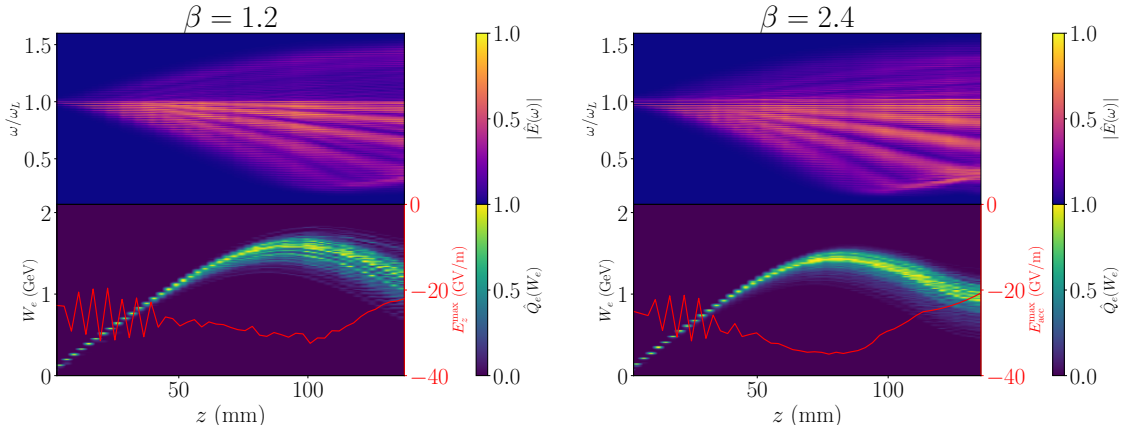
Taking into account the constraints set by the modulator stage (which sets a limit on W_{drive} for a given modulator spot size and plasma density [33]), relativistic detuning effects, optimizing the wake amplitude (by using a suitable modulator parameter β) and the evolution with z of the wakefield (caused by SPM and transverse mode excitation) one would get accelerators illustrated in Figure 4.6. These figures show the evolution of the laser spectra, maximum on-axis accelerating wakefield, and the energy of a test electron bunch. For these 2D PIC simulations, a 1 pC, 35 MeV Gaussian electron bunch is manually placed in phase with the peak accelerating wakefield with dimensions $x_{\text{rms}} = 4\,\mu\text{m}$, $z_{\text{rms}} = 1.5\,\mu\text{m}$ for $n_{00} = 2.5\times10^{17}\,\text{cm}^{-3}$. The bunch dimensions were scaled up by a factor of $\sqrt{2.5}$ for the $n_{00} = 1.0\times10^{17}\,\text{cm}^{-3}$ simulation.

For $n_{00} = 2.5 \times 10^{17}\,\mathrm{cm}^{-3}$, the observed propagation distance at which the maximum energy gain is achieved for the $\beta = 1.2$ case corresponds well with $L_\mathrm{d} = 93\,\mathrm{mm}$ predicted by Eq. (4.3) using $R_\infty^\mathrm{eff} = 46\,\mu\mathrm{m} \Rightarrow w_{0,\mathrm{eff}} = 30\,\mu\mathrm{m}$, with a laser-plasma energy transfer of 16%. According to Eq. (4.3), L_d is independent of β, but Figure 4.6(b) shows that increasing β to 2.4 causes L_d to decrease to 80 mm. The earlier onset of dephasing is primarily caused by the relativistic SPM pulse steepening process [121] as shown in Figure 4.4. This leads to $a_0 \sim 1$ for some of the pulses in the train, reducing their group velocities via relativistic effects on the plasma refractive index. The higher value of beta is also found to increase the laser-plasma energy transfer to 19%. This is primarily due to depletion effects occurring sooner due to SPM, which can be seen in the evolution of the laser spectrum. Despite this discrepancy, the higher β case only performs slightly worse with the mean energy gain in both cases being around $\sim 1.5\,\mathrm{GeV}$, which is in good agreement with the energy gain scaling law derived in Eq. (4.4) which predicts an energy gain of $\Delta W_e = 1.4\,\mathrm{GeV}$ for a relative wake amplitude of $E_\mathrm{max}/E_0 = 0.5$.

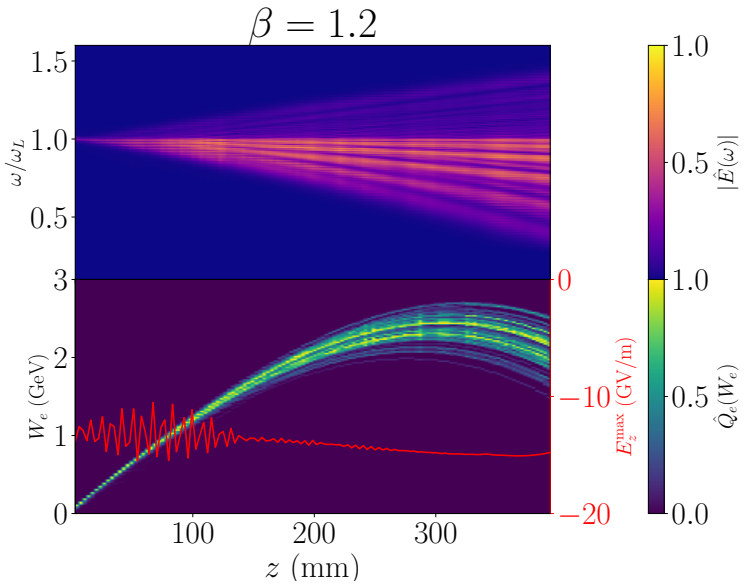
Figure 4.6(c) shows the result for a lower density accelerator stage with $n_{00} = 1.0 \times 10^{17}\,\mathrm{cm}^{-3}$ and $w_0 = 36\,\mu\mathrm{m}$ at $\beta = 1.2$. The evolution of the pulse train spectrum, accelerating field, and bunch energy is shown for lengths up to 280 mm. Even though this distance is insufficient to reach dephasing, a bunch of energy close to 3 GeV is obtained, which is again in good agreement with Eq. (4.4) which predicts an energy gain of $\Delta W_e = 2.9\,\mathrm{GeV}$. It is clear from this simulation that P-MoPAs operating at multi-GeV energy gains should be possible.

All three simulations shown in Figure 4.6 exhibit the expected oscillation in peak on-axis accelerating field due to transverse oscillations of the pulses in the train, as discussed in the previous section, and also observed in Figure. 4.3. On top of the oscillations, we also observe that the accelerating field temporarily grows in magnitude as the pulse train depletes due to SPM-induced pulse steepening and the GVD between pulses partially circumventing Rosenbluth-Liu detuning due to the strongly red-shifted trailing pulses having a slower group velocity, as was previously shown in Figure 4.4, as well as the red-shifting directly causing an increase in the

ponderomotive force exerted by the trailing pulses.



(a) $W_{\text{drive}} = 2.4\,\text{J}$, $R = 30\,\mu\text{m}$, $n_{00} = 2.5 \times 10^{17}\,\text{cm}^{-3}$ (b) $W_{\text{drive}} = 2.4\,\text{J}$, $R = 30\,\mu\text{m}$, $n_{00} = 2.5 \times 10^{17}\,\text{cm}^{-3}$



(c) $W_{\text{drive}} = 5.0\,\text{J}$, $R = 36\,\mu\text{m}$, $n_{00} = 1.0 \times 10^{17}\,\text{cm}^{-3}$

Figure 4.6: 2D PIC simulation results of accelerator performance at different modulation parameters β in a quasi-square channel of the same form used in Figure 4.3. The top panels display the normalized laser spectrum $|\hat{E}(\omega)|$ evolving with the propagation distance, whilst the bottom panels show the evolution of the normalized injected bunch electron energy spectrum $\hat{Q}_e(W_e)$ and maximum on-axis accelerating field $E_{\text{acc}}^{\max}$. Note that the oscillation of the on-axis accelerating field due to spot size oscillations is a continuous sinusoidal motion which disappears beyond 50 mm in (a,b) and 130 mm in (c), and only appears to be jagged in these plots due to sub-sampling.

Chapter 5

A P-MoPA-driven Water Window XFEL

We consider the P-MoPA as a potential kHz driver for a water-window X-ray free electron laser (XFEL). In previous chapters, we showed using both analytic theory and PIC simulations that the P-MoPA can provide multi-GeV energy gains with kHz-capable laser systems with experimentally plausible tolerances [33, 38]. Though these energies are suitable for driving X-ray light sources in the few-nanometer range, XFELs also require tight tolerances on electron bunch 6D brightness. In this chapter we develop a scheme based on previous studies of emittance preservation in beam-driven quasilinear wakefields [42, 43]. We adapt these methods to the P-MoPA, which requires additional considerations of effects arising from pulse propagation and direct pulse-bunch coupling effects, and propose experimental parameters in which the P-MoPA can be used for a kHz water-window XFEL.

5.1 Bunch Dynamics

Plasma wakefield accelerators must not only be able to achieve comparable energy gains to conventional RF cavities, but must also provide sufficiently low energy spreads and transverse emittances in order to compete with traditional accelerators. This is especially true when considering applications of plasma accelerators

for coherent X-ray light sources, which set stringent requirements on electron bunch quality. We therefore begin this chapter with a short review of bunch dynamics applied to plasma-based accelerators.

5.1.1 6D Phase Space

In general, a single-species bunch comprised of $N \ggg 1$ particles can be described using a smooth 6D phase space distribution function

$$\begin{aligned} &f(\boldsymbol{x}_\perp, \boldsymbol{p}_\perp, z, p_z, t)\,, \\ &N = \int f d\boldsymbol{x}_\perp d\boldsymbol{p}_\perp dz dp_z \end{aligned} \tag{5.1}$$

where z is the longitudinal direction of the bunch. This description along with the Boltzmann equation

$$\frac{\partial f}{\partial t} + \boldsymbol{v} \cdot \frac{\partial f}{\partial \boldsymbol{x}} + (\boldsymbol{F}_{\text{ext}} + \boldsymbol{F}_{\text{sc}}) \cdot \frac{\partial f}{\partial \boldsymbol{p}} = \left(\frac{\partial f}{\partial t}\right)_{\text{col}}\,, \tag{5.2}$$

where $\left(\frac{\partial f}{\partial t}\right)_{\text{col}}$ is the collision operator and $\boldsymbol{F}_{\text{ext}}$, $\boldsymbol{F}_{\text{sc}}$ are the external and space-charge forces, fully describe the bunch dynamics [123]. From the Boltzmann equation in Eq. (5.2), we can see that Liouville's theorem, which states that phase space density is conserved along phase space trajectories when under the influence of only Hamiltonian forces, only applies to this 6D distribution when all forces are conservative and collisions (including elastic) can be neglected. In the context of high-quality particle bunches, we will assume that the collision operator can be neglected (i.e. no scattering events), meaning we only need to consider the presence of non-conservative forces affecting beam quality. We note that even though the space-charge force is highly nonlinear due to its dependence on the distribution function, it is still a conservative force and therefore Liouville's theorem will still hold for this 6D distribution as long as the external force is also conservative and collisions can be neglected.

5.1.2 Emittance and Brightness

In practice, the high-dimensional 6D phase space makes it difficult to work with the Boltzmann equation analytically. In accelerator physics, we usually take moments and projections of the full 6D phase space and its longitudinal slices onto various 2D planes, e.g. the (x, p_x) plane. For some quantity q, the projected (p) and slice (s) expectation values are defined as

$$\begin{aligned}\langle q\rangle_{(\mathrm{p})}(t) &= \frac{\int q f d\boldsymbol{x}_\perp d\boldsymbol{p}_\perp dz dp_z}{N}\,,\\ \langle q\rangle_{(\mathrm{s})}(z,t) &= \frac{\int q f d\boldsymbol{x}_\perp d\boldsymbol{p}_\perp dp_z}{\int f d\boldsymbol{x}_\perp d\boldsymbol{p}_\perp dp_z}\,,\end{aligned} \tag{5.3}$$

from which we will construct bunch properties following the definitions in [124, 125].

The transverse emittance of a bunch is the area its distribution function occupies in transverse phase space. In physical terms, it measures how difficult it is to focus the bunch for a given focusing system. The definitions of phase emittance and normalized phase emittance in the (x, p_x) plane are given by

$$\begin{aligned}\epsilon_{\mathrm{ph}} &= \sqrt{\det(\mathrm{Cov}[x,p_x])} = \sqrt{\langle x^2\rangle\langle p_x^2\rangle - \langle x p_x\rangle^2}\,,\\ \epsilon_{\mathrm{ph,n}} &= \frac{\epsilon_{\mathrm{ph}}}{m_0 c}\,,\end{aligned} \tag{5.4}$$

the latter also being known as the rms emittance. We can also measure the emittance in trace-space (x, x'), where $x' = p_x/p_z$ is the angle. The trace emittance and normalized trace emittance are defined as

$$\begin{aligned}\epsilon_{\mathrm{tr}} &= \sqrt{\langle x^2\rangle\langle x'^2\rangle - \langle x x'\rangle^2}\,,\\ \epsilon_{\mathrm{tr,n}} &\approx \langle\beta\gamma\rangle\epsilon_{\mathrm{tr}}\end{aligned} \tag{5.5}$$

where β, γ are the normalized speed and relativistic Lorentz factor respectively. The expression for the normalized trace emittance is exact only when the energy spread is zero. All of these definitions can be applied to both the projected $\langle ...\rangle_{(\mathrm{p})}$ and slice $\langle ...\rangle_{(\mathrm{s})}$ cases. Note that the normalized phase and trace emittances are only equal

when $\langle xx' \rangle = 0$.

The bunch quality parameter that is most relevant to application in the FEL is the 6D normalized brightness, which is given by

$$B_{\mathrm{6D,n}} = \frac{Q}{\sqrt{\det(\Sigma_{\mathrm{6D}})}} \approx \frac{Q}{\epsilon_{\mathrm{n},x}\epsilon_{\mathrm{n},y}\epsilon_{\mathrm{n},z}} \tag{5.6}$$

where $Q = Ne$ is the total electron bunch charge and $\Sigma_{\mathrm{6D}} = \mathrm{Cov}[\boldsymbol{x}, \boldsymbol{p}/m_0 c]$ is the full 6D phase space covariance matrix, and the relation between the brightness and normalized emittances becomes exact so long as there are no cross-plane couplings [124]. The longitudinal normalized emittance $\epsilon_{\mathrm{n},z}$ scales with the bunch length σ_z and relative energy spread σ_E

$$\epsilon_{\mathrm{n},z} \approx \sigma_z \sigma_E \,. \tag{5.7}$$

The 6D brightness can also defined either for each slice or for the full projection, both of which are important for the FEL [126, 127]. Most FELs require a 6D brightness in the range of 10^{15}–10^{17} A m^{-2}rad^{-2}/0.1% [124, 128], corresponding with (slice) normalized emittances of 1.0 mm mrad or smaller. Therefore great care needs to be taken in preserving (normalized) emittance in the LWFA.

Even if we can assume that collisions are negligible and that the external forces are conservative, Liouville's theorem holding for the 6D phase space distribution alone does not necessarily imply emittance preservation. Firstly, for Liouville's theorem to apply for each of the planes (x, p_x), (y, p_y), (z, p_z), we also require that there are no couplings in the dynamics between each of the planes (e.g. via space-charge forces). On top of this, even if Liouville's theorem applies in each of the planes, we also need to avoid nonlinear/anharmonic forces acting on the bunch to prevent the growth of "effective" emittance due to coarse graining/filamentation [123, 129]. In this process, even though strictly speaking the phase space area is conserved, the shape of this area after many transverse oscillations becomes so "filamented" such that particle trajectories, in effect, occupy a larger phase space region. Therefore to take full advantage of Liouville's theorem to preserve emittance, bunches should be

emittance-matched to avoid undergoing large transverse oscillations and/or remain in regions where focusing forces are as linear/harmonic as possible.

5.1.3 Bunch Self-Fields

As a potential source of nonlinear forces acting on the bunch, it is important to be able to rule out the highly nonlinear space-charge forces in order to preserve emittance. Space-charge forces arise from a charged bunch's self-consistent electromagnetic fields due to its current and charge. In the absence of plasma, for an electron bunch traveling at a fixed highly relativistic velocity $v_\mathrm{b}\hat{z}$, the fields are determined by the following inhomogeneous wave equations

$$\begin{aligned}\left(\Delta - \frac{1}{c^2}\frac{\partial^2}{\partial t^2}\right)\boldsymbol{E} &= -\frac{e}{\epsilon_0}\nabla n_\mathrm{b} - \frac{ev_\mathrm{b}}{\epsilon_0 c^2}\frac{\partial n_\mathrm{b}}{\partial t}\hat{z}\,,\\ \left(\Delta - \frac{1}{c^2}\frac{\partial^2}{\partial t^2}\right)\boldsymbol{B} &= \frac{ev_\mathrm{b}}{\epsilon_0 c^2}\nabla\times(n_\mathrm{b}\hat{z})\,,\end{aligned} \tag{5.8}$$

where $n_\mathrm{b}(\boldsymbol{x},t)$ is the electron bunch density. Shifting to co-moving coordinates $\xi = z - v_\mathrm{b}t$, $\tau = t$ and taking the quasistatic approximation $\partial/\partial t \approx -v_\mathrm{b}\partial/\partial\xi$ then gives

$$\begin{aligned}\left(\Delta_\perp + \frac{1}{\gamma_\mathrm{b}^2}\frac{\partial^2}{\partial\xi^2}\right)\boldsymbol{E} &= -\frac{e}{\epsilon_0}\left(\nabla_\perp n_\mathrm{b} + \frac{1}{\gamma_\mathrm{b}^2}\frac{\partial n_\mathrm{b}}{\partial\xi}\hat{z}\right)\,,\\ \left(\Delta_\perp + \frac{1}{\gamma_\mathrm{b}^2}\frac{\partial^2}{\partial\xi^2}\right)\boldsymbol{B} &= \frac{ev_\mathrm{b}}{\epsilon_0 c^2}\nabla\times(n_\mathrm{b}\hat{z})\,,\end{aligned} \tag{5.9}$$

where $\gamma_\mathrm{b} = (1 - v_\mathrm{b}^2/c^2)^{-1/2}$ is the Lorentz factor. Finally, taking the cross product of $v_\mathrm{b}\hat{z}/c^2$ with the top equation yields the relation between the electric and magnetic fields

$$\boldsymbol{B} = \frac{v_\mathrm{b}}{c^2}(\hat{z}\times\boldsymbol{E})\,. \tag{5.10}$$

For example, consider an axisymmetric Gaussian bunch of radially uniform charge density of radius R and a Gaussian longitudinal profile of the form

$$n_{\mathrm{b}}(r,\xi) = \begin{cases} n_{\mathrm{b}0}\exp\left(-\frac{\xi^2}{2\sigma_z^2}\right) & r < R \\ 0 & r > R \end{cases}$$
$$n_{\mathrm{b}0} = \frac{-Q/e}{\pi R^2\sqrt{2\pi}\sigma_z} \tag{5.11}$$

where Q is the total bunch charge. In the highly relativistic limit $\gamma_{\mathrm{b}} \gg 1$ and assuming that the bunch dimensions obey the long, thin beam limit $\gamma_{\mathrm{b}}\sigma_z \gg R$ allows us to calculate the radial electric field within the bunch (i.e. $r < R$, $\xi \lesssim \sigma_z$) from Gauss's law, along with its consistent azimuthal magnetic field

$$E_r(r<R,\xi) = \frac{-en_{\mathrm{b}0}}{2\epsilon_0} r\exp\left(-\frac{\xi^2}{2\sigma_z^2}\right),$$
$$B_\theta(r<R,\xi) = \frac{-en_{\mathrm{b}0}v_{\mathrm{b}}}{2\epsilon_0 c^2} r\exp\left(-\frac{\xi^2}{2\sigma_z^2}\right), \tag{5.12}$$

By looking at Eq. (5.10), we can see that the azimuthal magnetic field contribution in the Lorentz force partially cancels out the radial electric field, suppressing the transverse force by a factor of γ_{b}^{-2}

$$\begin{aligned} F_r &= -e(E_r - v_{\mathrm{b}}B_\theta) \\ &= \frac{-eE_r}{\gamma_{\mathrm{b}}^2} \\ &= \frac{e^2 n_{\mathrm{b}0}}{2\gamma_{\mathrm{b}}^2\epsilon_0} r\exp\left(-\frac{\xi^2}{2\sigma_z^2}\right), \end{aligned} \tag{5.13}$$

meaning that the transverse space-charge force for an axisymmetric beam is strongly suppressed for highly relativistic bunches. Likewise, the axial field is also strongly suppressed by the Lorentz factor. To find the axial field, we can use Faraday's law in combination with the quasistatic approximation, which gives the following axial

field within the bunch under the influence of the Lorentz force

$$\frac{\partial E_z}{\partial r} = \frac{1}{\gamma_\mathrm{b}^2}\frac{\partial E_r}{\partial \xi}$$
$$\Rightarrow E_z(r < R, \xi) = \frac{e n_{\mathrm{b}0}}{4\gamma_\mathrm{b}^2 \sigma_z^2 \epsilon_0} r^2 \xi \exp\left(-\frac{\xi^2}{2\sigma_z^2}\right) . \tag{5.14}$$

For the highly relativistic electron bunches we will be considering later in this chapter, we can safely assume the long, thin beam limit $\gamma_\mathrm{b}\sigma_z \gg R$, therefore allowing us to neglect the effects of both transverse and axial space-charge forces on the bunch dynamics.

5.1.4 Transverse Equations of Motion

Now that we have also ruled out space-charge forces, we can now calculate the transverse dynamics of a highly relativistic electron bunch in the presence of external fields by considering the motion of single electrons in the bunch

$$\frac{\mathrm{d}\boldsymbol{p}}{\mathrm{d}t} = -e(\boldsymbol{E} + \boldsymbol{v} \times \boldsymbol{B}) . \tag{5.15}$$

Assuming that the electron is highly relativistic in the z direction such that $p_z \gg m_e c^2, p_x, p_y$, we can recover the coupled transverse equations of motion

$$\ddot{x} + \Gamma\dot{x} = -\frac{e}{\gamma m_e}\left(E_x + \dot{y}B_z - cB_y\right) ,$$
$$\ddot{y} + \Gamma\dot{y} = -\frac{e}{\gamma m_e}\left(E_y - \dot{x}B_z + cB_x\right) , \tag{5.16}$$

where $\Gamma = \dot{\gamma}/\gamma$ is the damping rate due to continuous acceleration. In most LWFA applications, we do not expect the presence of a strong axial magnetic field B_z. This allows us to decouple these equations and consider the transverse dynamics separately. If we can also assume that the bunch centroid is centered along the wakefield axis and that the bunch transverse size is small relative to that of the wake, then the focusing field $E_r - cB_\theta$ can be treated as an approximately linear function with transverse displacement. This then yields the nonlinear damped oscillator

equation

$$\begin{aligned} &\ddot{x} + \Gamma\dot{x} + \omega_\beta^2 x = 0\,, \\ &\omega_\beta^2 = \frac{e}{\gamma m_e}\frac{\partial\left(E_x - cB_y\right)}{\partial x}\Big|_{x=y=0} \end{aligned} \tag{5.17}$$

where ω_β is the betatron oscillation frequency. In the special case of no acceleration and for the focusing force to only be a function of the electron's longitudinal position z, then this reduces to Hill's equation [130]

$$x'' + K(z)x = 0 \tag{5.18}$$

where $x' = p_x/p_z \approx \dot{x}/c$ again signifies the small transverse deflection angle and $K(z) = \omega_\beta^2(z)/c^2$ is the focusing parameter. Solutions to this equation can be written in the form

$$x(z) = w_\mathrm{b}(z)e^{i\Phi(z)}\,, \quad x^*(z) = w_\mathrm{b}(z)e^{-i\Phi(z)} \tag{5.19}$$

where $w_\mathrm{b}(z)$ and $\Phi(z)$ are the amplitude and phase functions and x^* indicates the complex conjugate. Substituting this into Eq. (5.18) and using the fact that the focusing coefficient $K(z)$ is real, forces them to satisfy the betatron envelope and phase equations [131]

$$\begin{aligned} &w_\mathrm{b}'' + Kw_\mathrm{b} - \frac{1}{w_\mathrm{b}^3} = 0\,, \\ &\Phi' = \frac{1}{w_\mathrm{b}^2}\,. \end{aligned} \tag{5.20}$$

The betatron frequency is, in general, a function of both the wakefield amplitude and position of the electron. However, in the blowout regime, a simplification can be made where the betatron frequency is independent of the longitudinal coordinate. This will be relevant not only for LWFA in the blowout regime, but also for high-charge bunches which drive their own transverse blowout wake. In this regime, the transverse electric field in the neighborhood of the bunch is dominated by the ion

column it leaves behind, which gives the following radial electric field according to Gauss's law

$$E_r = \frac{r}{2}\frac{en_{00}}{\epsilon_0} = \frac{m_e\omega_{p0}^2 r}{2e}\,. \tag{5.21}$$

As there are no appreciable currents in the cavity, we do not expect any magnetic contribution to the focusing force. Substituting this expression into Eq. (5.17) then yields the blowout regime betatron oscillation frequency [132]

$$\omega_\beta = \frac{\omega_{p0}}{\sqrt{2\gamma}}\,. \tag{5.22}$$

5.1.5 Twiss Parameters

To describe the evolution of the entire relativistic electron bunch, it is convenient to introduce the Twiss parameters α, β, γ [130] (a.k.a. the Courant-Snyder parameters), which describe the elliptical shape of the bunch distribution in 2D transverse trace space (x, x')

$$\begin{aligned}
\sigma_x^2 &= \langle x^2 \rangle = \beta\epsilon_{\mathrm{tr}}\,,\\
\sigma_{x'}^2 &= \langle x'^2 \rangle = \gamma\epsilon_{\mathrm{tr}}\,,\\
\sigma_{xx'} &= \langle xx' \rangle = -\alpha\epsilon_{\mathrm{tr}}\,,
\end{aligned} \tag{5.23}$$

noting that β refers to the Twiss parameter rather than the P-MoPA modulator parameter in this context. The Twiss parameters are linked by the following relations

$$\begin{aligned}
\beta\gamma - \alpha^2 &= 1\,,\\
\alpha &= -\frac{\beta'}{2}\,.
\end{aligned} \tag{5.24}$$

If we can assume that electrons are under the influence of solely emittance-preserving harmonic forces, and that acceleration is slow enough such that $\Gamma \ll \omega_\beta$, the evolution of the entire electron bunch can be described using the betatron envelope equation derived in Eq. (5.20) by replacing the amplitude function w_{b} with the

Twiss parameter $\beta^{1/2}$ [131], yielding

$$\frac{1}{2}\beta\beta'' - \frac{1}{4}(\beta')^2 + K\beta^2 = 1\,, \tag{5.25}$$

from which we can trivially derive the matched Twiss parameters which prevent transverse oscillations of the bunch for a given linear focusing field

$$\begin{aligned}\beta_m &= K^{-1/2}\,,\\ \alpha_m &= 0\,,\\ \gamma_m &= 1/\beta_m\,.\end{aligned} \tag{5.26}$$

To prevent large betatron oscillations which could lead to emittance growth, the electron bunch at the start of acceleration must be as close to this emittance-matching condition as possible. For example, in the blowout regime where $\omega_\beta = \omega_{p0}/\sqrt{2\gamma_\mathrm{b}}$, where γ_b is the Lorentz factor of the bunch, the matched Twiss parameters and transverse bunch size are given by [42, 56]

$$\begin{aligned}\beta_m &= \left(\frac{\omega_{p0}^2}{2\gamma_\mathrm{b}c^2}\right)^{-1/2}\,,\\ \sigma_{\perp,m} &= (\beta_m\epsilon_\mathrm{tr})^{1/2} \approx \left(\beta_m\frac{\epsilon_\mathrm{tr,n}}{\gamma_\mathrm{b}}\right)^{1/2} = \left(\frac{2c^2\epsilon_\mathrm{tr,n}^2}{\omega_{p0}^2\gamma_\mathrm{b}}\right)^{1/4}\,,\end{aligned} \tag{5.27}$$

which corresponds to a $\sigma_{\perp,m} \sim 1\,\mu\mathrm{m}$ bunch size for an electron bunch with normalized emittance $\epsilon_\mathrm{n} = 1.0\,\mathrm{mm\,mrad}$, $E_\mathrm{k} \sim 0.1{-}1$ GeV energy and $n_{00} = 1.0{\times}10^{17}\,\mathrm{cm}^{-3}$ plasma density.

5.2 X-ray Free Electron Lasers

5.2.1 Motivation

The development of the X-ray free electron laser (XFEL) has enabled the probing of physics on the ultrashort ($\sim 1\,\mathrm{fs}$) and ultrasmall ($\sim 1\,\text{Å}$) scales, serving a plethora of applications in studying atomic/molecular/optical physics, condensed

matter physics, matter under extreme conditions, chemistry and biology [133–142].

The original FEL concept was introduced by Madey in 1971 [143], which he later demonstrated experimentally [144] with lasing at a wavelength of 3.4 µm. Ever since, there has been a continuous push to develop FELs capable of shorter and shorter wavelengths. In 2005, FLASH at DESY, Germany became the first operational soft X-ray FEL [145]. Four years later, LCLS at SLAC National Accelerator Laboratory, USA became the first hard X-ray FEL facility [146], achieving lasing at a wavelength of 1.5 Å. Since then, many more XFELs have opened worldwide, the leading hard X-ray facilities being LCLS (USA), SwissFEL (Switzerland), EuXFEL (Germany), PAL-XFEL (South Korea) and SACLA (Japan).

Table 5.1: Example XFEL slice (s) and projected (p) parameters, sourced from [128].

Name	λ_{min} (nm)	E_{k} (GeV)	Q (pC)	I_{p} (kA)	$B_{\mathrm{6D,n}}$ (A/m^2/0.1%)
EuXFEL	0.05	14.0	250	5.0	$< 4 \times 10^{17}$ (s) 7×10^{15} (p)
SACLA	0.06	8.45	300	4.0	5×10^{17} (s) 5×10^{15} (p)
PAL-XFEL	0.1	10.0	200	3.0	1.3×10^{17} (s) 2.1×10^{16} (p)
SwissFEL	0.1	5.8	200	3.0	5.8×10^{17} (s) 1.1×10^{16} (p)
LCLS	0.12	14	250	3.0	7.1×10^{16} (s) 5×10^{16} (p)
FERMI	4	1.5	500	0.6	6×10^{15} (s) 3×10^{14} (p)
FLASH I	6.5	1.0	500	2.5	1.9×10^{16} (s) 0.4×10^{15} (p)
FLASH II	4	1.0	1000	1.2	4×10^{15} (s) 1×10^{14} (p)

State-of-the-art XFELs are kilometer-scale facilities boasting price tags on the order of 1 billion USD, posing a serious investment for countries to consider. There has thus been great interest in the development of compact XFELs which can provide users with comparable performance at a much smaller scale and budget. The LWFA is a promising candidate, with the first proof-of-concept driving soft X-ray

undulator radiation demonstrated as early as 2009 [147], and more recent experiments have demonstrated LWFA-driven FEL lasing with gain at wavelengths down to 27 nm [148]. The high energy >1 GeV, peak current 1 kA and low emittance $0.1 - 1.0$ mm mrad bunches available from LWFAs [56] make them, in theory, well-suited for driving soft X-ray FELs. However, before LWFA-driven XFELs can become practical, they still have to overcome shot-to-shot stability and repetition rate limits before they can compete with conventional XFEL drivers.

In this chapter we propose the P-MoPA as a multi-kHz repetition rate high-quality electron bunch source suitable for driving an XFEL. We are specifically interested in studying the P-MoPA for driving soft X-ray undulator radiation in the "water-window". This lies between the K-absorption edges of carbon at 4.40 nm and oxygen at 2.33 nm, in which water is transparent but organic compounds are absorbing, ideal for microscopic imaging of biological material. Both FLASH [145] and FERMI [149] use 1 GeV electron beams to drive photon energies up to the water window, so the multi-GeV energies accessible by the P-MoPA is ideal for this wavelength range.

We start this section with a brief introduction to free electron lasing and derive the electron bunch requirements for a water-window XFEL. We then propose a scheme to achieve these bunch quality requirements based on previous studies of emittance preservation in beam-driven quasilinear wakefields [42, 43]. We study an external electron injection scheme using similar beam parameters as considered by the EuPRAXIA project [44–46], but envision a different injector based on recent developments in THz-driven beam compression [150–152] which can provide > 10 pC, sub-10 fs electron bunches with sub-10 fs synchronization.

5.2.2 Free Electron Lasing

Consider a single highly relativistic electron with Lorentz factor $\gamma_b \gg 1$ initially propagating in the z direction along the following sinusoidal magnetic field of period

λ_u generated by a planar undulator

$$\boldsymbol{B}_\mathrm{u} = B_\mathrm{u} \cos\left(\frac{2\pi z}{\lambda_\mathrm{u}}\right) \hat{y}\,. \tag{5.28}$$

As the electron oscillates in the transverse plane, it will radiate in the forward direction every half-period of the undulator. This radiation will then constructively interfere with a spectrum centered around the resonant wavelength λ_r and its harmonics n given by [153–160]

$$\begin{aligned} \lambda_\mathrm{r} &= \frac{\lambda_\mathrm{u}}{2n\gamma_\mathrm{b}^2}\left(1 + \frac{K_\mathrm{u}^2}{2} + \gamma_\mathrm{b}^2\theta^2\right)\,, \\ K_\mathrm{u} &= \frac{eB_u\lambda_\mathrm{u}}{2\pi m_e c} \end{aligned} \tag{5.29}$$

where θ is the observation angle and K_u is the undulator deflector parameter. This allows the radiation to be tuned by both the magnetic field strength and the electron energy. For example, consider an undulator of period $\lambda_\mathrm{u} = 25\,\mathrm{mm}$ with an undulator parameter of $K_\mathrm{u} = 1$ ($B_\mathrm{u} = 0.43\,\mathrm{T}$). The radiation wavelength emitted from such an undulator will have a resonant wavelength of $\lambda_\mathrm{r} = 5\,\mathrm{nm}$ for a $1\,\mathrm{GeV}$ electron beam and $\lambda_\mathrm{r} = 2\,\mathrm{nm}$ at $2\,\mathrm{GeV}$.

Undulators naturally have a homogeneous linewidth that scales inversely with the number of undulator periods N_u [161], which for the first harmonic is given by

$$\left[\frac{\Delta\lambda}{\lambda}\right]_\mathrm{n} \approx \frac{1}{N_\mathrm{u}}\,. \tag{5.30}$$

In practice, emittance and energy spread of the electron bunch will also contribute to the linewidth via inhomogeneous broadening. This can be understood by inspecting Eq. (5.29) and allowing a finite relative energy spread σ_E, beam width σ_y (along the undulator field) and divergence $\sigma_{x',y'}$ (in both directions), which again for the

first harmonic separately yield [161]

$$\begin{aligned}
\left[\frac{\Delta\lambda}{\lambda}\right]_{\sigma_E} &= 2\sigma_E\,, \\
\left[\frac{\Delta\lambda}{\lambda}\right]_{\sigma_y} &= \frac{2\pi^2 K_\mathrm{u}^2\sigma_y^2}{\lambda_\mathrm{u}^2(1+K_\mathrm{u}^2/2)} = \frac{2\pi^2 K_\mathrm{u}^2}{\lambda_\mathrm{u}^2(1+K_\mathrm{u}^2/2)}\frac{\beta_y\epsilon_{\mathrm{n}y}}{\gamma_\mathrm{b}}\,, \\
\left[\frac{\Delta\lambda}{\lambda}\right]_{\sigma_{x',y'}} &= \frac{\gamma_\mathrm{b}^2\sigma_{x',y'}^2}{1+K_\mathrm{u}^2/2} = \frac{\gamma_\mathrm{b}\gamma_{x,y}\epsilon_{\mathrm{n}x,y}}{1+K_\mathrm{u}^2/2}\,,
\end{aligned} \tag{5.31}$$

where we have assumed that $\alpha_{x,y} = 0$.

5.2.3 Bunch Requirements

In the previous section on bunch dynamics, we introduced the 6D normalized brightness $B_{\mathrm{6D,n}}$ in Eq. (5.6) as the most important parameter to consider when designing a FEL, and is approximately given by

$$B_{\mathrm{6D,n}} \approx \frac{Q}{\epsilon_{\mathrm{n},x}\epsilon_{\mathrm{n},y}\sigma_E\sigma_z}\,. \tag{5.32}$$

On top of the low transverse emittance requirements, there is also a strong constraint on the relative energy spread which is set by the FEL Pierce parameter ρ [162], which determines the gain length L_g of the FEL

$$\begin{aligned}
\sigma_E \ll \rho &= \left(\frac{1}{64\pi^2}\frac{I_\mathrm{p}}{I_\mathrm{A}}\frac{K_\mathrm{u}^2[JJ]^2\lambda_\mathrm{u}^2}{\gamma_\mathrm{b}^3\sigma_\perp^2}\right)^{1/3}\,, \\
I_\mathrm{p} &= \frac{Qc}{\sqrt{2\pi}\,\sigma_z}\,, \\
L_\mathrm{g} &= \frac{\lambda_\mathrm{u}}{4\pi\sqrt{3}\,\rho}
\end{aligned} \tag{5.33}$$

where $[JJ] = [J_0(s) - J_1(s)]$ with $s = K_\mathrm{u}^2/(4+2K_\mathrm{u}^2)$ for a planar undulator, I_p is the peak current, $I_\mathrm{A} \approx 17\,\mathrm{kA}$ is the Alfvén current and $\sigma_\perp$ is the rms transverse size of the electron bunch.

Though both slice and projected brightness are important for the FEL [126, 127], this sensitivity to the projected energy spread can be corrected for in some cases by

introducing a transverse field variation in the undulator to compensate for chromatic emittance growth [163]. We will therefore make slice brightness the key parameter to optimize for the P-MoPA. Looking at the water-window FEL examples in Table 5.1, XFEL lasing at $\lambda = 4\,\mathrm{nm}$ typically requires slice brightnesses on the order of $> 1 \times 10^{15}$ A m^{-2}rad^{-2}/0.1%, which will be our target for the P-MoPA driver.

On top of the low transverse emittance requirements for maximizing the brightness, the bunch trace emittance also needs to be smaller or approximately equal to the undulator radiation photon transverse trace-space [135]

$$\epsilon_{\mathrm{tr}} = \frac{\epsilon_{\mathrm{tr,n}}}{\gamma_{\mathrm{b}}} \lesssim \frac{\lambda}{4\pi}\,. \tag{5.34}$$

If the trace emittance is much smaller than this bound, then the undulator radiation will be diffraction-limited and the photon brightness will be given by [135]

$$B_{\mathrm{ph}} = \frac{N_{\mathrm{ph}}}{2\pi(\lambda/2)^2\sigma_t\sigma_\omega/\omega} \tag{5.35}$$

where N_{ph} is the photon count, σ_t is the duration and σ_ω is the frequency bandwidth. Substituting $\lambda = 4\,\mathrm{nm}$ into Eq. (5.34), we find that we require electron energies of $\gtrsim 1.6\,\mathrm{GeV}$ for a normalized emittance of $1.0\,\mathrm{mm\,mrad}$. Since we are aiming for acceleration in the range of 1–2 GeV, this condition is approximately satisfied, and so the undulator radiation emitted by our beam will be near diffraction-limited with a correction given by [135]

$$\begin{aligned} B_{\mathrm{ph}} &= \frac{N_{\mathrm{ph}}}{4\pi^2\Sigma 2\pi\sigma_t\sigma_\omega\omega} \\ \Sigma &= \sqrt{\sigma_x^2+\sigma_r^2}\sqrt{\sigma_{x'}^2+\sigma_{r'}^2}\sqrt{\sigma_y^2+\sigma_r^2}\sqrt{\sigma_{y'}^2+\sigma_{r'}^2}\,, \\ \sigma_r &= \frac{\sqrt{\lambda\lambda_{\mathrm{u}}N_{\mathrm{u}}}}{4\pi}\,, \\ \sigma_{r'} &= \sqrt{\frac{\lambda}{\lambda_{\mathrm{u}}N_{\mathrm{u}}}}\,, \end{aligned} \tag{5.36}$$

where σ_r and $\sigma_{r'}$ are the radiation beam radius and spread given by the homogeneous linewidth.

5.3 Emittance Matching in a P-MoPA

Now having established the bunch requirements for driving a 4 nm water-window XFEL, we now aim to meet these requirements and find realistic parameters for delivering these high-quality bunches with the P-MoPA. To achieve this, we consider an external injection scheme using similar beam parameters as the EuPRAXIA project [44–46], but envision a different injector based on recent developments in THz-driven beam compression [150–152] providing 150 MeV, $\epsilon_{\mathrm{n}} = 1.0\,\mathrm{mm\,mrad}$, $\sigma_E = 0.1\%$, $\sigma_z \sim 1\,\mu\mathrm{m}$ electron bunches. The goal is to then preserve the normalized emittance of these bunches within the accelerator stage and bring them up to at least 1 GeV, with a sufficiently high bunch charge to get the $\sim 1\,\mathrm{kA}$ peak currents required for a high-gain water-window XFEL.

5.3.1 Transverse Beam Loading

As the P-MoPA is operated in the quasilinear regime, we do not automatically get the benefits of the longitudinally uniform, emittance-preserving focusing fields provided by wakefields in the blowout regime. In the low-charge limit, the focusing fields would be provided purely by the laser-driven quasilinear wakefield, and would thus have both a longitudinal dependence and variation along the accelerator due to the long-propagation laser dynamics discussed in Chapter 4.

Fortunately, to get around this we can make use of the transverse beamloading technique [124]. In this scheme, which has been previously studied for emittance preservation in proton-driven quasilinear wakefields [42, 43], the electron bunch is provided with sufficient charge to locally drive a blowout wake. This then provides the desirable blowout focusing fields over the trailing half of the electron bunch, preserving emittance. The head of the bunch will still be subject to the focusing fields of the quasilinear wake, and is expected to only undergo slight emittance growth, preserving emittance much better than would be expected from head erosion [164, 165]. The maximum bunch charge in this scheme is limited by longitudinal beam loading which reduces the accelerating gradient with the addition of more

charge.

In this setup, we require the transverse size of the electron bunch to approximately obey the emittance matching condition for the blowout regime, as was derived previously in Eq. (5.27), and be small relative to the plasma wavelength

$$k_{p0}\sigma_{\perp,m} = k_{p0}\left(\frac{2c^2\epsilon_{\mathrm{n}}^2}{\omega_{p0}^2\gamma_{\mathrm{b}0}}\right)^{1/4} = \left(\frac{2k_{p0}^2\epsilon_{\mathrm{n}}^2}{\gamma_{\mathrm{b}0}}\right)^{1/4} \ll 1\,, \tag{5.37}$$

where $\gamma_{\mathrm{b}0} = 294$ is the Lorentz factor of the 150 MeV electron bunch at the entrance of the accelerator stage. An example snapshot of a PIC simulation of this setup is presented in Figure 5.1.

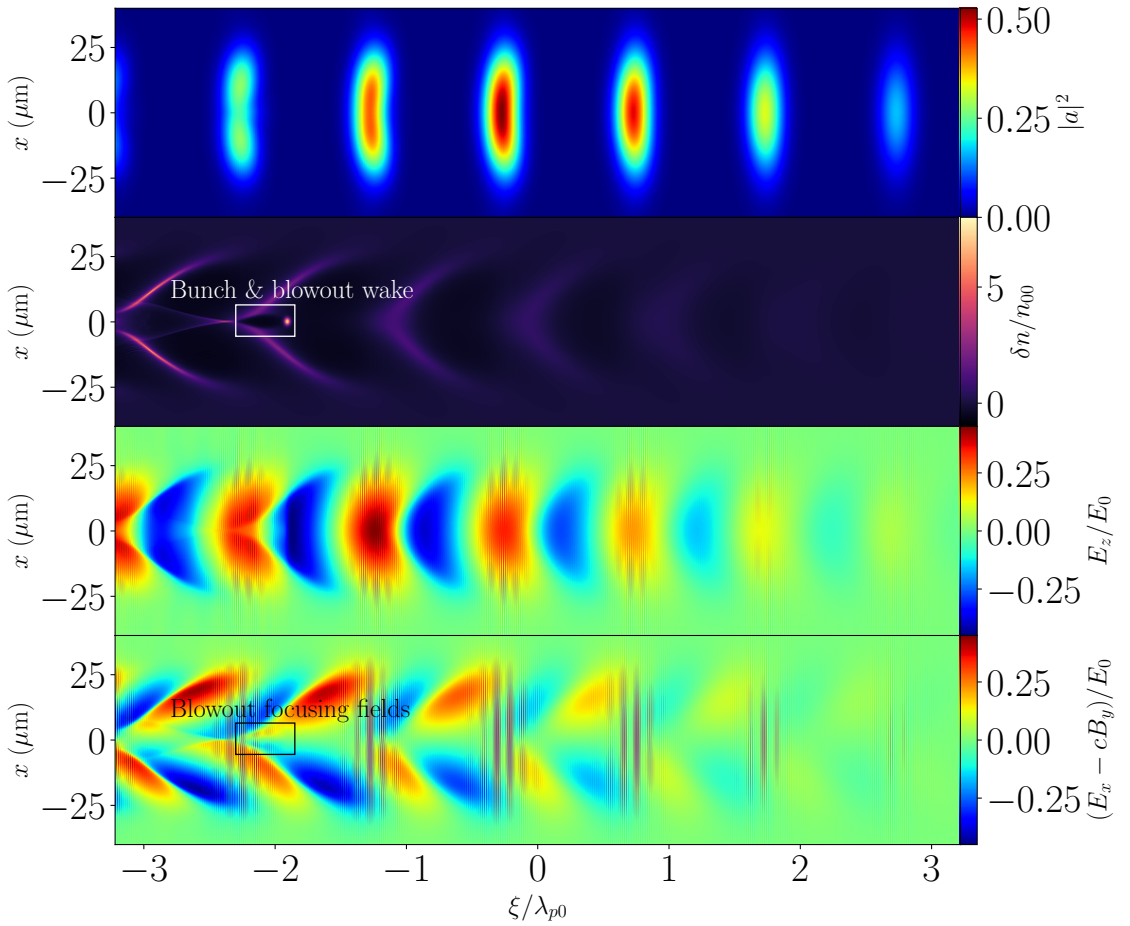


Figure 5.1: Early snapshot of a WarpX PIC simulation of a 150 MeV, 4.4 pC, 1.0 mm mrad electron bunch injected following the self-matching condition in Eq. (5.27) into a P-MoPA accelerator stage with $W_{\text{drive}} = 2.4$ J, modulator parameter $\beta = 1.2$, $n_{00} = 2.5 \times 10^{17}\,\text{cm}^{-3}$, $w_0 = 30\,\mu\text{m}$ in a matched parabolic plasma channel. The plasma forms a small blowout wake in response to the high density $n_{\text{b0}}/n_{00} = 8$ electron bunch, providing blowout focusing fields for the trailing half of the bunch. The head of the bunch remains focused due to the quasilinear focusing wakefields.

Using this emittance self-matching expression, we can then recover the following set of scaling laws for the bunch charge, 6D brightness, and peak current assuming conservation of normalized emittance ϵ_{n} in a transverse beam loaded quasilinear

accelerator stage

$$\begin{aligned} Q &= -en_{\mathrm{b0}}(2\pi)^{3/2}\sigma_{\perp,m}^2\sigma_z \\ &= -(2\pi)^{3/2}\frac{n_{\mathrm{b0}}}{n_{00}}\left(\frac{2}{\gamma_{\mathrm{b0}}}\right)^{1/2}\epsilon_0 E_0\epsilon_{\mathrm{n}}\sigma_z \\ B_{\mathrm{6D,n}} &\approx \frac{|Q|}{\epsilon_{\mathrm{n}}^2\sigma_z\sigma_E} \\ &= (2\pi)^{3/2}\frac{n_{\mathrm{b0}}}{n_{00}}\left(\frac{2}{\gamma_{\mathrm{b0}}}\right)^{1/2}\frac{\epsilon_0 E_0}{\epsilon_{\mathrm{n}}\sigma_E}\,, \\ I_{\mathrm{p}} &= \frac{|Q|c}{\sqrt{2\pi}\sigma_z} \\ &= 2\pi\frac{n_{\mathrm{b0}}}{n_{00}}\left(\frac{2}{\gamma_{\mathrm{b0}}}\right)^{1/2}\epsilon_0 E_0\epsilon_{\mathrm{n}}c\,, \end{aligned} \tag{5.38}$$

where n_{b0} is the initial peak bunch density and $E_0 = m_e\omega_{p0}c/e$ is the familiar cold nonrelativistic wavebreaking field. The peak electron bunch density relative to the background on-axis plasma density is held fixed around $n_{\mathrm{b0}}/n_{00} \approx 8$ in order to cause significant transverse beamloading, while not causing too much longitudinal beamloading which could lead to both energy spread and emittance growth via decoherence effects [166]. From these expressions we can see that the 6D brightness and peak current have a $\propto n_{00}^{1/2}$ plasma density scaling due to the dependence on E_0. It is therefore preferable to operate the P-MoPA at the highest plasma density possible while still providing the necessary $\sim 1\,\mathrm{GeV}$ energy gains required for a water-window XFEL. Below in Table 5.2 we outline the working point parameters for an emittance-preserving transverse beamloaded P-MoPA along with PIC simulation results shown in Figure 5.2. The apparent sudden increase in transverse bunch size at the entrance is due to the majority of the bunch not being in full transverse blowout fields, expanding to match the combination of its own partial blowout and the focusing fields of the quasilinear laser-driven wake. Though the projected energy spread grows to nearly 10% by the end of the accelerator stage, the slice energy spread remains small and can therefore be corrected for using techniques similar to the one outlined in [163]. The slight growth and then reduction of normalized emittance is due to the phenomenon of laser-driven betatron oscillations, which we

address later in this section and an example of which is shown in Figure 5.4. The longitudinal dependence on energy is approximately linear for the majority of the bunch, which is required for using the compensation technique outlined in [163].

Table 5.2: Proposed P-MoPA water-window XFEL parameters

Pulse Train		
Wavelength λ_L	1030 nm	
Energy W_{drive}	2.4 J	
Modulator parameter β	1.2	
Spot size w_0	30 µm	
Unmodulated duration τ_{FWHM}	1.0 ps	
Plasma		
On-axis plasma density n_{00}	$2.5 \times 10^{17}\,\mathrm{cm}^{-3}$	
Acceleration length L_{acc}	70 mm	
Wakefield amplitude (quasilinear) E_z/E_0	~ 0.4	
Electron Bunch	**Before**	**After**
Charge $\lvert Q\rvert$	4.4 pC	4.4 pC
Energy E_{k}	150 MeV	1 GeV
Energy spread (projected) $\sigma_{E,(p)}$	0.1%	9.5%
Energy spread (slice) $\sigma_{E,(s)}$	0.1%	$\sim 0.1\%$
Norm. emittance ϵ_{n}	1.0 mm mrad	1.0 mm mrad
RMS size $\sigma_\perp$	0.9 µm	0.7 µm
Twiss parameter β	0.26 mm	1.0 mm
Twiss parameter γ	$3.9\,\mathrm{mm}^{-1}$	$1.0\,\mathrm{mm}^{-1}$
RMS length σ_z	1.0 µm	1.0 µm
Peak current I_{p}	0.5 kA	0.5 kA
Brightness (slice) $B_{\mathrm{6D,n}}$		$> 1 \times 10^{15}$ A/m^2/0.1%
Undulator		
Period λ_{u}	20 mm	
Magnetic field B_{u}	0.54 T	

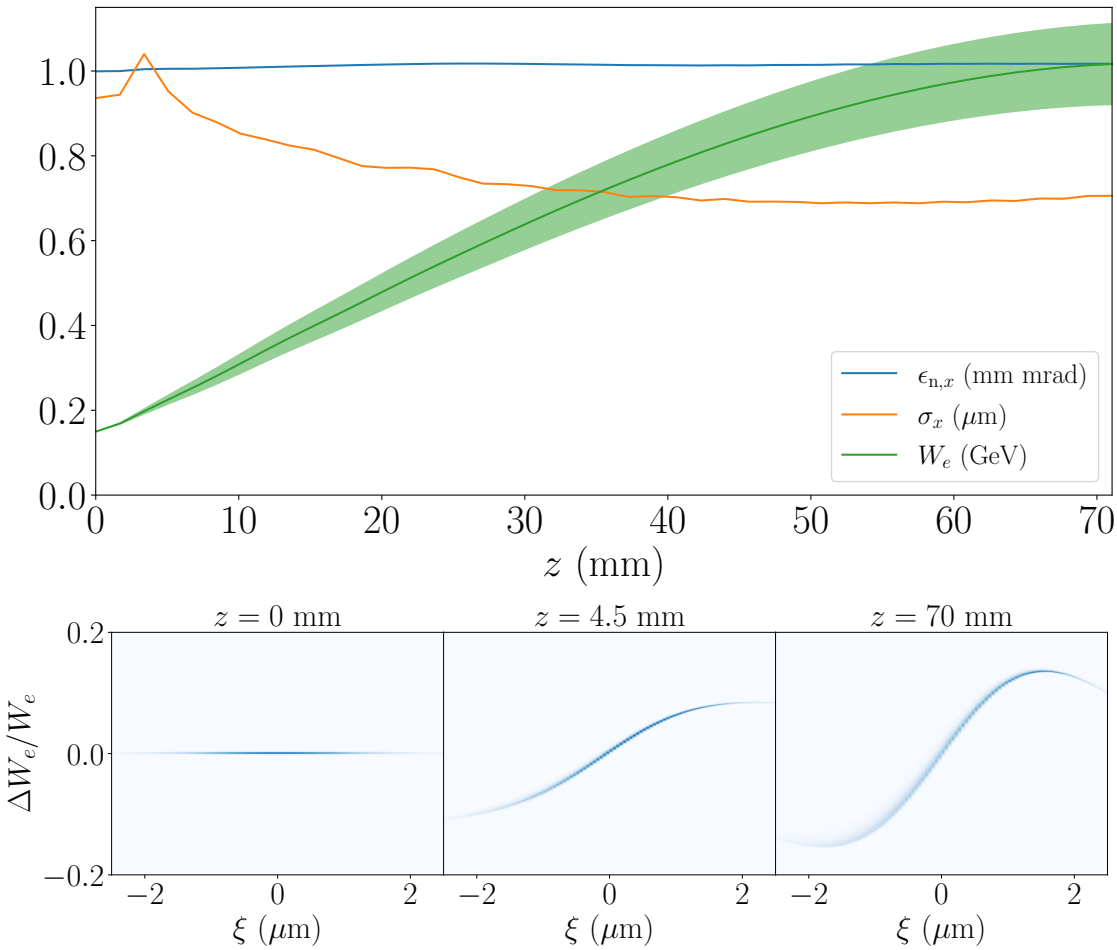


Figure 5.2: WarpX PIC simulation results of a P-MoPA accelerator stage using a matched parabolic plasma channel with input parameters outlined in Table 5.2. (Top) projected quantities of transverse normalized emittance $\epsilon_{n,x}$ (blue), transverse size σ_x (orange), bunch energy W_e (green) and its spread. (Bottom) relative energy distribution $\Delta W_e/W_e$ versus longitudinal coordinate ξ at various propagation distances. A fine square grid of resolution of $\Delta x = \Delta z = 34.2\,\mathrm{nm}$ was used to avoid numerical instabilities like the numerical Cherenkov instability (NCI) [167].

5.3.2 Plasma In- and Out-Matching

To preserve emittance in the P-MoPA accelerator stage for transfer into an FEL, we also need to consider the emittance growth along the plasma entrance and exit ramps, as contemporary focusing optics alone cannot yet provide the sufficiently small transverse bunch sizes $\sim 1\,\mu\mathrm{m}$ required to match into the plasma accelerator stage [168]. We will start with out-matching as its previously developed methods are the easiest to adapt to the P-MoPA. We will then address the different approach

required by the P-MoPA for the in-ramp.

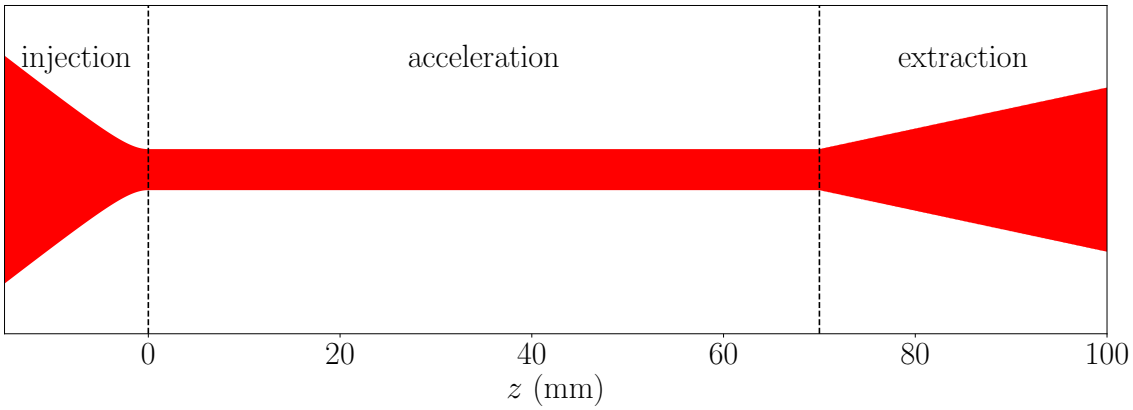


Figure 5.3: Schematic diagram of the in- and out-matching technique, adapted from [169]. The solid red indicates the spot size of the transverse laser profile. In the injection region, the laser pulse provides an increasing focusing wakefield to the electron bunch to focus the bunch to a sufficiently small transverse bunch size $\sigma_\perp$ to match to the accelerating section. After acceleration, a funnel-shaped channel allows the laser spot size to grow approximately linearly with propagation, which allows for the bunch transverse size to grow slowly and prevent emittance growth associated with the high projected energy spread the electron bunch [125].

Out-Matching

Due to the high (projected) energy spread and high divergences associated with electron bunches from plasma sources, emittance will rapidly grow in drift space [125]. To combat this, previous studies for the EuPRAXIA project [46] considered using an adiabatic plasma ramp whose focusing coefficient $K(z)$ takes the following form [170]

$$\begin{aligned} K(z) &= \frac{K_0}{(1+gz)^4}\,, \\ g &= -\frac{K_0'}{4K_0} \end{aligned} \tag{5.39}$$

where $g\beta_0 \ll 1$ is the adiabatic taper parameter with K_0 and K_0' being the initial focusing strength at the accelerator exit and its derivative. It has been proposed to achieve such a taper by allowing the laser spot size to evolve linearly with propagation distance by implementing a conical plasma channel with a linearly growing

matched spot size [169], such that the wake focusing force is given by

$$\begin{aligned} w(z) &\approx w_0(1+gz)\,, \quad K \propto |a|^2 w^{-2} \propto w^{-4} \\ \Rightarrow K(z) &= \frac{K_0}{(1+gz)^4}\,. \end{aligned} \tag{5.40}$$

Since this method relies only on spot size variation, it can also work with a pulse train. This method has also been previously simulated to work for electron bunches which drive a blowout [169], and therefore can be applied identically to a P-MoPA stage.

In-Matching

Unlike for single-pulse LWFA, we cannot use the same adiabatic density up-ramp technique that was proposed in [169] to perform emittance in-matching due to the pulse train resonance condition. Instead, we can focus the pulse train in uniform plasma before coupling into a guiding channel, and take advantage of the gradually increasing focusing wakefields as the train focuses to perform emittance matching.

The transverse focusing fields of a wakefield driven by a Gaussian pulse propagating in uniform underdense plasma will scale with $\propto |a|^2 w^{-2} \propto w^{-4}$. Assuming no dephasing between the pulse train and the externally injected bunch, ignoring the energy gain in the accelerator, the focusing parameter $K(z)$ can thus be written as

$$K(z) = \begin{cases} \frac{K_0}{(1+z^2/z_R^2)^2} & z < 0 \\ K_0 & z \geq 0 \end{cases} \tag{5.41}$$

where K_0 is the wakefield focusing strength at the beam focus in the uniform plasma section, which we have assumed is equal to the focusing strength in the plasma channel. We can the substitute this into Hill's equation in Eq. (5.25) with the matching condition $\beta(z \geq 0) = 1/\sqrt{K_0}$ and back-propagate to find the required uniform plasma section length required for a given initial bunch β.

5.3.3 Laser-Driven Betatron Oscillation

When driving quasilinear wakefields with P-MoPA pulse trains, the highest accelerating gradient bucket, where we would ideally inject the electron bunch, is expected to contain a small but nonzero amount of laser light between pulses. Since there is a mismatch between the superluminal phase velocity of the laser light and the velocity of the bunch, the resulting phase-slip will drive transverse oscillations along the bunch. If this time-varying driving force is resonant with the betatron frequency, the bunch will undergo exponentially growing betatron oscillations, which eventually breaks up the bunch. This process can be very useful, and in fact has been proposed as a source of attosecond X-ray and gamma-ray pulses directly from LWFA plasmas [171–174]. However, if we want to preserve emittance for driving a FEL, we must either avoid or quickly pass this resonance.

To model this effect, consider the motion of a single electron under the influence of a linearly polarized Gaussian laser pulse with finite spot size w_0 and of some small fixed amplitude $a_0 \ll 1$ propagating in a matched parabolic plasma channel

$$\begin{aligned} &\frac{1}{m_e c}\frac{\mathrm{d}\boldsymbol{p}}{\mathrm{d}t} = c\nabla\phi + \frac{\partial \boldsymbol{a}}{\partial t} - \boldsymbol{v}\times(\nabla\times\boldsymbol{a})\,, \\ &\boldsymbol{a} = a_0 e^{-r^2/w_0^2}\left(\cos[\omega_L(z/v_\phi - t)]\hat{x} + \frac{2v_\phi x}{\omega_L w_0^2}\sin[\omega_L(z/v_\phi - t)]\hat{z}\right)\,, \end{aligned} \tag{5.42}$$

where we have included the first order axial field correction to the paraxial wave solution, which results from requiring zero electric field divergence in vacuum. The superluminal phase velocity v_ϕ of a Gaussian laser pulse propagating in a parabolic plasma channel as derived in Eq. (2.42), which includes contributions from both the plasma density and finite spot size effects, is given by

$$\frac{v_\phi}{c} = 1 + \frac{\omega_{p0}^2}{2k_L^2 c^2} + \frac{2}{k_L^2 w_0^2}\,. \tag{5.43}$$

Assuming that the electron is highly relativistic in the z direction such that $p_z \gg m_e c^2, p_{x,y}$ and that the electron remains near the laser axis $x^2, y^2 \ll w_0^2$, we can then

recover the driven nonlinear damped oscillator equation

$$\begin{aligned}\ddot{x} + \Gamma\dot{x} + \omega_\beta^2 x &= \frac{c}{\gamma}\left[\frac{\partial \boldsymbol{a}}{\partial t} - \boldsymbol{v}\times(\nabla\times\boldsymbol{a})\right]\cdot\hat{x} \\ &= \frac{c}{\gamma}\left[\frac{\mathrm{d}a_x}{\mathrm{d}t} - \dot{x}\frac{\partial a_x}{\partial x} - c\frac{\partial a_z}{\partial x}\right] \\ &= \frac{a_0\omega_{p0}^2 c}{2\gamma\omega_L}\sin[\omega_L\xi/v_\phi - (1-c/v_\phi)\omega_L t]\,, \end{aligned} \tag{5.44}$$

where $\Gamma = \dot{\gamma}/\gamma$ is the damping rate due to the continuous relativistic mass increase from wakefield acceleration and $\xi = z - ct$ is the longitudinal position of the electron relative to the entire electron bunch. This nonlinear ODE predicts rapid growth of betatron oscillations when both the damping is weak $\Gamma \ll \omega_\beta$ and the laser source term is resonant with betatron oscillations $(1 - c/v_\phi)\omega_L = \omega_\beta$. For an accelerator operating in the quasilinear regime, where the accelerating field is comparable to the cold wavebreaking field $E_0 = m_e\omega_{p0}c/e$, the damping rate before dephasing will scale as $\Gamma \sim eE_0/\gamma m_e c = \omega_{p0}/\gamma = \sqrt{2/\gamma}\,\omega_\beta$ (assuming the betatron frequency of the blowout regime, which is valid for strong transverse beamloading). Therefore the transverse motion for a highly relativistic electron is underdamped, and is completely undamped towards the end of the accelerator when acceleration stops as the wakefield dephases from the electron.

If our intention is to preserve bunch emittance, then we want the laser source term to be well below resonance throughout the accelerator. Assuming the blowout regime for the betatron frequency, this sets the following requirement on the maximum electron bunch energy to remain stable

$$\begin{aligned}&\left(\frac{\omega_{p0}^2}{2\omega_L^2} + \frac{2c^2}{\omega_L^2 w_0^2}\right)\omega_L < \frac{\omega_{p0}}{\sqrt{2\gamma}} \\ &\Rightarrow \frac{E_\mathrm{k}}{m_e c^2} < \frac{2\omega_L^2/\omega_{p0}^2}{(1 + 4/k_{p0}^2 w_0^2)^2}\,. \end{aligned} \tag{5.45}$$

For example, for $n_{00} = 2.5\times10^{17}\,\mathrm{cm}^{-3}$, $w_0 = 30\,\mu\mathrm{m}$ and $\lambda_L = 1030\,\mathrm{nm}$, the electron bunch energy must not approach 2 GeV to avoid laser-driven amplification of betatron oscillations. Note that Eq. (5.45) was derived with the blowout betatron

frequency, which is the best case scenario. For example, if the betatron frequency at the head of the electron bunch is only half of the blowout betatron frequency, then the resonance condition is hit at 0.5 GeV, which is below our 1 GeV target energy.

Fortunately, another effect to consider that is unique to the P-MoPA is that electron bunches will co-propagate in increasingly blue-shifted light. As was previously discussed in Chapter 4 and was demonstrated previously in Fig 4.4, as the pulse train depletes and the bunch dephases, the accelerating bunch will co-propagate with blue-shifted light rather than red-shifted due to the nature of P-MoPA pulse trains. This allows for much easier avoidance of the laser-betatron resonance.

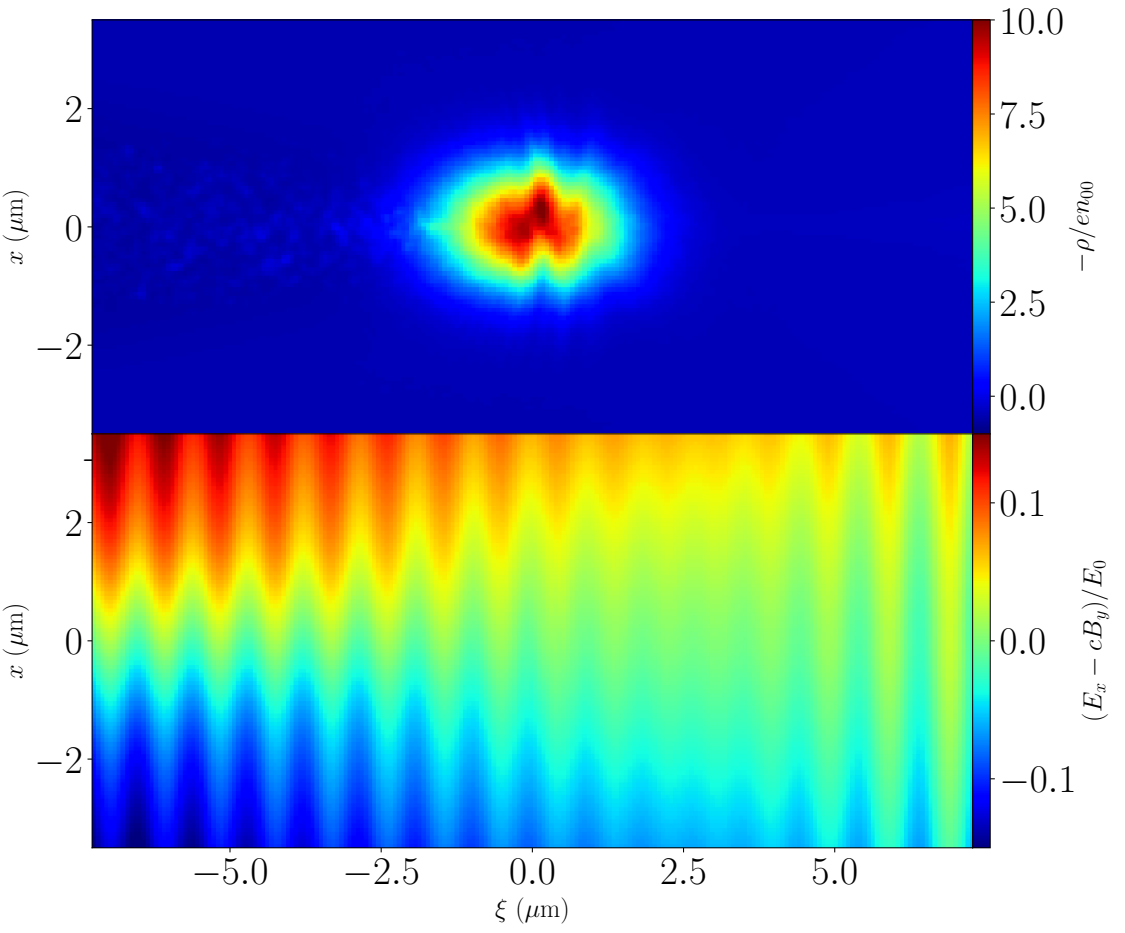


Figure 5.4: Final snapshot of the 1 GeV electron bunch and transverse fields from same PIC simulation of the accelerator stage presented in Figure 5.2. The laser light between the P-MoPA pulses drives transverse betatron oscillations whose phase varies along the electron bunch due to both the superluminal phase velocity of the laser driver and longitudinal energy spread effects. Despite this effect, both the slice and projected emittances remain small throughout the accelerator stage.

5.4 Summary

In this chapter, we studied the viability of the P-MoPA as a potential kHz driver for a 4 nm water-window XFEL, envisioning an external injection scheme based on recent developments in THz-driven beam compression [150–152] providing 150 MeV, $\epsilon_{\mathrm{n}} = 1.0\,\mathrm{mm\,mrad}$, $\sigma_E = 0.1\%$, $\sigma_z \sim 1\,\mu\mathrm{m}$ electron bunches.

By adapting the transverse beam loading technique from previous high-charge emittance matching studies in beam-driven quasilinear wakefield acceleration [42, 43] to the P-MoPA, we arrived at a set of working point parameters outlined in Table 5.2, backed up by PIC simulation results, in which the P-MoPA can accelerate bunches to sufficiently high 1 GeV energies whilst maintaining the high bunch qualities required for XFEL lasing at 4 nm.

We also considered emittance preserving techniques at the entrance and exit ramps of the accelerator stage. For the out-ramp we concluded that the same technique proposed in the EuPRAXIA project [46] would also work for the P-MoPA, whilst for the in-ramp a slight variation on the technique proposed by [46] can be used appropriate for pulse trains.

Finally, we characterized the effect of laser-driven betatron oscillations, which are expected in some capacity for P-MoPA pulse trains. Despite their presence, we find in PIC simulations that no catastrophic betatron resonance occurs and that a high bunch quality is maintained.

Chapter 6

Conclusion

6.1 Contributions

Achieving kHz repetition-rate LWFA has been a highly active research avenue in recent years due to its necessity for LWFA to be practical for a wide array of potential commercial applications [175–181]. However, all methods implemented to date have been limited to energy gains in the 10–50 MeV range due to the 50–100 mJ energies available from kHz repetition rate femtosecond-class pulses of current laser systems [98, 182]. This thesis presents progress towards the Plasma-Modulated Plasma Accelerator (P-MoPA), which aims to be the first multi-GeV kHz repetition rate LWFA by taking advantage of the multi-joule picosecond-duration pulses available at kHz from pre-existing laser technology [2–4].

The P-MoPA builds off of recent advancements in the HOFI pre-formed plasma waveguide technique, which has been experimentally demonstrated to be stable at kHz operation [64]. In Chapter 2, we developed the pulse propagation theory necessary to describe the physics of LWFA in the long (100–300 mm) HOFI channels required for multi-GeV energy gains. This theory was benchmarked with well-known laser-plasma dynamics and instabilities, and significantly contributed to the analysis of data from the first experimental demonstration of resonantly excited wakefields by a pulse train propagating in a plasma channel [39], the data collection portion of which had been completed prior to the author joining the Oxford group.

Using the theory developed in Chapter 2 in combination with running particle-in-cell (PIC) simulations using the open source code WarpX [40] on the ARCHER2 UK national supercomputing service [41], Chapter 3 discovered the properties and design constraints of the modulator stage of the P-MoPA [33]. The first major result is that the spectral modulation of the drive pulse remains independent of transverse coordinate despite transverse wake structure introduced by the waveguide's transverse profile, which is ideal for later compression into a pulse train using a dispersive optical system. The second main result is that the stability of the modulator is determined by a type of envelope self-modulation (SM) instability, seeded simultaneously by the presence of the seed wake and an initial laser-channel mismatch. To avoid the onset of this instability, we first found via simulations and later confirmed analytically that this sets a limit on the total pulse energy the modulator can accept for a given set of laser-plasma parameters and channel matching quality.

With the results in Chapter 3, in Chapter 4 we found an experimentally plausible parameter space where the modulator can accept multi-joule drive pulses whilst remaining stable, suitable for use in the P-MoPA accelerator stage. We again combined both our theory from Chapter 2 with PIC simulations, with which we demonstrated the viability of kHz repetition rate multi-GeV LWFA driven by pulse trains obeying the modulator design constraints found in Chapter 3 [38].

Finally, in Chapter 5 we evaluated the potential of the P-MoPA as a kHz driver for a water-window X-ray free electron laser (XFEL). On top of the multi-GeV energy gains required for this application, stringent constraints are set on the electron bunch 6D brightness. This chapter developed a scheme based on previous studies for high-charge bunch emittance preservation in beam-driven quasilinear wakefields [42, 43] and adapted it to the P-MoPA, involving extra considerations arising from pulse propagation effects. Informed by these constraints, we proposed experimental parameters in which the P-MoPA can be used for a kHz water-window XFEL.

6.2 Future Work

6.2.1 P-MoPA Proof of Concept

The first step would be to have an experimental proof-of-concept of the modulator stage of the P-MoPA scheme, which is currently in progress using the PFS-Pro Yb:YAG laser system at CALA [98, 183, 184] in a collaboration with the Oxford group and LMU Munich. In a sense, a related form of controlled spectral modulation by co-propagating with a wake has already been demonstrated in the extremely low intensity limit in the Frequency Domain Holography (FDH) wakefield probing technique [185], proving that the concept is sound. What is left to demonstrate is performing this spectral modulation in a plasma channel, doing so at kHz repetition rates, and spectrally modulating multi-joule pulses in a stable manner following the design constraints outlined in Chapter 3. Once this has been achieved, we would be ready to form pulse trains to perform the first kHz GeV-scale LWFA experiments.

6.2.2 CHOFI Channel Profile Tuning

Much of the work presented in this thesis highlighted the importance of the exact transverse channel profile influencing wake structure, which becomes especially important for pulse trains like in the P-MoPA scheme. It would therefore be extremely advantageous to have experimental control over the channel profiles. Based on recent research in modeling the formation of (C)HOFI channels [70], it seems very plausible that the exact profiles of specifically CHOFI channels can be tuned between parabolic and quasi-square (i.e. similar to step-index) by changing the tightness of the axicon focus. Making the axicon focus tighter would reduce the radius of the initial cylinder of $\sim 10\,\mathrm{eV}$ OFI electrons which drives the cylindrical hydrodynamic blast wave which forms the waveguide. This, hypothetically, would change the waveguide from "HOFI-dominated guiding" (i.e. parabolic waveguide formed by the expanding OFI electrons) consistent with the example in [70], to "CHOFI-dominated guiding" (i.e. quasi-square waveguide formed primarily by the neutral gas collar around the blastwave, ionized by a conditioning pulse). We would

therefore propose to investigate this possibility for tailor-made (C)HOFI channel profiles both numerically with the tools developed in [70] and experimentally.

Appendix A

A Numerical Method for Evaluating Wakefields in Plasma Channels

To solve Eq. (2.88) numerically, we first rewrite it as a linear system of three PDEs

$$D\frac{\partial^2 \vec{u}}{\partial \xi^2} = -M\vec{u} + \vec{d} \tag{A.1}$$

where we have used the following definitions

$$\vec{u}(r,\xi) = \begin{pmatrix} \delta\phi \\ \left(\Delta_\perp - k_p^2(r)\right)\delta\phi \\ \frac{\partial}{\partial r}\delta\phi \end{pmatrix} \qquad \vec{d}(r,\xi) = \begin{pmatrix} k_p^2(r)\left(\Delta_\perp - k_p^2(r)\right)|a(r,\xi)|^2/4 \\ 0 \\ 0 \end{pmatrix}$$

$$M(r) = \begin{bmatrix} 0 & k_p^2(r) & 0 \\ \frac{\partial}{\partial r} & 0 & -1 \\ \left(\Delta_\perp - k_p^2(r)\right) & -1 & 0 \end{bmatrix} \qquad D(r) = \begin{bmatrix} 0 & 1 & -\frac{\mathrm{d}\ln n_0}{\mathrm{d}r} \\ \frac{\partial}{\partial r} & 0 & -1 \\ \left(\Delta_\perp - k_p^2(r)\right) & -1 & 0 \end{bmatrix} \tag{A.2}$$

We then write discretized forms of these operators by replacing the r-derivative operators with matrix operators which approximate gradients with a finite differences scheme in $\Delta r = R/N_r$ (whilst taking care of boundary conditions and using a

sufficiently large R)

$$\begin{aligned}
\frac{\partial}{\partial r} f(r) \to \frac{\mathcal{R}}{2\Delta r} \left[f(\Delta r/2), f(3\Delta r/2), ..., f((N_r + 1/2)\Delta r) \right]^\top \\
\mathcal{R}_{i,i+1} = -\mathcal{R}_{i+1,i} = 1, \;\; \mathcal{R}_{i,j\neq i\pm 1} = 0\,, \\
\frac{\partial^2}{\partial r^2} f(r) \to \frac{\mathcal{S}}{(\Delta r)^2} \left[f(\Delta r/2), f(3\Delta r/2), ..., f((N_r + 1/2)\Delta r) \right]^\top \\
\mathcal{S}_{i,i} = -2, \;\; \mathcal{S}_{i,i+1} = \mathcal{S}_{i+1,i} = 1, \;\; \mathcal{S}_{i,j\neq(i,i\pm 1)} = 0\,. \qquad \text{(A.3)}
\end{aligned}$$

To enforce appropriate boundary conditions on-axis and at the radial boundary, we also require $\mathcal{R}_{0,0} = -\mathcal{R}_{N_r,N_r} = 1$ and $\mathcal{S}_{0,0} = \mathcal{S}_{N_r,N_r} = -1$. This allows us to compute the inverse of the discretized $3N_r \times 3N_r$ matrix D with which we can iterate $\vec{u}$ backward in ξ (forward in time)

$$\vec{u}_{n-1} = -\vec{u}_{n+1} + 2\vec{u}_n + (\Delta\xi)^2 D^{-1} \left(-M\vec{u}_n + \vec{d} \right) \qquad \text{(A.4)}$$

Appendix B

Down-Ramp Injection in Multipulse Quasilinear Wakefields

The goal of density down-ramp injection is to provide a controlled electron injection mechanism while operating the LWFA below the wavebreaking field to avoid self-injection. The idea behind the density downramp is that it increases the length of the plasma bubble by increasing the plasma wavelength $\lambda_p \propto n_e^{-1/2}$. This temporarily reduces the plasma wave phase velocity, which injects electrons and causes self-trapping.

For long density down-ramp transitions $L_{\rm ramp} > \lambda_p$, the wakefield phase velocity driven by a single pulse in 1D is given by [20]

$$v_\phi^{\rm wf} = v_g \left[1 + \frac{1}{k_p}\frac{\partial k_p}{\partial z}(z - v_g t)\right] \approx c\left(1 - \frac{\xi}{2n_e}\frac{dn_e}{d\xi}\right) \tag{B.1}$$

where $\xi = 0$ is approximately the position of the short single laser pulse. Injection will occur when this reduced wake phase velocity is equal to the axial velocity of electrons $v_e = v_\phi^{\rm wf}$, which in the 1D linear regime is given by $v_e/c = -\phi \sim E_{\rm max}/E_0$. Due to the gradual injection process, this method typically results in large energy spreads and emittances [20].

However, this changes when the wakefield is driven by pulse trains, where the resonance condition suppresses the wakefield amplitude until the down-ramp density

is near the resonant density. For example, for a pulse train comprising of $N = 5$ pulses, a large amplitude wakefield capable of trapping is only driven when the down-ramp density is within $\sim 20\%$ of the resonant density. This localizes the injection region which, in principle, will reduce the energy spread and emittance typically associated with long down-ramp injection schemes. As we are interested in injection in the highest accelerating gradient bucket immediately trailing the pulse train, the wakefield phase velocity in this region is approximately given by

$$v_\phi^{\mathrm{wf}} = c\left(1 + \frac{\lambda_p}{2n_e}\frac{dn_e}{d\xi}\right) . \tag{B.2}$$

For injection of the highest energy electrons in the wake, we require $v_\phi^{\mathrm{wf}} = v_e$, where v_e/c scales with the wakefield amplitude E_{max}/E_0. This sets the following minimum wakefield amplitude requirement for injection

$$\frac{E_{\mathrm{max}}}{E_0} > 1 + \frac{\lambda_p}{2n_e}\frac{dn_e}{d\xi} . \tag{B.3}$$

For example, a pulse train that excites a quasilinear wakefield of amplitude $E_{\mathrm{max}}/E_0 = 0.5$ requires a minimum downramp gradient of $|dn_e/d\xi| > n_e/\lambda_p$ for injection to occur in the primary accelerating bucket. Even at this large wakefield amplitude, we notice that the required gradient for injection into the first bucket already violates the long down-ramp assumption. Therefore if we want sufficient injection into the first accelerating bucket we should instead consider shock down-ramp injection.

Shock down-ramp injection occurs when $L_{\mathrm{ramp}} < \lambda_p$, such that the plasma wavelength undergoes a sudden increase, causing near-immediate injection of electrons of the previous smaller wake into the new larger wake. In this scenario, we instead have to worry about accelerating these electrons quickly enough so that they can become relativistic before they dephase into a defocusing portion of the wakefield and are ejected.

For wakefields in uniform plasma, the overlap between accelerating and focusing fields is a quarter of a plasma wavelength, so electrons can only fall behind within that length before becoming relativistic for them to remain trapped. This trapping

condition can be written as

$$\int_{t_i}^{\infty} dt[c - v(t)] < \lambda_{p0}/4 \tag{B.4}$$

where $v(t)$ is the longitudinal velocity of injected electrons and t_i is the time immediately before injection. For linear wakefields, the maximum initial fluid velocity of electrons at injection is approximately given by

$$\frac{v(t_i)}{c} \approx \frac{E_{\max}}{E_0}\,. \tag{B.5}$$

Note that we have included the work done by the injecting wakefield. To calculate a lower bound on this integral (i.e. the case where electrons require the full accelerating-focusing region to become relativistic), we can approximate the work done by both the wake at injection and the main wake normalized by the electron rest energy as

$$W(t) \approx \frac{eE_{\max}}{2m_e c^2}\left(\lambda_{p0} + c(t - t_i)\right) \tag{B.6}$$

where we have approximated the work done by the injection wakefield to be instantaneous and assumed that the injection wakefield does work over λ_{p0} as it slows to meet the fluid electrons. Imposing the trapping condition then yields

$$\begin{aligned} &\int_{t_i}^{\infty} dt\left(1 - \sqrt{1 - (1 + W(t))^{-2}}\right) < T_{p0}/4 \\ &\Rightarrow \frac{E_{\max}}{E_0} > 0.3 \end{aligned} \tag{B.7}$$

which states that the max wakefield must exceed a certain fraction of the wave-breaking field in order to trap injected electrons. Note that is an estimate of the absolute minimum wakefield amplitude required for this injection scheme to work, and in experiment a higher wake amplitude up to ~ 0.5 should be targeted.

References

[1] O. Jakobsson, S. M. Hooker, and R. Walczak. "Gev-Scale Accelerators Driven by Plasma-Modulated Pulses from Kilohertz Lasers". In: *Phys. Rev. Lett.* 127 (18 Oct. 2021), p. 184801. DOI: 10.1103/PhysRevLett.127.184801. URL: https://link.aps.org/doi/10.1103/PhysRevLett.127.184801.

[2] Clemens Herkommer et al. "Ultrafast thin-disk multipass amplifier with 720 mJ operating at kilohertz repetition rate for applications in atmospheric research". In: *Opt. Express* 28.20 (Sept. 2020), pp. 30164–30173. DOI: 10.1364/OE.404185. URL: https://opg.optica.org/oe/abstract.cfm?URI=oe-28-20-30164.

[3] Simon Nagel et al. "Thin-disk laser system operating above 10 kW at near fundamental mode beam quality". In: *Opt. Lett.* 46.5 (Mar. 2021), pp. 965–968. DOI: 10.1364/OL.416432. URL: https://opg.optica.org/ol/abstract.cfm?URI=ol-46-5-965.

[4] Produit, Thomas et al. "The laser lightning rod project". In: *Eur. Phys. J. Appl. Phys.* 93.1 (2021), p. 10504. DOI: 10.1051/epjap/2020200243. URL: https://doi.org/10.1051/epjap/2020200243.

[5] R. J. Van de Graaff, K. T. Compton, and L. C. Van Atta. "The Electrostatic Production of High Voltage for Nuclear Investigations". In: *Phys. Rev.* 43 (3 1933), pp. 149–157. DOI: 10.1103/PhysRev.43.149. URL: https://link.aps.org/doi/10.1103/PhysRev.43.149.

[6] Ernest O. Lawrence and M. Stanley Livingston. "The Production of High Speed Light Ions Without the Use of High Voltages". In: *Phys. Rev.* 40 (1

1932), pp. 19–35. DOI: 10.1103/PhysRev.40.19. URL: https://link.aps.org/doi/10.1103/PhysRev.40.19.

[7] R. Wideröe. "Über ein neues Prinzip zur Herstellung hoher Spannungen". In: *Archiv für Elektrotechnik* 21 (4 1928), 387—406. DOI: 10.1007/BF01656341. URL: https://doi.org/10.1007/BF01656341.

[8] J. D. Cockcroft and E. T. S. Walton. "Experiments with High Velocity Positive Ions. (I) Further Developments in the Method of Obtaining High Velocity Positive Ions". In: *Proceedings of the Royal Society of London. Series A, Containing Papers of a Mathematical and Physical Character* 136.830 (1932), pp. 619–630. ISSN: 09501207. URL: http://www.jstor.org/stable/95811 (visited on 03/04/2024).

[9] Vladimir D Shiltsev. "High-energy particle colliders: past 20 years, next 20 years, and beyond". In: *Physics-Uspekhi* 55.10 (2012), p. 965. DOI: 10.3367/UFNe.0182.201210d.1033. URL: https://dx.doi.org/10.3367/UFNe.0182.201210d.1033.

[10] A. P. Chernyaev and S. M. Varzar. "Particle accelerators in modern world". In: *Phys. Atom. Nuclei* 77 (10 2014), 1203—1215. DOI: 10.1134/S1063778814100032. URL: https://doi.org/10.1134/S1063778814100032.

[11] Andrew Burnett et al. "UK XFEL Science Case". In: *STFC-UKRI* (2020).

[12] D.A Jaroszynski et al. "Radiation sources based on laser–plasma interactions". In: *Philosophical Transactions of the Royal Society A: Mathematical, Physical and Engineering Sciences* 364.1840 (2006), pp. 689–710. DOI: 10.1098/rsta.2005.1732. eprint: https://royalsocietypublishing.org/doi/pdf/10.1098/rsta.2005.1732. URL: https://royalsocietypublishing.org/doi/abs/10.1098/rsta.2005.1732.

[13] M. E. Couprie. "Towards compact Free Electron–Laser based on laser plasma accelerators". In: *Nuclear Instruments and Methods in Physics Research Section A: Accelerators, Spectrometers, Detectors and Associated Equipment* 909 (2018). 3rd European Advanced Accelerator Concepts workshop (EAAC2017),

pp. 5–15. ISSN: 0168-9002. DOI: https://doi.org/10.1016/j.nima.2018.02.090. URL: https://www.sciencedirect.com/science/article/pii/S0168900218302729.

[14] K. Nakajima. "Laser-driven electron beam and radiation sources for basic, medical and industrial sciences". In: *Proceedings of the Japan Academy, Series B* 91.6 (2015), pp. 223–245. DOI: 10.2183/pjab.91.223. URL: https://doi.org/10.2183/pjab.91.223.

[15] L. Labate et al. "Toward an effective use of laser-driven very high energy electrons for radiotherapy: Feasibility assessment of multi-field and intensity modulation irradiation schemes". In: *Sci. Rep.* 10 (Oct. 2020), p. 17307. DOI: 10.1038/s41598-020-74256-w. URL: https://doi.org/10.1038/s41598-020-74256-w.

[16] A. Modena et al. "Electron acceleration from the breaking of relativistic plasma waves". In: *Nature* 377 (Oct. 1995), pp. 606–608. DOI: 10.1038/377606a0. URL: https://doi.org/10.1038/377606a0.

[17] D. Umstadter et al. "Nonlinear Optics in Relativistic Plasmas and Laser Wake Field Acceleration of Electrons". In: *Science* 273.5274 (1996), pp. 472–475. DOI: 10.1126/science.273.5274.472. eprint: https://www.science.org/doi/pdf/10.1126/science.273.5274.472. URL: https://www.science.org/doi/abs/10.1126/science.273.5274.472.

[18] John M. Dawson. "Nonlinear Electron Oscillations in a Cold Plasma". In: *Phys. Rev.* 113 (2 1959), pp. 383–387. DOI: 10.1103/PhysRev.113.383. URL: https://link.aps.org/doi/10.1103/PhysRev.113.383.

[19] E. Esarey et al. "Overview of plasma-based accelerator concepts". In: *IEEE Transactions on Plasma Science* 24.2 (1996), pp. 252–288. DOI: 10.1109/27.509991.

[20] J. Wenz and S. Karsch. "Physics of Laser-Wakefield Accelerators (LWFA)". In: CERN–Accelerator–School course on High Gradient Wakefield Accelerators, Sesimbra, (Portugal). 2019.

[21] T. Tajima and J. M. Dawson. "Laser Electron Accelerator". In: *Phys. Rev. Lett.* 43 (4 1979), pp. 267–270. DOI: 10.1103/PhysRevLett.43.267. URL: https://link.aps.org/doi/10.1103/PhysRevLett.43.267.

[22] Donna Strickland and Gerard Mourou. "Compression of amplified chirped optical pulses". In: *Optics Communications* 56.3 (1985), pp. 219–221. ISSN: 0030-4018. DOI: https://doi.org/10.1016/0030-4018(85)90120-8. URL: https://www.sciencedirect.com/science/article/pii/0030401885901208.

[23] S. Mangles, C. Murphy, Z. Najmudin, et al. "Monoenergetic beams of relativistic electrons from intense laser-plasma interactions". In: *Nature* 431 (2004), pp. 535–538. DOI: 10.1038/nature02939. URL: https://doi.org/10.1038/nature02939.

[24] W. Leemans, B. Nagler, A. Gonsalves, et al. "GeV electron beams from a centimetre-scale accelerator". In: *Nature Phys.* 2 (10 2006), 696—699. DOI: 10.1038/nphys418. URL: https://doi.org/10.1038/nphys418.

[25] S. Kneip et al. "Near-GeV Acceleration of Electrons by a Nonlinear Plasma Wave Driven by a Self-Guided Laser Pulse". In: *Phys. Rev. Lett.* 103 (3 2009), p. 035002. DOI: 10.1103/PhysRevLett.103.035002. URL: https://link.aps.org/doi/10.1103/PhysRevLett.103.035002.

[26] X. Wang, R. Zgadzaj, N. Fazel, et al. "Quasi-monoenergetic laser-plasma acceleration of electrons to 2 GeV". In: *Nat. Commun.* 4 (1 2013). DOI: 10.1038/ncomms2988. URL: https://doi.org/10.1038/ncomms2988.

[27] B. Miao et al. "Multi-GeV Electron Bunches from an All-Optical Laser Wakefield Accelerator". In: *Phys. Rev. X* 12 (3 2022), p. 031038. DOI: 10.1103/PhysRevX.12.031038. URL: https://link.aps.org/doi/10.1103/PhysRevX.12.031038.

[28] K. Oubrerie, A. Leblanc, O. Kononenko, et al. "Controlled acceleration of GeV electron beams in an all-optical plasma waveguide". In: *Light Sci. Appl.*

11 (180 2022). DOI: 10.1038/s41377-022-00862-0. URL: https://doi.org/10.1038/s41377-022-00862-0.

[29] Zhiyong Qin et al. "Multi-GeV cascaded laser wakefield acceleration in a hybrid capillary discharge waveguide". In: *New Journal of Physics* 24.7 (2022), p. 073048. DOI: 10.1088/1367-2630/ac81e2. URL: https://dx.doi.org/10.1088/1367-2630/ac81e2.

[30] Constantin Aniculaesei et al. "The acceleration of a high-charge electron bunch to 10 GeV in a 10-cm nanoparticle-assisted wakefield accelerator". In: *Matter and Radiation at Extremes* 9.1 (Nov. 2023), p. 014001. ISSN: 2468-2047. DOI: 10.1063/5.0161687. eprint: https://pubs.aip.org/aip/mre/article-pdf/doi/10.1063/5.0161687/18286148/014001_1_5.0161687.pdf. URL: https://doi.org/10.1063/5.0161687.

[31] Jay W. Dawson et al. "High average power lasers for future particle accelerators". In: *AIP Conference Proceedings* 1507.1 (2012), pp. 147–153. DOI: 10.1063/1.4773687. eprint: https://aip.scitation.org/doi/pdf/10.1063/1.4773687. URL: https://aip.scitation.org/doi/abs/10.1063/1.4773687.

[32] B. Hidding et al. "Plasma Wakefield Accelerator Research 2019–2040: A community-driven UK roadmap compiled by the Plasma Wakefield Accelerator Steering Committee (PWASC)". In: *PWASC* (2019). URL: https://www.pwasc.org.uk/uk-roadmap.

[33] J. J. van de Wetering, S. M. Hooker, and R. Walczak. "Stability of the modulator in a plasma-modulated plasma accelerator". In: *Phys. Rev. E* 108 (1 July 2023), p. 015204. DOI: 10.1103/PhysRevE.108.015204. URL: https://link.aps.org/doi/10.1103/PhysRevE.108.015204.

[34] R. J. Shalloo et al. "Hydrodynamic optical-field-ionized plasma channels". In: *Phys. Rev. E* 97 (5 2018), p. 053203. DOI: 10.1103/PhysRevE.97.053203. URL: https://link.aps.org/doi/10.1103/PhysRevE.97.053203.

[35] R. J. Shalloo et al. "Low-density hydrodynamic optical-field-ionized plasma channels generated with an axicon lens". In: *Phys. Rev. Accel. Beams* 22 (4 2019), p. 041302. DOI: 10.1103/PhysRevAccelBeams.22.041302. URL: https://link.aps.org/doi/10.1103/PhysRevAccelBeams.22.041302.

[36] A. Picksley et al. "Guiding of high-intensity laser pulses in 100-mm-long hydrodynamic optical-field-ionized plasma channels". In: *Phys. Rev. Accel. Beams* 23 (8 2020), p. 081303. DOI: 10.1103/PhysRevAccelBeams.23.081303. URL: https://link.aps.org/doi/10.1103/PhysRevAccelBeams.23.081303.

[37] A. Picksley et al. "Meter-scale conditioned hydrodynamic optical-field-ionized plasma channels". In: *Phys. Rev. E* 102 (5 Nov. 2020), p. 053201. DOI: 10.1103/PhysRevE.102.053201. URL: https://link.aps.org/doi/10.1103/PhysRevE.102.053201.

[38] J. J. van de Wetering, S. M. Hooker, and R. Walczak. "Multi-GeV wakefield acceleration in a plasma-modulated plasma accelerator". In: *Phys. Rev. E* 109 (2 2024), p. 025206. DOI: 10.1103/PhysRevE.109.025206. URL: https://link.aps.org/doi/10.1103/PhysRevE.109.025206.

[39] A. J. Ross et al. "Resonant excitation of plasma waves in a plasma channel". In: *Phys. Rev. Res.* 6 (2 2024), p. L022001. DOI: 10.1103/PhysRevResearch.6.L022001. URL: https://link.aps.org/doi/10.1103/PhysRevResearch.6.L022001.

[40] L. Fedeli et al. "Pushing the Frontier in the Design of Laser-Based Electron Accelerators with Groundbreaking Mesh-Refined Particle-In-Cell Simulations on Exascale-Class Supercomputers". In: *2022 SC22: International Conference for High Performance Computing, Networking, Storage and Analysis (SC) (SC)*. Los Alamitos, CA, USA: IEEE Computer Society, Nov. 2022, pp. 25–36. URL: https://doi.ieeecomputersociety.org/.

[41] https://www.archer2.ac.uk.

[42] Veronica K. Berglyd Olsen, Erik Adli, and Patric Muggli. "Emittance preservation of an electron beam in a loaded quasilinear plasma wakefield". In: *Phys. Rev. Accel. Beams* 21 (1 Jan. 2018), p. 011301. DOI: 10.1103/PhysRevAccelBeams.21.011301. URL: https://link.aps.org/doi/10.1103/PhysRevAccelBeams.21.011301.

[43] John P. Farmer et al. *Injection tolerances and self-matching in a quasilinear wakefield accelerator*. 2022. arXiv: 2203.11622 [physics.acc-ph].

[44] P A Walker et al. "Horizon 2020 EuPRAXIA design study". In: *Journal of Physics: Conference Series* 874.1 (2017), p. 012029. DOI: 10.1088/1742-6596/874/1/012029. URL: https://dx.doi.org/10.1088/1742-6596/874/1/012029.

[45] R.W. Assmann, M.K. Weikum, T. Akhter, et al. "EuPRAXIA Conceptual Design Report". In: *Phys. J. Spec. Top.* 229 (2020), 3675—4284. DOI: 10.1140/epjst/e2020-000127-8. URL: https://doi.org/10.1140/epjst/e2020-000127-8.

[46] Xiangkun Li, Antoine Chancé, and Phu Anh Phi Nghiem. "Preserving emittance by matching out and matching in plasma wakefield acceleration stage". In: *Phys. Rev. Accel. Beams* 22 (2 Feb. 2019), p. 021304. DOI: 10.1103/PhysRevAccelBeams.22.021304. URL: https://link.aps.org/doi/10.1103/PhysRevAccelBeams.22.021304.

[47] Wolfram Research, Inc. *Mathematica, Version 13.3*. Champaign, IL, 2023.

[48] I. S. Gradshteyn and I. M. Ryzhik. *Table of integrals, series, and products*. Seventh. Translated from the Russian, Translation edited and with a preface by Alan Jeffrey and Daniel Zwillinger, With one CD-ROM (Windows, Macintosh and UNIX). Elsevier/Academic Press, Amsterdam, 2007, pp. xlviii+1171.

[49] E. Esarey et al. "Optically guided laser wake-field acceleration*". In: *Physics of Fluids B: Plasma Physics* 5.7 (July 1993), pp. 2690–2697. ISSN: 0899-8221. DOI: 10.1063/1.860707. eprint: https://pubs.aip.org/aip/

pfb/article-pdf/5/7/2690/12264365/2690_1_online.pdf. URL: https://doi.org/10.1063/1.860707.

[50] H. Alfvén. "On the Existence of Electromagnetic-Hydrodynamic Waves". In: *Arkiv for Matematik, Astronomi och Fysik* 29B (Jan. 1943), pp. 1–7.

[51] C. G. Durfee, J. Lynch, and H. M. Milchberg. "Development of a plasma waveguide for high-intensity laser pulses". In: *Phys. Rev. E* 51 (3 1995), pp. 2368–2389. DOI: 10.1103/PhysRevE.51.2368. URL: https://link.aps.org/doi/10.1103/PhysRevE.51.2368.

[52] E. Esarey et al. "Thermal effects in plasma-based acceleratorsa)". In: *Physics of Plasmas* 14.5 (May 2007), p. 056707. ISSN: 1070-664X. DOI: 10.1063/1.2714022. eprint: https://pubs.aip.org/aip/pop/article-pdf/doi/10.1063/1.2714022/13891651/056707_1_online.pdf. URL: https://doi.org/10.1063/1.2714022.

[53] A.A. Vlasov. *Many-particle theory and its application to plasma*. New York, Gordon and Breach, 1961.

[54] Y.L. Klimontovich and D. Haar. *The Statistical Theory of Non-Equilibrium Processes in a Plasma: International Series of Monographs in Natural Philosophy, Vol. 9*. v. 9. Elsevier Science, 2013. ISBN: 9781483214627. URL: https://books.google.co.uk/books?id=SbU3BQAAQBAJ.

[55] B. A. Shadwick, G. M. Tarkenton, and E. H. Esarey. "Hamiltonian Description of Low-Temperature Relativistic Plasmas". In: *Phys. Rev. Lett.* 93 (17 2004), p. 175002. DOI: 10.1103/PhysRevLett.93.175002. URL: https://link.aps.org/doi/10.1103/PhysRevLett.93.175002.

[56] E. Esarey, C. B. Schroeder, and W. P. Leemans. "Physics of laser-driven plasma-based electron accelerators". In: *Rev. Mod. Phys.* 81 (3 Aug. 2009), pp. 1229–1285. DOI: 10.1103/RevModPhys.81.1229. URL: https://link.aps.org/doi/10.1103/RevModPhys.81.1229.

[57] C. B. Schroeder, E. Esarey, and B. A. Shadwick. "Warm wave breaking of nonlinear plasma waves with arbitrary phase velocities". In: *Phys. Rev. E* 72 (5 2005), p. 055401. DOI: 10.1103/PhysRevE.72.055401. URL: https://link.aps.org/doi/10.1103/PhysRevE.72.055401.

[58] S. V. Bulanov et al. "Transverse-Wake Wave Breaking". In: *Phys. Rev. Lett.* 78 (22 1997), pp. 4205–4208. DOI: 10.1103/PhysRevLett.78.4205. URL: https://link.aps.org/doi/10.1103/PhysRevLett.78.4205.

[59] A. Zigler et al. "Optical guiding of high-intensity laser pulses in a long plasma channel formed by a slow capillary discharge". In: *J. Opt. Soc. Am. B* 13.1 (1996), pp. 68–71. DOI: 10.1364/JOSAB.13.000068. URL: https://opg.optica.org/josab/abstract.cfm?URI=josab-13-1-68.

[60] S. M. Hooker, D. J. Spence, and R. A. Smith. "Guiding of high-intensity picosecond laser pulses in a discharge-ablated capillary waveguide". In: *J. Opt. Soc. Am. B* 17.1 (2000), pp. 90–98. DOI: 10.1364/JOSAB.17.000090. URL: https://opg.optica.org/josab/abstract.cfm?URI=josab-17-1-90.

[61] L. C. Johnson and T. K. Chu. "Measurements of electron density evolution and beam self-focusing in a laser-produced plasma". In: *Phys. Rev. Lett.* 32 (10 1974), pp. 517–520. DOI: 10.1103/PhysRevLett.32.517. URL: https://link.aps.org/doi/10.1103/PhysRevLett.32.517.

[62] C. G. Durfee and H. M. Milchberg. "Light pipe for high intensity laser pulses". In: *Phys. Rev. Lett.* 71 (15 1993), pp. 2409–2412. DOI: 10.1103/PhysRevLett.71.2409. URL: https://link.aps.org/doi/10.1103/PhysRevLett.71.2409.

[63] V. Kumarappan, K. Y. Kim, and H. M. Milchberg. "Guiding of Intense Laser Pulses in Plasma Waveguides Produced from Efficient, Femtosecond End-Pumped Heating of Clustered Gases". In: *Phys. Rev. Lett.* 94 (20 2005), p. 205004. DOI: 10.1103/PhysRevLett.94.205004. URL: https://link.aps.org/doi/10.1103/PhysRevLett.94.205004.

[64] A. Alejo et al. "Demonstration of kilohertz operation of hydrodynamic optical-field-ionized plasma channels". In: *Phys. Rev. Accel. Beams* 25 (1 Jan. 2022), p. 011301. DOI: 10.1103/PhysRevAccelBeams.25.011301. URL: https://link.aps.org/doi/10.1103/PhysRevAccelBeams.25.011301.

[65] S. Steinke et al. "Multistage coupling of independent laser-plasma accelerators". In: *Nature* 530 (Feb. 2016), pp. 190–193. DOI: 10.1038/nature16525. URL: https://doi.org/10.1038/nature16525.

[66] C.N. Kurtz and W. Streifer. "Guided Waves in Inhomogeneous Focusing Media Part I: Formulation, Solution for Quadratic Inhomogeneity". In: *IEEE Transactions on Microwave Theory and Techniques* 17.1 (1969), pp. 11–15. DOI: 10.1109/TMTT.1969.1126872.

[67] W.J. Firth. "Propagation of laser beams through inhomogeneous media". In: *Optics Communications* 22.2 (1977), pp. 226–230. ISSN: 0030-4018. DOI: https://doi.org/10.1016/0030-4018(77)90024-4. URL: https://www.sciencedirect.com/science/article/pii/0030401877900244.

[68] E. Esarey and W. P. Leemans. "Nonparaxial propagation of ultrashort laser pulses in plasma channels". In: *Phys. Rev. E* 59 (1 Jan. 1999), pp. 1082–1095. DOI: 10.1103/PhysRevE.59.1082. URL: https://link.aps.org/doi/10.1103/PhysRevE.59.1082.

[69] Milton Abramowitz and Irene A. Stegun. *Handbook of mathematical functions : with formulas, graphs, and mathematical tables*. eng. 10th printing, with corrections. National Bureau of Standards applied mathematics series ; 55. Washington, D.C: United States Department of Commerce, 1972. ISBN: 9781591242178.

[70] S. M. Mewes et al. "Demonstration of tunability of HOFI waveguides via start-to-end simulations". In: *Phys. Rev. Res.* 5 (3 2023), p. 033112. DOI: 10.1103/PhysRevResearch.5.033112. URL: https://link.aps.org/doi/10.1103/PhysRevResearch.5.033112.

[71] Ernst Brinkmeyer. "Spot size of graded-index single-mode fibers: profile-independent representation and new determination method". In: *Appl. Opt.* 18.6 (Mar. 1979), pp. 932–937. DOI: 10.1364/AO.18.000932. URL: https://opg.optica.org/ao/abstract.cfm?URI=ao-18-6-932.

[72] Eric Esarey, Jonathan Krall, and Phillip Sprangle. "Envelope analysis of intense laser pulse self-modulation in plasmas". In: *Phys. Rev. Lett.* 72 (18 1994), pp. 2887–2890. DOI: 10.1103/PhysRevLett.72.2887. URL: https://link.aps.org/doi/10.1103/PhysRevLett.72.2887.

[73] N.E. Andreev et al. "Theory of the resonance modulational instability of short laser pulses in homogeneous plasma and plasma channels". In: *Plasma Physics Reports* 22 (May 1996), pp. 379–389.

[74] David Forslund, Joseph Kindel, and Erick Lindman. "Theory of stimulated scattering processes in laser-irradiated plasmas". In: *Physics of Fluids* 18 (Aug. 1975), pp. 1002–1016. DOI: 10.1063/1.861248.

[75] M. V. Ammosov, N. B. Delone, and V. P. Krainov. "Tunnel ionization of complex atoms and of atomic ions in an alternating electromagnetic field". In: *SovietPhys. JETP* 64 (1986), p. 1191.

[76] A. M. Perelomov, V. S. Popov, and M. V. Terent'ev. "Ionization of Atoms in an Alternating Electric Field". In: *Soviet Journal of Experimental and Theoretical Physics* 23 (Nov. 1966), p. 924.

[77] L V Keldysh. "IONIZATION IN THE FIELD OF A STRONG ELECTROMAGNETIC WAVE". In: *Zh. Eksperim. i Teor. Fiz.* 47 (Nov. 1964). URL: https://www.osti.gov/biblio/4662394.

[78] A.M. Perelomov and V.S. Popov. "Ionization of Atoms in an Alternating Electrical Field. III." In: *Soviet Journal of Experimental and Theoretical Physics* 25 (Aug. 1967), p. 336.

[79] F A Ilkov, J E Decker, and S L Chin. "Ionization of atoms in the tunnelling regime with experimental evidence using Hg atoms". In: *Journal of Physics B: Atomic, Molecular and Optical Physics* 25.19 (1992), p. 4005. DOI: 10.

1088/0953-4075/25/19/011. URL: https://dx.doi.org/10.1088/0953-4075/25/19/011.

[80] I. Yu. Kostyukov and A. A. Golovanov. "Field ionization in short and extremely intense laser pulses". In: *Phys. Rev. A* 98 (4 2018), p. 043407. DOI: 10.1103/PhysRevA.98.043407. URL: https://link.aps.org/doi/10.1103/PhysRevA.98.043407.

[81] Armin Scrinzi, Michael Geissler, and Thomas Brabec. "Ionization Above the Coulomb Barrier". In: *Phys. Rev. Lett.* 83 (4 1999), pp. 706–709. DOI: 10.1103/PhysRevLett.83.706. URL: https://link.aps.org/doi/10.1103/PhysRevLett.83.706.

[82] Qingbin Zhang, Pengfei Lan, and Peixiang Lu. "Empirical formula for over-barrier strong-field ionization". In: *Phys. Rev. A* 90 (4 2014), p. 043410. DOI: 10.1103/PhysRevA.90.043410. URL: https://link.aps.org/doi/10.1103/PhysRevA.90.043410.

[83] Wm. M. Wood, C. W. Siders, and M. C. Downer. "Measurement of femtosecond ionization dynamics of atmospheric density gases by spectral blueshifting". In: *Phys. Rev. Lett.* 67 (25 1991), pp. 3523–3526. DOI: 10.1103/PhysRevLett.67.3523. URL: https://link.aps.org/doi/10.1103/PhysRevLett.67.3523.

[84] S.C. Rae. "Spectral blueshifting and spatial defocusing of intense laser pulses in dense gases". In: *Optics Communications* 104.4 (1994), pp. 330–335. ISSN: 0030-4018. DOI: https://doi.org/10.1016/0030-4018(94)90565-7. URL: https://www.sciencedirect.com/science/article/pii/0030401894905657.

[85] S.C. Rae. "Ionization-induced defocusing of intense laser pulses in high-pressure gases". In: *Optics Communications* 97.1 (1993), pp. 25–28. ISSN: 0030-4018. DOI: https://doi.org/10.1016/0030-4018(93)90611-8. URL: https://www.sciencedirect.com/science/article/pii/0030401893906118.

[86] E. Wigner. "On the Quantum Correction For Thermodynamic Equilibrium". In: *Phys. Rev.* 40 (5 1932), pp. 749–759. DOI: 10.1103/PhysRev.40.749. URL: https://link.aps.org/doi/10.1103/PhysRev.40.749.

[87] J. VILLE. "Theorie et application dela notion de signal analysis". In: *Cables et Transmissions* 2.1 (1948), pp. 61–74.

[88] Miguel A. Alonso. "Wigner functions in optics: describing beams as ray bundles and pulses as particle ensembles". In: *Adv. Opt. Photon.* 3.4 (2011), pp. 272–365. DOI: 10.1364/AOP.3.000272. URL: https://opg.optica.org/aop/abstract.cfm?URI=aop-3-4-272.

[89] N. E. Andreev et al. "Structure of the wake field in plasma channels". In: *Physics of Plasmas* 4.4 (1997), pp. 1145–1153. DOI: 10.1063/1.872186. eprint: https://doi.org/10.1063/1.872186. URL: https://doi.org/10.1063/1.872186.

[90] C. Benedetti et al. "Quasi-matched propagation of ultra-short, intense laser pulses in plasma channels". In: *Physics of Plasmas* 19.5 (May 2012), p. 053101. ISSN: 1070-664X. DOI: 10.1063/1.4707393. eprint: https://pubs.aip.org/aip/pop/article-pdf/doi/10.1063/1.4707393/13985299/053101_1_online.pdf. URL: https://doi.org/10.1063/1.4707393.

[91] R.J. Shalloo et al. "Generation of laser pulse trains for tests of multi-pulse laser wakefield acceleration". In: *Nuclear Instruments and Methods in Physics Research Section A: Accelerators, Spectrometers, Detectors and Associated Equipment* 829 (2016). 2nd European Advanced Accelerator Concepts Workshop - EAAC 2015, pp. 383–385. ISSN: 0168-9002. DOI: https://doi.org/10.1016/j.nima.2016.02.044. URL: https://www.sciencedirect.com/science/article/pii/S0168900216002114.

[92] J. Cowley et al. "Excitation and Control of Plasma Wakefields by Multiple Laser Pulses". In: *Phys. Rev. Lett.* 119 (4 2017), p. 044802. DOI: 10.1103/PhysRevLett.119.044802. URL: https://link.aps.org/doi/10.1103/PhysRevLett.119.044802.

[93] L Feder et al. "Self-waveguiding of relativistic laser pulses in neutral gas channels". In: *Physical Review Research* 2.4 (Nov. 2020), p. 043173. DOI: 10.1103/physrevresearch.2.043173.

[94] O. Jakobsson. "Seeded Self-Modulation for kHz Laser Wakefield Acceleration". unpublished notes. 2020.

[95] P. Gibbon. "The self-trapping of light waves by beatwave excitation". In: *Physics of Fluids B: Plasma Physics* 2 (1990), p. 2196.

[96] A. J. Gonsalves et al. "Plasma channel diagnostic based on laser centroid oscillations". In: *Physics of Plasmas* 17.5 (2010), p. 056706. DOI: 10.1063/1.3357175. eprint: https://doi.org/10.1063/1.3357175. URL: https://doi.org/10.1063/1.3357175.

[97] Donald R. Herriott and Harry J. Schulte. "Folded Optical Delay Lines". In: *Appl. Opt.* 4.8 (1965), pp. 883–889. DOI: 10.1364/AO.4.000883. URL: https://opg.optica.org/ao/abstract.cfm?URI=ao-4-8-883.

[98] Martin Kaumanns et al. "Spectral broadening of 112 mJ, 1.3 ps pulses at 5 kHz in a LG10 multipass cell with compressibility to 37 fs". In: *Opt. Lett.* 46.5 (2021), pp. 929–932. DOI: 10.1364/OL.416734. URL: https://opg.optica.org/ol/abstract.cfm?URI=ol-46-5-929.

[99] William Kruer. *The physics of laser plasma interactions*. crc Press, 2019.

[100] J. F. Drake et al. "Parametric instabilities of electromagnetic waves in plasmas". In: *The Physics of Fluids* 17.4 (Apr. 1974), pp. 778–785. ISSN: 0031-9171. DOI: 10.1063/1.1694789. eprint: https://pubs.aip.org/aip/pfl/article-pdf/17/4/778/12379298/778_1_online.pdf. URL: https://doi.org/10.1063/1.1694789.

[101] C. B. Darrow et al. "Strongly coupled stimulated Raman backscatter from subpicosecond laser-plasma interactions". In: *Phys. Rev. Lett.* 69 (3 1992), pp. 442–445. DOI: 10.1103/PhysRevLett.69.442. URL: https://link.aps.org/doi/10.1103/PhysRevLett.69.442.

[102] G. Shvets, J. S. Wurtele, and B. A. Shadwick. "Analysis and simulation of Raman backscatter in underdense plasmas". In: *Physics of Plasmas* 4.5 (May 1997), pp. 1872–1880. ISSN: 1070-664X. DOI: 10.1063/1.872330. eprint: https://pubs.aip.org/aip/pop/article-pdf/4/5/1872/19309314/1872_1_online.pdf. URL: https://doi.org/10.1063/1.872330.

[103] G. Shvets et al. "Superradiant Amplification of an Ultrashort Laser Pulse in a Plasma by a Counterpropagating Pump". In: *Phys. Rev. Lett.* 81 (22 1998), pp. 4879–4882. DOI: 10.1103/PhysRevLett.81.4879. URL: https://link.aps.org/doi/10.1103/PhysRevLett.81.4879.

[104] M. J. Everett et al. "Coupling between High-Frequency Plasma Waves in Laser-Plasma Interactions". In: *Phys. Rev. Lett.* 74 (12 1995), pp. 2236–2239. DOI: 10.1103/PhysRevLett.74.2236. URL: https://link.aps.org/doi/10.1103/PhysRevLett.74.2236.

[105] S M Hooker et al. "Multi-pulse laser wakefield acceleration: a new route to efficient, high-repetition-rate plasma accelerators and high flux radiation sources". In: *Journal of Physics B: Atomic, Molecular and Optical Physics* 47.23 (Nov. 2014), p. 234003. DOI: 10.1088/0953-4075/47/23/234003. URL: https://dx.doi.org/10.1088/0953-4075/47/23/234003.

[106] James D. Sadler et al. "Overcoming the dephasing limit in multiple-pulse laser wakefield acceleration". In: *Phys. Rev. Accel. Beams* 23 (2 Feb. 2020), p. 021303. DOI: 10.1103/PhysRevAccelBeams.23.021303. URL: https://link.aps.org/doi/10.1103/PhysRevAccelBeams.23.021303.

[107] C. B. Schroeder et al. "Physics considerations for laser-plasma linear colliders". In: *Phys. Rev. ST Accel. Beams* 13 (10 2010), p. 101301. DOI: 10.1103/PhysRevSTAB.13.101301. URL: https://link.aps.org/doi/10.1103/PhysRevSTAB.13.101301.

[108] W. K. H. Panofsky and W. A. Wenzel. "Some Considerations Concerning the Transverse Deflection of Charged Particles in Radio-Frequency Fields". In: *Review of Scientific Instruments* 27.11 (Dec. 2004), pp. 967–967. ISSN:

0034-6748. DOI: 10.1063/1.1715427. eprint: https://pubs.aip.org/aip/rsi/article-pdf/27/11/967/8340739/967_1_online.pdf. URL: https://doi.org/10.1063/1.1715427.

[109] L. M. Gorbunov and V. I. Kirsanov. "Excitation of plasma waves by an electromagnetic wave packet". In: *Sov. Phys. JETP* 66 (2 July 1987), p. 290. URL: http://jetp.ras.ru/cgi-bin/e/index/e/66/2/p290?a=list.

[110] N.E. Andreev et al. "On laser wakefield acceleration in plasma channels". In: *Nuclear Instruments and Methods in Physics Research Section A: Accelerators, Spectrometers, Detectors and Associated Equipment* 410.3 (1998), pp. 469–476. ISSN: 0168-9002. DOI: https://doi.org/10.1016/S0168-9002(98)00181-8. URL: https://www.sciencedirect.com/science/article/pii/S0168900298001818.

[111] F. Amiranoff et al. "Observation of modulational instability in Nd-laser beat-wave experiments". In: *Phys. Rev. Lett.* 68 (25 1992), pp. 3710–3713. DOI: 10.1103/PhysRevLett.68.3710. URL: https://link.aps.org/doi/10.1103/PhysRevLett.68.3710.

[112] A. von Boetticher, R. Walczak, and S. M. Hooker. "Modulational instability in large-amplitude linear laser wakefields". In: *Phys. Rev. E* 107 (2 Feb. 2023), p. L023201. DOI: 10.1103/PhysRevE.107.L023201. URL: https://link.aps.org/doi/10.1103/PhysRevE.107.L023201.

[113] B Miao et al. "Optical Guiding in Meter-Scale Plasma Waveguides". In: *Physical Review Letters* 125.7 (Aug. 2020), pp. 074801 –13. DOI: 10.1103/physrevlett.125.074801.

[114] G. N. Watson. *A treatise on the theory of Bessel functions*. Second. Cambridge University Press, 1966.

[115] M. N. Rosenbluth and C. S. Liu. "Excitation of Plasma Waves by Two Laser Beams". In: *Phys. Rev. Lett.* 29 (11 Sept. 1972), pp. 701–705. DOI: 10.1103/PhysRevLett.29.701. URL: https://link.aps.org/doi/10.1103/PhysRevLett.29.701.

[116] E. Esarey et al. "Optically guided laser wake-field acceleration*". In: *Physics of Fluids B: Plasma Physics* 5.7 (1993), pp. 2690–2697. DOI: 10.1063/1.860707. eprint: https://doi.org/10.1063/1.860707. URL: https://doi.org/10.1063/1.860707.

[117] N E Andreev et al. "The theory of laser self-resonant wake field excitation". In: *Physica Scripta* 49.1 (Jan. 1994), p. 101. DOI: 10.1088/0031-8949/49/1/014. URL: https://dx.doi.org/10.1088/0031-8949/49/1/014.

[118] Patrick Mora and Thomas M. Antonsen Jr. "Kinetic modeling of intense, short laser pulses propagating in tenuous plasmas". In: *Physics of Plasmas* 4.1 (1997), pp. 217–229. DOI: 10.1063/1.872134. eprint: https://doi.org/10.1063/1.872134. URL: https://doi.org/10.1063/1.872134.

[119] W. Zhu, J. P. Palastro, and T. M. Antonsen. "Studies of spectral modification and limitations of the modified paraxial equation in laser wakefield simulations". In: *Physics of Plasmas* 19.3 (2012), p. 033105. DOI: 10.1063/1.3691837. eprint: https://doi.org/10.1063/1.3691837. URL: https://doi.org/10.1063/1.3691837.

[120] B. Z. Djordjević et al. "Filtering higher-order laser modes using leaky plasma channels". In: *Physics of Plasmas* 25.1 (Jan. 2018), p. 013103. DOI: 10.1063/1.5006198. URL: https://doi.org/10.1063/1.5006198.

[121] W.B. Mori. "The physics of the nonlinear optics of plasmas at relativistic intensities for short-pulse lasers". In: *IEEE Journal of Quantum Electronics* 33.11 (1997), pp. 1942–1953. DOI: 10.1109/3.641309.

[122] M. J. V. Streeter et al. "Observation of Laser Power Amplification in a Self-Injecting Laser Wakefield Accelerator". In: *Phys. Rev. Lett.* 120 (25 2018), p. 254801. DOI: 10.1103/PhysRevLett.120.254801. URL: https://link.aps.org/doi/10.1103/PhysRevLett.120.254801.

[123] A. Sørensen. "Liouville's theorem and emittance". In: *CAS - CERN Accelerator School: 3rd General Accelerator Physics Course* (1989), pp. 18–36. DOI: 10.5170/CERN-1989-005.18. URL: https://cds.cern.ch/record/367259.

[124] C.A. Lindstrøm and M. Thévenet. "Emittance preservation in advanced accelerators". In: *Journal of Instrumentation* 17.05 (May 2022), P05016. DOI: 10.1088/1748-0221/17/05/P05016. URL: https://dx.doi.org/10.1088/1748-0221/17/05/P05016.

[125] Klaus Floettmann. "Some basic features of the beam emittance". In: *Phys. Rev. ST Accel. Beams* 6 (3 2003), p. 034202. DOI: 10.1103/PhysRevSTAB.6.034202. URL: https://link.aps.org/doi/10.1103/PhysRevSTAB.6.034202.

[126] R. Bonifacio, B. W. J. McNeil, and P. Pierini. "Superradiance in the high-gain free-electron laser". In: *Phys. Rev. A* 40 (8 1989), pp. 4467–4475. DOI: 10.1103/PhysRevA.40.4467. URL: https://link.aps.org/doi/10.1103/PhysRevA.40.4467.

[127] S. Di Mitri. "On the Importance of Electron Beam Brightness in High Gain Free Electron Lasers". In: *Photonics* 2 (June 2015), pp. 317–341. DOI: 10.3390/photonics2020317.

[128] S. Di Mitri and M. Cornacchia. "Electron beam brightness in linac drivers for free-electron-lasers". In: *Physics Reports* 539.1 (2014). Electron beam brightness in linac drivers for free-electron-lasers, pp. 1–48. ISSN: 0370-1573. DOI: https://doi.org/10.1016/j.physrep.2014.01.005. URL: https://www.sciencedirect.com/science/article/pii/S0370157314000088.

[129] D. Möhl. "Sources of emittance growth". In: *CAS - CERN Accelerator School: small accelerators* (2006), pp. 45–69. DOI: 10.5170/CERN-2006-012.45. URL: https://cds.cern.ch/record/1005037.

[130] E.D Courant and H.S Snyder. "Theory of the alternating-gradient synchrotron". In: *Annals of Physics* 3.1 (1958), pp. 1–48. ISSN: 0003-4916. DOI: https://doi.org/10.1016/0003-4916(58)90012-5. URL: https://www.sciencedirect.com/science/article/pii/0003491658900125.

[131] S. Y. Lee. *Accelerator Physics, 4th Edition*. World Scientific Publishing Co. Pte. Ltd., 2019. ISBN: 978-981-3274-69-3.

[132] C. Gahn et al. "Multi-MeV Electron Beam Generation by Direct Laser Acceleration in High-Density Plasma Channels". In: *Phys. Rev. Lett.* 83 (23 1999), pp. 4772–4775. DOI: 10.1103/PhysRevLett.83.4772. URL: https://link.aps.org/doi/10.1103/PhysRevLett.83.4772.

[133] K. J. Gaffney and H. N. Chapman. "Imaging Atomic Structure and Dynamics with Ultrafast X-ray Scattering". In: *Science* 316.5830 (2007), pp. 1444–1448. DOI: 10.1126/science.1135923. eprint: https://www.science.org/doi/pdf/10.1126/science.1135923. URL: https://www.science.org/doi/abs/10.1126/science.1135923.

[134] Christoph Bostedt et al. "Linac Coherent Light Source: The first five years". In: *Rev. Mod. Phys.* 88 (1 Mar. 2016), p. 015007. DOI: 10.1103/RevModPhys.88.015007. URL: https://link.aps.org/doi/10.1103/RevModPhys.88.015007.

[135] C. Pellegrini, A. Marinelli, and S. Reiche. "The physics of x-ray free-electron lasers". In: *Rev. Mod. Phys.* 88 (1 Mar. 2016), p. 015006. DOI: 10.1103/RevModPhys.88.015006. URL: https://link.aps.org/doi/10.1103/RevModPhys.88.015006.

[136] W. Ackermann, G. Asova, V. Ayvazyan, et al. "Operation of a free-electron laser from the extreme ultraviolet to the water window". In: *Nat. Photonics* (1 2007), p. 336. DOI: 10.1038/nphoton.2007.76. URL: https://doi.org/10.1038/nphoton.2007.76.

[137] Z. Huang and I. Lindau. "SACLA hard-X-ray compact FEL". In: *Nat. Photonics* (6 2012), pp. 505–506. DOI: 10.1038/nphoton.2012.184. URL: https://doi.org/10.1038/nphoton.2012.184.

[138] E. Allaria et al. "The FERMI free-electron lasers". In: *Journal of Synchrotron Radiation* 22.3 (May 2015), pp. 485–491. DOI: 10.1107/S1600577515005366. URL: https://doi.org/10.1107/S1600577515005366.

[139] In Soo Ko et al. "Construction and Commissioning of PAL-XFEL Facility". In: *Applied Sciences* 7.5 (2017). ISSN: 2076-3417. DOI: 10.3390/app7050479. URL: https://www.mdpi.com/2076-3417/7/5/479.

[140] M. Harmand, R. Coffee, M. Bionta, et al. "Achieving few-femtosecond time-sorting at hard X-ray free-electron lasers". In: *Nat. Photonics* (7 2013), pp. 215–218. DOI: doi.org/10.1038/nphoton.2013.11. URL: https://doi.org/10.1038/nphoton.2013.11.

[141] H. S. Kang, C. K. Min, H. Heo, et al. "Hard X-ray free-electron laser with femtosecond-scale timing jitter". In: *Nat. Photonics* (11 2017), pp. 708–713. DOI: doi.org/10.1038/s41566-017-0029-8. URL: https://doi.org/10.1038/s41566-017-0029-8.

[142] S. Schulz, I. Grguraš, C. Behrens, et al. "Femtosecond all-optical synchronization of an X-ray free-electron laser". In: *Nat. Commun.* (6 2014), p. 5938. DOI: doi.org/10.1038/ncomms6938. URL: https://doi.org/10.1038/ncomms6938.

[143] John M. J. Madey. "Stimulated Emission of Bremsstrahlung in a Periodic Magnetic Field". In: *Journal of Applied Physics* 42.5 (Dec. 2003), pp. 1906–1913. ISSN: 0021-8979. DOI: 10.1063/1.1660466. eprint: https://pubs.aip.org/aip/jap/article-pdf/42/5/1906/10561673/1906_1_online.pdf. URL: https://doi.org/10.1063/1.1660466.

[144] D. A. G. Deacon et al. "First Operation of a Free-Electron Laser". In: *Phys. Rev. Lett.* 38 (16 Apr. 1977), pp. 892–894. DOI: 10.1103/PhysRevLett.38.892. URL: https://link.aps.org/doi/10.1103/PhysRevLett.38.892.

[145] W. Ackermann, G. Asova, V. Ayvazyan, et al. "Operation of a free-electron laser from the extreme ultraviolet to the water window". In: *Nat. Photonics* (1 2007), pp. 336–342. DOI: 10.1038/nphoton.2007.76. URL: https://doi.org/10.1038/nphoton.2007.76.

[146] P. Emma, R. Akre, J. Arthur, et al. "First lasing and operation of an ångstrom-wavelength free-electron laser". In: *Nat. Photonics* (4 2010), p. 641. DOI: 10.1038/nphoton.2010.176. URL: https://doi.org/10.1038/nphoton.2010.176.

[147] M. Fuchs, R. Weingartner, A. Popp, et al. "Laser-driven soft-X-ray undulator source". In: *Nature Phys.* 5 (2009), 826—829. DOI: 10.1038/nphys1404. URL: https://doi.org/10.1038/nphys1404.

[148] W. Wang, K. Feng, L. Ke, et al. "Free-electron lasing at 27 nanometres based on a laser wakefield accelerator". In: *Nature* 595 (2021), pp. 516–520. DOI: 10.1038/s41586-021-03678-x. URL: https://doi.org/10.1038/s41586-021-03678-x.

[149] E. Allaria, R. Appio, L. Badano, et al. "Highly coherent and stable pulses from the FERMI seeded free-electron laser in the extreme ultraviolet". In: *Nat. Photonics* (6 2012), pp. 699–704. DOI: 10.1038/nphoton.2012.233. URL: https://doi.org/10.1038/nphoton.2012.233.

[150] E. C. Snively et al. "Femtosecond Compression Dynamics and Timing Jitter Suppression in a THz-driven Electron Bunch Compressor". In: *Phys. Rev. Lett.* 124 (5 2020), p. 054801. DOI: 10.1103/PhysRevLett.124.054801. URL: https://link.aps.org/doi/10.1103/PhysRevLett.124.054801.

[151] Lingrong Zhao et al. "Femtosecond Relativistic Electron Beam with Reduced Timing Jitter from THz Driven Beam Compression". In: *Phys. Rev. Lett.* 124 (5 2020), p. 054802. DOI: 10.1103/PhysRevLett.124.054802. URL: https://link.aps.org/doi/10.1103/PhysRevLett.124.054802.

[152] M.T. Hibberd, A.L. Healy, D.S. Lake, et al. "Acceleration of relativistic beams using laser-generated terahertz pulses". In: *Nat. Photonics* 14 (2020), pp. 755–759. DOI: 10.1038/s41566-020-0674-1. URL: https://doi.org/10.1038/s41566-020-0674-1.

[153] A.F. Medvedev and M.M. Nikitin. "Undulator radiation". In: *Soviet Physics Journal* 17.10 (1974), 1452—1453. DOI: 10.1007/BF00891308. URL: https://doi.org/10.1007/BF00891308.

[154] A. Hofmann. "Quasi-monochromatic synchrotron radiation from undulators". In: *Nuclear Instruments and Methods* 152.1 (1978), pp. 17–21. ISSN: 0029-554X. DOI: https://doi.org/10.1016/0029-554X(78)90231-8. URL: https://www.sciencedirect.com/science/article/pii/0029554X78902318.

[155] R. Coïsson. "Angular-spectral distribution and polarization of synchrotron radiation from a "short" magnet". In: *Phys. Rev. A* 20 (2 1979), pp. 524–528. DOI: 10.1103/PhysRevA.20.524. URL: https://link.aps.org/doi/10.1103/PhysRevA.20.524.

[156] R. Coïsson. "Spatial coherence of synchrotron radiation". In: *Applied Optics* 34.5 (1995). Cited by: 49; All Open Access, Green Open Access, 904—908. DOI: 10.1364/AO.34.000904. URL: https://www.scopus.com/inward/record.uri?eid=2-s2.0-0029253786&doi=10.1364%2fAO.34.000904&partnerID=40&md5=7993df170871cc061b4451a334fc5b21.

[157] R.P. Walker. "Near field effects in off-axis undulator radiation". In: *Nuclear Instruments and Methods in Physics Research Section A: Accelerators, Spectrometers, Detectors and Associated Equipment* 267.2 (1988), pp. 537–546. ISSN: 0168-9002. DOI: https://doi.org/10.1016/0168-9002(88)90496-2. URL: https://www.sciencedirect.com/science/article/pii/0168900288904962.

[158] R.P. Walker. "Interference effects in undulator and wiggler radiation sources". In: *Nuclear Instruments and Methods in Physics Research Section A: Accelerators, Spectrometers, Detectors and Associated Equipment* 335.1 (1993), pp. 328–337. ISSN: 0168-9002. DOI: https://doi.org/10.1016/0168-9002(93)90288-S. URL: https://www.sciencedirect.com/science/article/pii/016890029390288S.

[159] Kwang-Je Kim. "Brightness, coherence and propagation characteristics of synchrotron radiation". In: *Nuclear Instruments and Methods in Physics Research Section A: Accelerators, Spectrometers, Detectors and Associated Equipment* 246.1 (1986), pp. 71–76. ISSN: 0168-9002. DOI: https://doi.org/10.1016/0168-9002(86)90048-3. URL: https://www.sciencedirect.com/science/article/pii/0168900286900483.

[160] Gianluca Geloni et al. "Transverse coherence properties of X-ray beams in third-generation synchrotron radiation sources". In: *Nuclear Instruments and Methods in Physics Research Section A: Accelerators, Spectrometers, Detectors and Associated Equipment* 588.3 (2008), pp. 463–493. ISSN: 0168-9002. DOI: https://doi.org/10.1016/j.nima.2008.01.089. URL: https://www.sciencedirect.com/science/article/pii/S0168900208001605.

[161] A. Ghaith et al. "Undulator design for a laser-plasma-based free-electron-laser". In: *Physics Reports* 937 (2021). Undulator design for a laser-plasma-based free-electron-laser, pp. 1–73. ISSN: 0370-1573. DOI: https://doi.org/10.1016/j.physrep.2021.09.001. URL: https://www.sciencedirect.com/science/article/pii/S0370157321003434.

[162] R. Bonifacio, C. Pellegrini, and L.M. Narducci. "Collective instabilities and high-gain regime in a free electron laser". In: *Optics Communications* 50.6 (1984), pp. 373–378. ISSN: 0030-4018. DOI: https://doi.org/10.1016/0030-4018(84)90105-6. URL: https://www.sciencedirect.com/science/article/pii/0030401884901056.

[163] Zhirong Huang, Yuantao Ding, and Carl B. Schroeder. "Compact X-ray Free-Electron Laser from a Laser-Plasma Accelerator Using a Transverse-Gradient Undulator". In: *Phys. Rev. Lett.* 109 (20 2012), p. 204801. DOI: 10.1103/PhysRevLett.109.204801. URL: https://link.aps.org/doi/10.1103/PhysRevLett.109.204801.

[164] M. Zhou et al. "Beam head erosion in self-ionized plasma wakefield accelerators". In: *2007 IEEE Particle Accelerator Conference (PAC)*. 2007, pp. 3064–3066. DOI: 10.1109/PAC.2007.4440669.

[165] W. An et al. "Strategies for mitigating the ionization-induced beam head erosion problem in an electron-beam-driven plasma wakefield accelerator". In: *Phys. Rev. ST Accel. Beams* 16 (10 2013), p. 101301. DOI: 10.1103/PhysRevSTAB.16.101301. URL: https://link.aps.org/doi/10.1103/PhysRevSTAB.16.101301.

[166] T. Mehrling et al. "Transverse emittance growth in staged laser-wakefield acceleration". In: *Phys. Rev. ST Accel. Beams* 15 (11 2012), p. 111303. DOI: 10.1103/PhysRevSTAB.15.111303. URL: https://link.aps.org/doi/10.1103/PhysRevSTAB.15.111303.

[167] J.-L. Vay et al. "Numerical methods for instability mitigation in the modeling of laser wakefield accelerators in a Lorentz-boosted frame". In: *Journal of Computational Physics* 230.15 (2011), pp. 5908–5929. ISSN: 0021-9991. DOI: https://doi.org/10.1016/j.jcp.2011.04.003. URL: https://www.sciencedirect.com/science/article/pii/S0021999111002270.

[168] R. D'Arcy et al. "FLASHForward: plasma wakefield accelerator science for high-average-power applications". In: *Philosophical Transactions of the Royal Society A: Mathematical, Physical and Engineering Sciences* 377.2151 (2019), p. 20180392. DOI: 10.1098/rsta.2018.0392. eprint: https://royalsocietypublishing.org/doi/pdf/10.1098/rsta.2018.0392. URL: https://royalsocietypublishing.org/doi/abs/10.1098/rsta.2018.0392.

[169] I. Dornmair, K. Floettmann, and A. R. Maier. "Emittance conservation by tailored focusing profiles in a plasma accelerator". In: *Phys. Rev. ST Accel. Beams* 18 (4 Apr. 2015), p. 041302. DOI: 10.1103/PhysRevSTAB.18.041302. URL: https://link.aps.org/doi/10.1103/PhysRevSTAB.18.041302.

[170] Klaus Floettmann. "Adiabatic matching section for plasma accelerated beams". In: *Phys. Rev. ST Accel. Beams* 17 (5 2014), p. 054402. DOI: 10.1103/

PhysRevSTAB.17.054402. URL: https://link.aps.org/doi/10.1103/PhysRevSTAB.17.054402.

[171] Károly Németh et al. "Laser-Driven Coherent Betatron Oscillation in a Laser-Wakefield Cavity". In: *Phys. Rev. Lett.* 100 (9 2008), p. 095002. DOI: 10.1103/PhysRevLett.100.095002. URL: https://link.aps.org/doi/10.1103/PhysRevLett.100.095002.

[172] V. Horný et al. "Attosecond betatron radiation pulse train". In: *Scientific Reports* 10 (2020), p. 15074. DOI: 10.1038/s41598-020-72053-z. URL: https://doi.org/10.1038/s41598-020-72053-z.

[173] S. Cipiccia et al. "Gamma-rays from harmonically resonant betatron oscillations in a plasma wake". In: *Nature Physics* 7 (2011), 867—871. DOI: 10.1038/nphys2090. URL: https://doi.org/10.1038/nphys2090.

[174] J. Vieira et al. "Generalized superradiance for producing broadband coherent radiation with transversely modulated arbitrarily diluted bunches". In: *Nature Physics* 17 (2021), 99—104. DOI: 10.1038/s41567-020-0995-5. URL: https://doi.org/10.1038/s41567-020-0995-5.

[175] A. J. Goers et al. "Multi-MeV Electron Acceleration by Subterawatt Laser Pulses". In: *Phys. Rev. Lett.* 115 (19 2015), p. 194802. DOI: 10.1103/PhysRevLett.115.194802. URL: https://link.aps.org/doi/10.1103/PhysRevLett.115.194802.

[176] D. Guénot, D. Gustas, A. Vernier, et al. "Relativistic electron beams driven by kHz single-cycle light pulses." In: *Nature Photon.* 11 (5 2017), 293—296. DOI: 10.1038/nphoton.2017.46. URL: https://doi.org/10.1038/nphoton.2017.46.

[177] D. Gustas et al. "High-charge relativistic electron bunches from a kHz laser-plasma accelerator". In: *Phys. Rev. Accel. Beams* 21 (1 2018), p. 013401. DOI: 10.1103/PhysRevAccelBeams.21.013401. URL: https://link.aps.org/doi/10.1103/PhysRevAccelBeams.21.013401.

[178] F. Salehi et al. "Laser-Accelerated, Low-Divergence 15-MeV Quasimonoenergetic Electron Bunches at 1 kHz". In: *Phys. Rev. X* 11 (2 2021), p. 021055. DOI: 10.1103/PhysRevX.11.021055. URL: https://link.aps.org/doi/10.1103/PhysRevX.11.021055.

[179] P. W. Lai et al. "Laser wakefield acceleration of 10-MeV-scale electrons driven by 1-TW multi-cycle laser pulses in a sub-millimeter nitrogen gas cell". In: *Phys. Plasmas* 30.1 (2023), p. 010703. DOI: 10.1063/5.0131155.

[180] C. M. Lazzarini et al. *50 MeV electron beams accelerated by a terawatt scalable kHz laser*. 2023. arXiv: 2302.11415 [physics.plasm-ph].

[181] Zhongtao Xiang et al. "Ultrahigh-brightness 50 MeV electron beam generation from laser wakefield acceleration in a weakly nonlinear regime". In: *Matter and Radiation at Extremes* 9.3 (Feb. 2024), p. 035201. ISSN: 2468-2047. DOI: 10.1063/5.0189460. eprint: https://pubs.aip.org/aip/mre/article-pdf/doi/10.1063/5.0189460/19713388/035201_1_5.0189460.pdf. URL: https://doi.org/10.1063/5.0189460.

[182] S Toth et al. "SYLOS lasers – the frontier of few-cycle, multi-TW, kHz lasers for ultrafast applications at extreme light infrastructure attosecond light pulse source". In: *Journal of Physics: Photonics* 2.4 (2020), p. 045003. DOI: 10.1088/2515-7647/ab9fe1. URL: https://dx.doi.org/10.1088/2515-7647/ab9fe1.

[183] Thomas Nubbemeyer et al. "1 kW, 200 mJ picosecond thin-disk laser system". In: *Opt. Lett.* 42.7 (2017), pp. 1381–1384. DOI: 10.1364/OL.42.001381. URL: https://opg.optica.org/ol/abstract.cfm?URI=ol-42-7-1381.

[184] Martin Kaumanns et al. "Multipass spectral broadening of 18 mJ pulses compressible from 1.3 ps to 41 fs". In: *Opt. Lett.* 43.23 (2018), pp. 5877–5880. DOI: 10.1364/OL.43.005877. URL: https://opg.optica.org/ol/abstract.cfm?URI=ol-43-23-5877.

[185] N. H. Matlis et al. "Single-Shot, Real-Time Measurement of Laser Wakefields Using Frequency Domain Holography (FDH)". In: *Conference on Lasers and Electro-Optics/Quantum Electronics and Laser Science Conference and Photonic Applications Systems Technologies*. Optica Publishing Group, 2006, JWC3. URL: https://opg.optica.org/abstract.cfm?URI=QELS-2006-JWC3.